Hyperfine interactions and quantum information processing in quantum dots

A dissertation presented
by

Jacob Mason Taylor

to
The Department of Physics
in partial fulfillment of the requirements
for the degree of
Doctor of Philosophy
in the subject of

Physics

Harvard University
Cambridge, Massachusetts
August 2006

©2006 - Jacob Mason Taylor

All rights reserved.

Thesis advisor

Mikhail D. Lukin

Author

Jacob Mason Taylor

Hyperfine interactions and quantum information processing in quantum dots

Abstract

This thesis explores the feasibility of using electron spins in semiconductor quantum dots as fundamental building blocks for quantum information processing. We start from a general perspective, evaluating the possible limits to operation of such a spin-based system. We show that the coherence properties of electron spins are limited by their interaction with lattice nuclear spins. We then consider approaches that take advantage of the long coherence and relaxation times of the lattice nuclear spins to mitigate their effect on the electron spin, and show how they could be used as a resource for long-term quantum memory in the solid-state.

Next, we develop techniques for experimentally probing electron spin–nuclear spin interactions in quantum dots, and demonstrate the controlled creation and measurement of entangled electron spin states. A new paradigm for quantum information processing in the presence of nuclear spins emerges—one that uses two electron spins to form a single quantum bit. We demonstrate theoretically and experimentally the potential for long-lived quantum memory using this system system, and find improved, specialized approaches to quantum communication and quantum computing using pairs of electron spins. Finally, we consider methods for scaling the system to large numbers of quantum bits such that techniques for robust computation, including fault-tolerant computation, might be realized.

Contents

Title Page i
Abstract iii
Table of Contents iv
List of Figures vii
List of Tables ix
Citations to Previously Published Work x
Acknowledgments xi
Dedication xiv

1 Introduction **1**
1.1 Background 1
1.2 Overview 2
1.3 Hyperfine interactions in a single quantum dot 4

2 Dephasing of quantum bits by a quasi-static mesoscopic environment **11**
2.1 The physical system 14
2.2 Free evolution 22
2.3 Driven-evolution 27
2.4 Application to experimental systems 37
2.5 Methods to mitigate bath effects 42
2.6 Conclusions 47

3 Long-lived quantum memory in a mesoscopic environment **49**
3.1 Nuclear ensemble memory 50
3.2 Preparation and control of a mesoscopic environment 60

4 Quantum information processing using localized ensembles of nuclear spins **71**
4.1 Qubits and quantum operations 73
4.2 Error mechanisms 82
4.3 Materials and estimates 89
4.4 Conclusions 90

5 Quantum measurement of a mesoscopic spin ensemble 93
5.1 Phase estimation . . . 95
5.2 The measurement scheme . . . 97
5.3 Performance of the scheme . . . 102
5.4 Errors and Fluctuations in A_z . . . 103
5.5 Example: Estimating collective nuclear spin in a quantum dot . . . 107
5.6 Conclusions . . . 111

6 Relaxation, dephasing, and quantum control of electron spins in double quantum dots 113
6.1 Electron spins in a double quantum dot . . . 115
6.2 Nuclear-spin-mediated relaxation in double dots . . . 130
6.3 Quantum control of two electron spin states . . . 138
6.4 Exchange gates and echo techniques . . . 159
6.5 Conclusions . . . 167

7 Electronic pumping of nuclear spin polarization in a double quantum dot 171
7.1 Experimental setup . . . 173
7.2 Electron spin-nuclear spin interactions . . . 176
7.3 Nuclear spin polarization . . . 179
7.4 Theory of polarization in the weak polarization limit . . . 183
7.5 Conclusions . . . 185

8 Robust non-local entanglement generation in quantum dots 187
8.1 A single electron quantum repeater . . . 190
8.2 Limits to the single-electron scheme . . . 202
8.3 Two electron encoding . . . 206
8.4 Conclusions . . . 215

9 Cavity quantum electrodynamics with semiconductor double-dot molecules on a chip 217
9.1 Effective Hamiltonian . . . 219
9.2 Operating point . . . 221
9.3 Generalized approach . . . 223
9.4 Noise and decoherence . . . 223
9.5 Quantum control . . . 225
9.6 Conclusions . . . 228

10 Fault-tolerant architecture for quantum computation using electrically controlled semiconductor spins 229
10.1 Protected qubits and quantum gates . . . 231
10.2 Errors in quantum operations . . . 236
10.3 Fault tolerance and error thresholds . . . 240
10.4 Methods . . . 244

10.5 Outlook 246

A Details for Chapters 1: breakdown of the quasi-static approximation 249

B Details for Chapter 2: spin bath-related integrals and models 255
B.1 Integrals involved in driven evolution 255
B.2 Comparison with superconducting qubits: model 257

C Details for Chapter 6: inelastic decay and charge-based dephasing 259
C.1 Adiabatic elimination for nuclear-spin-mediated inelastic decay 259
C.2 Dephasing power spectra 261

D Reprint of Ref. [96], "Triplet-singlet spin relaxation via nuclei in a double quantum dot" 265

E Details for Chapter 7: spin diffusion via nuclear dipole-dipole interactions 271

F Details for Chapter 8: electron spin-based quantum repeaters and $m_s = 0$ measurement methods 275
F.1 Measurement-based preparation 275
F.2 Purification with $m_s = 0$ measurement for single electron proposal 277
F.3 Adiabatic preparation 281

Bibliography 285

List of Figures

1.1 Electron spin in a quantum dot interacting with lattice nuclear spins 5

2.1 Heirarcichal system–bath–environment coupling 17
2.2 Free-induction decay 24
2.3 Low-power lineshape 30
2.4 Rabi oscillations 34
2.5 Rabi oscillations with decorrelation of the bath 37
2.6 Comparison of theory to superconducting qubit experiments 41

3.1 Storage of electron spin states in an ensemble of nuclear spins 52
3.2 Transfer characteristics for different nuclear polarizations 58
3.3 Dark state polarization and entropy 63
3.4 Dark state interaction parameters 69
3.5 Quantum memory fidelity with dark states 70

4.1 Quantum dot based approaches for nuclear ensemble-based computation . . 73
4.2 Level structure for nuclear ensemble qubits 80
4.3 A network of small scale quantum computing devices 81
4.4 Error for nuclear ensemble computation 90

5.1 Illustration of the first two steps of the measurement procedure 98
5.2 Estimation in the presence of preparation and measurement error 104

6.1 Experimental setup 116
6.2 Charge and orbital states for a double dot 119
6.3 Exact solution: charge and orbital states 121
6.4 The far detuned and charge transition regimes 122
6.5 A double quantum dot in the (1,1) configuration 124
6.6 Level structure: far detuned and charge transition cases 125
6.7 Cycle and measuring exchange 128
6.8 Energy level structure as a function of detuning 132
6.9 Field dependence of spin-blockade 136
6.10 Charge signal of spin blockade 137

6.11 Rapid- and slow-adiabatic passage . . . 140
6.12 Pulse sequences . . . 144
6.13 Measuring T_2^* . . . 147
6.14 Exchange oscillations . . . 153
6.15 Dephasing in the far detuned and charge transition regimes . . . 155
6.16 Decay of exchange oscillations . . . 158
6.17 Expected echo signal . . . 162
6.18 Singlet-triplet spin echo . . . 164

7.1 Schematic of the experimental setup . . . 174
7.2 Time and energy dependence of the singlet–T_+ resonance . . . 178
7.3 The singlet–T_+ crossing . . . 180
7.4 Polarization: simulation and experiment . . . 182

8.1 Scheme for entanglement generation and purification with four spins . . . 189
8.2 Generating and measuring entanglement in a double quantum dot . . . 192
8.3 Purification curve for single spins . . . 198
8.4 Measurement scheme for purification . . . 209
8.5 Gate network for entanglement generation . . . 210
8.6 Gate network for purification . . . 213

9.1 Two double quantum dots interacting via a transmission line resonator . . . 219
9.2 Coupling between a double quantum dot and a resonator . . . 224
9.3 Dephasing and double dot–resonator coupling . . . 226

10.1 Architecture for quantum computation . . . 232
10.2 Logical qubit . . . 233
10.3 Long-range qubit transport . . . 237
10.4 Teleportation-based gates . . . 243

F.1 Projective measurement with gradients . . . 278
F.2 Four-dot exchange . . . 282
F.3 Adiabatic preparation with four dots . . . 284

List of Tables

1.1 Time, energy, and magnetic field scales for electron and nuclear spins in a single and double quantum dots, from fast to slow. 9

2.1 Fitted values for the experiments of Ref. [128] 41

3.1 Adiabatic transfer with ESR spin echo. 65

4.1 Error budget for computation 82

Citations to Previously Published Work

Many of the chapters of this thesis have appeared in print elsewhere. By chapter number, they are:

- Chapter 2: "Dephasing of Quantum Bits by a Quasi-Static Mesoscopic Environment," J. M. Taylor and M. D. Lukin (e-print: quant-ph/0512059), to appear in the QUPON conference proceedings.
- Chapter 3: "Long-Lived Memory for Mesoscopic Quantum Bits," J. M. Taylor, C. M. Marcus, and M. D. Lukin, *Phys. Rev. Lett.* **90** (2003), pp. 206803–6, and "Controlling a Mesoscopic Spin Environment by Quantum Bit Manipulation," J. M. Taylor, A. Imamoglu, and M. D. Lukin, *Phys. Rev. Lett.* **91** (2003), pp. 246802–5.
- Chapter 4: A shorter version is available as "Quantum Information Processing using Localized Ensembles of Nuclear Spins," J. M. Taylor, G. Giedke, H. Christ, B. Paredes, J. I. Cirac, P. Zoller, M. D. Lukin, and A. Imamoglu (eprint: cond-mat/0407640).
- Chapter 5: "Scheme for Quantum Measurement of the Nuclear Spin Polarization in Quantum Dots," G. Giedke, J. M. Taylor, D. D'Alessandro, M. D. Lukin, and A. Imamoglu (e-print: quant-ph/0508144), to appear in Phys. Rev. A.
- Chapters 1 and 6: the theoretical work appears in "Relaxation, Dephasing, and Quantum Control of Electron Spins in Double Quantum Dots," J. M. Taylor, J. R. Petta, A. C. Johnson, A. Yacoby, C. M. Marcus, and M. D. Lukin (e-print: cond-mat/0602470), submitted to Phys. Rev. B, while the experimental work appears in "Coherent Manipulation of Coupled Electron Spins in Semiconductor Quantum Dots," J. R. Petta, A. C. Johnson, J. M. Taylor, E. A. Laird, A. Yacoby, M. D. Lukin, C. M. Marcus, M. P. Hanson, and A. C. Gossard *Science* **309** (2005), pp. 2180–4.
- Chapter 8: the final section appears in "Solid-state Circuit for Spin Entanglement Generation and Purification," J. M. Taylor, W. Dür, P. Zoller, A. Yacoby, C. M. Marcus, and M. D. Lukin, *Phys. Rev. Lett.* **94** (2005), pp. 236803-1–4.
- Chapter 9: "Cavity quantum electrodynamics with semiconductor double-dot molecules on a chip," J. M. Taylor and M. D. Lukin (e-print: cond-mat/0605144), submitted to Phys. Rev. Lett.
- Chapter 10: "Fault-tolerant Architecture for Quantum Computation Using Electrically Controlled Semiconductor Spins," J. M. Taylor, H.-A. Engel, W. Dür, P. Zoller, A. Yacoby, C. M. Marcus, and M. D. Lukin, *Nature Physics* **1** (2005), pp. 177–83.

Chapter 7 has not appeared elsewhere. At the beginning of each chapter, all contributing authors are listed, in the same order as the corresponding publications.

Acknowledgments

In the course my doctoral studies, innumerable people provided help at every stage. I cannot hope to encompass everyone, but I will start by thanking my adviser, Prof. Mikhail Lukin, for his support from day one for this project and for my scientific career. I feel blessed to have had such an enjoyable graduate school experience, and I attribute this in large part to the dedication Misha shows to his students.

Similarly, at an early stage in graduate school, Prof. Charles Marcus encouraged an effective and no-nonsense collaboration, which has been long and fruitful. Charlie's support in training a theorist to run a dilution refrigerator and his insistence on thinking even when doing the most mundane of tasks have been formative experiences for me. I also acknowledge Prof. Bertrand Halperin's aid both in feedback on my thesis topic and related, intriguing questions from a condensed-matter perspective, and in support of my scientific career. It was a rare occasion that discussion with Burt was not immediately useful.

Beyond my committee, my long-time collaborators in Zürich and Innsbruck deserve great thanks. My first scientific visit with Prof. Atac Imamoğlu and his research group at ETH Zürich taught me the beauty of directed visits and focused inquiry. I am also indebted in particular to Geza Giedke and Mete Atatüre for discussions and their hospitality during my many stays in Zürich.

Collaboration and visits with Prof. Peter Zoller and the IQOQI groups at Innsbruck were also a critical part of the present study. Beyond the amazing depth of knowledge and insight Peter brings to any problem of interest, I am lucky to have found such support, both on scientific grounds and personal grounds, such as when minor tragedy (in the form of a skiing accident) struck. The help of Peter, Prof. Reiner Blatt, Hans-Peter Bücher, Andrew Daly, and the rest of the Innsbruck quantum information crowd helped me feel at home even when staying at a hospital in a foreign country. I also would like to thank Wolfgang Dür for helping me develop ill-formed creative ideas into robust protocols.

In addition to many fruitful scientific discussions, I would like to thank my co-workers and colleagues in both Misha's and Charlie's groups for providing a welcoming environment and fun times. I would particularly single out Axel André and Caspar van der Wal for helping me orient to life in the group and graduate school more generally, and Lillian Childress and Anders Sorensen for encouraging me to develop better collaborative skills and being generally great to worry about science with.

Within the Marcus group, I learned more about experimental physics that I anticipated possible from Jason Petta, Alex Johnson, Nathaniel Craig, and Amir Yacoby, while discussions with Mike Biercuk and Dominic Zumbühl (and frozen blueberries) were a critical part of staying happy while running an experiment. Joshua Folk also had a strong influence upon the way that I now approach experiments. I also have enjoyed many other interactions within the condensed matter community at Harvard, particularly with Hansres Engel.

There are many others that have been crucial in the process of developing a scientific career—Ron Walsworth, for keeping a clean perspective on the larger picture of life as a physicist; Dave Philips for being Dave; James Babb and Alex Dalgarno, for getting me started; Rick Heller, for early encouragement; and Josh Grindlay and Peter Edmonds for supporting me in research and life for so long.

I have many friends who have supported me throughout five years of graduate student, from working on problem sets to working on Halo. Thanks to Steve and Iva and the puppet show eight, DS, Geoff, Katerina, Hollywood, Jay Mack, Chewie, Grok, Jeff, Buffy, Jonathan, Lisa, Lily, Dan, Mike—hard to imagine how one would survive graduate school without friends like these.

My parents have been more supportive of this process that one could hope for, encouraging and complementing the work accomplished and the work to come, and available

to talk at any time. And finally, Jean is, as always for me, an inspiration in life and love.

Dedicated to my parents,
who taught me that
curiosity never killed the cat.

Chapter 1

Introduction

1.1 Background

Magnetic interactions have been a central point of study in physics throughout the 19th and 20th centuries. Much of our understanding of atomic physics and solid state physics is based upon theories of the quantum mechanical nature of the intrinsic magnetic dipoles (spins) of fundamental particles. Over the last decade, spin has also become a paradigm connecting the ideas of computation to quantum mechanical systems. Spin-1/2 particles, with two distinct quantized states, bear a marked similarity to a classical bit, and may be considered as a quantum bit, or qubit. However, by going beyond the approximations leading to the emergence of classical mechanics and thermodynamics, quantum mechanical systems such as spins may achieve a substantially larger range of dynamics than classical systems. It was suggested early on [70] that quantum mechanical systems could perform computations and simulations of staggering complexity. Later work showed that certain problems, such as factoring, could be solved exponentially faster by a quantum mechanical computation system [60]. This arises mathematically as the dynamics of the classical system are governed by a polynomial number of equations in the number of bits, while a quantum

mechanical system of interacting spins may have exponentially many non-trivial equations of motion in the number of quantum bits.

Finding a practical approach for harnessing the complexity of quantum mechanics for controlled simulation or computation remains an outstanding challenge for modern physics. We must manipulate, cause to interact, and, in a controlled manner, measure many physically distinct quantum mechanical objects such that no undesired "collapse" of the wavefunction occurs. The collapse occurs when the state of the computation system becomes entangled with the state the environment in which our quantum mechanical system exists. On the one hand we want to isolate our computation system as well as possible from the environment; but on the other hand, we require a connection to the outside world to reliably manipulate the system. These contradictory requirements present the primary difficulty for the development of a quantum mechanical computer.

1.2 Overview

This thesis focuses on the interplay between physical systems, their environment, and quantum information science. The work considers, almost exclusively, electron spins in quantum dots as potential quantum bits and their environment of lattice nuclear spins. We start by considering lattice nuclear spins as an unwanted source of noise for electron spins, then elaborate on methods for mitigating this effect, as well as manipulating the nuclear spins and potentially using the interaction as a resource for quantum information protocols. Finally, we consider how larger scale architectures for quantum computing using electron spins may be made insensitive to this potential source of noise, in the process suggesting a path towards robust, many qubit quantum computation.

A quantum dot is formed in a semiconductor structure by confining electrons to

a physically small region at low temperatures. Loss and Divincenzo [122] were the first to suggest that the spin of single electrons in such structures could be used for quantum computing. There are several advantages: the spin is weakly coupled to almost everything in the system, leading to potentially long lifetimes for the information stored in the spin state of the electron, while the quantum dot system could be engineered using modern semiconductor technology, possibly leading to very large scale integration of many quantum bits onto a single computer chip. However, the greatest disadvantage is the hyperfine coupling of the electron spin in a quantum dot to the lattice nuclear spins of the semiconductor, which is orders of magnitude stronger than the coupling to phonons and other noise sources [122, 134, 103, 82].

We start with a review of hyperfine interactions in a single quantum dot. The next several chapters investigate how lattice nuclear spins may be considered a substantial source of noise for quantum information processing using electron spins (Chapter 2) but also be coherent manipulated to provide a potential resource for quantum computation (Chapters 3 and 4). Other techniques for reducing the errors due to nuclear spins, either by measurement (Chapter 5) or by passive encoding of information in noise-less subspaces using pairs of electron spins (Chapters 6 and 8) are investigated. In the process, some new ideas for implementing quantum information protocols with pairs of electron spins were realized, and these are developed in Chapters 6, 7, and 10. Concurrent with this theoretical work, experimental investigations in collaboration with the Marcus group at Harvard confirmed the theoretical approaches suggested here and are included in Chapter 6. Additional experimental work, in which we attempt to directly manipulate the nuclear spins using our control of the electron spin, is detailed in Chapter 7.

Finally, we shift focus from individual electron spins to the intriguing question of connection: how can quantum information be efficiently shared at long distances using a

semiconductor, and can long-range interactions lead to large-scale computation? Protocols for quantum communication using electron spins are developed in Chapter 8. Chapter 9 develops ideas for converting electron spin information into the existence or absence of a microwave photon in an on-chip resonator, while Chapter 10 considers the scalability of a two-spin-based architecture using controlled transport of single spins.

1.3 Hyperfine interactions in a single quantum dot

We begin by reviewing the basic physics of hyperfine interactions for electron spins in single GaAs quantum dots. The material of this section reviews the established theory for single quantum dots [164, 134, 103, 43] and considers dynamical corrections to the model of Refs. [164, 134]. This model will be used in subsequent chapters. Additional terms, such as spin-orbit coupling, are neglected; theory [105, 104, 82] and experiment [87, 96] have demonstrated that spin-orbit related terms lead to dephasing and relaxation on time scales of milliseconds, whereas we will focus on interaction times on the order of nanoseconds to microseconds. On these time scales, the orbital degrees of freedom, with characteristic level spacings $\upsilon \sim 0.5-1$ meV, may be averaged over. The resulting low energy dynamics are due entirely to a single, ground orbital state of the electron with a two spin states. We remark that other III-V semiconductors have similar behavior—all III-V alloys have non-vanishing nuclear spin components.

1.3.1 Electron spin Hamiltonian for a single quantum dot

The Hamiltonian for the Kramer's doublet of the ground orbital state of the quantum dot (denoted by the spin-1/2 vector $\hat{\vec{S}}$) including hyperfine contact interactions with

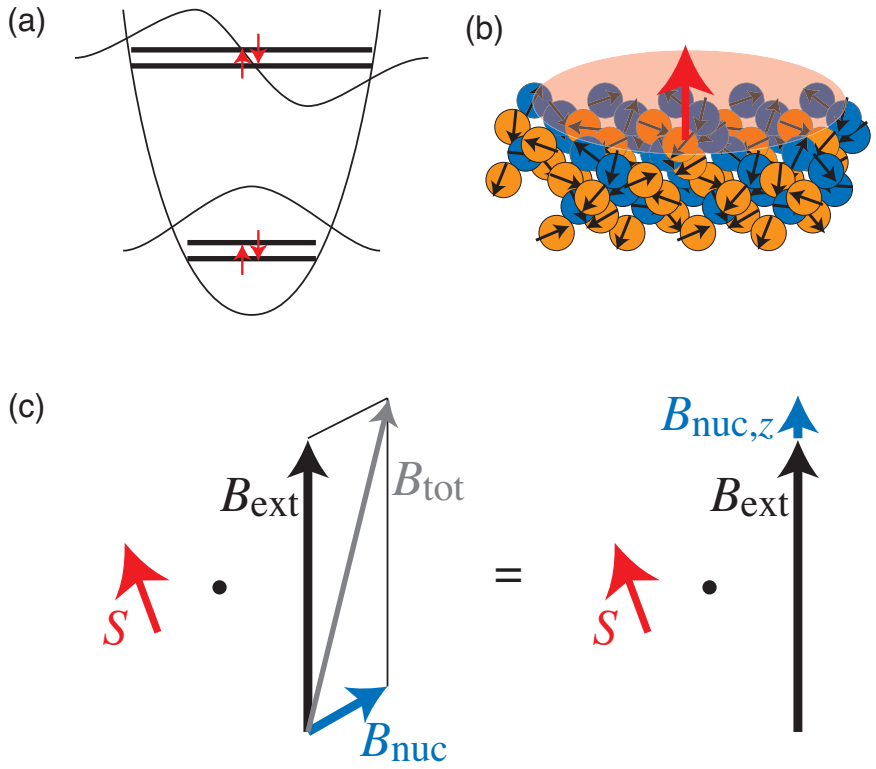

Figure 1.1: (a) A schematic potential and energly level diagram for a single quantum dot, in which one electron is confined to the low energy spectrum of a three dimensional potential. Only the first and second orbital excited states, each a Kramer's doublet, are shown. (b) The lowest orbital state has a spin-1/2 electron (red cloud) interacting with the lattice nuclear spins (blue and orange spheres). (c) Effective magnetic field due to both external field and the nuclear field. When the external field is large, the transverse components of the nuclear field are neglected in a rotating wave approximation.

lattice nuclei (spins $\hat{\vec{I}}^{\beta,j}$) is [147, 134]

$$H = \hbar\gamma_e \vec{B}_{ext} \cdot \hat{\vec{S}} + \hbar\gamma_e \sum_{\beta,j} b_{\beta,j} \alpha_j \hat{\vec{S}} \cdot \hat{\vec{I}}^{\beta,j} \tag{1.1}$$

where $\gamma_e = g^* \mu_B / \hbar$ is the gyromagnetic ratio for electron spin $\hat{\vec{S}}$; sums are over nuclear species (β) and unit cells (j). Anisotropy in the spin interaction is neglected as the conduction band electrons' s-state character have a large contact term and weak long-range dipole terms. Correspondingly, b_β is the effective hyperfine field due to species β within a unit cell, with $b_{^{75}\mathrm{As}} = -1.84$ T, $b_{^{69}\mathrm{Ga}} = -1.52$ T, and $b_{^{71}\mathrm{Ga}} = -1.95$ T for GaAs [147]. The coefficient $\alpha_j = v_0 |\psi(\vec{r}_j)|^2$ is the probability of the electron being at unit cell j, v_0 is the volume of the unit cell (2 nuclei), and $\psi(r)$ the envelope wavefunction of the localized electron.

It is convenient to rewrite the Hamiltonian using a collective operator for the nuclear spins, $\hat{\vec{B}}_{\mathrm{nuc}} = \sum_\beta b_\beta \sum_j \alpha_j \hat{\vec{I}}^{\beta,j}$. This operator allows us to write the Hamiltonian as an electron spin interacting with an external magnetic field, $\vec{B}_{\mathrm{ext}}$ and an intrinsic field, $\hat{\vec{B}}_{\mathrm{nuc}}$:

$$H_{\mathrm{eff}} = \hbar\gamma_e (\vec{B}_{\mathrm{ext}} + \hat{\vec{B}}_{\mathrm{nuc}}) \cdot \hat{\vec{S}} \; . \tag{1.2}$$

In electron spin resonance, the effect of this nuclear field on the Larmor precession frequency of the electron spin is known as the Overhauser shift, while in nuclear magnetic resonance, the effect of the electron spin on the nuclear spin precession frequency is the Knight shift.

Several characteristic values [147, 134] for this interaction are noted in Table 1.1. The maximum nuclear field value (all spins fully polarized with value $I = 3/2$) is $h_0 = \sum_\beta b_\beta (x_\beta I^\beta) \sum_k \alpha_k$, where the relative population of nuclear species is $x_{^{75}\mathrm{As}} = 1$, $x_{^{69}\mathrm{Ga}} = 0.6$, and $x_{^{71}\mathrm{Ga}} = 0.4$ for GaAs, giving $b_0 = 5.3$ T. Second, when the nuclear spins may be described by a density matrix $\rho = \hat{1}/(2I+1)^N$ (infinite temperature approximation for N

nuclei), the root-mean-square (rms) strength of the field[1] is

$$B_{\rm nuc} = \sqrt{\langle|\hat{\vec{B}}_{\rm nuc}|^2\rangle/3} = \sqrt{\sum_{\beta,k} b_\beta^2 \alpha_k^2 \langle|\hat{\vec{I}}^{\beta,k}|^2\rangle/3} \tag{1.3}$$

$$= \sqrt{(\sum_\beta x_\beta b_\beta^2) I(I+1) v_0/3 \int d^3r \ |\psi(r)|^4} \tag{1.4}$$

$$= h_1/\sqrt{N} \ . \tag{1.5}$$

where we have replaced $\sum_j v_0$ with $\int d^3r$. The characteristic strength parameter is $h_1 = \sqrt{2I(I+1)/3\sum_\beta x_\beta b_\beta^2} = 4.0$ T for GaAs, and N is defined as the number of nuclei with which the electron has significant overlap, i.e., $N = 2/[\int d^3r \ |\psi(r)|^4 v_0]$.

While these numerical values are specific for GaAs quantum dots, in general dots in other materials with non-zero nuclear spin may be described by similar parameters: a maximum field strength parameter h_0 and a rms field strength parameter, $B_{\rm nuc} = h_1/\sqrt{N}$.

1.3.2 The quasi-static approximation for nuclear spins

By writing the Hamiltonian (Eq. 1.2) with nuclei as an effective magnetic field, we have implicitly indicated that the field may be considered on a similar footing to the external magnetic field, i.e., the operator $\hat{\vec{B}}_{\rm nuc}$ may be replaced by the classical vector $\vec{B}_{\rm nuc}$, and expectation values $\langle\rangle_{\rm nuc}$ are replaced by averages over the different initial classical field values. The distribution used for averagine in the large N limit is

$$P(\vec{B}) = \frac{1}{(2\pi B_{\rm nuc}^2)^{3/2}} \exp(-(\vec{B}\cdot\vec{B})/2B_{\rm nuc}^2) \ . \tag{1.6}$$

This is the quasi-static approximation (QSA[2]) used in Refs. [164, 134]: we assume that over time scales corresponding to electron spin evolution, the nuclear terms do not vary.

[1] A different convention than that of Ref. [134] is used: gaussians are always described by their rms, rather than $\sqrt{2}$ times their rms. Thus our value of $B_{\rm nuc} = \Delta_B/\sqrt{2}$, and similarly for other values to follow.

[2] The QSA is designated the quasi-stationary fluctuating fields approximation in Ref. [134].

In terms of dephasing, we cite the results of Ref. [134]. At zero external magnetic field in the Heisenberg picture, the electron spin $\hat{\vec{S}}$ evolves to:

$$\langle \hat{\vec{S}}(t) \rangle_{\rm nuc} = \frac{\hat{\vec{S}}(0)}{3}(1 + 2(1 - (\gamma_e B_{\rm nuc} t)^2) e^{-(\gamma_e B_{\rm nuc} t)^2}). \tag{1.7}$$

On the other hand, for large external magnetic fields, spin flips are not allowed by energy conservation, but transverse spin components (e.g., $\hat{S}_x$) decay as:

$$\langle \hat{S}_x \rangle_{\rm nuc} = \frac{\hat{S}_x}{2}(1 + e^{-\frac{1}{2}(\gamma_e B_{\rm nuc} t)^2}) \ . \tag{1.8}$$

A time-ensemble-averaged dephasing time due to nuclei in a single dot at large external magnetic field is

$$T_2^* = \frac{1}{\Omega_{\rm nuc}} = \frac{1}{\gamma_e B_{\rm nuc}} \ . \tag{1.9}$$

This definition is appropriate when considering the decay of coherence of a single electron in a single quantum dot.

Generalizing to all field values, for times longer than T_2^*,

$$\hat{\vec{S}}(t \gg \Omega_{\rm nuc}^{-1}) = \langle (\hat{\vec{S}}(t=0) \cdot \vec{n}) \vec{n} \rangle_{\rm nuc} \tag{1.10}$$

gives the average electron spin value, averaged over a time $\tau = 2\pi/\omega$.

The assumptions underlying the QSA are immediately applicable our pulsed experiments [96, 151]. The interactions with the nuclear spins during a pulse sequence ("run") occurs on sub-microsecond timescales, but each data point corresponds to integrating over many runs, taking a total time of order seconds. If the nuclear field decorrelates slower than the run interation time, but faster than integration time, the QSA is an appropriate description of the system. Each integration has an opportunity to sample many configurations of the nuclear field, but each run sees one, static configuration. If individual runs' interaction times become on the order of the decorrelation of the nuclei, corrections to the QSA may no longer be neglected.

Type	Time	Energy	Magnetic field	Typical value
Charge				
Charging energy		E_c		5 meV
Orbital level spacing		υ		1 meV
Single dot two-electron exchange near $B_{\text{ext}} = 0$		J		300 μeV
Double-dot tunnel coupling		T_c		10 μeV
Double-dot inelastic tunneling		$\Gamma(\epsilon)$		0.01–100 neV
Electron spin				
Larmor precession	t_L	$\hbar\gamma_e B_{\text{ext}}$	B_{ext}	0–200 μeV
Fully polarized overhauser shift		AI	h_0	130 μeV
(Random) overhauser shift	T_2^*	$\hbar\gamma_e B_{\text{nuc}}$	$B_{\text{nuc}} = \frac{h_1}{\sqrt{N}}$	0.1–1 μeV
Nuclear spin species β				
Larmor precession	$t_{nL,\beta}$	$\hbar\gamma_\beta B_{\text{ext}}$	B_{ext}	0–100 neV
Knight shift	$t_{K,\beta}$	$\hbar\gamma_e B_{\text{nuc}}\lambda_{\beta,j} \approx \frac{\hbar\gamma_e B_{\text{nuc}}}{\sqrt{N}}$	$\frac{\gamma_e B_{\text{nuc}}}{\gamma_\beta\sqrt{N}}$	0.1–10 neV
Dipole-dipole interaction (nearest neighbor)	t_{dd}	$\frac{(\hbar\gamma_\beta)^2}{v_0}$	$\frac{\hbar\gamma_\beta}{v_0}$	0.01 neV

Table 1.1: Time, energy, and magnetic field scales for electron and nuclear spins in a single and double quantum dots, from fast to slow.

At low magnetic fields, the QSA is valid up to the single electron spin-nuclear spin interaction time ($O(\hbar N/A)$), which is of order microseconds. In contrast, at large external fields, the regime of validity for the QSA is extended—we may eliminate evolution due to terms non-commuting with the Zeeman interaction (secular approximation or rotating wave approximation). This yields an effective Hamiltonian

$$H_{\text{eff}} = \hbar\gamma_e(B_{\text{ext}} + B_{\text{nuc},z})\hat{S}_z \ . \tag{1.11}$$

The z axis is set to be parallel to the external magnetic field. Corrections to the QSA have a simple interpretation in the large field limit. As the Zeeman energy suppresses spin-flip processes, we may write the corrections to H_{eff} by seting $B_{\text{nuc},z} = B_z + \delta\hat{B}_z(t)$, where B_z is the QSA term, and $\delta\hat{B}_z(t)$ are fluctuations beyond the QSA (Appendix A). When the number of nuclei N is large and fluctuations small, to leading order $\delta\hat{B}_z$ is described by its

fourier transformed correlation function:

$$\langle \delta\hat{B}_z(t+\tau)\delta\hat{B}_z(t)\rangle = \int d\omega\ S(\omega)e^{i\omega\tau} \tag{1.12}$$

where $S(\omega)$ has a high frequency cutoff $\gamma \ll \gamma_e B_{\rm nuc}$.

Thus, at high magnetic field, nuclei contribute as a low frequency phase noise term to the electron spin evolution. The form of $S(\omega)$ depends on the detailed parameters of the nuclear spin Hamiltonian and the nuclear spin-nuclear spin interactions. We calculate the high frequency components (short time behavior) using a perturbation theory analysis in Appendix A, and find a high frequency cutoff $\gamma \sim \gamma_e B_{\rm nuc}^2/B_{\rm ext}N$. In terms of the parameters considered in Table 1.1, we have $\hbar\gamma \sim 10^{-4} - 0.1$ neV. We remark that the initial decay of the correlation function is quadratic, indicating that beyond the high frequency cutoff $S(\omega)$ decays faster than $1/\omega^2$. This is true as well for decay of the field due to nuclear dipole-dipole interactions when the timescales are short [146]. This arises from the finite lattice spacing, leading to an appreciable time (order tens of microseconds) over which the dipole-dipole interaction is reversible and the correlation decay occurs as a quadratic in time. The decay of the power spectrum above the cutoff is important for understanding the shape the echo envelope, which we detail in section 6.4.

In summary, this section has reviewed the interaction of an electron spin with nuclear spins in a single quantum dot. At large external magnetic field, the electron spin dephases on a time scale set by the average nuclear field, $B_{\rm nuc}$. The field itself is quasi-static, varying slowly when compared to the electron spin dephasing time T_2^*, and as such may be correctable using techniques such as spin-echo (investigated in section 6.4). The initial corrections, calculated in appendix A, indicate that first corrections to the QSA enter on a timescale of microseconds.

Chapter 2

Dephasing of quantum bits by a quasi-static mesoscopic environment

J. M. Taylor and M. D. Lukin

Department of Physics, Harvard University, Cambridge, MA 02138 USA

We examine coherent processes in a two-state quantum system that is strongly coupled to a mesoscopic spin bath and weakly coupled to other environmental degrees of freedom. Our analysis is specifically aimed at understanding the quantum dynamics of solid-state quantum bits such as electron spins in semiconductor structures and superconducting islands. The role of mesoscopic degrees of freedom with long correlation times (local degrees of freedom such as nuclear spins and charge traps) in qubit-related dephasing is discussed in terms of a *quasi-static* bath. A mathematical framework simultaneously describing coupling to the slow mesoscopic bath and a Markovian environment is developed and the dephasing and decoherence properties of the total system are investigated. The model is applied to several specific examples with direct relevance to current experiments. Comparisons to experiments suggests that such quasi-static degrees of freedom play an important role in current qubit implementations. Several methods of mitigating the bath-induced error are considered.

Solid-state quantum information research attempts the difficult task of separating a

few local degrees of freedom from a strongly coupled environment. This necessitates a clever choice of logical basis to minimize the dominant couplings and environmental preparation through cooling. Electron spin in quantum dots has been suggested as a quantum bit [122, 93], where orbital degrees of freedom do not carry quantum information. As a result, the individual quantum bits are relatively well isolated from non-local degrees of freedom, interacting strongly with only a local spin environment [134, 103, 43, 183, 38, 96, 112, 151] and weakly to phonons through spin-orbit coupling [75, 82, 87, 61, 96]. Josephson junctions and cooper-pair boxes in superconducting systems can be engineered for decreased coupling to local degrees of freedom [194], and several different approaches to superconductor-based quantum bit devices have shown remarkable promise as quantum computation devices [149, 31, 194, 128]. However, superconductor designs may strongly interact with local charge traps and magnetic impurities [167, 126, 69], leading to errors from local noise.

In this paper we examine the problem of coupling to the local environment for a solid-state system. By focusing on quantum information-related tasks, the detrimental effect of local degrees of freedom on specific operations can be assessed. In our model, so-called non-local degrees of freedom [170] (such as phonons and photons) are assumed to be weakly coupled and considered in the normal Markovian limits. However, local coupled systems corresponding to spins, charge-traps, and other finite-level systems, can be interpreted in terms of a finite set of nearby spins that may be strongly coupled to the qubit. In some cases, such as an electron spin in a quantum dot, this heuristic picture corresponds exactly to the actual hyperfine coupling between electron spin and lattice nuclear spins. In those systems, the local environment consists of 10^4–10^6 lattice nuclear spins, and the coupling can be strong [134, 103, 183, 181]. For superconductor-based designs, the quantum bit couples both to actual spins and to charge degrees of freedom such as $1/f$-type fluctuators [197], which can be modeled as two-level systems. Thus, analysis of the most general coupling of

a qubit to a mesoscopic collection of spins yields an understanding both of limitations in current experiments and of methods for improving the operation and design of solid-state quantum computation devices. We remark that several works have analyzed this type of situation in detail for specific implementations, in superconducting qubits [69, 126] and in quantum dot qubits [43, 38, 39, 90, 110]. We also note that recent work focusing on quantum dot-based systems parallels several significant elements of the current paper [110]; the results were arrived at independently. The present work focuses on the generality of the model and its impact in the context of quantum information processing.

We begin by considering a spin-1/2 system (the "qubit") coupled to a finite number of spin-1/2 degrees of freedom (the "mesoscopic bath") to both weak and strong driving fields. Inclusion of weaker, non-local couplings (the "Markovian environement") through a Born-Markov approximation reveals a natural hierarchy. A separation of time scales indicates that the local environment is quasi-static with respect to experimental time scales with long-lived correlation functions. However, over many experimental runs, the local environment fluctuates sufficiently to defy efficient characterization and correction by means of direct measurement. The generic nature of the coupling allows bath characterization using only a few parameters. Then, detailed analysis of specific operations (phase evolution, Rabi oscillations, spin-echo) and comparison to experimental results is possible. While such a spin-bath model has been considered previously [207, 153, 157, 134, 126, 69], the significance of the mesoscopic and quasi-static limits has not been emphasized.

We find that a quasi-static, mesoscopic environments results in fast dephasing, induces power-law decay and non-trivial phase shifts for driven (Rabi) oscillations of the qubit, and may be corrected for using echo techniques. The generality of the model suggests it may be appropriate for many systems with strong coupling to a stable local environment. In addition, comparison to experiments suggest this model can help explain the reduced

contrast and long coherence times of current solid-state qubit systems, indicating that the local environments of current solid-state qubits both have long correlation times and play a crucial role in the dynamics of the qubit. Several methods of mitigating the effects of the bath are considered, all of which take advantage of the long correlation time to reduce errors. Some of these techniques are extensions of established passive error correction [204] and quantum bang-bang ideas [192], while another, the preparation of coherences in the environment to reduce dephasing (environmental squeezing) is introduced in this context for the first time.

2.1 The physical system

Consider a relatively well-isolated two-level system (a qubit) in a solid-state environment. This could be a true spin-1/2 system such an electron spin or an anharmonic system such as a hybrid flux-charge superconductor qubits [1]. The qubit is coupled to a collection of spin-1/2 systems comprising the mesoscopic bath. In addition to these potentially strongly coupled degrees of freedom, other, weaker couplings to bosonic fields (phonons, photons, and large collections of spins that can be mapped to the spin-boson model [71]) are included as a Markovian environment, and act as a thermal reservoir. Qualitatively, this leads to a heirarchy of couplings. The qubit plus mesoscopic bath are treated quantum mechanically, while the additional coupling to the larger environment (the thermal reservoir) is included via a Born-Markov approximation. Thus, the reservoir plays the role of thermalizing the mesoscopic bath over long time scales and providing additional decay and dephasing of the system. By assuming slow internal dynamics and thermalization for the mesoscopic bath, a quasi-static regime is investigated, in contrast with the usual Markovian

[1] The breakdown of the two-level approximation in superconductor-based qubit designs has already been explored in great detail [22] and we instead focus on other sources of error due to local spins, charge traps, etc.

approximations for baths.

Starting from first principles, the Hamiltonian is introduced. A transformation to the rotating frame allows for adiabatic elimination which simplifies the interaction, after which the quasi-static assumption is considered. An explicit bath model is chosen, and the role of the thermal reservoir included through a Linblad-form Louivillian.

2.1.1 Hamiltonian

The qubit, 2-level system, is described by the spin-1/2 operators $\hat{S}_x, \hat{S}_y$, and $\hat{S}_z$. An external biasing field produces a static energy difference between the two levels of angular frequency ω. This serves as a convenient definition of z-axis. A driving field, with Rabi frequency Ω and oscillating with angular frequency ν, is applied along a transverse axis in the $x-y$ plane. In most systems, ω is fixed, and modulation of Ω turns on and off rotations around the transverse axis. The relative phase of the driving field to the biasing field controls the axis about which rotations occur. We choose the phase such that rotations occur around the x-axis. The Hamiltonian is

$$\hat{H}_{\rm sys} = \omega \hat{S}_z + 2\Omega \cos(\nu t)\hat{S}_x, \tag{2.1}$$

in units where $\hbar = 1$. This Hamiltonian is commonly encountered in quantum optics, NMR, ESR, and solid-state quantum information devices. For solid-state qubit systems, ω and ν are typically $\sim 1 - 100$ ns^{-1} and $\Omega \sim 0.01 - 1$ ns^{-1}.

Adding the most general environmental coupling possible, the total Hamiltonian is

$$\hat{H}_{tot} = \hat{H}_{\rm sys} + \tilde{\lambda}\hat{\vec{S}} \cdot \hat{\vec{E}} + \hat{H}_E \tag{2.2}$$

where $\tilde{\lambda}$ is a coupling constant to the environment and $\hat{\vec{E}}$ is a vector of environmental operators. The tilde terms indicate that this coupling includes both the mesoscopic spin

bath and the Markovian environment. All of the internal environmental dynamics, including thermalization, is encompassed in $\hat{H}_E$.

Separating the environment E into the mesoscopic spin bath and Markovian environment, the interaction and environment terms in the Hamiltonian can be rewritten:

$$\tilde{\lambda}\hat{\vec{S}} \cdot \hat{\vec{E}} + \hat{H}_E = \lambda \hat{\vec{S}} \cdot \hat{\vec{A}} + \lambda_C \hat{\vec{S}} \cdot \hat{\vec{C}} + \hat{H}_A + \hat{H}_C + \hat{H}_{AC}. \tag{2.3}$$

The A terms denote the quasi-static bath degrees of freedom, while the C terms correspond to a larger environment that can be treated in a Born-Markov approximation. Qualitatively, the complete picture of bath and environment drawn in this paper is hierarchical in nature (Fig. 2.1), with the system (qubit) coupled to a mesoscopic spin bath, both of which are coupled to larger environments.

This paper focuses on the regime of strong system–bath coupling and weak system–environment and environment–bath coupling. In this limit, we can treat the Markovian environment's effects entirely through a Lindblad form Louivillian acting on the combined system–bath. We write the effective Hamiltonian as

$$\hat{H}_{\text{eff}} = \hat{H}_{\text{sys}} + \lambda \hat{\vec{S}} \cdot \hat{\vec{A}} + \hat{H}_A \ , \tag{2.4}$$

while superoperator describing evolution of the system–bath density matrix $\hat{\rho}$ is given by the differential equation

$$\dot{\hat{\rho}} = i[\hat{\rho}, \hat{H}_{\text{eff}}] + \mathcal{L}_{\text{env}}\hat{\rho} \ . \tag{2.5}$$

The Louivillian, $\mathcal{L}_{\text{env}}$, is described below.

Regarding other limits, the weak system-bath limit can be treated pertubatively when the bath-environment coupling and/or system-environment coupling is stronger. When the system-environment coupling can be experimentally controlled, such as during qubit manipulation, the system degree of freedom could be used to transfer entropy from the

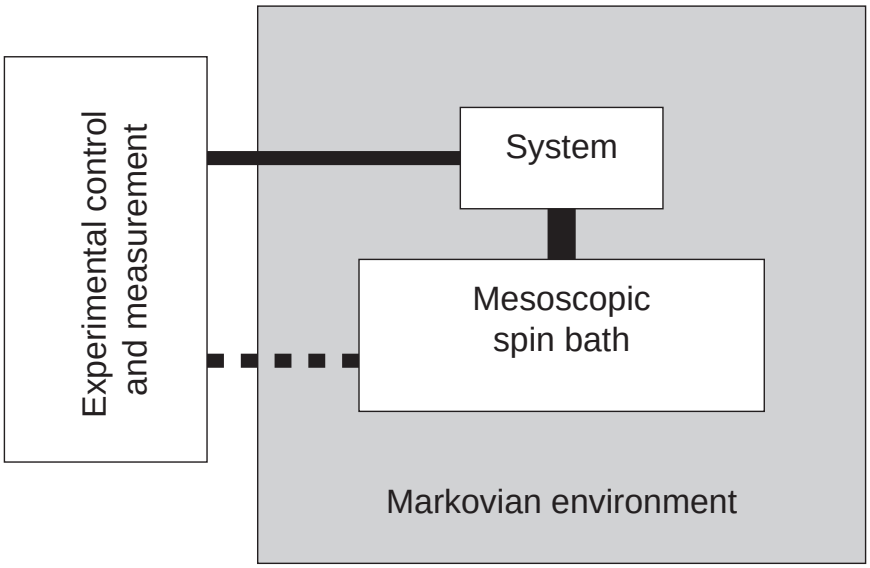

Figure 2.1: Heirarcichal system–bath–environment coupling. External control of the system (qubit) and measurement are independent of the environment The mesoscopic spin bath is strongly coupled to the system, while the environment provides weak dephasing of the system and spin bath degrees of freedom. Internal dynamics of the spin bath can be ergodic, but some experimental control of the bath may be achieved in limited situations (e.g., through NMR) as indicated.

bath to the environment in a controlled manner, yielding non-thermal initial states of the mesoscopic spin bath. The usefulness of this final point will be discussed later.

In many cases, the bias field ω is large ($|\omega| \gg |\Omega|, |\lambda|$). This is similar to the quantum optical case; accordingly, the standard recipe of transformation into a rotating frame and a rotating wave approximation is also valid here, and off-axis (flip-flop) terms are removed, resulting in a Jaynes-Cummings-like Hamiltonian. Roughly speaking, energy cannot be conserved when the system spin flips through changes of the bath state. However, the additional coupling to the bath leads to terms not found in the Jaynes-Cummings Hamiltonian.

More explicitly, applying the unitary transformation $U = \exp(-i\omega\hat{S}_z t)$, the Hamil-

tonian is

$$\begin{aligned}\hat{\tilde{H}}_{\text{eff}} &= \Omega/2[e^{i\nu t}+e^{-i\nu t}][e^{i\omega t}\hat{S}_+ + e^{-i\omega t}\hat{S}_-] + \\ &\quad \lambda\hat{S}_z\hat{A}_z + \lambda/4[e^{i\omega t}\hat{S}_+\hat{A}_- + e^{-i\omega t}\hat{S}_-\hat{A}_+] + \\ &\quad \hat{H}_A. \end{aligned} \tag{2.6}$$

When the detuning of the driving field is small, $\delta = (\nu - \omega) \ll \omega$, the highly oscillatory terms in this rotating Hamiltonian can be neglected. To do so, the propagator $\hat{U}(t) = \hat{T}\exp(-i\int_0^t \hat{\tilde{H}}(t')dt')$ is formally expanded over one period of the applied unitary transformation, $\tau = 4\pi/\omega$, and a Magnus expansion [123] gives

$$\hat{U}(\tau) = \exp[-i\tau(\sum_{k=0}^{\infty}\hat{H}_k)] \tag{2.7}$$

$$\begin{aligned}\hat{H}_0 &= 1/\tau\int_0^\tau \hat{\tilde{H}}(t)\,dt \\ &= \Omega/2[\hat{S}_+ + \hat{S}_-] + (\delta + \lambda\hat{A}_z)\hat{S}_z + \hat{H}_B \end{aligned} \tag{2.8}$$

$$\hat{H}_1 = -i/2\tau\int_0^\tau\int_0^{t_1}[\hat{\tilde{H}}(t_2),\hat{\tilde{H}}(t_1)]\,dt_2\,dt_1. \tag{2.9}$$

The first term $\hat{H}_0$ will be used hereafter. Neglecting $\hat{H}_1$ and higher terms of the expansion if formally equivalent to the rotating wave approximation used to derive the Jaynes-Cummings Hamiltonian.

2.1.2 Quasi-static bath assumptions

In standard analyses, usually the bath dynamics are fast relative to the system dynamics, and a Born-Markov approximation is appropriate. However, when the internal bath dynamics are much slower than the system dynamics, the internal bath correlation functions are long lived, and we can consider a *quasi-static* bath. In this picture, one collective bath operator (here $\hat{A}_z$) has, in the Heisenberg picture, a long-lived correlator.

In particular,

$$1 - \frac{\langle \hat{A}_z(t+\tau)\hat{A}_z(t)\rangle}{\langle \hat{A}_z^2\rangle} \ll 1 \tag{2.10}$$

for $\tau \gtrsim 1/\Omega$. The quasi-static limit is approached when this is satisfied for $\tau > t_{\rm expt}$ (the time for a single experimental run) but not for $\tau \simeq t_{\rm tot}$ (the time to generate enough runs to characterize $\hat{A}_z$).

We consider this in detail. Internal dynamics of the spin bath and coupling to the Markovian environment will result in a decay of correlations. A general description of the correlator is

$$\langle \hat{A}_z(t)\hat{A}_z(t')\rangle = \int d\omega\ S(\omega)e^{i\omega(t-t')} \tag{2.11}$$

where the spectral function $S(\omega)$ has some high frequency cutoff, Γ, set by the internal dynamics of the bath [41]. When $\Gamma \gg \Omega$, the Markovian limit may be reached, and the quasi-static theory developed here is no longer necessary.

When $\Gamma \to 0$, the thermalization time goes to infinity. Then, while the state of the bath is initially unknown, a series of measurements can be used to estimate the detuning of the system, and thus the value of $\lambda\hat{A}_z$ (see, *e.g.*, Refs. [80, 110]). If the manipulation process has a measurement time for a single projection of $\tau_m \gtrsim 1/\Omega$, after n such measurements, the error of $\langle \hat{A}_z\rangle$ will be

$$\Delta(\langle \hat{A}_z\rangle) \simeq \frac{\lambda}{\Omega\sqrt{n}}. \tag{2.12}$$

This procedure is exactly that of a classical phase estimation algorithm. It takes a time $\propto n$ to generate a $\sqrt{n}$ improvement in the knowledge of the current value of $\hat{A}_z$.

In between lies the quasi-static limit, where a single experiment (*i.e.*, preparation of a given qubit state, evolution under H_0 for a specified time, followed by projective measurement) can be performed well within the correlation time, but not enough experiments can be performed to well estimate $\hat{A}_z$. Qualitatively speaking, this is equivalent to taking

a thermal average for the ensemble of measurements, and mathematically the same as the result for the simultaneous measurement of a large number of exactly similar systems. The uncertain knowledge of $\hat{A}_z$ leads to dephasing when attempting specific quantum information operations.

As a typical case, consider an internal bath Hamiltonian $H_A = \hbar \sum_k \omega_{B,k} \hat{B}_z^k$ and a coupling with $\hat{\vec{A}} = \sum_k \alpha_k \hat{\vec{B}}^k$. This could describe nuclear spins for quantum-dot systems, or charge traps. As $[\hat{H}_A, \hat{A}_+] = \sum_k \alpha_k \omega_{B,k} \hat{B}_+^k$, the rotating-wave approximation is valid if $\omega_{B,k} \ll \omega$ for all k. Then, the application of a large bias field ω, e.g., due to a static magnetic field, makes the interaction essentially static and classical, whereby the system experiences a fluctuating (classical) field $\hat{\vec{A}}$; fluctuations are due to corrections to the rotating wave approximation and coupling to the Markovian environment. Non-classical correlations of the bath, produced by off-resonant interactions [110] or preparation techniques (e.g., Chapter 3) return the problem to the fully quantum domain.

For example, for electron spin in quantum dots, where the bath is lattice nuclear spins, dipolar diffusion processes lead to flip-flop interactions wherein a spin inside the dot is exchanged with that of a spin outside the dot, producing ergodic dynamics within the bath on ms timescales [45, 203]. In contrast, spin-lattice relaxation (coupling to the larger environment) can be minutes to hours in time. Over time, the dipole diffusion destroys the correlations of the $\hat{A}_z$ parameter. Detailed calculations, using the method of moments, suggest that diffusion in dots is within an order of magnitude of the bulk diffusion rate [48], and this diffusion decorrelates $\hat{A}_z$ no faster than the time scale set by the NMR linewidth (10 ms^{-1} for GaAs [146]). Thus the primary effect of spin-lattice relaxation (coupling to a Markovian environment) is to produce an initial thermal state of nuclear spins, while dipole-dipole interactions lead to decorrelation of $\hat{A}_z$ (internal bath dynamics).

For concreteness, we choose for our mesoscopic spin bath of N spin-1/2 systems

to have the form

$$\hat{A}_z = \sum_k \alpha_k \hat{I}_z^k \tag{2.13}$$

where $\hat{I}_z^k$ is the spin component corresponding to the kth bath spin, and an internal Hamiltonian giving the quasi-static limit. As many bath variables scale as $\sqrt{N\bar{\alpha^2}}$, we normalize the α_k such that $\bar{\alpha^2} = 1/N$, thus keeping λ as the sole bath strength parameter. The bars above quantities denote statistical averages over static variables. As we have assumed all bath spins are spin-1/2, we can choose the z axis without loss of generality.

2.1.3 Markovian environment effects

The principle effects of the Markovian environment are two-fold: it leads to relaxation of the qubit system, and it leads to long-time thermalization of the mesoscopic spin bath. We have established that the internal dynamics of the quasi-static bath, combined with coupling to the Markovian environment, will lead to decorrelation of $\hat{A}_z$ and dynamic thermalization. For a weakly coupled Markovian environment, with equilibriation times for the bath that are much longer than experimental times, the main effect of the Markovian environment is to produce an initial mesoscopic spin bath state of the form $\rho_A \propto e^{-H_A/k_{\rm B}T}$.

In general, the additional Markovian environment degrees of freedom will also couple to the system, leading to relaxation and decoherence that we can model with a Lindblad form of the Louivillian of the combined system-spin bath density matrix. Formally, tracing over the environment yields a superoperator (see Eqn. 2.5)

$$\begin{aligned}\mathcal{L}_{\rm env}\rho &= 2\gamma_s[2\hat{S}_-\rho\hat{S}_+ - \rho\hat{S}_+\hat{S}_- - \hat{S}_+\hat{S}_-\rho] \\ &\quad + \sum_k 2\Gamma_k\Big[2\hat{I}_-\rho\hat{I}_+ - \rho\hat{I}_+\hat{I}_- - \hat{I}_+\hat{I}_-\rho \\ &\quad + 2\hat{I}_+\rho\hat{I}_- - \rho\hat{I}_-\hat{I}_+ - \hat{I}_-\hat{I}_+\rho\Big]\end{aligned} \tag{2.14}$$

corresponding to the Markovian environment. We presume that the spin-bath is in the high

temperature limit, while the qubit system only has spontaneous decay. This is consistent with the rotating wave approximation. The resulting equations, with pure radiative decay for the system, are cumbersome to work with, and we will sometimes use the input-output operator formalism, which is formally equivalent by the quantum fluctuation-dissipation theorem.

2.2 Free evolution

In this section, free evolution for a variety of experimentally-relevant situations is considered. Free evolution corresponds to the case of $\Omega = 0$, *i.e.*, the absence of driving field. In quantum information, free evolution is equivalent to phase rotations (Z rotations), and the behavior of free evolution is an indicator of how good a quantum memory the chosen qubit provides. The decay of coherence during free evolution due to the mesoscopic spin bath may be severe; however, we consider spin-echo methods as a means of mitigating the bath's effects.

Equation 2.8 is the basic Hamiltonian used hereafter; $\hat{A}_z$ is given by Eqn. 2.13. For free evolution, $\Omega = 0$, and the Hamiltonian is

$$\hat{H}_{FID} = (\lambda \hat{A}_z + \delta)\hat{S}_z \ . \tag{2.15}$$

For time-dependent $\hat{A}_z$ such that $[\hat{A}_z(t), \hat{A}_z(t')] = 0$ (appropriate for the specific baths consider in section II), the exact propagator from $t = 0$ to time t is

$$U_{FID}(t) = \exp[-i(\delta t + \lambda \int_0^t \hat{A}_z(t')dt')\hat{S}_z] \ . \tag{2.16}$$

In the quasi static limit, we may usually replace $\int_0^t \hat{A}_z(t')dt'$ with $\hat{A}_z t$, simplifying evaluation of the propagator.

2.2.1 Free induction decay

To illustrate free evolution, we start by studying free induction decay (FID), considered for this case by [207] and for a dynamical spin bath by [185]. FID corresponds to the decay experienced by a spin coherence (e.g., a density matrix element $|\uparrow\rangle\langle\downarrow|$) during evolution in a Ramsey-type experiment. The system is prepared in the state $|+\rangle = 1/\sqrt{2}(|\uparrow\rangle+|\downarrow\rangle)$, with $\langle\hat{S}_+(0)\rangle = 1/2$, for example, by rotations induced by control of Ω (considered below). The driving field is turned off ($\Omega = 0$) and the system evolves according to the $\hat{S}_z$ coupling only. Then,

$$\Phi_{FID} = \frac{\langle\hat{S}_+(t)\rangle}{\langle\hat{S}_+(0)\rangle} = \Big\langle \exp[-i(\lambda\hat{A}_z + \delta)t]\Big\rangle_{bath} \tag{2.17}$$

For an uncorrelated bath ($\langle\hat{I}_z^k\hat{I}_z^j\rangle = \langle\hat{I}_z^k\rangle\langle\hat{I}_z^j\rangle$ for $k \neq j$) we can write this in terms of individual bath couplings [2]

$$\Phi_{FID} = e^{-i\delta t}\prod_k \big[\cos(\lambda\alpha_k t/2) - i\langle 2\hat{I}_z^k\rangle \sin(\lambda\alpha_k t/2)\big]. \tag{2.18}$$

The minimum of the projection of the actually final state of the desired final state, $F_{FID} = |\Phi_{FID}|^2$ is bounded from below by $(\mathrm{Min}_k[|\langle 2\hat{I}_z^k\rangle|])^N$. Thus, initial bath polarization for finite N limits the maximum decay.

The initial decay of this coherence is quadratic, giving

$$F_{FID} \simeq 1 - \frac{(\lambda t)^2}{2}\sum_k 2\alpha_k^2(1 - \langle 2\hat{I}_z^k\rangle^2), \tag{2.19}$$

as shown in the inset of Figure 2.2. For a large number of spins, the intermediate time decay converges to a Gaussian, $\exp[-(\gamma_{FID}t)^2/2]$, with a rate

$$\gamma_{FID} = \lambda\sqrt{\sum_k \alpha_k^2(1 - \langle 2\hat{I}_z^k\rangle^2)}. \tag{2.20}$$

[2] For an arbitrary, quasi-static bath (*i.e.*, not necessary a spin-bath) with a density matrix that is diagonal in the eigenbasis of $\hat{A}_z$, $\Phi_{FID} = e^{-i\delta t}\int_{-\infty}^{\infty} d\Lambda\rho(\Lambda)e^{-i\Lambda t}$, demonstrating that Φ_{FID} is exactly the inverse Fourier transform of the bath degree of freedom in this case.

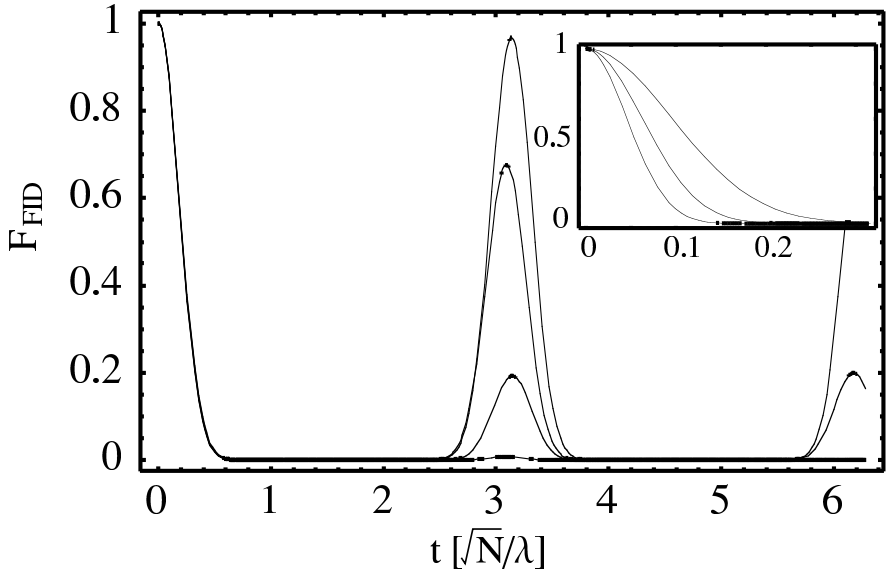

Figure 2.2: FID evolution (F_{FID}) in time scales $\sqrt{N}/\lambda$ for increasing inhomogeneity, $\sigma_\alpha = \{0.1, 0.3, 0.6, 1\}/\sqrt{N}, N = 30, P = 0$. The inset shows increasing decay in the short time limit due to increasing inhomogeneity, $\sigma_\alpha = \{5, 10, 20\}/\sqrt{N}, N = 30, P = 0$.

When the inhomogeneity in the α_k coefficients is low, the system experiences mesoscopic revival on a time scale given by the single spin coupling strength, $\lambda\bar{\alpha} \simeq \lambda/\sqrt{N}$. This type of revival is shown in Figure 2.2, where a Gaussian distribution of α_k of increasing widths are used, and a bath polarization $P = \langle 2\hat{I}_z \rangle = 0$ is assumed. These mesoscopic effects for finite spin systems have been investigated in great detail elsewhere [207], and we refer readers to those works for a detailed description. In most physical settings, inhomogeneity is large and revival will not be observed. However, for systems where N is small, fluctuations can become substantial even with a large inhomogeneity in the α_k's, and such fluctuations have been observed experimentally [185].

To put the results in an experimental context, we consider a Ramsey fringe experiment. A system is prepared in the $|\downarrow\rangle$ state. A $\pi/2$ pulse is applied along x (denoted $R^x_{\pi/2}$), and then at a later time t, an opposite, $-\pi/2$ pulse is applied. Afterwards, a projective measurement on z measures the rotation of the $\hat{S}_y$ eigenstate due to environmental effects

and detuning. In terms of actual experimental implementations, preparation of a spin-down eigenstate and measurement along the $\hat{S}_z$ axis is enough, if we use two $\pi/2$-pulses with a delay t. Formally, in the limit of perfect pulses the propagator is

$$U_{FID}(t) = R^x_{-\pi/2} \exp[-i\lambda \hat{A}_z \hat{S}_z t] R^x_{\pi/2}. \tag{2.21}$$

In the limit of perfect pulses, the probability of measuring the final state in the $|\downarrow\rangle$ state is given by F_{FID} as a function of the delay time, t. If the system is coupled to a spin bath, it will show Gaussian-type decay in the initial time period. This decay is limited in extent for baths of finite polarization (non-infinite temperature). For a small bath size, mesoscopic fluctations and revival after the initial decay may be evident.

For a series of sequential measurements, the finite correlation time of the bath will be evident. For example, for fixed interaction time τ, a series of measurements $\{M_k\}$ giving 1 for $|\downarrow\rangle$ and 0 for $|\uparrow\rangle$ at times t_k will manifest correlations due to the correlations of $\hat{A}_z$ at the different times, t_k. Assuming the quasi-static limit, such that $\hat{M}_k = \cos^2(\lambda \hat{A}_z(t_k)\tau/2)$, we find

$$\langle M_j M_k \rangle - \langle M \rangle^2 = \frac{1}{8} \exp[-(\lambda\tau)^2 \int d\omega S(\omega)(e^{i\omega(t_j - t_k)} - 1)] \tag{2.22}$$

where the cutoff Γ of $S(\omega)$ is such that $\Gamma\tau \ll 1$. Thus, the correlation function for a series of measurements with $\tau\Gamma \ll 1$ in principle allow reconstruction of the spectral function describing $\hat{A}_z$. We note that $\gamma_{FID} = \lambda\sqrt{\int S(\omega) d\omega}$.

2.2.2 Spin-echo decay

As the bath correlation time is long, spin-echo techniques can exactly cancel this type of dephasing. For spin-echo, a π-pulse is applied in between the two $\pi/2$-pulses; the time delays before and after the π-pulse are t_1 and t_2, respectively. The total evolution is

thus

$$\begin{aligned} U_{SE}(t_2;t_1) &= R^x_{\pi/2}\exp[-i\lambda\hat{A}_z\hat{S}_z t_2]R^x_\pi \\ &\quad \exp[-i\lambda\hat{A}_z\hat{S}_z t_1]R^x_{\pi/2} \qquad (2.23) \\ &= R^x_{-\pi/2}\left(R^x_{-\pi}\exp[-i\lambda\hat{A}_z\hat{S}_z t_2]R^x_\pi\right) \\ &\quad \exp[-i\lambda\hat{A}_z\hat{S}_z t_1]R^x_{\pi/2} \qquad (2.24) \\ &= R^x_{-\pi/2}\exp[-i\lambda\hat{A}_z\hat{S}_z(t_1-t_2)]R^x_{\pi/2}, \qquad (2.25) \end{aligned}$$

which is the original FID propagator (Eqn. 2.21) with $t \to (t_1 - t_2)/2$. The previous results hold but now as a function of the time difference. In particular, no decay occurs when $t_1 = t_2$! The probability of measuring $|\downarrow\rangle$ is

$$\begin{aligned} F_{SE}(t_1,t_2) &= \langle\cos^2[\lambda\hat{A}_z(t_1-t_2)/2]\rangle \\ &= \frac{1}{2}\{1+\exp[-\gamma^2_{FID}(t_1-t_2)^2/2]\}. \qquad (2.26) \end{aligned}$$

Spin-echo fidelity ($F_{SE}(t,t)$) is limited both by the imperfections in the rotations, $R^x_{\pi/2}$ and R^x_π, Markovian processes that directly lead to decay of $\hat{S}_z$, and decay of the correlation function of $\hat{A}_z$, *i.e.*, in the interaction picture, $\hat{A}_z(t) \neq \hat{A}_z(t')$ for t much later than t'. The first type of error, examined in detail below, does not depend on the total time $t_1 + t_2$, while the latter errors do. Neglecting imperfections in rotations, the effect of a correlated bath on spin-echo is a textbook problem, and we merely cite the result here:

$$\begin{aligned} F_{SE}(t,t) &= \frac{1}{2} + \frac{e^{-2\gamma t}}{2} \qquad (2.27) \\ &\quad \times\exp[-\lambda^2\int S(\omega)\sin^4(\omega t/2)/(\omega/2)^2 d\omega] \end{aligned}$$

where we assume $\hat{A}_z$ is a Gaussian variable described by the spectral function $S(\omega)$, as per Equation 2.11. The results of a spin echo experiment allow an alternative method of extracting the correlation function associated with the mesoscopic spin bath. For a

spectral function describing the bath with cutoff $\Gamma \ll 1/t$, the echo will decay according to $\exp[-2\gamma t - \lambda^2\Gamma^2 t^4/4]$.

For free evolution ($\Omega = 0$), used for phase gates and quantum memory, we find that a mesoscopic spin bath leads to dephasing in the quasi-static limit, with a time scale given by $1/\lambda$. Sequential measurements in a Ramsey-type experiment allow for reconstruction of the of the spectral function associated with the bath. Furthermore, spin-echo can be used to reduce the dephasing dramatically.

2.3 Driven-evolution

While the free evolution of the system is illustrative of quantum memory, a critical operation for quantum information processing is rotations about an axis perpendicular to the applied bias. This is achieved by a pulse in the transverse coupling field strength, Ω, leading to driven oscillations between $|\uparrow\rangle$ and $|\downarrow\rangle$. These Rabi oscillations form the basis for the x-axis rotations used, for example, in Ramsey-fringe experiments, and more generally for producing a universal set of single qubit gates.

In practice, the perfect rotations (Rabi pulses) needed to produce perfect rotations are unavailable, due to the finite power available for such pulses. We now consider in detail rotations obtained by driving the system (non-zero Ω in Eqn. 2.8) in the presence of the mesoscopic spin bath and Markovian environment. In the Heisenberg picture, the single-spin (system) operator equations of motion are given by

$$\frac{d\hat{\vec{S}}}{dt} = i[H_0, \hat{\vec{S}}]. \tag{2.28}$$

For time independent $\hat{A}_z$ (quasi-static limit) we can solve these equations exactly, noting

that $d/dt\ \hat{\vec{S}} = \hat{\omega}\vec{n} \times \hat{\vec{S}}$, where

$$\hat{\omega} = \sqrt{(\lambda \hat{A}_z + \delta)^2 + \Omega^2}; \tag{2.29}$$

$$\hat{\vec{n}} = \hat{\omega}^{-1} \begin{pmatrix} \Omega \\ 0 \\ \lambda \hat{A}_z + \delta \end{pmatrix}. \tag{2.30}$$

This evolution corresponds to the optical Bloch equations, giving driven rotations of the qubit Bloch vector on the Bloch sphere about an axis $\vec{n}$ at frequency $\hat{\omega}$. The dependence these quantities upon the state of the bath leads to shot-to-shot fluctuations, which broadens ensemble or sequential measurements.

Alternatively, we may write the propagator for $\hat{H}_0$ as

$$\hat{U}(t) = \cos(\hat{\omega}t/2)\hat{1} - 2i \sin(\hat{\omega}t/2)\hat{\vec{n}} \cdot \hat{\vec{S}} \tag{2.31}$$

where we have taken the quasi-static limit, such that $\frac{d}{dt}\hat{A}_z \simeq 0$.

Returning to Equations 2.29–2.30, we calculate the rotation of an initial z eigenstate with $\langle \hat{S}_z(t=0) \rangle = 1/2$, *i.e.*, determine the Rabi oscillations expected for the initial state $|\uparrow\rangle$. The field Ω leads to population and coherence oscillations. Considering the z and y components together, we define

$$\hat{f} = \frac{(\lambda \hat{A}_z + \delta)^2}{(\lambda \hat{A}_z + \delta)^2 + \Omega^2} \tag{2.32}$$

$$\hat{\zeta}(t) = \frac{\Omega^2 \exp(-i\sqrt{(\lambda \hat{A}_z + \delta)^2 + \Omega^2}\, t)}{(\lambda \hat{A}_z + \delta)^2 + \Omega^2}. \tag{2.33}$$

Then, $\langle 2\hat{S}_z(t) \rangle = \mathrm{Re}[\langle \hat{f} + \hat{\zeta}(t) \rangle]$ and $\langle 2\hat{S}_y(t) \rangle = \mathrm{Im}[\langle \hat{\zeta}(t) \rangle]$. The value of $\langle \hat{f} \rangle$ is a measure of the maximum contrast of population oscillations, and also gives the steady-state population difference and lineshape; this is approximately maximal for $\delta = -\lambda \langle \hat{A}_z \rangle$. $\langle \hat{\zeta}(t) \rangle$ gives the oscillatory part of coherence and population.

2.3.1 Steady-state behavior

For long times, the steady state behavior will be given by $\langle\hat{f}\rangle$, which measures the population difference between $\uparrow$ and $\downarrow$. This gives the measureable response of the system to CW excitations of the system. A simple estimate of $\langle\hat{f}\rangle$ is provided by writing $\hat{A}_z$ as $\langle\hat{A}_z\rangle + \delta\hat{A}_z$, and assuming $\langle(a+\hat{A}_z)^{-2}\rangle = \langle(a+\langle\hat{A}_z\rangle)^2 + \langle\Delta\hat{A}_z^2\rangle)^{-1}\rangle$. Then,

$$\langle\hat{f}\rangle = \frac{1}{1+\Omega^2/[(\delta+\lambda\langle\hat{A}_z\rangle)^2+\lambda^2\langle\Delta\hat{A}_z^2\rangle]}. \tag{2.34}$$

This has a maxima at the mean bath detuning, $\lambda\langle\hat{A}_z\rangle$, and as such this point would be the observed zero in detuning. Differences from this observed zero, denoted $\tilde{\delta}$, gives an absorption spectrum of

$$\langle\hat{f}\rangle = 1 - \frac{\Omega^2}{\tilde{\delta}^2+\lambda^2\langle\Delta\hat{A}_z^2\rangle+\Omega^2} \tag{2.35}$$

which behaves as a Lorenztian with a linewidth given by the combined power broadening and bath broadening for $\Omega \ll \lambda\langle\Delta\hat{A}_z^2\rangle^{1/2}$.

The approximations used for this simple estimate break down for large bath strength. To find this behavior in the strong bath limit, where higher order moments are important, we need not assume that the bath density matrix is uncorrelated, as before, but rather that the bath density matrix is diagonal in an eigenbasis of the bath operator, $\hat{A}_z$. [3] This would be appropriate for nuclei interacting with an electron spin in a quantum dot at finite magnetic field, or for charge traps capacitively coupled to the system.

We can evaluate $\langle\hat{f}\rangle$ by tracing over the bath density matrix, replacing $\rho_{bath} = \sum_{\lambda A_z}\rho_{\lambda A_z}|\lambda A_z\rangle\langle\lambda A_z|$ with $\rho(\Lambda)$. The integrals involved are solved in Appendix B.1. We note that the result is

$$\langle\hat{f}\rangle \simeq 1 - \rho(-\delta)\sqrt{2\pi\Omega/u} \tag{2.36}$$

[3] By assuming the bath density matrix is diagonal in the $\hat{A}_z$ eigenbasis, the result derived (Eqn. 2.40) in fact is generally true for any bath that is non-singular ($\rho_{sym}(\omega \geq \Omega)$ not singular) and satisfies $u \geq 0$, not just a spin-bath. However, the spin-bath provides a natural case for $[\hat{H}_B, \hat{A}_z] \simeq 0$, as mentioned in the text.

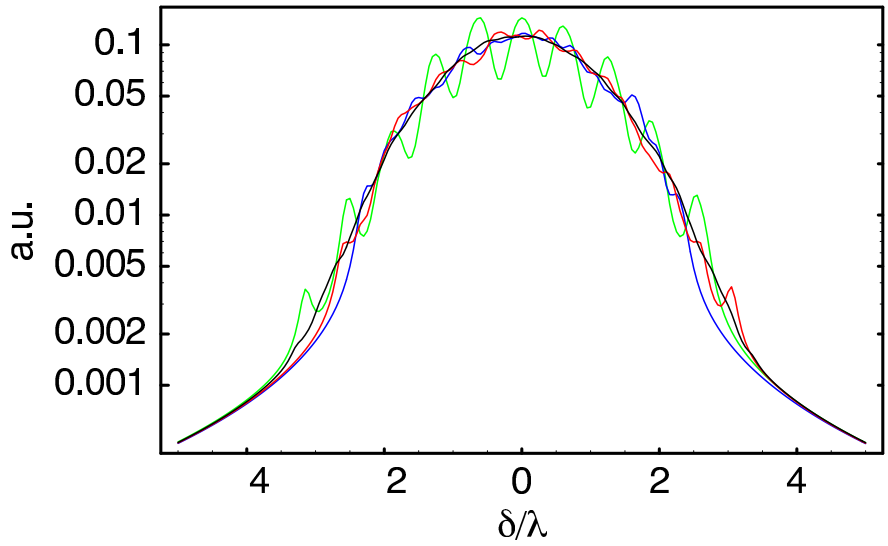

Figure 2.3: Lineshapes for a bath with $N = 10$ and increasing inhomogeneity [$\sigma_\alpha = 0.1$(green),0.5(red),1(blue)]. The additional line is $N = 20, \sigma_\alpha = 0.5$ (black).

for the lineshape. This has assumed that u^{-1} is a frequency scale over which the bath density of states is relatively flat, and as such can be Taylor expanded to second order. This time scale is

$$u = \frac{5}{4\Omega} - \frac{\Omega\rho''(-\delta)}{\rho(-\delta)}. \tag{2.37}$$

In other words, driven oscillations can measure the bath density of states as a function of detuning, convolved with a kernel of width u^{-1}. We plot several lineshapes in Fig. 2.3.

Essentially, we find that the steady-state behavior of the system indicates a maximum of population in the state opposite the initial state at a detuning $\delta = -\lambda\langle\hat{A}_z\rangle$. In addition, in the weak field limit, the line shape provides a sensitive measure of diagonal components of the bath's density matrix, so long as a calibration of Ω independent of the bath exists.

2.3.2 Time-dependent behavior

We now consider the actual, observable population and coherence oscillations induced by a driving (Rabi) field. Looking at the explicit time dependence, we consider the envelope of oscillations given by $|\hat{\zeta}(t)|$. The initial decay is quadratic, $(1-\langle f\rangle)[1-(\gamma_{\Omega,0}t)^2/2]$, and when renormalized to give maximal contrast, it has a width

$$\gamma_{\Omega,0} = \sqrt{-\frac{d^2}{dt^2}\Big|\frac{\langle\hat{\zeta}(t)\rangle}{(1-\langle\hat{f}\rangle)}\Big|_{t=0}} \tag{2.38}$$

$$= \frac{\Omega^2}{1-\langle\hat{f}\rangle}\times \tag{2.39}$$

$$\sqrt{\left\langle\frac{1}{(\lambda\hat{A}_z+\delta)^2+\Omega^2}\right\rangle-\left\langle\frac{1}{\sqrt{(\lambda\hat{A}_z+\delta)^2+\Omega^2}}\right\rangle^2}.$$

This suggests that measurements of such short time decay will measure second order moments of the bath operators.

While the short time behavior is consistent with Gaussian decay, as would be expected from a non-Markovian, non-dissipative bath, the long time behavior is a power law.

The integrals involved are solved in Appendix B.1; essentially we solve for $\langle\hat{\zeta}(t)\rangle$, and find

$$\langle\zeta(t)\rangle \approx \rho(-\delta)e^{-i\Omega t}\frac{\sqrt{2\pi\Omega}e^{-i\theta(t)}}{\sqrt{\tau(t)}}. \tag{2.40}$$

where the time scale for phase shift, and phase shift angle, are given by

$$\tau(t) = \sqrt{t^2+u^2} \tag{2.41}$$

$$\theta(t) = 1/2\tan^{-1}\left[t/u\right], \tag{2.42}$$

and u is the same as Eqn. 2.37.

We note that this result is much more robust than Eqn. 2.36, due to the oscillatory terms in the integrand canceling out behavior in the exponential tail. This solution encompasses the long time behavior ($t \gg \Omega^{-1}$), and breaks down if ρ_{sym} is singular for $\omega \geq \Omega$ or

if $u < 0$ [4]. The lack of dependence of the effective Rabi frequency on the detuning follows naturally from situations where the density of states at $-\delta$, $\rho(-\delta)$ is sizeable: that portion of the density of states is resonant, and the resonant behavior dominates. When $u < 0$, we may be in the detuning dominated regime, and these results no longer hold.

2.3.3 Discussion

The long-time behavior, Eqn. 2.40, may seem peculiar at first. The power-law decay envelope comes from the portion of the bath density of states that is "on-resonance" with the oscillations. In particular, for short times, Rabi oscillations are insensitive to detunings less than the Rabi frequency. This window narrows for longer time, leading to the observed power law behavior. More curiously, for times $t \gg u$, there is an overall phase shift of $\pi/4$ that is independent of many of the parameters of the bath. This dynamic shift eludes a similar immediate qualitative description, arising from the continuity of the bath density of states and the pole induced by probing of the bath (by means of the applied Rabi field) that is insensitive to first derivatives of the bath, *i.e.*, bath variables come in only in their quadrature and higher moments.

It is crucial to distinguish these results from more standard inhomogeneous broadening results. Unlike the case of Doppler broadening, for example, in this system the individual system detunings do not change as a function of time. When the correlation function is short-lived, the behavior would instead follow directly from the well understood results describing inhomogenous broadening due to Doppler shifts of laser-induced Rabi oscillations.To extend these results to describing inhomogeneous broadening in ensembles of self-assembled quantum dots, for example, would require considering the additional effect of inhomogeneity in the Rabi strength, Ω, and it is unclear that the corresponding phase

[4] Well-separated singularities in ρ_{sym} can be treated as additional stationary phase integral terms, and for each, corresponding oscillations at the resonance with different time-scales u_j will emerge.

shift would behave in a similar manner to the case of a single Rabi frequency. As such, that analysis is beyond the scope of this paper.

To compare these analytical results to exact solutions, we solve the system for finite spin, where we exactly evaluate the trace for finite N. In the homogeneous case, the Dicke picture of collective angular momentum allows us to go to large N, while the inhomogeneous case requires exponential operations for the exact value, but can be simulated through stochastic modeling of the trace function. We compare several different values of inhomogeneity and bath size N in Figure 2.4, and show strong quantitative agreement between the short time and long time approximations with the numerical evolution. We also show the convergence to full contrast for a fixed time and varying Rabi power.

The previous analysis assumed that the bath density of states could be taken as a Gaussian, which can be shown to reduce to the assumption of Gaussian noise [78]. However, inclusion of non-Gaussian effects leads in the general cases to integrals without easy solution.

The deviation from Gaussian noise for the fourth order at $T = \infty$ is

$$\frac{\langle \hat{A}_z^4 \rangle - 3\langle \hat{A}_z^2 \rangle^2}{3\langle \hat{A}_z^2 \rangle^2} \simeq -2/N. \tag{2.43}$$

To investigate the role non-Gaussian effects play, simulations with finite numbers of spin were conducted; the thermodynamic limit recovers Gaussian statistics. For small inhomogeneity, Fig. 2.4c indicates that increasing spin number decreases the amplitude of fluctuations from the expected Rabi signal. Increasing inhomogeneity leads to an apparent additional reduction of fluctuations, though quantifying this effect remains difficult.

2.3.4 Inclusion of the Markovian environment

For completeness, we now add the coupling of the qubit to an additional, Markovian environment, with a corresponding "radiative" decay to the ground state with a rate

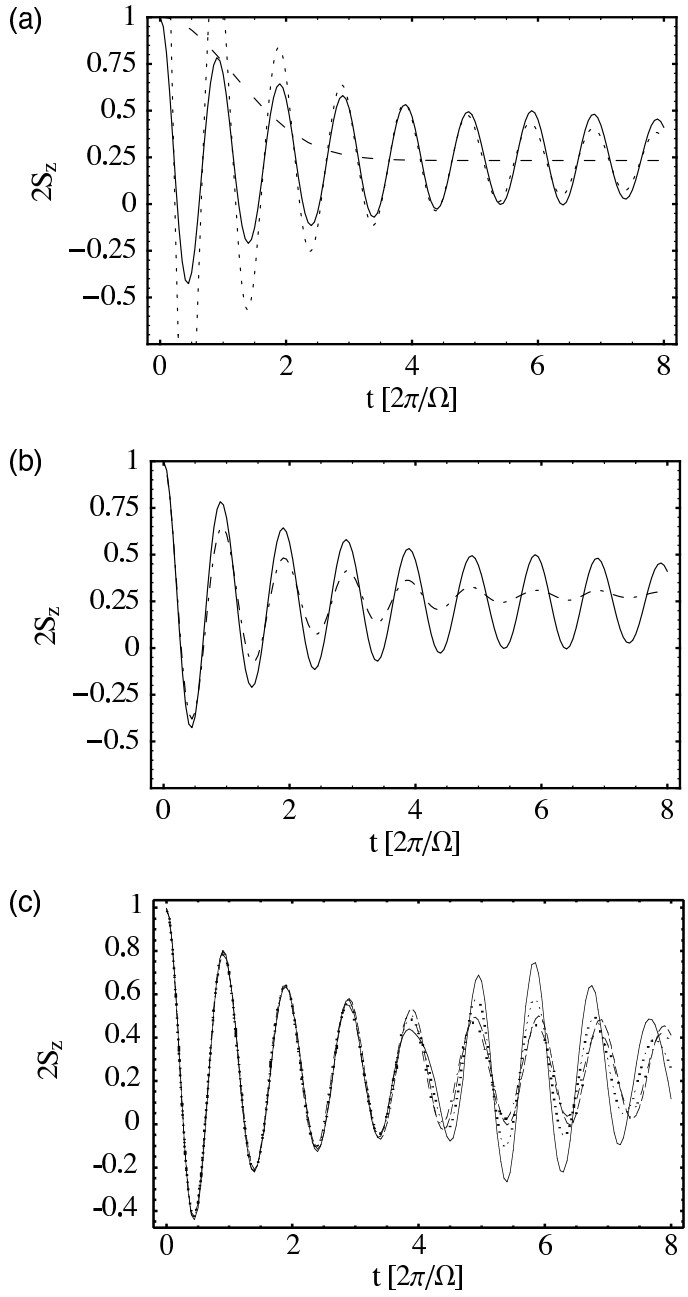

Figure 2.4: (a) Comparison of short time and long time theoretical results to analytic results, with $\sigma_\alpha = \bar{\alpha}/2$, $\lambda = 1$, $N = 20$, and $\Omega = 2\pi$. The exact solution (solid line) compares well with the short time decay (dashed line) and the long time tail plus phase shift (dotted line). (b) Comparison of the same exact result with the case with $\gamma = 0.5$ (dotted line). (c) Fluctuations for N =6 (solid),10 (dashed), 14 (dashed-dotted), and 20 (dotted).

γ. The optical Bloch equations must now be modified to include this decay, and exact solutions, while available, are cumbersome. However, the case of FID, with $\Omega = 0$, is immediately understandable. In the Heisenberg picture, we write

$$\frac{d\hat{S}_+}{dt} = -\gamma\hat{S}_+ + i\lambda\hat{A}_z\hat{S}_+ + \hat{\mathcal{F}}_+, \tag{2.44}$$

where the stochastic input field $\hat{\mathcal{F}}_+$ has the standard Markovian kernel, $\langle\hat{\mathcal{F}}_-(t)\hat{\mathcal{F}}_+(t')\rangle = 2\gamma\delta(t-t')$. Solving this equation of motion exactly for $\langle\hat{S}_+(t=0)\rangle = 1/2$ gives

$$\Phi_{FID,\gamma} = \frac{\langle\hat{S}_+(t)\rangle}{\langle\hat{S}_+(0)\rangle} = \Big\langle\exp(-i\lambda\hat{A}_z t - \gamma t)\Big\rangle_{bath} = \Phi_{FID}e^{-\gamma t}. \tag{2.45}$$

The Markovian environment results in *irreversible* exponential decay, which would be unaffected by any spin-echo experiment. For long correlation time baths, spin-echo experiments provide a direct measure of the Markovian component of the decay.

For the case with $\Omega \neq 0$, we use the analytical evolution for solving the Kraus operator form for the Bloch vector, $d\hat{\vec{S}}/dt = M\hat{\vec{S}} + \vec{u}$ and evaluating the expectation values of all functions of $\hat{A}_z$ at each time point. The results are cumbersome, and checked only numerically. Qualitatively comparing the result, shown in Figure 2.4b, to the $\gamma = 0$ case, we see that the crucial features of phase shift and fast initial damping with long-lived oscillations remain, but that the steady state population difference is shifted, and the oscillations are eventually damped by the exponential tail. The corresponding lineshape is approximately

$$\langle\hat{f}\rangle = 1 - \Big\langle\tfrac{\Omega\gamma}{[(\gamma/2)^2+(\lambda\hat{A}_z+\delta)^2+\Omega^2]}\Big\rangle \tag{2.46}$$

Finally, we now consider the effect decorrelation of $\hat{A}_z$ plays in the observed oscillations. Unlike the case of free evolution, $[H_0(t), H_0(t')] \neq 0$, leading to difficulties in analytical evaluation of the propagator including decorrelation effects. We can, however, consider it partially by use of a Magnus expansion, in the limit of weak to intermediate strength mesoscopic spin bath.

Formally, we transform H_0 to the interaction picture with respect to $\Omega\hat{S}_x$, and with $\delta = 0$, giving

$$\tilde{H} = \lambda\hat{A}_z[\cos(\Omega t)\hat{S}_z + \sin(\Omega t)\hat{S}_y] \tag{2.47}$$

If we assume $\hat{A}_z$ varies on time scales much longer than $1/\Omega$, we can use a magnus expansion. The expansion of this Hamiltonian at peaks in the expected oscillations ($\tau = 2\pi/\Omega$) yeilds

$$U_{eff}(\tau) = \exp[-i\tau(H_0 + H_1 + \ldots)] \tag{2.48}$$

with

$$H_0 = 0 \tag{2.49}$$

$$H_1 = 2(\lambda\hat{A}_z)^2/\Omega\hat{S}_y \ . \tag{2.50}$$

We neglect higher order contributions by assuming that $\langle\hat{A}_z^2\rangle^4\lambda^4/\Omega^4 \ll 1$. Thus, the envelope of oscillations should be determined by

$$U_{eff}(t) = \exp[-i\int_0^t \frac{2(\lambda\hat{A}_z(t'))^2}{\Omega}dt'\hat{S}_y] \ . \tag{2.51}$$

where we have assumed that over a time τ, $\hat{A}_z(t)$ is fixed. We note that this form of quadratic noise has been investigated in detail [126]. The lowest order perturbative expansion requires determining the spectral function

$$S_{A^2}(\omega) = \int \frac{d\tau}{2\pi}\langle\hat{A}_z(t+\tau)^2\hat{A}_z(t)^2\rangle e^{-i\omega\tau} \ . \tag{2.52}$$

Assuming Gaussian statistics for $\hat{A}_z$, we find

$$\langle Az(t)^2\hat{A}_z(t')^2\rangle = (\int d\omega S(\omega))^2 + 2(\int d\omega S(\omega)e^{i\omega(t-t')})^2 \tag{2.53}$$

The resulting decay of oscillations should be given by

$$\exp(-\frac{4\lambda^4}{\Omega^2}\int d\omega S_{A^2}(\omega)\frac{\sin^2(\omega t/2)}{(\omega/2)^2}) \tag{2.54}$$

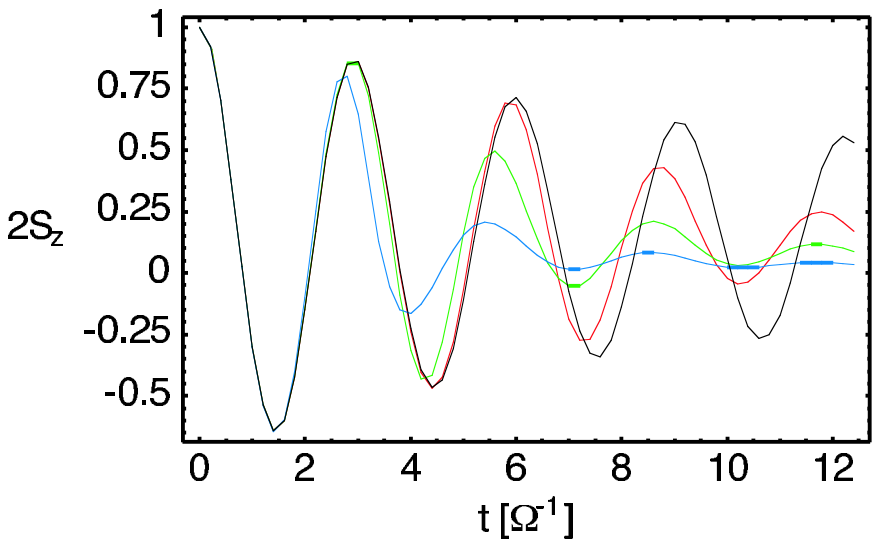

Figure 2.5: Expected value of $2\hat{S}_z$ as a function of time for an initial state $\hat{S}_z = 1/2$, with driving and low frequency noise $\lambda = \Omega/2$. Decorrelation rates of 0 (black), $\Omega/100$ (red), $\Omega/30$ (green) and $\Omega/10$ (blue) are shown. It is apparent that decorrelation leads to steady state values of zero, faster than $1/\sqrt{t}$ decay, and reduced phase shift (from $\pi/4$).

Oscillations with low frequency noise for $S(\Omega)$ are shown in Fig. 2.5.

We remark that for time independent $\hat{A}_z$ and a Gaussian density of states we can evaluate the expected envelope of oscillations,

$$\langle U_{eff}(t)\rangle = (1 + 2it\rho''(0)/\rho(0)\Omega)^{-1/2} \ , \tag{2.55}$$

reproducing the $1/\sqrt{t}$ long-time tail found by more exact means. Furthermore, as $\langle \hat{A}_z^2\rangle \neq 0$ in general, a phase shift due to small rotations around $\hat{S}_y$ after each Rabi oscillation should be expected.

2.4 Application to experimental systems

We now consider the physical systems where the quasi-static bath assumptions are valid. One case is nuclear spins interacting with an electron spin in a quantum dot. There, the dominant internal bath Hamiltonian is aligned with the bath-interaction, and

$[\hat{H}_B, \hat{A}_z] = 0$ identically [183, 131]. Another system is superconducting qubits, where charge-traps and other few-state fluctuators play a similar role. Finally, some NMR systems with one probed spin (e.g., a Carbon-13) is coupled to many spins (e.g., nearby hydrogens).

2.4.1 Electron spin in quantum dots

The hyperfine interaction between the electron and the nuclear spins is given by

$$H_{QD} = \gamma_e B_0 \hat{S}_z + \lambda_{QD} \sum_k \alpha_k \hat{\vec{S}} \cdot \hat{\vec{I}} + \gamma_n B_0 \sum_k \hat{I}_z^k \tag{2.56}$$

where the $\alpha_k \propto |\psi(r_k)|^2$ are weighted by the electron wavefunction's overlap with lattice site k. For GaAs quantum dots with N nuclear spins, $\lambda_{QD} \simeq 207\text{ns}^{-1}/\sqrt{N}$ [147], with the normalization condition $\sum_k \alpha_k^2 = 1$. Identifying $\gamma_e B_0 = \omega$ and adding a time dependent ESR field in the x-axis the model Hamiltonian is recovered, with $\lambda = \lambda_{QD}$. In the case of a large applied magnetic field ($\omega \gg \lambda_{QD}$), the results heretofore derived hold.

While experiments investigating ESR and spin dephasing in single quantum dots are ongoing, the contraints imposed by the quasi-static limit make standard ESR technically difficult to achieve. For small quantum dots (e.g. single electron quantum dots), $\lambda_{QD} \gtrsim 0.1$ ns^{-1} ($N \simeq 10^5$). If the decorrelation rate Γ is determined by dipolar-diffusion processes, it can be no faster than 10 ms^{-1}, the linewidth of NMR in bulk GaAs, and the quasi-static limit is appropriate. For the quasi-static field to be overcome, either many measurements must be taken in the correlation time of the bath, or ESR field's Rabi frequency Ω must be much larger than 0.1 ns^{-1}. This latter requirement may be quite difficult for current experimental parameters. Active correction sequences may lower this rate, by averaging through NMR pulses the dipolar interaction [196, 131], making it possible to perform accurate phase estimation within the enhanced correlation time of the bath.

There is another important situation where the mesoscopic bath picture holds: during an exchange gate [122, 151]. In particular, for two tunnel coupled quantum dots,

each in the single-electron regime, the overall Hamiltonian is

$$H_{DQD} = H^1_{QD} + H^2_{QD} + J\hat{\vec{S}}^1 \cdot \hat{\vec{S}}^2 \tag{2.57}$$

where J is the exchange interaction between the two dots. While the $m_s = \pm 1$ triplet states ($|\uparrow\uparrow\rangle, |\downarrow\downarrow\rangle$) are well separated by Zeeman energy, the $m_s = 0$ states ($|\uparrow\downarrow\rangle, |\downarrow\uparrow\rangle$) are nearly degenerate. In the basis $\{|\uparrow\downarrow\rangle, |\downarrow\uparrow\rangle\}$, this two-level system is described by the Hamiltonian

$$H_{m_s=0} = \begin{pmatrix} -\lambda \hat{A}_z^{(DQD)}/2 & \Omega/2 \\ \Omega/2 & \lambda \hat{A}_z^{(DQD)}/2 \end{pmatrix} \tag{2.58}$$

where $\lambda \hat{A}_z^{(DQD)} = \sum_{k,i=1,2} \lambda^i_{QD} (-)^i \alpha^i_k \hat{I}^{k,i}_z$ is the bath parameter for this two-level system, and $\Omega = J$. This Hamiltonian maps exactly to Equation 2.8.

Recently experiments demonstrated coherent oscillations driven by controlled exchange interactions [151]. The system was prepared in an eigenstate of the mesoscopic spin bath interaction (e.g., the $|\uparrow\downarrow\rangle$ state) and coherent oscillations between $|\uparrow\downarrow\rangle$ and $|\downarrow\uparrow\rangle$ were driven by applying a pulse of non-zero Ω for finite time. These experiments correspond exactly to the driven evolution examined in the previous section. As such, for small exchange values ($\Omega \simeq \lambda$) we expect the exchange operations to exhibit the characteristic power-law decay and phase shift found in this work. Our approach agrees with system-specific theoretical predictions of Ref. [39].

2.4.2 Superconducting qubits

The quasi-static assumptions also hold for bistable two-level fluctuators, where the $\hat{I}_z$ eigenvalues denote which state is populated, and the dominant interaction with a charge system is a conditional capacitive energy, leading to a $\hat{S}_z \hat{I}_z$ interaction between the two. Furthermore, $1/f$-type two-level fluctuators, considered the source of most Josephson junction dephasing [100, 76], are quasi-static in the high frequency regime, *i.e.*, above the

bath cutoff. Curiously, the spin-boson model [24] does not fulfill this criterion. Other pseudo-spin systems, such as flux qubits, may or may not have this structure, depending on the bath degrees of freedom.

The extension of our results to superconducting qubit experiments is motivated by results characterized by low contrast, long-lived Rabi oscillations, similar to those exhibited in our model. For a system with some minimum time of applied Rabi field (as is often the case in these experiments) the initial, fast decay could be encompassed by oscillations occurring within this minimum time, while the observable oscillations correspond to the long-time tail.

Of the superconducting qubit experiments, we focus on Ref. [128], as 1/f noise is a dominant term for similar devices in CW behavior. In addition, there are observed resonances with flucuators in the measurement spectrum [167], which suggests that coherent coupling to these two-level systems may be possible. A model which includes preparation and measurement errors is considered in Appendix B.2; we note the results here. We find that in the low power regime, our model explains the observed behavior, but at higher powers incoherent heating due to driving microwaves play an important role as well.

Fitting the parameters from Appendix B.2 to the Rabi oscillations shown in Ref. [128] yield the values in Table 2.1. The results are consistent with bath domination for low power ($\Omega < 0.5\text{ns}^{-1}$) and heating / preparation error dominating at high power. This gives the characteristic low contrast oscillations observed, even though the static measurement efficiency is quite high (order 75-85%). The resulting oscillations are compared to Ref. [128] in Fig. 2.6.

Table 2.1: Fitted values (explained in Appendix B.2) for the model describing the experiments of Ref. [128]. The values in parenthesis are the 90% confidence intervals of the fit.

$M_{\uparrow\uparrow}$	0.75(4)
$M_{\downarrow\downarrow}$	1.00(3)
Γ	0.10(4) ns^{-1}
λ	0.27(1) ns^{-1}

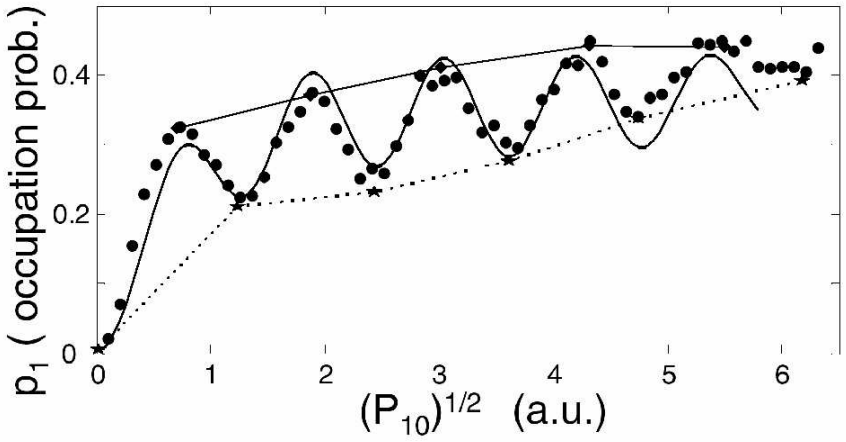

Figure 2.6: Plot of oscillations reproduced from Ref. [128] (filled circles). The probability of spin flip, $P_1 = \frac{1}{2} - \langle \hat{S}_z(t) \rangle$ is plotted versus Rabi frequency $\Omega \propto P_{10}^{1/2}$ a fixed Rabi evolution time of 25 ns. Overlaid for the given fit parameters are the expected values from our model (solid line).

2.4.3 Other systems

Under certain conditions, NMR systems may be described by a quasi-static mesoscopic spin bath . For example, large molecules or crystalline structures with long correlation times and coherent dynamics within the molecule, where one or few spins are coupled to many adjacent spins in a static configuration, may be described by our model. In contrast, liquid state NMR with small molecules has bath characteristics dominated by transient couplings to other molecules, and our model is inappropriate.

One example is in cross-polarization experiments on solid-state ferrocene, where defocusing sequences are applied to generate a Hamiltonian equivalent to Eqn. 2.8 [27]. By direct observation of the cross-polarization signal, driven evolution may be observed. We remark that previous experiments, investigating spin-bath coupling in free evolution [185] will not show this behavior. System specific work [42] is in general agreement with our results.

2.5 Methods to mitigate bath effects

While the strongly coupled mesoscopic spin bath leads to dephasing during free evolution and reduced contrast and a dynamical phase shift during driven evolution, the long-time correlation of the bath allows for correction. We start by considering spin-echo-type passive error correction, which can be implemented if a sufficiently strong Rabi frequency for driving is available. We then consider how entropy transfer from the quasi-static bath to the environment (bath-cooling) may be an effective alternative means of reducing the damping due to the bath. In essence, for specific bath models, it may be possible to prepare coherences in the bath which effectively reduce the uncertainties engendered by the bath. The inherently quantum mechanical nature of this leads us to consider this

mechanism as environmental squeezing.

2.5.1 Passive error correction

With strong Rabi power ($\Omega \gg \lambda$), high fidelity Rabi oscillations are possible even in the presence of the mesoscopic spin bath. This is the power-broadened limit. The error of such pulses scales as $(\lambda/\Omega)^2$ and as such determining the quasi-static bath strength for a given system will yield the required Rabi power to overcome the effects of the bath through passive error correction.

In this limit, spin-echo techniques work well to greatly extend the lifetime of oscillations, and passive error correction [204] will be straightforward to implement. Higher order pulse sequences than those considered in Section III may lead to further improvement [68]. Other techniques, such as quantum bang-bang [192], are already implicit in this analysis in the form of coherent averaging theory [131].

2.5.2 Cooling the bath

When experimental limitations of Rabi power or other experimental difficulties make minimization of the coupling strength impossible, the quasi-static bath remains a problem uncorrectable by passive error correction. Then, active cooling techniques may be a useful alternative. We now outline how, for the specific case of scalar interactions with the bath, qubit manipulation may lead to efficient entropy transfer from the mesoscopic spin bath to the qubit system. By exploiting resonances between the bath and system, we may cool the bath degrees of freedom. Furthermore, in the quasi-static limit, coherences developed between bath spins can lead to additional improvements through a form of squeezing.

To illustrate cooling, the explicit case of an electron spin in a quantum dot is illu-

minating. For that system, the full spin-coupling (including the terms previously neglected in the rotating wave approximation) is a scalar interaction [183],

$$\lambda\hat{\vec{S}}\cdot\hat{\vec{A}} = \lambda\hat{\vec{S}}\cdot\left(\sum_k \alpha_k\hat{\vec{I}}^k\right). \tag{2.59}$$

The dominant terms in the internal Hamiltonian of the nuclear spins is

$$H_A = \sum_k \omega_k \hat{I}_z^k \ , \tag{2.60}$$

due to the Larmor precession of the nuclear spins in the external magnetic field. When the effective splitting of the qubit (electron spin) is comparable to ω_k, the electron spin comes into resonance with the nuclear spins. In essence, by tuning the system near such a "noise-resonance", the bath can be driven in a double-resonance manner (analogous to electron-nuclear double resonance, ENDOR), where the on-axis $(z-z)$ coupling is offset by the changing frequency of the applied Rabi field. Before, the internal spin dynamics were considered to be much slower, *i.e.*, $\omega_k \ll |\omega + \lambda\langle\hat{A}_z\rangle|$. For double-resonance, this condition is no longer satisfied, and the quasi-static approximations begin to break down.

For this resonant regime, the reader is referred to previous work on electron spin cooling [94, 181] for the details of the process. The benefits of cooling are outlined here. In the fully cooled state, the quasi-static bath acts entirely as an additional detuning on the system, as $\langle\hat{A}_z\rangle^2 = \langle\hat{A}_z^2\rangle$. Near such high polarization, the quasi-static bath effects do not supress Rabi and Ramsey-type effects, as the bath strength parameter at high temperature $(\lambda\sqrt{\langle\hat{A}_z^2\rangle})$ is greatly reduced at low temperature. Quantitatively, this improvement is given by the ratio of γ_{FID} (Eqn. 2.20) at high and low polarizations, which is $\eta = \sqrt{1/(1-P)}$ for a polarization P of the bath (neglecting inhomogeneous corrections). In terms of experimental observables, it should result in an increase in the observed contrast of Rabi oscillations and improved Ramsey signals as if the bath strength parameter, λ, had been reduce by the improvement factor η. The improvements will be limited by coherences developed within

the bath, by the correlation time of the quasi-static bath, which will limit the lifetime of the cooling, and by other, non-local (and correspondingly difficult to cool) degrees of freedom, implicit in the Markovian environment component of this model.

Cooling could proceed along the following lines. The system is prepared in a $|\downarrow\rangle$ state by coupling to the Markovian environment, *e.g.*, by moving to a strongly coupled region of parameter space. This is the current preparation method for superconductor-based qubit designs; in quantum dots, the energy difference between spin states due to zeeman splitting or exchange interactions allows preparation by controlled coupling to a nearby Fermi sea [151]. Then a weak, negatively detuned Rabi field is applied for a short time (order one Rabi flop). This process is repeated many times. Including state measurement after the Rabi field will allow measurement of the cooling efficiency, as the bath will lead to additional flip to the $|\uparrow\rangle$ state in the far detuned regime. In some cases, where the natural frequencies of the bath degrees of freedom are large, resonances between the bath and system may be observed. Tuning to the "red" side of these resonances will also force cooling to occur.

As cooling is effected only through the logical basis states (the qubit states of up and down), it is not necessarily efficient. For a simple scalar coupling (*e.g.* a hyperfine interaction), cooling proceeds due to the action of the $\hat{A}_-$ operator, where

$$\hat{A}_- = \sum_k \alpha_k \hat{I}_-^k \tag{2.61}$$

However, states $|\mathcal{D}\rangle$ with the property $\hat{A}_-|\mathcal{D}\rangle = 0$ cannot cool under this action. This is similar in practice to single mode cooling, and as such it does not greatly improve the bath polarization or entropy [181] for intermediate or larger bath sizes. However, these states do have a useful symmetry property, namely they are "dark" under the action of the collective lowering operator. Thus, the natural state of the density matrix after many cycles of cooling

is

$$\hat{\rho} = \sum_{\beta} \rho(\beta) |\mathcal{D}(\beta)\rangle \tag{2.62}$$

where the sum is over other degeneracies (see [4, 181] for details). We now indicate how cooling limited to polarizations such that η remains order unity can still be sufficient to greatly reduce the dephasing induced by the mesoscopic spin bath.

In particular, if this cooling can be applied along the axis of Rabi oscillations (rather than the z axis), the effects of such marginal cooling are immediately apparent. In particular, the component of noise in the x and y axes are averaged by the bias, ω, while the z axis is only averaged by the driving field, Ω. If the z component of the bath noise can be reduced, the corresponding Rabi and Ramsey signals will be improved. In the case of homogeneous coupling ($\alpha_k = 1/\sqrt{N}$) to the environment, it can be shown immediately that cooling into dark states decreases the quadrature in the non-cooled axes, *i.e.*,

$$\langle \hat{A}_z^2 \rangle = 1/\sqrt{N} \tag{2.63}$$

which is a $\sqrt{N}$ improvement over the uncooled state. As the other quadratures correspond to noise suppressed by the bias, the effect on experiment is immediate and possible quite useful. Such Rabi-axis cooling can be achieved for nuclei in quantum dots by first cooling along the natural (z) axis, followed by a NMR $\pi/2$-pulse to rotate the nuclear coherences to be parallel to the driving field.

The coherences between spins in the bath have a limited lifetime, determined by the decay of the correlation functions of the bath. Therefore, for this process to be useful, the qubit-bath interaction must be much faster than the bath decorrelation time, but this is exactly the quasi-static approximation already made. Before each run of a Rabi oscillation-type experiment, a cooling sequence could be applied, to keep the bath degrees of freedom. The resulting oscillations should reflect the "cooled" bath results, and as such could provide

a substantial improvement over uncooled systems.

2.6 Conclusions

The response of a two-level system (a qubit) with driving fields coupled to a local, mesoscopic collection of finite-level systems and with additional coupling to a larger, Markovian environment has analyzed in this paper. The natural simplifications of the Hamiltonian lead to a quasi-static regime, wherein bath correlation functions are long-lived when compared to experimental manipulation and measurement time scales. However, decorrelation of the bath and dynamic thermalization processes lead to apparent decay when a single-qubit is manipulated and measured repeatedly. The large variations of bias produced by the quasi-static bath can be difficult to correct with limited Rabi frequency ranges accessible to experiments.

The simple case of free induction decay demonstrates the role increasing bath strength and non-Markovian effects have to play on the short term, non-exponential decay, while finite number effects can lead to revivals and fluctuations, distinctly mesoscopic effects. This illustrates explicitly the non-Gaussian nature of the bath.

In the presence of weak fields, a line-shape distinctive to the spin-bath model is discovered, though inclusion of additional (Markovian) decoherence and dephasing recovers the expected Lorentzian behavior. As the driving field's strength is increased, Rabi oscillations are possible, but for short times there may be a phase shift of order $\pi/4$ and fast initial decay of the oscillation envelope. However, longer times, with only a power law decay going as $t^{-1/2}$, will most likely be dominated by other, exponential decay processes. As a result, a quasi-static bath could lead to reduced contrast of oscillations that may be consistent with experimental observations of superconducting qubit devices. In addition, experiments with

single- and double-quantum dots may probe this quasi-static bath model more directly.

Finally, the role of passive error correction, quantum bang-bang, and environment cooling have been considered, with each appropriate for different ranges of parameters. It may be that as the understanding of quasi-static, local baths increases the means to mitigate their effect will become more apparent. This is a first and crucial step towards that end.

The authors would like to thank A. Imamoglu, D. Loss, J. M. Martinis, H. Pastawski, A. Sorensen, and C. van der Wal for helpful discussions. This work has been supported in part by NSF and ARO.

Chapter 3

Long-lived quantum memory in a mesoscopic environment

J.M. Taylor[1], A. Imamoglu[2], C. M. Marcus[1], and M.D. Lukin[1]

[1] Department of Physics, Harvard University, Cambridge, Massachusetts 02138, USA
[2] Institute of Quantum Electronics, ETH-Hönggerberg, HPT G 12, Zürich, Switzerland

We describe a technique to create long-lived quantum memory for quantum bits in mesoscopic systems. Specifically we show that electronic spin coherence can be reversibly mapped onto the collective state of the surrounding nuclei. The coherent transfer can be efficient and fast and it can be used, when combined with standard resonance techniques, to reversibly store coherent superpositions on the time scale of seconds. This method can also allow for "engineering" entangled states of nuclear ensembles and efficiently manipulating the stored states. We also present a unified description of cooling and manipulation of a mesoscopic bath of nuclear spins via coupling to a single quantum system of electronic spin (quantum bit). We show that a bath cooled by the quantum bit rapidly saturates. Although the resulting saturated states of the spin bath ("dark states") generally have low degrees of polarization and purity, their symmetry properties make them a valuable resource for the coherent manipulation of quantum bits. Specifically, we demonstrate that the dark states of nuclear ensembles can be used to provide a robust, long-lived quantum memory for qubit states.

An intriguing challenge for modern science and technology is the coherent manipulation of quantum systems coupled to realistic environments. Interest in these problems is

in part due to fundamental aspects of quantum control and decoherence, but this research has also been stimulated by recent developments in quantum information science [141]. Although over past decades much progress has been made in the controlled manipulation of isolated atomic and optical systems [136], the complex environment of a solid-state system makes it significantly more challenging to achieve a similar degree of control.

Spin degrees of freedom of electrons confined in semiconductor quantum dots are attractive qubit candidates [122, 19]. Relatively long decoherence times are expected for such systems and techniques for the coherent manipulation and measurement of electron spins are now being developed. For the latter, coupling of spin and charge degrees of freedom is probably necessary. Experimental measurements of the spin relaxation times indicate sub-MHz rates [75], although it is not yet clear what will determine the ultimate coherence lifetimes. Spin-orbit coupling of electron spins to phonons will be the dominant mechanisms for electron-spin decoherence considered in this paper.

3.1 Nuclear ensemble memory

This section describes a technique for greatly extending the lifetimes of electron-spin qubits in confined structures by coherently mapping an arbitrary spin superposition state into the spins of proximal, polarized nuclei. This is achieved by effective control of the spin-exchange part of hyperfine contact interaction. After the transfer is completed, the resulting superpositions could be stored for a very long time – up to seconds – and mapped back into the electron spin degrees of freedom on demand. We further show that the stored states can be manipulated using an extension of standard resonance techniques.

Although it is widely known that nuclear spins can possess exceptionally long coherence times due to their weak environmental coupling, single nuclear spins are very

difficult to manipulate and measure in practice [99]. In the present approach these problems are circumvented by using collective nuclear degrees of freedom, which do not require individual addressing and control. We demonstrate that such collective states are extremely robust with respect to realistic imperfections, such as partial initial polarization and spin diffusion, and decoherence. As a result the present technique allows combines the strengths of electron spin (or charge) manipulation with the excellent long-term memory provided by nuclei.

When uncontrolled, the coupling of electronic spin degrees of freedom to nuclei may be considered an environmental decoherence process. Interesting features of this process arise from its non-Markovian nature [103, 134, 102]. The present paper shows that properly controlled coupling of electrons to nuclei can be used to greatly extend the effective coherence time of electron spins. This study parallels recent work involving the use of atomic ensembles as quantum information carriers [53].

To illustrate the technique, consider a single electron localized in quantum dot. The effective Hamiltonian for the electron and N spin-I_0 nuclei in a magnetic field B_0 along the z-axis is

$$\hat{H} = g^* \mu_B B_0 \hat{S}_z + g_n \mu_n B_0 \sum_j \hat{I}_z^j + \hat{V}_{HF}; \tag{3.1}$$

The first two terms of Eq. 3.1 correspond to the Zeeman energy of the electronic and nuclear spins; the third term is the hyperfine contact interaction between the s-state conduction electrons and the nuclei in the dot, $\hat{V}_{HF} = \sum_j a_j \hat{\vec{I}}^j \cdot \hat{\vec{S}}$. The coefficients $a_j = A v_0 |\psi(\vec{r}_j)|^2$ correspond to the one-electron hyperfine interaction with the nuclear spin at site $\vec{r}_j$, where A is the hyperfine contact interaction constant, v_0 is the volume of a unit cell, and $\psi(\vec{r})$ is the envelope function of the localized electron. Spin-orbit effects are strongly suppressed in confined structures [86]; they main contribution to relaxation of electron-spin coherence. The hyperfine term can be written $\hat{V}_{HF} = \hat{V}_D + \hat{V}_\Omega$ where $\hat{V}_D = \sum_j a_j \hat{I}_z^j \hat{S}_z$ and $\hat{V}_\Omega =$

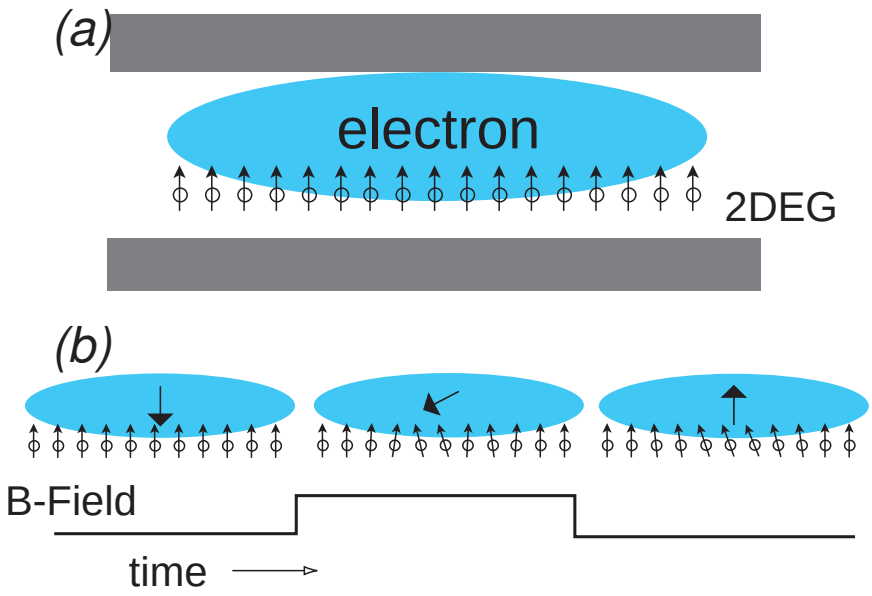

Figure 3.1: (a) A schematic of an electron trapped in a quantum dot with polarized nuclei. (b) Storage, where a pulse in the magnetic field starts amd brings the spins into resonance. After the electron spin has flipped (π-pulse) the pulse is ended. Readout is the same process in reverse.

$\sum_j a_j/2(\hat{I}^j_-\hat{S}_+ + \hat{I}^j_+\hat{S}_-)$. $\hat{V}_D$ produces an effective magnetic field for the electron $\hat{B}_{\text{eff}} = B_0 - 1/g^*\mu_B \sum_j a_j \hat{I}^j_z$, which results in the well-known Overhauser shift. However, when $g^*\mu_B\hat{B}_{\text{eff}} \ll \hat{V}_\Omega$, spin exchange becomes the dominate effect.

3.1.1 Fully polarized case

We start with a perfectly polarized nuclear ensemble $|\mathbf{0}\rangle_n = |I_0, ..., I_0\rangle_n$, as shown in Fig. 3.1(a). Due to a total angular momentum conservation only a spin-down initial electron state can undergo non-trivial evolution. When the dynamics are governed by $\hat{V}_\Omega$ ($\hat{B}_{\text{eff}} \to 0$), there is a coherent exchange of excitations between electronic and nuclear degrees of freedom. For the inital state $|\downarrow\rangle_e \otimes |\mathbf{0}\rangle_n$, spin-exchange couples this state to the

collective nuclear excitation with one flipped spin $|\uparrow\rangle_e \otimes |\mathbf{1}\rangle_n$ with

$$|\mathbf{1}\rangle_n \equiv (\sum_j |a_j|^2)^{-1/2} \sum_j a_j |I_0, ..., (I_0 - 1)_j, ..., I_0\rangle_n.$$

Hence the evolution is given by the two-level dynamics

$$\begin{bmatrix} |\downarrow\rangle|\mathbf{0}\rangle \\ |\uparrow\rangle|\mathbf{1}\rangle \end{bmatrix}(t) = \begin{bmatrix} \cos(\Omega t/2) & -i\sin(\Omega t/2) \\ i\sin(\Omega t/2) & \cos(\Omega t/2) \end{bmatrix} \begin{bmatrix} |\downarrow\rangle|\mathbf{0}\rangle \\ |\uparrow\rangle|\mathbf{1}\rangle \end{bmatrix}(0),$$

The ensemble displays Rabi-oscillations with an effective Rabi rate:

$$\Omega = \sqrt{2I_0 \sum_j |a_j|^2}.$$

At the same time, the spin-up electronic state $|\uparrow\rangle_e \otimes |\mathbf{0}\rangle_n$ is an eigenstate of both $\hat{V}_D$ and V_Ω. Hence, by pulsing the applied field to go from $g^*\mu_B \hat{B}_{\text{eff}} \gg \hat{V}_\Omega$ to $\hat{B}_{\text{eff}} \sim 0$ for a time $t = \pi/\Omega$ as diagramed in Fig. 3.1(b), an arbitrary superposition of electronic state will undergo the following evolution:

$$(\alpha|\uparrow\rangle_e + \beta|\downarrow\rangle_e) \otimes |\mathbf{0}\rangle_n \rightarrow |\uparrow\rangle_e \otimes (\alpha|\mathbf{0}\rangle_n + i\beta|\mathbf{1}\rangle_n),$$

demonstrating that an electronic spin state can be coherently mapped into nuclei.

The Rabi-flopping process can be controlled by removing the electron from the dot or by changing the effective magnetic field, B_0. Away from the resonance condition ($|B_{\text{eff}}| \gg \Omega/g^*\mu_B$), the system is far detuned and no evolution will occur. For the perfectly polarized state the effective detuning is $\delta = (g^*\mu_B - g_n\mu_n)B_0 + I_0 A + (I_0 - 1)A/N$. The Rabi frequency depends upon the distribution of the a_j coefficients, $\Omega = \sqrt{2I_0}A/\sqrt{N}(1 + (\Delta\bar{a}^2)/\bar{a}^2)^{1/2}$ with bars denoting averages over the set $\{a_j\}$. For a GaAs dot with 10^4 nuclei and $\Delta\bar{a}^2 \sim \bar{a}^2$, $A \approx 90\mu$eV and $I_0 = 3/2$, and the speed of transfer is determined by $\Omega/2\pi \simeq 0.6$ GHz, which exceeds the expected spin coherence time by three orders of magnitude. The resonance condition is fulfilled for $|B_{\text{eff}}| \ll 50$mT. Retrieval of the stored qubit can be implemented

by reversing this process: we either inject a spin-polarized electron into the dot or change the effective magnetic field, bringing the levels into resonance, and Rabi oscillations pick up at the same point as before. The rise time of such a pulse must be much less than the Rabi time for high fidelity transfer. This requirement can be greatly alleviated by using adiabatic passage techniques (see e.g. Ref. [53]).

Before proceeding with a detailed description of the coherence properties and imperfections we note that the above results can be easily generalized to the preparation of complex collective nuclear states. For example, injection of a series of spin-down electrons into spin-up polarized nuclei will lead to a progressive increase of the nuclear spin. In the basis of collective angular momentum, $\hat{\vec{I}} = \sum_i \hat{\vec{I}}^i$, we define the total angular momentum nuclear states $|\mathbf{m}\rangle_n = |I = NI_0, I_z = I - m\rangle_n$. Each electron can effect the transfer $|\downarrow\rangle_e \otimes |\mathbf{m}\rangle_n \rightarrow |\uparrow\rangle_e \otimes |\mathbf{m}+\mathbf{1}\rangle_n$. When injected electrons are prepared in different superposition states this process can be used to effectively "engineer" collective states of nuclear ensembles. In fact using a proper sequence of electrons an arbitrary state of the type $|\mathbf{\Psi}\rangle_n = \sum_{m=0}^{I} c_m |\mathbf{m}\rangle_n$ can be prepared [1]. We note in particular that the highly entangled states of the kind $(|\mathbf{0}\rangle_n + |\mathbf{m}\rangle_n)/\sqrt{2}$, with large $\mathbf{m}$ could be used for high-resolution NMR spectroscopy in analogy with related atomic physics studies [13, 91]. Such states can also be prepared by manipulating one electron in the dot with fast electron-spin resonance (ESR) pulses.

Injection of polarized electrons, combined with ESR pulses, can also be used to perform manipulation of the stored nuclear state. For example, the qubit stored in nuclear spin could be mapped into the injected electron and an ESR pulse can be used to rotate it. Subsequently, it can be mapped back to nuclei. Alternatively virtual, off-resonant ($|\delta| \gg \Omega$)

[1] For spin-1/2 nuclei considering a reverse process $|\Psi\rangle \rightarrow |\mathbf{0}\rangle$ provides a proof, in direct analogy to C.K. Law and J.H. Eberly, Phys. Rev. Lett. **76**, 1055 (1996). The same argument applies to larger nuclear spin I_0 when $\mathbf{m} \ll I$.

coupling of storage states to electron spin can be used to shift the resonance frequencies of transitions $|\mathbf{m}\rangle_n \rightarrow |\mathbf{m}+\mathbf{1}\rangle_n$ relative to each other. For example in the case of two lowest states $m = 1, 2$ the differential shift is on the order of $\Omega^4/|\delta|^3$. Whenever this shift is large compared to decoherence rate and the spectral width of excitation pulse, the lowest two states of collective manifold $|\mathbf{0}\rangle_n, |\mathbf{1}\rangle_n$ can be considered as an effective two level system and can be manipulated through NMR pulses and other means. These ideas could be extended to the spin-exchange coupled qubits proposal [122].

3.1.2 Imperfections

We now turn to the consideration of various decoherence mechanisms and imperfections that limit the performance of the storage technique. To evaluate the effects of spatial inhomogeneity we note that the collective state $|\uparrow\rangle_e \otimes |1\rangle_n$ is not an eigenstate of $\hat{V}_D$ unless the a_j's are identical. The effect is determined by the distribution of eigenenergies under $\hat{V}_D$ of the states $|\uparrow\rangle_e \otimes |I_0, ..., I_0 - 1_j, ..., I_0\rangle_n$, given by

$$E_j = (g^*\mu_B/2 - g_N\mu_N I_0)B_0 + I_0 A/2 - a_j/2$$

Since $\Delta\bar{E}^2 \sim \Delta\bar{a}^2$, the inhomogeneous linewidth is $\sim \bar{a} = A/N$. Hence inhomogeneous broadening is smaller than the relevant time scale for Rabi-flopping by a factor of $\sqrt{N}$, and is negligible during transfer operation. After the mapping, its effect can be mitigated by either removing the electron from the dot, thereby turning off the hyperfine interaction entirely, or by using ESR spin-echo techniques to reverse the phase evolution [25].

The leading decoherence process for the stored state is nuclear-spin diffusion, with dephasing rates in the kHz domain. Thermal effects associated with spin-lattice coupling are on the order of minutes even for room-temperature samples [131]. However, techniques from NMR can be used to mitigate this effect [131, 147]. By applying fast NMR pulse

sequences [196] to rotate the nuclear spins the time average of the leading terms in the dipole-dipole Hamiltonian can be reduced to zero, leaving only residual dephasing due to second-order dipolar effects, pulse imperfections and terms due to the finite length of the averaging sequence. These phenomena have been studed for several decades for solid-state NMR systems and well-developed techniques routinely reduce T_2 by several orders of magnitude [131], down to sub-Hz levels. Hence, coherent qubit storage on the time scale of seconds seems feasible.

To evaluate the effects of partial polarization on the storage fidelity, we use the Heisenberg picture. In the homogeneous case ($a_i = a = A/N$), the Dicke-like collective operators defined above yield $\hat{I}^2$ and $\hat{J}_z = \hat{S}_z + \hat{I}_z$ as the constants of motion. We consider operator equations of motion $\dot{\hat{A}} = i[\hat{A}, \hat{H}]$, for the three operators $\hat{S}_z, \hat{S}_+\hat{I}_-$, and $\hat{S}_-\hat{I}_+$, which commute with the constants of motion. We replace $\hat{I}_z$ terms in the resulting equations with $\hat{J}_z - \hat{S}_z$ and use the identity $\hat{I}_+\hat{I}_- = \hat{I}^2 - \hat{J}_z^2 - [\hat{I}_-, \hat{I}_+]/2$ to put the equations in terms of constants of motion and the three operators we look to solve:

$$\begin{aligned} \frac{d}{dt}\hat{S}_z &= a\frac{\hat{S}_+\hat{I}_- - (\hat{S}_+\hat{I}_-)^\dagger}{2i} \qquad (3.2) \\ \frac{d}{dt}(\hat{S}_+\hat{I}_-) &= i[(g^*\mu_B - g_n\mu_n)B_0 + a(\hat{J}_z - 1)](\hat{S}_+\hat{I}_-) \\ &- ia(\hat{I}^2 - \hat{J}_z^2 + 1/4)\hat{S}_z. \qquad (3.3) \end{aligned}$$

It is convenient to choose new constants of motion, $\hat{\delta} = ((g^*\mu_B - g_n\mu_n)B_0 + a(\hat{J}_z - 1))$ and $\hat{\Omega} = a(\hat{I^2} - \hat{J}_z^2 + 1/4)^{1/2}$. These commute with each other and with $\hat{S}_z, \hat{S}_+\hat{I}_-$. As these equations are similar to those for two-level atoms in a field, we make the Bloch vector identifications:

$$\begin{aligned} \hat{U} &= -a/\hat{\Omega}\frac{\hat{S}_+\hat{I}_- + (\hat{S}_+\hat{I}_-)^\dagger}{2}, \\ \hat{V} &= -a/\hat{\Omega}\frac{\hat{S}_+\hat{I}_- - (\hat{S}_+\hat{I}_-)^\dagger}{2i}, \\ \hat{W} &= \hat{S}_z. \qquad (3.4) \end{aligned}$$

and Eqns. 3–4 become $\dot{\hat{\vec{M}}} = \hat{\vec{M}} \times \hat{\vec{\omega}}$ with $\hat{\vec{\omega}} = (\hat{\Omega}, 0, -\hat{\delta})$. The Bloch vector operator, $\hat{\vec{M}}$, will rotate about the axis defined by $\hat{\vec{\omega}}$ at a frequency $\hat{\omega}_0 = \sqrt{\hat{\delta}^2 + \hat{\Omega}^2}$. For no initial electron spin-nuclear spin correlation, we can easily solve for $\hat{S}_z$ and find

$$\langle \hat{S}_z(t) \rangle = \langle \frac{\hat{\delta}^2 + \hat{\Omega}^2 \cos(\hat{\omega}_0 t)}{\hat{\omega}_0^2} S_z(0) \rangle. \tag{3.5}$$

For the perfectly polarized nuclear state, Eq. 3.5 gives $\langle \hat{S}_z \rangle = -1/2 \cos(A\sqrt{2I_0/N}t)$ for the spin-down species and 1/2 for the spin-up species, exactly replicating the fully polarized behavior. In the case of partial polarization, even though we will set $\langle \hat{\delta} \rangle = 0$, $\langle \hat{\delta}^2 \rangle$ remains finite. The first part of Eq. 3.5 prevents complete transfer, to order $\langle \hat{\delta}^2 \rangle / \langle \hat{\omega}_0^2 \rangle$. For partial polarization $P < 1$, $\langle \hat{\omega}_0^2 \rangle \approx a^2 N(2I_0 + O(1-P))$. In a thermal state, all 2-particle expectation values factor, so $\langle \hat{\delta} \rangle = 0$ and

$$\langle \hat{\delta}^2 \rangle = a^2(\langle \hat{J}_z^2 \rangle - \langle \hat{J}_z \rangle^2) \approx Na^2(1-P)2I_0. \tag{3.6}$$

Accordingly, the error scales as

$$\frac{\langle \hat{\delta}^2 \rangle}{\langle \hat{\omega}_0^2 \rangle} \approx 1 - P. \tag{3.7}$$

Remarkably, this result demonstrates that efficient transfer is possible even with many nuclei in the "wrong" state as long as the average polarization per nuclei is high.

We modeled this system numerically with an initial thermal nuclear state. Oscillation of $\langle \hat{S}_z \rangle$ for several polarizations is shown in Fig. 3.2(a). The effect of partial polarization is immediately apparent; the transfer peak is less than 1/2, and the Rabi frequency decreases. We define fidelity, minimum for the spin-down initial state, as $F = \mathrm{Tr}[\rho_0(1/2 + \hat{S}_z(\pi/\langle\hat{\Omega}\rangle))^2]$. Fig. 3.2(b) shows that the analytical estimate is close to the numerically calculated values; thus, the transfer error can, to a large extent, be explained by the thermal uncertainty in $\hat{\delta}$. The residual effect most likely stems from phase mismatching, as measured by the broadening of ω_0, such that at $t = (\pi\langle\omega_0\rangle)^{-1}$, $\langle\cos(\omega_0 t)\rangle = 1 - O(1-P)$.

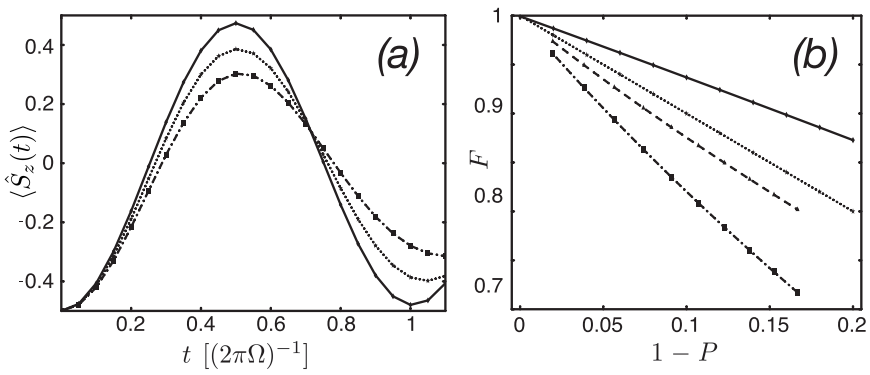

Figure 3.2: *(a)* The evolution of $\langle S_z(t) \rangle$ for three nuclear polarizations, $P = 0.96$ (solid curve), 0.82 (dotted), and 0.67 (dot-dash) versus time in units of the $P = 1$ Rabi time. *(b)* Solid line: Storage fidelity F for inhomogeneous effects ($N = 10^4$) versus error in nuclear polarization, $1 - P$. Dotted line: analytical estimate of thermal effects. Dashed line: numerical simulations of thermal effects. Dot-dash line: product of inhomogeneous and thermal results.

Inhomogeneous broadening for a thermal initial nuclear state is somewhat more pronounced than the fully polarized case first considered. The $\hat{V}_D$ inhomogeneity causes slow dephasing of the stored state, and the inhomogeneous coupling in $\hat{V}_\Omega$ results in leakage in readout of the stored state into a set of states orthogonal to the original nuclear state. The results shown in Fig. 3.2(b) were calculated for a distribution of a_i's corresponding to a gaussian $|\psi(\vec{r})|^2$. We plot the estimated fidelity for a complete storage and readout cycle as a function of the initial polarization of nuclear spins. The total expected fidelity, is approximated by the product of these two results (Fig. 3.2(b)). Hence, only modest nuclear polarizations are required to obtain a high fidelity of storage.

In summary, we have demonstrated that is possible to reliably map the quantum state of a spin qubit onto long-lived collective nuclear spin states. The resulting states have long coherence times, and can be retrieved on demand. Furthermore, the stored states can be efficiently manipulated and similar techniques can be used for quantum state engineering of collective nuclear states.

Experimental implementation of these ideas requires preparation of nuclear spin polarizations in the vicinity of confined electrons. Optical pumping of nuclear spins has demonstrated polarizations in GaAs 2D electron gases on the order of 90% [158] and 65% in self-assembled dots [77], and forced spin-flips through quantum hall edge states [52] has a claim of a similarly high polarization ability (85%). We anticipate that combining either of these techniques with electron localization in quantum dots would be a promising avenue of study. The methods outlined in this paper can be used to further increase the nuclear polarization. A current of spin-polarized electrons passing through the quantum dot with a dwell time $\tau_{\rm dwell} < \pi/\Omega_0$ will result in spin transfer, thereby increasing nuclear polarization. By keeping $B_{\rm eff}$ tuned to zero with increasing nuclear polarization the spin flip-flop remains resonant and, when combined with dephasing to prevent saturation, leads to efficient cooling, similar to a recent proposal [67].

Coherence properties of the spin-exchange process could be probed in transport measurements. For example, sending spin polarized currents through the quantum dot in which the spin-exchange interaction is tuned to resonance will result in collapses and revivals of the electron spin polarization that will be a periodic function of the dwell time in the dot. Those can be measured using spin-filter techniques. For a given polarization P and $\tau_{\rm dwell}$, the spin will be rotated by $\Omega(P)\tau_{\rm dwell}/\pi$. Note that repolarization will be necessary after $\sim\sqrt{N}$ nuclear spins have been flipped.

Practical applications of the storage and retrieval techniques and manipulation of stored states requires time-varying control over the spin-exchange coupling. This can be accomplished by using a pulsed magnetic field of order 50mT for a few ns, by engineering the electron g-factors [159, 130], or by optical AC Stark shifts [158] These techniques can be combined with a number of avenues for entanglement and manipulation of the electronic spin and charge states currently under exploration [7, 122]. Finally, quantum memory can

facilitate implementation and reduce scaling problems for more ambitious tasks such as quantum error correction [175] or quantum repeaters [53].

3.2 Preparation and control of a mesoscopic environment

This section demonstrates that a single quantum system (qubit) can be used to prepare and control a mesoscopic environment, turning the bath into a useful resource. We consider a system consisting of a single electronic spin in a semiconductor quantum dot interacting with a mesoscopic bath of nuclear spins within the confined volume. Recently it has been shown that cooling the spin bath to high values of polarization and purity greatly reduces the associated decoherence [103]. Furthermore, due to the bath's intrinsic memory, it can be used as a long-lived quantum memory for qubits and for quantum state engineering of collective nuclear states [183]. However, achieving a high degree of nuclear polarization in a quantum dot remains a major experimental challenge. Most ideas under exploration use the hyperfine contact interaction between electron spins and the bath. Some work *in situ*, using either spin-polarized currents [67] or optical pumping [77, 94]. Other techniques use a different geometry for cooling, such as quantum Hall edge state tunneling near a quantum point contact [52].

We focus on *in situ* manipulation, when the qubit degrees of freedom are themselves used to cool nuclei. We show that such a qubit-based cooling process rapidly saturates resulting in non-thermal states of the nuclear bath with low polarization and purity. However, the symmetry properties of such "dark states" allow for complete control of the qubit's interaction with the environment. We illustrate this by showing that the mesoscopic bath prepared in saturated states can be used to provide a long-lived quantum memory for qubit states. A combination of adiabatic passage techniques and spin-echo results in near unity

storage fidelity even for the bath with vanishingly small polarization. Before proceeding we also note that the idea of using qubit states to cool the environment is now widely applied in atomic systems such as trapped ions [108] or microwave cavity QED [154].

A simple Hamiltonian can describe a single electron spin confined in a quantum dot interacting with an applied external magnetic field B_0 and with N spin-I_0 surrounding nuclei via the hyperfine contact interaction:

$$\hat{H} = g^* \mu_B B_0 \hat{S}_z + g_n \mu_n B_0 \sum_j \hat{I}_z^j + a \sum_j \alpha_j \hat{\vec{S}} \cdot \hat{\vec{I}}^j, \tag{3.8}$$

where $\hat{I}_{z,\pm}^j$ and $\hat{S}_{z,\pm}$ are spin operators for nuclei and electrons, respectively. The hyperfine interaction is split into a field aligned (Overhauser) component $\hat{V}_{zz} = a\hat{A}_z\hat{S}_z$ and a Jaynes-Cummings type component, $\hat{H}_{JC} = a/2(\hat{A}_+\hat{S}_- + \hat{A}_-\hat{S}_+)$. We use collective operators $\hat{A}_{z,\pm} = \sum_j \alpha_j \hat{I}_{z,\pm}^j$, $\alpha_j = Nv_0|\psi(r_j)|^2$ is the weight of the electron wavefunction at the jth lattice site, and a is the average hyperfine interaction constant per nucleus.

3.2.1 Polarization of nuclei

Nuclear degrees of freedom are cooled by cycling spin-polarization through the quantum dot. A spin-down electron is injected from leads connected to a polarized reservoir or by means of optical excitation. It interacts for some short time τ, and then is ejected / recombined. Each iteration can cool the bath by flipping a nuclear spin through $\hat{H}_{JC}$. If the energy difference of the injected electron spin and the flipped electron spin, $\langle\Delta\rangle = (g^*\mu_B - g_n\mu_n)B_0 + a\langle\hat{A}_z - 1\rangle$ is large compared to the inverse time of interaction, τ^{-1}, energy conservation considerations block the spin-flip process. However, changing the applied field to maintain $\langle\Delta\rangle\tau \ll 1$ allows cooling to continue efficiently [94].

Regardless of the exact details of the process, cooling *will* saturate. The system is

driven into a statistical mixture of "dark states" $|\mathcal{D}\rangle$, defined by [94]

$$\hat{A}_-|\mathcal{D}\rangle = 0. \tag{3.9}$$

To cool past this point of saturation, either dark states must couple to other states of the bath or the geometric coupling coefficients α_k must change [94]. When high polarization is achieved, previous results hold [103, 183]. When these mechanisms are slow compared to the cooling rate, an appropriate mixture of dark states well approximates the steady state of the bath.

The homogeneous case illustrates the essential features of cooling. With $\alpha_k = 1$, we rewrite $\hat{A}_{z,\pm}$ as collective nuclear angular momentum operators $\hat{J}_{z,\pm}$; correspondingly, $\hat{J}^2$ becomes a conserved quantity. The Dicke basis, characterized by total (nuclear) angular momentum J $(0, 1/2 \leq J \leq N/2)$, its projection into the z axis m_J, and a permutation group quantum number β, is then appropriate [4]. The operator $\hat{J}_-$ changes neither J nor β, but nuclei in a state $|J, m_J, \beta\rangle$ are cooled to the state with lowest m_J (dark state) $|J, -J, \beta\rangle$. For an initial thermal bath of nuclei with polarization P_0, the corresponding steady state solution is found by summing over $-J \leq m_J \leq J$. Tracing over β, we find

$$\hat{\rho}_{ss} = \sum_J \rho_n(J)|J,-J\rangle\langle J,-J| = \left(\frac{1-P_0^2}{4}\right)^{N/2} \frac{1}{2P_0}$$
$$\times \sum_J D(J) \left[\frac{(1+P_0)^{J+1}}{(1-P_0)^J} - \frac{(1-P_0)^{J+1}}{(1+P_0)^J}\right] |J,-J\rangle\langle J,-J|. \tag{3.10}$$

$D(J)$ denotes the number of β quantum numbers allowed for a given J and is independent of m_J. In the case of spin-1/2 nuclei, $D(J) = \binom{N}{N/2-J} - \binom{N}{N/2-J-1}$. The resulting nuclear polarization P and Von Neumann entropy associated with the "cooled" ensemble are shown in Figure 3.3 as a function of initial thermal polarization P_0. The differences shown in Fig. 3.3 between the thermal and saturated baths become negligible for large N, but the dynamics of the two baths differ dramatically. In essence, even though the purity and

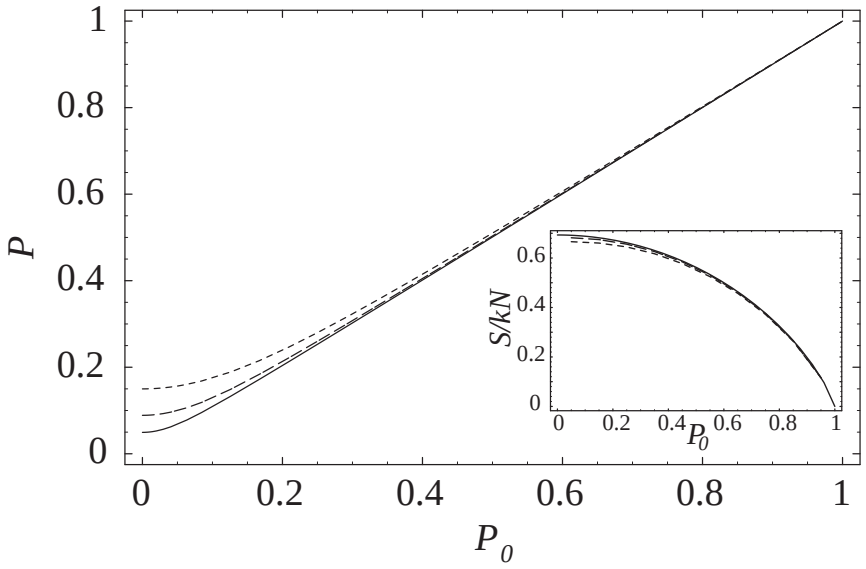

Figure 3.3: Saturated state polarization P versus initial thermal polarization P_0 for N=100(dotted), 300(dashed) and 10^3 (solid). Inset shows entropy per spin.

polarization are low, the symmetry properties of the dark states restricts evolution of the combined electronic-nuclear system to two levels.

3.2.2 Quantum memory with dark states

We illustrate the reversible nature of the coupling between dark states and the single spin by showing how a quantum state can be stored into collective nuclear states. An arbitrary qubit state $|\Psi\rangle = u|\uparrow\rangle + v|\downarrow\rangle$ will be mapped into the bath states. With just a pure state $|J, -J\rangle$, spin-down is decoupled entirely, while spin-up couples nuclei to the collective state $|J, -J+1\rangle$ with a Rabi frequency $\Omega_J = a\sqrt{2|J|}$. As

$$\hat{H}_{JC}^2|\uparrow\rangle|J,-J\rangle = \frac{a^2}{2}J|\uparrow\rangle|J,-J\rangle,$$

the motion is given by the cyclic dynamics of a two-level system. Near resonance ($|\langle\Delta^2\rangle| \lesssim |\Omega_J|^2$), the qubit will oscillate fully between electronic and nuclear states. For high polarization P this is in direct analogy to the case discussed in Ref. 4. However, for low P, all

states of the mixture must be in resonance; the range of J with significant probability goes as the width of the binomial distribution, $\sqrt{N}$, while the width of the resonance, given by $\langle\Omega_J\rangle/a$, goes as $\sqrt{PN}$. In this regime, the resonance is much narrower than the range of populated J states.

This problem can be solved with adiabatic passage [121]. By sweeping the detuning from far negative to far positive, the system passes through the series of avoided crossings and for each J

$$(u|\uparrow\rangle + v|\downarrow\rangle)|J,-J\rangle \rightarrow |\downarrow\rangle(ue^{i\phi_J}|J,-J+1\rangle + v|J,-J\rangle.$$

Adiabatic passage is not sensitive to the exact value of the coupling constant (Rabi frequency) between individual pairs of levels, and is robust provided the sweep rate of the detuning is sufficiently slow.

In general, the relative phase ϕ_J accumulated depends on the details of the detuning sweep. Sweeping the detuning back reverses storage, but the final state, $(ue^{2i\phi_J}|\uparrow\rangle+v|\downarrow\rangle)|J,-J\rangle$, has an additional non-trivial phase which reduces the final off-diagonal matrix element of electronic spin density matrix: $\rho_{\uparrow\downarrow} = uv^*[\sum_J \rho_n(J)e^{2i\phi_J}]$. Spin-echo avoids this strong dephasing by exactly compensating the adiabatically acquired phase. [2] An example sequence is presented in Table 3.1. The two waiting segments should be symmetric, to compensate for other arbitrary J-dependent phases. [3] Thus a mixture of saturated states can be used as an ideal quantum memory.

In practice, the electron-spin decoherence rate γ limits the minimum speed of the

[2]The necessity of spin echo can also be understood by considering the spin-wave modes, $\hat{J}^k_+ = \sum_j e^{i\vec{k}\cdot\vec{r}_j}\hat{I}^j_+$. The cooling process only cools the completely symmetric mode ($\hat{J}^{(k=0)}_+$, or in the inhomogeneous case, $\hat{A}_+$), while $\hat{V}_{zz}$ couples the spin to *all* modes, dephasing the electron spin state. Spin-echo exactly cancels the $\hat{V}_{zz}$ evolution. We note that in the far-off resonant (large effective field) regime, $\hat{V}_{zz}$ is the only relevant system-bath coupling, and thus dephasing is reversible.

[3]Even without adiabatic transfer and at low field, a spin-echo pulse train applied faster than $\langle\Omega_J\rangle \sim 10^8\mathrm{s}^{-1}$ will entirely cancel phase and spin-exchange evolution, thereby decoupling electron spin from nuclei and completely suppressing nuclear spin-related dephasing.

state	process	$\Delta(t)$
$(u\|\uparrow\rangle + v\|\downarrow\rangle)\|J,-J\rangle$	start	Δ_i
$\|\downarrow\rangle(ue^{i\phi_J}\|J,-J+1\rangle + v\|J,-J\rangle)$	store	$\rightarrow \Delta_f$
	wait	Δ_f
$(ue^{2i\phi_J}\|\uparrow\rangle + v\|\downarrow\rangle)\|J,-J\rangle$	retrieve	$\Delta_i \leftarrow$
$(iv\|\uparrow\rangle + ue^{2i\phi_J}\|\downarrow\rangle)\|J,-J\rangle$	$\pi-$pulse	Δ_i
$\|\downarrow\rangle(ive^{i\phi_J}\|J,-J+1\rangle + ue^{2i\phi_J}\|J,-J\rangle)$	store	$\rightarrow \Delta_f$
	wait	Δ_f
$(ive^{2i\phi_J}\|\uparrow\rangle + ue^{2i\phi_J}\|\downarrow\rangle)\|J,-J\rangle$	retrieve	$\Delta_i \leftarrow$
$e^{2i\phi_J}(u\|\uparrow\rangle - v\|\downarrow\rangle)\|J,-J\rangle$	$\pi-$pulse	Δ_i

Table 3.1: Adiabatic transfer with ESR spin echo.

adiabatic sweep, the induced error scaling as $p_\gamma \simeq \gamma T$ with T as the characteristic duration of the storage procedure. For a saturated ensemble state, $T \simeq 4\langle\Omega_J\rangle/\xi$, where $\xi = \langle\dot{\Delta}\rangle$ is the rate of change of the detuning. Assuming a tangent-like pulse shape [4] we find the non-adiabatic flip probability

$$p_{na} \simeq \xi^2/32\langle\Omega_J\rangle^4 = 1/2T^2\langle\Omega_J\rangle^2. \tag{3.11}$$

The total error probability is then $p_{tot} = p_\gamma + p_{na}$. Minimizing this for T gives $T_{min} = (\gamma\langle\Omega_J\rangle^2)^{-1/3}$ and

$$p_{tot,min} = 3/2(\gamma/\langle\Omega_J\rangle)^{2/3}. \tag{3.12}$$

We defer numerical analysis of this error to the end to allow inclusion of inhomogeneous corrections.

The saturated state lifetime, the storage lifetime, and the maximum polarization are limited by nuclear spin dephasing. Spin diffusion due to dipolar nuclear coupling is the dominant term for this dephasing in GaAs and is on the order of 6×10^4 s^{-1} [147]. This rate also provides an estimate for heating from proximal thermal spins. The competition between heating and cooling will likely determine the steady-state polarization of the dark-state

[4] The pulse is of the form $\Delta(t) = (\Delta_i+\Delta_f)/2+(\Delta_i-\Delta_f)/\epsilon_1\tan[\xi\pi(t-T/2+\epsilon_2)/2+\epsilon_3]$ with parameters $\epsilon_{1,2,3}$ set to give proper starting and ending detunings.

mixture. Active correction pulse sequences such as WHH-4 can lead to sub-Hz decoherence rates and lowered spin diffusion [131], suggesting storage lifetimes on the order of seconds may be feasible. Finally, we note that these results generalize to higher spin by using the appropriate multinomial form of $D(J)$.

3.2.3 Extension to inhomogeneous coupling

We now extend these results to realistic inhomogeneous coupling between electrons and nuclei by developing a one-to-one mapping between the explicit homogeneous Dicke basis and its inhomogeneous equivalent. A dicke state $|J, -J, \beta\rangle$ in the individual spin basis is

$$|J, -J = n - N/2, \beta\rangle = \sum_{\{j\}_n} c_{J,\beta}(\{j\})|\{j\}\rangle \tag{3.13}$$

where the set $\{j\}_n$ labels n spins that are pointing up; the rest point down. As $\hat{J}_-|J, -J, \beta\rangle = 0$, the c-numbers $c_{J,\beta}(\{j\})$ must satisfy

$$\sum_{l \notin \{i\}_{n-1}} c_{N/2-n,\beta}(\{i\} + l) = 0 \tag{3.14}$$

for all $\{i\}_{n-1}$. Furthermore, $\hat{J}_-$ is invariant under permutation so there exists a representation for dark states where every individual spin configuration is equally probable, *i.e.* $|c_{J,\beta}(\{i\})|^2 = |c_{J,\beta}(\{j\})|^2 = \binom{N}{N/2-J}^{-1}$. Using this explicit representation for homogeneous dark states, we construct a mapping to the more general inhomogeneous case ($\hat{A}_-|\mathcal{D}(n,\beta)\rangle = 0$). For each dark state $|J, -J = n - N/2, \beta\rangle$, its inhomogeneous counterpart is

$$|\mathcal{D}(n,\beta)\rangle = \mathcal{N}_{0,0}^{-1/2} \sum_{\{j\}_n} \left(\prod_{k \in \{j\}} \frac{1}{\alpha_k} \right) c_{N/2-n,\beta}(\{j\})|\{j\}\rangle, \tag{3.15}$$

as can be checked by direct calculation. The exact form of the normalization constant $\mathcal{N}_{0,0}$ is defined below.

To quantify inhomogeneous effects, first we note that $\hat{A}_-\hat{A}_+$ maps $|\mathcal{D}(n,\beta)\rangle$ into an orthogonal state $|\mathcal{O}(n,\beta)\rangle$, $\hat{A}_-\hat{A}_+|\mathcal{D}(n,\beta)\rangle = |\Omega_n|^2|\mathcal{D}(n,\beta)\rangle + |\chi_n|^2|\mathcal{O}(n,\beta)\rangle$ with

$$\begin{aligned}\Omega_n &= a\sqrt{\langle\mathcal{D}(n,\beta)|\hat{A}_-\hat{A}_+|\mathcal{D}(n,\beta)\rangle},\\ \chi_n &= a\left(\langle\mathcal{D}(n,\beta)|\hat{A}_-\hat{A}_+\hat{A}_-\hat{A}_+|\mathcal{D}(n,\beta)\rangle - |\Omega_n|^4\right)^{1/4}.\end{aligned}$$

Non-zero χ_n indicates that an inhomogeneous equivalent of $\hat{J}^2$ is not conserved under inhomogeneous raising and lowering operators. Second, inhomogeneous dark states are also not eigenstates of $\hat{A}_z$, *i.e.* $\hat{V}_{zz}|\mathcal{D}(n,\beta)\rangle = \delta_n|\mathcal{D}(n,\beta)\rangle + \omega_n|\mathcal{B}(n,\beta)\rangle$, where

$$\omega_n = \sqrt{\langle\mathcal{D}(n,\beta)|\hat{V}_{zz}^2|\mathcal{D}(n,\beta)\rangle - \langle\mathcal{D}(n,\beta)|\hat{V}_{zz}|\mathcal{D}(n,\beta)\rangle^2}.$$

If the symmetry breaking terms (χ_n,ω_n) are small relative to Ω_n, cooling will proceed similarly to the homogeneous case. The final state density matrix should then be of the type $\hat{\rho} = \sum_{n,\beta}\rho(n)|\mathcal{D}(n,\beta)\rangle\langle\mathcal{D}(n,\beta)|$. When χ_n and ω_n are small we can use Eqn. 3.10 as an estimate for $\rho(n)$. After reaching saturation, cooling slows to a rate governed by the transfer of dark states into other states.

Adiabatic transfer of a quantum state follows the prescription for the homogeneous case. However, the symmetry breaking terms lead to additional errors. When $\chi_n \ll \Omega_n$, the rate of transfer is given by Ω_n but the final state is an admixture of $|\mathcal{D}(n,\beta)\rangle$ and $|\mathcal{O}(n,\beta)\rangle$, leading to an error of order χ_n^2/Ω_n^2. The error from ω_n we estimate in the worst case by considering it as an incoherent loss mechanism. The effective decoherence rate become $\gamma_{eff,n} = \sqrt{\omega_n^2+\gamma^2}$, the spin-decoherence rate optimization used for the homogeneous case holds, and the resulting probability of error for the full sequence goes as $3/2(\gamma_{eff,n}/\Omega_n)^{2/3}$. Combining these, the total probability of error goes as

$$p_{tot} = 1 - \sum_n\left\{\left(\frac{\Omega_n^2}{\Omega_n^2+\chi_n^2}\right)^4\left[1-3\left(\frac{\gamma_{eff,n}}{\Omega_n}\right)^{2/3}\right]\rho(n)\right\}.$$

We now consider adiabatic transfer errors numerically. The explicit form of the inhomogeneous dark states (3.15) allows us to express the relevant parameters as functions of the geometric coupling constants, α_k:

$$\Omega_n^2/a^2 = \sum_k \alpha_k^2 - 2\mathcal{N}_{2,1}(n)/\mathcal{N}_{0,0}(n), \tag{3.16}$$

$$\chi_n^4/a^4 = \frac{4\mathcal{N}_{2,2}(n)}{\mathcal{N}_{0,0}(n)} - \left(\frac{2\mathcal{N}_{2,1}(n)}{\mathcal{N}_{0,0}(n)}\right)^2, \tag{3.17}$$

$$\omega_n^2/a^2 = \frac{\mathcal{N}_{1,2}(n)}{\mathcal{N}_{0,0}(n)} - \left(\frac{\mathcal{N}_{1,1}(n)}{\mathcal{N}_{0,0}(n)}\right)^2, \tag{3.18}$$

with

$$\mathcal{N}_{\mu,\nu}(n) = \binom{N}{n}^{-1} \sum_{\{j\}_n} \left(\prod_{k\in\{j\}_n} 1/\alpha_k^2\right) \left[\sum_{k\in\{j\}_n} \alpha_k^\mu\right]^\nu .$$

To estimate the required $N_{\mu,\nu}$ we average over a statistically significant fraction of the allowed $\{j\}_n$ for each n sublevel. The α_k's are drawn from an oblate Gaussian electron wavefunction of ratio $(1, 1, 1/3)$, and we omit spins with $\alpha_k < 1/N$. We plot the three parameters $\Omega_n, \chi_n, \omega_n$ versus n in Figure 3.4. The perturbative treatment used above is justified as $\Omega_n \gg \omega_n$, χ_n for all n. It also shows that increasing N improves this ratio.

In Figure 3.5 we plot total probability of error for the saturated mixture as a function of the final saturated polarization P. We used the hyperfine constant for GaAs, $aN \simeq 2 \times 10^{10}$ s^{-1} and $\gamma \sim 6 \times 10^6$ s^{-1}. Adiabatic transfer requires a small change of effective field ($\simeq$ 100 mT) over 10-100 ns, which could be implemented through g-factor engineering [159] or spin-dependent optical stark shifts [94]. For 10^4 nuclei, transfer times of $100ns$ and fidelities better than 0.8 are possible with realistic spin decoherence rates even for vanishingly small polarizations. The error decreases further with increasing N.

In conclusion we have demonstrated that electron spin qubits can be used to effectively prepare and manipulate a local nuclear spin environment. Specifically, long coherence times and high fidelities for the storage of electron spin states into nuclear spins

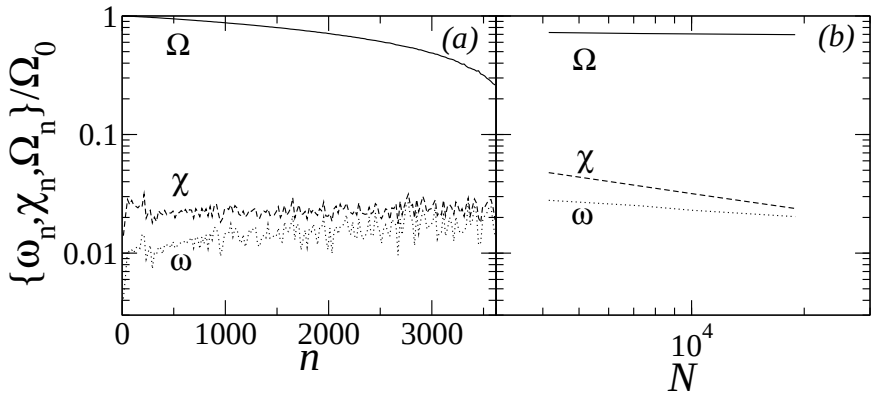

Figure 3.4: *(a)* Ω_n (solid), ω_n (dotted) and χ_n (dashed) versus number of flipped spins n with $N = 7280$. Values are averaged over every 20 n values and scaled by $\Omega_0 = A/\sqrt{N}$. *(b)* Average values of Ω_n/Ω_0, ω_n/Ω_n, and χ_n/Ω_n vs. N.

can be achieved provided the same qubit is used for the cooling process. Such "coherent" cooling and storage is effective for nuclear spin preparation due to their long coherence times. Related techniques can be used for engineering quantum states of nuclear spins from a saturated bath state [183, 116]. We further note that the techniques described in the present letter may be applicable to other systems involving mesoscopic spin baths. For example, we anticipate that similar methods may be used to prepare the local environment of superconducting qubits.

We thank J.A. Folk, Y. Yamamoto, and D. Loss for helpful discussions for the first section, and A. Sorensen, C.M. Marcus, and G. Giedke for the second section. JT thanks the quantum optics group at ETH for kind hospitality during his stay. The work at Harvard was supported by ARO, NSF, Alfred P. Sloan Foundation, and David and Lucile Packard Foundation.

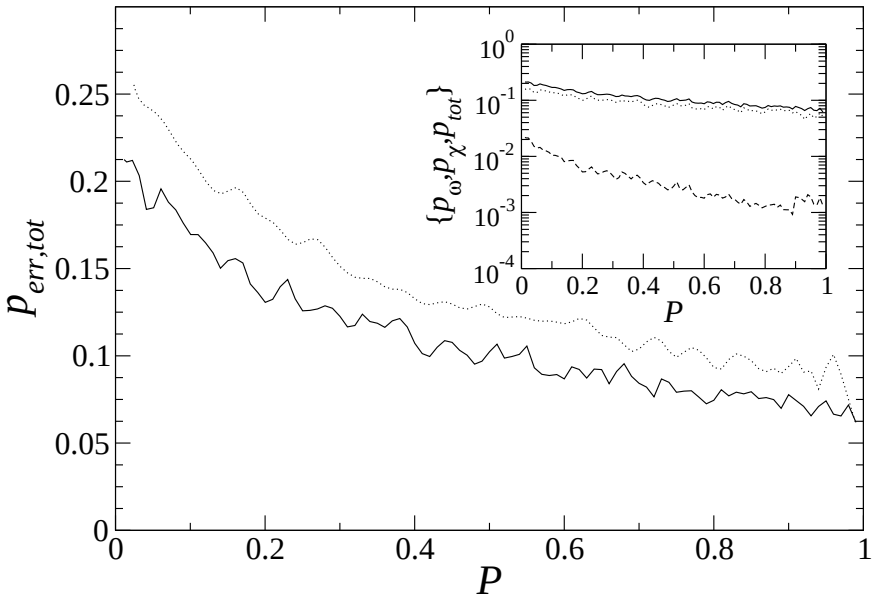

Figure 3.5: Expected error of transfer and recovery for the inhomogeneous case versus final polarization P for $N = 4145$ (dotted) and 18924 (solid). Iinset shows the error due to ω_n (dotted) and χ_n (dashed), and total error (solid) for N=18924.

Chapter 4

Quantum information processing using localized ensembles of nuclear spins

J. M. Taylor[1], G. Giedke[2], H. Christ[3], B. Paredes[3], J. I. Cirac[3], P. Zoller[4], M. D. Lukin[1], and A. Imamoglu[2]

[1] Department of Physics, Harvard University, Cambridge, Massachusetts 02138, USA
[2] Institut für Quantenelektronik, ETH Zürich, Wolfgang-Pauli-Straße 16, CH-8093 Zürich, Switzerland
[3] Max-Planck-Institut für Quantenoptik, Hans-Kopfermann-Straße 1, Garching, D-85748, Germany
[4] Institut für Theoretische Physik, Universität Innsbruck, Technikerstraße 24, A-6020 Innsbruck, Austria

We describe a technique for quantum information processing based on localized ensembles of nuclear spins with long coherence times. A qubit is identified as the presence or absence of a collective excitation of a mesoscopic ensemble of nuclear spins surrounding a single quantum dot. Long-range coupling is implemented by transporting electrons or by pregenerating entanglement by optical means. All single and two-qubit operations can be effected using hyperfine interactions and single-electron spin rotations, hence the proposed scheme avoids gate errors arising from entanglement between spin and orbital degrees of freedom. This scheme is particularly well suited for applications where long lived memory and long range coupling are essential.

Nuclear spin degrees of freedom have attracted considerable attention as potential carriers of quantum information due to their exceptionally long coherence times. Early bulk NMR work [40] has substantially enriched our understanding of the key features of quantum computation [17, 160], but the fundamental difficulties in scaling bulk NMR to a large number of qubits motivated efforts to use single, individually addressable nuclear spins in semiconductors as qubits [99], where computation is primarily mediated by the hyperfine interaction between electron and nuclear spin. While possibly scalable, such a scheme is limited by the fact that the electron wave-function is spread over many lattice sites, reducing the strength of the hyperfine interaction. In addition, two-qubit operations in Ref. [99] rely upon exchange coupling, making them susceptible to fast orbital decoherence mechanisms [16].

Recently, a method for robust storage of quantum information in localized ensembles of nuclear spins was suggested [183, 181], where it was shown that the collective hyperfine coupling between nuclear and electron spin degrees of freedom provides a controllable mechanism for coherent storage and manipulation of quantum states. These nuclear spin ensembles correspond, for example, to the lattice nuclei in a quantum dot. As a quantum memory, such nuclear ensembles are robust with respect to variations in dot characteristics and provide high fidelity storage without requiring a very high-degree of nuclear spin polarization.

In this article, we describe a technique to efficiently process quantum information stored in localized nuclear spin ensembles. Specifically, these ensembles enable a robust, scalable implementation of quantum computation protocols, unencumbered by the difficulties faced by single spin impurity or bulk NMR approaches. The fundamental interaction that allows for spin manipulation in our scheme is hyperfine coupling: as a result, the orbital and spin degrees of freedom remain unentangled throughout the two-qubit gate operations,

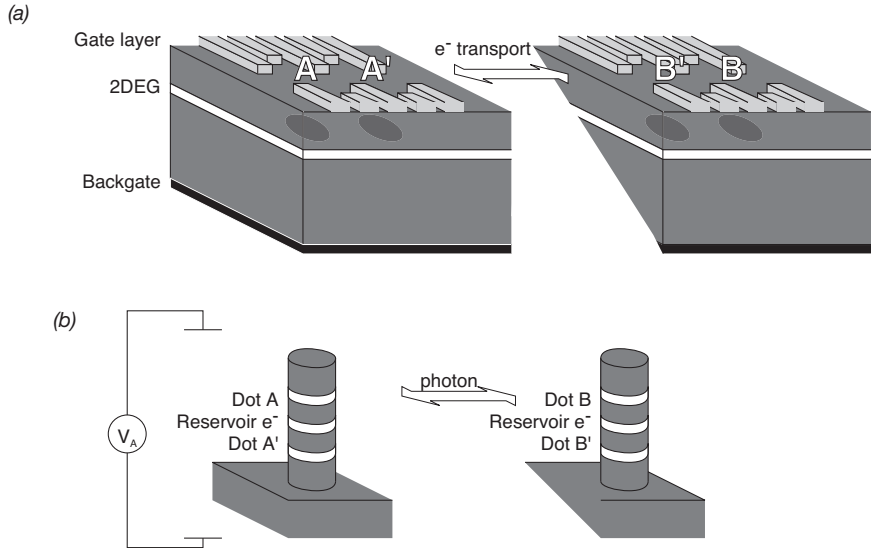

Figure 4.1: (a) Electrically defined (lateral) quantum dots connected by ballistic transport *e.g.* through a series of quantum dots. Nearby rf-SETs (not shown) would provide measurement. (b) Nanowhiskers [11] with several optically active dots. Tasks between A and A' are achieved via shuttling of an electron from the reservoir dot via a potential difference, V_A. Long distances tasks are performed through photon-based entanglement generation between A' and B'. [23]

mitigating the effects of orbital decoherence on gate fidelity. We describe two mechanisms for long-range coherent coupling between such memory qubits, one based based on electron spin transport and the other on preparing entanglement optically. A unique feature of the present aproach is that it combines long-lived memory with a potential for long-range coupling on a microchip. These features have recently been shown to be of critical importance for the scalability of solid-state quantum computation approaches [177].

4.1 Qubits and quantum operations

The scheme proposed here can be realized using either electrically [122] or optically [93] manipulated quantum dots. A illustration of both implementations is given in Fig. 4.1.

In general, we will consider interactions within a small quantum dot, where the local electrostatic potential determines the number of electrons within the quantum dot. Two regimes are used: no electrons in the dot and one electron in the dot. Quantum computing using electrons in quantum dots has been studied extensively, both for electrically coupled nearby quantum dots [122] or optically coupled quantum dots within a microcavity [93]. The approach presented here relies upon the fundamental ideas introduced in those works for preparing, manipulating, and measuring electron spins. However, we explicitly include coupling to the dominant dephasing mechanism, the lattice nuclear spins in the quantum dot [134, 103, 43]. By controlling the nuclear spins and the nuclear spin–electron spin interaction, we will use collective excitations of the nuclear spins within a single quantum dot as a qubit degree of freedom. This is a natural extension of previous ideas to store and retrieve the quantum state of electron spins in the collective nuclear spin degrees of freedom [183, 181]. However, we now consider how to accomplish a universal set of quantum operations.

We start by reviewing single electron spin operations in quantum dots, then consider preparation of nuclear states and computation using the collective excitations of nuclear spins. After that, techniques for building larger scale devices are considered. Errors and limits to the techniques are developed in the following section.

4.1.1 Electron spin manipulation and measurement: a review

Single spin operations in quantum dots have been considered in great detail elsewhere [19]; we only briefly cover the specific operations available here.

A single electron spin in a quantum dot can be prepared in a known state by applying a large external magnetic field. For example, in electrically coupled quantum dots, when the resulting Zeeman energy splitting of the ground-state doublet, ϵ_z is much

larger than k_bT, turning on coupling to a nearby Fermi sea results in fast filling of the ground state of the dot, $|\downarrow\rangle$. Similarly, when the system is in the first excited state, $|\uparrow\rangle$, coupling to the Fermi sea leads to state-selective ionization: only the $|\uparrow\rangle$ spin escapes the dot, while the $|\downarrow\rangle$ spin remains trapped within the dot. By measuring the local electrostatic configuration of the dot (whether it has zero or one electrons) the two measurement results can be distinguished using, for example, an rf-SET or a nearby quantum point contact. These techniques have been used to measure spin-relaxation in single quantum dots [87, 61]. Other approaches have been suggested [62] and, for example, two-electron spin states can also be measured [151].

Optical quantum dots can be prepared in a given state by a combination of optical pumping and magnetic field tuning [93, 85]. Essentially, in optical pumping a circularly polarized laser field selectively excites only one of the two electron spin states to the (optically excited) trion state, leaving the other state untouched. As the trion state can decay to either electron spin state, eventually the system ends in the state which is not excited by the laser. This technique can also be used to measure the spin state of the system, as it induces state-dependent absorption and flouresence. Experiments on single quantum dots have been successful in preparing and measuring spin states [14, 57].

Single electron spins are constantly precessing around the external magnetic field axis (defined to be z), which naturally produces z rotations of the two-level spin system, i.e., logical z rotations. Rotations about an axis perpendicular to this, necessary for universal computation, can be achieved either directly by electron spin resonance with driving magnetic fields [122] or by driving a Raman transition through a far-detuned trion state [93, 57].

Taken together, these techniques allow for single electron spin preparation, manipulation, and measurement *in situ*. Control of the local electrostatic potentially and a nearby Fermi sea allows for fast change of the number of electrons in a given quantum dot.

Our approach can be improved further if the electron's charge degree of freedom can be deterministically moved, as in a charge-coupled device or electron pump [144]. This allows for motion of the spin degrees of freedom by using the charge degree of freedom, and has been investigated elsewhere (see Chapters 10 and 8).

4.1.2 Electron spin–nuclear spin interactions

The Hamiltonian describing a single electron interacting with the nuclear spins in a quantum dot is [134, 103, 43, 162]

$$H = \hbar B \gamma_S \hat{S}_z + \hbar B \sum_k \gamma_I^{(k)} I_z^{(k)} + \hbar a \hat{\vec{S}} \cdot \hat{\vec{A}}. \tag{4.1}$$

The first and second terms describe the coupling of the electron and the nuclear spins to an external magnetic field, with effective gyromagnetic ratios $\gamma_S, \gamma_I^{(k)}$. The last term is the electron coupling to collective nuclear degrees of freedom, defined by

$$\hat{A}_{\pm,z} = \sum_k \alpha_k \hat{I}_{\pm,z}^{(k)} \ .$$

The α_k's are proportional to the probability density of the electron at the location of the corresponding nuclei and are normalized such that $\sum_k \alpha_k^2 = N$; $a = A/\sqrt{N}$ is the average hyperfine interaction when the nuclear spins are unpolarized. Both A and N depend upon the specific material and dot construction; typical numbers are $A \sim 10 - 100$ ns^{-1} and $N = 10^4 - 10^6$ nuclei. In addition, nuclear spin evolution due to additional terms (such as the intrinsic dipole-dipole interaction between nuclear spins) is substantially slower than the hyperfine interaction terms, with typical rates on the order of ms^{-1} [147]. As such, they have long coherence times and can be driven far out of equilibrium [143].

The nuclear ensemble in each dot is prepared using polarized electron spins [94, 181]. For example, the system can be prepared (as described above) with an electron spin $|\downarrow\rangle$. Then, changing the Zeeman splitting of the electron spin such that $\epsilon_z - a\langle \hat{A}_z \rangle$ changes

sign leads to a Landau-Zener transition from $|\downarrow\rangle$ to $|\uparrow\rangle$ with an accompanying nuclear spin flip. By repeating this cycle at a rate much faster than the nuclear spin out-diffusion [146], a highly polarized state might be achieved (but see Chapter 3 for complications and improvements to the process, and Chapter 7 for an example of slower polarization).

We illustrate our techniques for quantum computation using nuclear spin ensembles by considering the fully polarized case (when the nuclear state is $|0\rangle = |-I, \ldots, -I\rangle$ for N spin-I nuclei). In this simple case we detail how to perform single qubit and two-qubit gates. Corrections, such as working with some unpolarized spins, and sources of error are considered in the next section.

Excitations out of the fully polarized state due to the coupling to the nuclear spins produce an orthonormal set of collective nuclear spin states $|m\rangle \propto (\hat{A}_+)^m|0\rangle$, where m is the number of excitations. In addition, there are $N-1$ additional nuclear spin states with one spin flipped, and $N^2-N-I-1$ additional states with two spins fliped. Such additional states are denoted $|m,\beta\rangle$, where β labels the additional parameters of the state. Their main effect is to cause $|m\rangle$ to change to $|m,\beta\rangle$, which is a leakage errors. However, this leakage is slow when compared to the collective interaction time, a and is of order $a/\sqrt{N}$ [103].

When an electron is confined in the dot, evolution over times much shorter than $(a/\sqrt{N})^{-1}$ is restricted to subspaces spanned by $\{|m-1\rangle|\uparrow\rangle, |m\rangle|\downarrow\rangle\}$ [103, 183]. Using Pauli matrices, the Hamiltonian for each subspace with a fixed excitation number m is $H^{(m)} = \hbar\delta_m\sigma_z^{(m)} + \hbar\Omega_m\sigma_x^{(m)}$, with

$$\Omega_m = a/2\sqrt{\langle m-1|\hat{A}_-\hat{A}_+|m-1\rangle}; \tag{4.2a}$$

$$\begin{aligned}\delta_m &= a/4(\langle m|\hat{A}_z|m\rangle + \langle m-1|\hat{A}_z|m-1\rangle) \\ &\quad +[\gamma_S - (\langle m|K_z|m\rangle - \langle m-1|K_z|m-1\rangle)]B/2,\end{aligned} \tag{4.2b}$$

where $K_z = \sum \gamma_I^{(k)} I_z^{(k)}$ is a sum over nuclear spin operators, weighted by individual nuclear

spin gyromagnetic ratios. When Overhauser shift and Zeeman energy sum to zero ($|\delta_m| \ll \Omega_m$) and coherent flip-flop (Rabi) oscillations occur at rate Ω_m between the electron spin and nuclear spins systems. The energy level structure of the coupled electron-nuclear system is shown in Fig. 4.2 along with the coupling strengths for $m \leq 2$: since $\Omega_{m+1} = \eta_m \Omega_m$ where $\eta_m = \sqrt{m+1}[1 - \mathcal{O}(m/N)]$, it is easy to note the analogy with the celebrated Jaynes-Cummings (JC) model of quantum optics [1]. We use the nonlinearity of such a JC-type two-level system coupled to a nearly-bosonic mode to effect elementary quantum gates.

Quantum information stored in the $m = 0, 1$ manifold can be mapped reliably from nuclear states to electron spin and back [181] via a generalized rotation :

$$R_{en}^{xy}(\pi/2, 0)(\alpha|0\rangle + \beta|1\rangle)|\downarrow\rangle = |0\rangle(\alpha|\downarrow\rangle + i\beta|\uparrow\rangle), \tag{4.3}$$

where

$$R_{en}^{xy}(\theta, \phi) = e^{i\phi\hat{S}_z} e^{-i\theta H/(\hbar\Omega_1)} e^{-i\phi\hat{S}_z}. \tag{4.4}$$

The transfer of quantum information from the nuclear ensemble to electron spin allows for fast single qubit operations to be performed: after a $|\downarrow\rangle$ electron is injected into the dot, the quantum information is transferred to the electron spin, and then the operation is performed on the electron. Finally, the quantum information is mapped back to the nuclear ensemble. A z-axis rotation can be accomplished by waiting in a static magnetic field or through a laser-induced spin-dependent AC Stark shift [92]. x-axis rotations can be done via ESR [122, 190] (with $\Omega_{\rm ESR} \gtrsim 1$ ns^{-1}) or optical Raman spin flips through a virtual trion state (with $\Omega_{\rm opt,ESR} \gtrsim 10$ ns^{-1}) [93]. Measurement of the ensemble nuclear spin state can be implemented by mapping the quantum information to electron spin, and carrying out an electron spin measurement either by state selective ionization followed by charge measurement with a rf-SET [87, 61] or by detecting fluorescence in a spin-dependent cycling transition [92, 85].

[1] Detailed study of this analogy will be reported elsewhere; H. Christ *et al.*, in preparation.

To perform a two-qubit gate between quantum dots A and A', a single electron can be used as to transfer quantum information between the dots: the state of nuclear spin qubit A is mapped onto the electron, which is then moved to A', where a controlled-phase (CP) gate between the nuclear and the electronic qubit is applied using the nonlinearity of the interaction. The electron can be transferred between quantum dots by adiabatic passage (Chapter 6); such transfer is robust with respect to most charge-related errors.

Following Ref. [30], a two-qubit CP-gate (up to single qubit gates) is given by

$$R_{en}^{xy}(\pi/4,0)R_{en}^{xy}(\pi/\eta,-\pi/2)R_{en}^{xy}(-\pi/4,0). \tag{4.5}$$

In the computational basis, this corresponds to

$$\begin{pmatrix} 1 & 0 & 0 & 0 \\ 0 & e^{i\pi/\eta} & 0 & 0 \\ 0 & 0 & e^{-i\pi/\eta} & 0 \\ 0 & 0 & 0 & -1 \end{pmatrix}. \tag{4.6}$$

After this operation, the quantum information carried by the electron spin is mapped back onto the nuclear spin ensemble A. Applying a z-rotation of $-\pi/\eta$ to qubit A and one ofπ/η to qubit A' yields a CP gate. We note that such electron spin transport, e.g. through undoped nanowires or an array of quantum dots, is a relatively robust and fast means of implementing long-range two-qubit gates [144].

4.1.3 Integration and scaling

So far we developed a means for local one- and two-qubit operations. As a larger scale system, with many qubits, is developed, the task of controlling qubits using classical electronics or other mechanisms becomes increasingly challenging. To mitigate these difficulties, and to leverage the long memory of the collective nuclear spin qubits, beyond small scale devices with few qubits, teleportation-based approaches may be more appropriate.

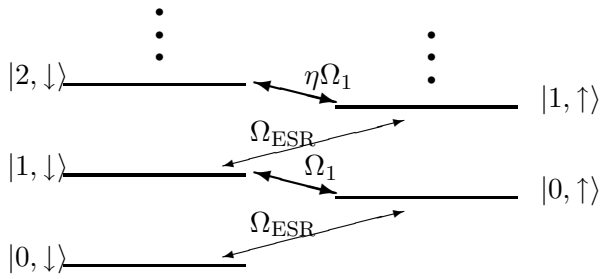

Figure 4.2: Level structure of the combined electron spin and nuclear dark state plus excited states. For $N \to \infty$, the coupling between the two excitation manifold is stronger by $\eta \to \sqrt{2}$.

For distant dots or in optical systems, where electron spin transport between ensembles is difficult or impossible, it could be easier to generate entanglement off-line, apply local purification protocols and then use it to effect non-local gates, following [34]. Entanglement between distant electron spins can be generated optically, using spin-flip optical Raman transitions [23], or electronically, such as through adiabatic splitting of a spin singlet in a double dot [151]. The electron-nuclear state mapping procedure can then ensure that the distant nuclear spin ensembles are entangled. Starting with the entangled nuclear state $\frac{1}{\sqrt{2}}(|01\rangle + |10\rangle)$ (between dots A' and B', cf. Fig. 4.1), we can implement a CP gate on dots A and B (deterministically) by performing local unitaries and measurements of AA' and BB' as follows: (i) perform a $\mathrm{CNOT}_{A\to A'}$ then measure A'. (ii) Perform a CP gate $|10\rangle \to -|10\rangle$ at BB' followed by a Hadamard gate and measurement at B'. (iii) Local phase flips $|0\rangle \to -|0\rangle$ at A (B) if the measurement outcomes at B'(A') were "1" complete the CP gate between A and B [2].

To implement larger scale devices, a general device topology with low-bandwidth connections between devices could be useful, such as that shown in Fig. 4.3. In particular, when the set of quantum operations to be performed in the intermediate future is well understood (such as when operating error correction circuitry [166, 171]), entanglement can

[2] Both imperfect entanglement and measurement errors lead only to phase-flip errors; thus, error correcting codes optimized for such errors may yield more favorable fault-tolerant thresholds.

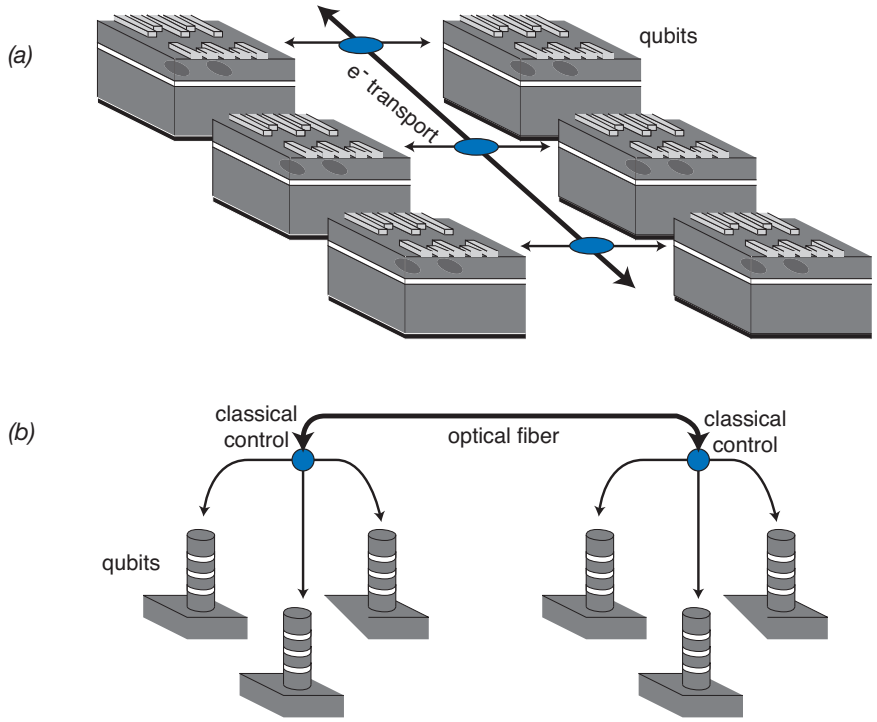

Figure 4.3: A network of small scale quantum computing devices. Each set of qubits is connected via a longer-range couple; the couple is used to generate and purify entangled pairs for later use in non-local logical gates, as described in the text. (a) Implemntation using electron spin transport such as single electron CCDs [144]. The blue circles represent classically controlled switching / generation circuits. (b) Implementation using optically-generated entanglement. Fiber optics and switching networks using, e.g., micromechanical mirrors or large-scale EOM plates [174], are used to generate desired entalged pairs in advance of logical operations.

be prepared in advance over the low-bandwidth channels. Then the gate proceeds at the expected time, while the same channels are used for preparing other entangled pairs for the next operation. The scaling properties of such teleportation-based topologies remain largely unexplored [145], but we expect the level of non-locality afforded to be comparable to highly connected topologies such as those assumed in most fault tolerant threshold calculations [172, 173, 3]. This leads to overall favorable scaling for computation using our approach.

Source	Error per operation
e^- spin preparation	$\exp(-g^*\mu_B B/k_b T)$
[optical]	η
e^- Z-gate (Zeeman)	$1/2(\delta B_{ext}/B_{ext})^2$
[optical]	$\Gamma_{opt}/\Delta_{opt}$
e^- X-gate (ESR)	Γ_{ph}/Ω_{ESR}
[optical]	$\Gamma_{opt}/\Delta_{opt}$
e^- spin measurement	Max[$\exp(-g^*\mu_B B/k_b T)$, $10^2\Gamma_{ph}/g^*\mu_B B$]
[optical]	$\epsilon\Gamma_{ph}/\Gamma_{opt}$
e^- spin transport	$0.0005(L/100\text{nm})$
[narrowed]	$L\gamma_{ph}/(1\text{mm/s})$
Stored qubit [WHH]	$\sim(\gamma_{DD}25\cdot 8/(g_n\mu_n B))^3$
[strain]	$< 10^{-4}$
Transfer/Gate	*(sum in quadrature of:)*
Dipole-dipole	$\pi^2\gamma_{DD}/A$
e^- spin-orbit	$\pi\Gamma_{ph}\sqrt{N}/A$
Species inhomogeneity	$(B(g_n^1\mu_n^1 - g_n^2\mu_n^2))^2 N/A^2$
Polarization width	$(\Delta P)^2 N$
Rabi width	$(\Delta P)^2$
Leakage from logical subspace	$\beta(\lvert b_{n,\uparrow}\rvert^2 + \lvert b_{n,\downarrow}\rvert^2 + \lvert c_{n,\downarrow}\rvert)N/A^2$
Strain	$< 10^{-7}$

Table 4.1: Formulaic error budget for computation. η is the selection rule violation for circularly polarized light, ϵ is the collection efficiency for photons emitted from the dot, and β is a factor stemming from the Lanczos expansion (typical $\beta \simeq 0.05 - 0.1$).

4.2 Error mechanisms

We now analyze various sources of errors due to finite polarization, inhomogeneity, nuclear spin dynamics, and electron spin decoherence. To understand the role of finite polarization, the specific cooling procedure must be examined. By developing an overall error budget (Table 4.1), dominant noise terms can be identified and procedures for mitigating their effect determined. In particular, Hamiltonian averaging (such as WaHuHa pulse sequences) and active metrology can play a crucial role in improving the overall fidelity of the system.

4.2.1 Finite polarization and dark states

When the nuclear ensemble starts as a thermal mixture, cooling to dark states can be achieved by coupling polarized electron spins to the nuclear ensemble [94]. Regardless of the details of cooling, the final density matrix will be a statistical mixture of dark states $|\mathcal{D}(n,\beta)\rangle$, where $\hat{A}_-|\mathcal{D}(n,\beta)\rangle = 0$. n is the number of spin excitations ($n = 0$ is the fully polarized state) and β is the permutation group quantum number [4]. It was recently shown [181] that dark states have the same symmetry properties as the fully polarized state, and a manifold of excited states can be defined from a given dark state, $|m(n,\beta)\rangle \propto (\hat{A}_+)^m|\mathcal{D}(n,\beta)\rangle$. Hence the above considerations for perfectly polarized nuclei map directly to the case when the nuclear ensembles start in any given dark state, not just the fully polarized state.

In practice, the cooled nuclear ensemble density matrix is a mixture of different dark states, i.e. $\hat{\rho} = \sum_{n,\beta} \rho_{n,\beta}|\mathcal{D}(n,\beta)\rangle\langle\mathcal{D}(n,\beta)|$. As each dark state has a different $\delta_m(n,\beta), \Omega_m(n,\beta)$, interaction times and applied magnetic fields can only produce $R_{en}^{xy}(\theta,\phi)$ with the desired angle θ for some fraction of the given mixture. The inhomogeneous mixture effects can be characterized by examining the subgroups of dark states with different detunings, which lead to errors in Rabi oscillations $p \simeq (\sigma_\delta/\Omega_1)^2$, where σ_δ is the standard deviation of possible δ_1 values over the distribution $\rho_{n,\beta}$. In the homogeneous case with spin-1/2 nuclei,

$$\sigma_\delta \simeq a\sqrt{N(1-P^2)} \ . \tag{4.7}$$

Even at high ($P \sim 0.95$) polarizations, the effect of different detunings can be substantial ($p \sim 0.03$). This provides the strongest limit to realization of R_{en}^{xy} [3]. The inhomogeneous nature of the hyperfine coupling leads to further errors, which have been considered in some detail elsewhere [181]. We note that the estimated error is substantially less than that due

[3] A similar analysis shows that $\sigma_\Omega \simeq (a/\Omega_1)\sigma_\delta$ and is negligible in comparison to detuning-based errors.

to Eqn. 4.7, and can be neglected.

In this case, the logical states of the system (the m-excitation manifolds) are no longer eigenstates of $\hat{J}_z = \hat{A}_z + \hat{S}_z$ and of $\hat{A}^2$. As a consequence, there is a nonzero probability that the system moves out of the computational subspace during the gate operation. We estimate these leakage errors using the techniques developed in Refs.[183, 181], and find that the resulting gate error p_{inhom} decreases with increasing number of nuclei: for $N \sim 10^5$ at high polarizations ($P > 0.95$) $p_{\text{inhom}} \lesssim 10^{-3}$ [4]. We note that a similar error emerges due to the differences in Zeeman energy associated to different nuclear species. For materials like GaAs, with gyromagnetic ratios varying greatly from species to species, this limits the effectiveness of gate operations at high magnetic field, resulting in the errors in the range of 10^{-3} as indicated in Fig.3. Optical manipulation (e.g. tuning the system into resonance via spin-dependent AC optical Stark shifts) may mitigate this difficulty. Finally, in between gate operations the errors associated with inhomogeneous evolution may be eliminated by refocusing sequences of NMR pulses.

A dramatic improvement can be seen if, before using a given nuclear ensemble, a series of measurements is made to determine the effective Overhauser field in the dot. This is exactly a sequential phase estimation problem, with an approximate improvement in width of $\sqrt{N_m}$ where N_m is the number of measurements used [81]. A more efficient procedure, and its limits, is considered in Chapter 5.

Finally, we estimate the errors inherent in the transfer process due to inhomogeneity of the coupling and due to inhomogeneity of Zeeman terms for different species.

Doing so indicates that for weak coupling out of the logical subspace, the error scales as $\beta(|b_{n,\uparrow}|^2 + |b_{n,\downarrow}|^2 + |c_{n,\downarrow}|^2)T^2$ where T is the time of the gate procedure and β is a prefactor dependent upon d_n, e_n, and f_n. Maximization of the error as a function of

[4] For a manifold based on a dark state $|\mathcal{D}(n,\beta)\rangle$ the value of p_{inhom} can be estimated, using the results of Chapter 3, as $(\chi_n^2 + \omega_n^2)/\Omega^2$.

these final three parameters demonstrates that $\beta \lesssim 0.12$, and the worst error occurs when $d_n \simeq \omega_{n,\uparrow}, f_n \simeq \omega_{n+1,\downarrow}$ and $e_n \simeq \Omega_n$.

The expected error (defined as the projection of the final unitary on the desired unitary, traced) of a transfer operation is plotted as a function of final polarization of the dark state ensemble in figure 4.4, for a density matrix narrowed by a factor of 20. For achievable polarizations of 90%, dots of size 10^4 have fidelities on the order of 10^{-4}. The error for the two-qubit operation is limited by three times this, assuming correlated errors. We note that smaller dots produce better results at higher polarizations due to their greater coupling strengths, but larger dots (with less inherent inhomogeneity) perform well at lower polarizations. The limits for GaAs are due to the large species inhomogeneity and incommeasurate requirement of sufficient magnetic field to due effective coherent averaging of dipole-dipole interactions.

4.2.2 Nuclear spin dephasing

We now show that for the logical basis states we have chosen, there is no collective enhancement of decoherence. Starting with a single spin error, i.e. $\hat{E}_j = \vec{n} \cdot \hat{\vec{I}}^j$, we note that the logical states $|0\rangle, |1\rangle, |2\rangle$ are mapped to new states $|x(0)\rangle = \hat{E}_j|0\rangle$ and similarly for $|x(1)\rangle, |x(2)\rangle$. These new states have, up to order $1/\sqrt{PN}$, the same properties as the original logical states. That is, before the properties of the logical basis were defined in relation to the operators $\hat{A}_\pm$, in the form $\frac{\eta_k\Omega}{a}|k+1\rangle = \hat{A}_+|k\rangle; \frac{\eta_{k+1}\Omega}{a}|k\rangle = \hat{A}_-|k+1\rangle$. For states $|x(k)\rangle$, these properties are

$$\hat{A}_+|x(k)\rangle = \frac{\eta_k\Omega}{a}|x(k+1)\rangle + [\hat{A}_+, \hat{E}_j]|k\rangle, \tag{4.8a}$$

$$\hat{A}_-|x(k+1)\rangle = \frac{\eta_{k+1}\Omega}{a}|x(k)\rangle + [\hat{A}_-, \hat{E}_j]|k+1\rangle. \tag{4.8b}$$

The error term in each is bounded, $|a[\hat{A}_+, \hat{E}_j]/\Omega| = |a\lambda_j(n_z\hat{I}^j_+ + n_-\hat{I}^j_z)/\Omega| \leq a\lambda_j/\Omega \simeq 1/\sqrt{PN}$ (and similarly for $\hat{A}_-$). Therefore, after a single spin event, due for example to decoherence, the new states, $|x(k)\rangle$, have the same behavior as the original logical states, with errors over a logical operation of order $(a\lambda_j/\Omega)^2 \sim 1/PN$. If errors add incoherently, a single-spin decoherence mechanism acting on every spin with a rate γ will lead to an error of rate for the logical states of $N\gamma/PN \simeq \gamma$.

The main mechanism for such spin decoherence is due to nuclear dipole-dipole interactions, and has a rate for a single spin of $\gamma_{DD} \sim 60\text{ms}^{-1}$, which by the above argument leads to a similar error rate for our chosen logical basis. However, active correction of this decay mechanism can be performed with NMR pulse sequences that average the dipole-dipole Hamiltonian, such as WaHuHa, improving the error rate to $\tau^2_{whh}\gamma^3_{DD}$ [196, 131]. After correction dark state coherences could have lifetimes on the order of 0.1-1s for moderate cycle times τ_{whh}. Additional error due to quadrupolar terms from inhomogeneous strain terms are easily estimated and found negligible ($\sim 10^{-7}$ per cycle of computation).

4.2.3 Electron spin-related errors

The errors of manipulation of single electron spins in quantum dots via microwave or optical fields have been considered in detail elsewhere [122, 190, 93, 85]; we focus on errors particular to our system. Electron spin decoherence will most likely be limited by different Overhauser shifts corresponding to different detunings, with error going as $p \simeq (\sigma_\delta/\Omega_{\text{ESR}})^2$; fast ESR ($\sim 6\text{ns}^{-1}$) will mitigate this effect; with optical fields, even faster effective Rabi-oscillations are predicted ($\Omega_{\text{opt,ESR}} \sim 50\text{ns}^{-1}$) with errors then limited by spontaneous emission to $\sim 10^{-3}$. As for measurement, the fundamental limit will be set by relaxation of the electron spin due to mechanisms other than nuclei, which has a time scale $\Gamma^{-1} \sim$ 0.1-10ms, based on recent measurements of the spin relaxation time at high

magnetic fields [75, 87].

Preparation can be provided either by high magnetic fields and low temperature, appropriate for lateral quantum dots, or through circularly polarized light and spin pumping in optical dots. A z rotation of the electron spin can be done by means of the external Zeeman field and an appropriate waiting time, with near unit fidelity, or by an optical AC stark shift, where fidelity is limited by the suppressed spontaneous emission probability. Microwave ESR fields or an optical Raman process yeilds x rotations of the electron spin, limited by the intrinsic (phononic) decoherence of the electron or spontaneous decay events for the Raman process. Measurement for lateral quantum dot architectures can be done using rf-SETs for charge detection and using energy resolution provided by the magnetic field, analogous to successful single spin measurements already made [87]. Optical quantum dots can be measured through a cycling transition. In both cases, the measurement error scales inversely with the measurement time.

4.2.4 Transport and scaling errors

Moving individual electron spins over short to medium distances incurs phase errors due to uncertainty in the local nuclear field of the transport channel. The error induced by randomly oriented nuclei during transit can be estimated by the time averaged hyperfine field the electron wavepacket encounters over the whole process. The field felt is roughly $A/\sqrt{nLhl}$, where n is the density of lattice nuclei, L is the length of the channel, and hl is the transverse area of the channel. The time scale for transfer depends upon the degree of transverse confinement. Working in the ground state of the transverse channel only means the wavepacket can only have energies $\ll \hbar^2\pi^2/(2m^*l^2)$. For a 50 nm wide, 10 nm high channel, the maximum transfer velocity is correspondingly $\ll 30\mu$m ns^{-1} in GaAs. For a separation of 1 μm, the expected dephasing due to thermal nuclei is $\simeq 5 \times 10^{-5}$ for

a 3 ns transfer. Alternatively, we can take advantage of the long correlation time of the nuclear spin effective field, with either active metrology (as mentioned above) or by sending the electron spins in a decoherence free subspace.[5]

To assess the quality of the non-local gate implementation in a realistic setting, we consider the effects of imperfect resource states and measurement errors on the gate fidelity. Fortunately, both errors simply translate into phase-flip errors of the output state. This is seen as follows:

Assume that an entangled state ρ with fidelity $F = \langle\Psi_+|\rho|\Psi_+\rangle$ is used to implement the gate. Assume that the state is diagonal in the Bell basis, i.e., $\rho = F|\Psi_+\rangle\langle\Psi_+| + p_1|\Psi_-\rangle\langle\Psi_-| + p_2|\Phi_+\rangle\langle\Phi_+| + p_3|\Phi_-\rangle\langle\Phi_-|$ with $\sum p_k = 1 - F$. This can always be achieved by local operations and the standard entanglement distillation protocols [9, 49] lead such states. The unwanted states $|\Psi_-\rangle, |\Phi_+\rangle, |\Phi_-\rangle$ differ from $|\Psi_+\rangle$ by simple unitaries, namely $\sigma_z^B, \sigma_x^B, \sigma_z^B\sigma_x^B$, i.e., all acting at B. Commuting them with the operations in the protocol we see that the outcome of the result is affected in two ways only: (i) Ψ_-, i.e. the application of σ_z^B before our protocol is equivalent to replacing $P^{B'}$ by $P^{B'}\sigma_x^{B'}$, i.e. the measurement result b is flipped: $b \to b \oplus 1$, since this affects what operation is performed at A, the final state is off by a phase flip at A. (ii) Similarly, using a resource state Φ_+ has the effect of a phase flip error at B, and consequently Φ_- combines both these errors. Clearly, the $(1 - F)p_k$ give the respective probabilities for the phase-flips to occur.

Measurement errors have largely the same effect: the dominant term here is expected to be a be a bit-flip error, i.e., with some probability the qubit is projected into $|0(1)\rangle$ but a result $a = 1(0)$ is recorded. Relying on these erroneous results, the conditional phase-flip operations that complete our protocol again result in phase flip errors of the output state.

[5] Using two electrons in a total $m_s = 0$ state makes the combined electron spin wavefunction insensitive to local field fluctuations.

Taking everything together, denoting by p_m the probability of a measurement error and $F = 1 - \epsilon$, the total error probability is (to first order in the small parameters) $\epsilon - 2p_m$ (to second order the probability of error is reduced, since some of the errors correct themselves). Since all errors are phase flips, it is possible to protect against them with less effort than for general errors. E.g., a three-qubit code [142] suffices to correct single phase flips.

4.3 Materials and estimates

We consider three materials with demonstrated electronic and optical quantum dots (GaAs, $N = 10^5$; InAs, $N = 10^{4.6}$; CdSe, $N = 10^4$). The expected error of a two-qubit gate operation, defined as $\mathrm{Tr}[U_{\mathrm{perfect}} U^{\dagger}_{\mathrm{actual}}]/4$, where U_{perfect} is given by Eqn. 4.6, is plotted in Fig. 4.4. As the error is dominated by detuning error, it is material independent, and is a few percent at 95% polarizations.

To combat these errors, a series of measurements may be made to determine the effective detuning of the system better than the thermal mixture limit σ_δ. This can be done *e.g.* by a measurement made with the single electron in the quantum dot, in direct analogy to single ion Ramsey interferometry in atomic clocks [108]; the distribution is then narrowed, with $\tilde{\sigma}_\delta \simeq \sigma_\delta/\sqrt{n}$, where n is the number of measurements. Using the approach of Chapter 5, an improvement in the uncertainty of the mixture's detuning of a factor of 10 yields high fidelity operation, as shown in the inset to Fig. 4.4. Smaller dots produce better results at higher polarizations due to their greater coupling strengths. The limits for GaAs are due to the large species inhomogeneity and the incommensurate requirement of sufficient magnetic field to perform effective coherent averaging of dipole-dipole interactions. Low species inhomogeneity allows for higher magnetic field, faster WaHuHa-type correction

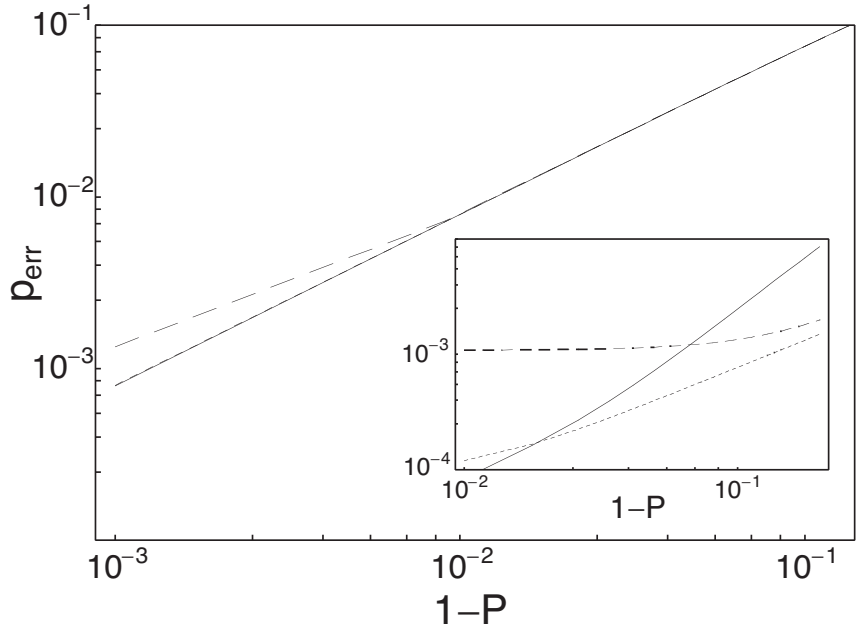

Figure 4.4: For a cooled dark state density matrix (c.f. [181]), expected error for a controlled-phase operation between electron spin and nuclear spin as a function of polarization (CdSe: solid, InAs: dotted, GaAs: dashed; in the main figure, CdSe and InAs are indistinguishable). Inset shows effects of narrowing by a factor of 10 for different materials.

sequences, and fewer errors in the transfer operation. This would be the case for quantum dots defined in nanotubes with isotopically enhanced ^{13}C or CdSe quantum dots. Materials with low spin-orbit interaction will also reduce electron spin dephasing.

4.4 Conclusions

In conclusion, we have detailed a scheme for quantum information processing using dynamically defined qubits composed of collective excitations of nuclear spins in a quantum dot. By taking advantage of spin transport or optically-pregenerated electronic entanglement, long distance two-qubit gates are accessible, improving the expected fault tolerant threshold. For small dots with near-homogeneous Zeeman splittings (e.g. CdSe, InAs) large but finite polarization (95%) is already sufficient to reach an error rate in two-qubit opera-

tions of order a few percent. Given the suppression of dipolar diffusion in lithographically isolated structures (e.g. vertical quantum dots, nanowhiskers, self-assembled quantum dots) these polarizations may be within reach. Moderate polarizations [77] have been already achieved, and techniques to improve upon this have been considered [94]. Our calculations indicate that the dominant source of error may be mitigated through narrowing the mixture of dark states.

We gratefully acknowledge helpful conversations with A. Sørensen. The work at Harvard was supported by ARO, NSF, Alfred P. Sloan Foundation, and David and Lucile Packard Foundation. I. Cirac acknowledges DFG (SFB 631). The work at ETH was supported by Nanoscience NCCR.

Chapter 5

Quantum measurement of a mesoscopic spin ensemble

G. Giedke[1,4], J. M. Taylor[2], D. D'Alessandro[3], M. D. Lukin[2], and A. Imamoglu[1]

[1] Institut für Quantenelektronik, ETH Zürich, Wolfgang-Pauli-Straße 16, 8093 Zürich, Switzerland
[2] Department of Physics, Harvard University, Cambridge, MA 02138, USA
[3] Department of Mathematics, Iowa State University, Ames, IA 50011, USA
[4] Max-Planck–Institut für Quantenoptik, H.-Kopfermann-Str., 85748 Garching, Germany

We describe a method for precise estimation of the polarization of a mesoscopic spin ensemble by using its coupling to a single two-level system. Our approach requires a minimal number of measurements on the two-level system for a given measurement precision. We consider the application of this method to the case of nuclear spin ensemble defined by a single electron-charged quantum dot: we show that decreasing the electron spin dephasing due to nuclei and increasing the fidelity of nuclear-spin-based quantum memory could be within the reach of present day experiments.

Decoherence of quantum systems induced by interactions with low-frequency reservoirs is endemic in solid-state quantum information processing (QIP) [96, 95]. A frequently encountered scenario is the coupling of a two-level system (qubit) to a mesoscopic bath of two-level systems such as defects or background spins. The manifestly non-Markovian

nature of system-reservoir coupling in this scenario presents challenges for the description of the long term dynamics as well as for fault tolerant quantum error correction [2, 186]. The primary experimental signature of a low-frequency reservoir is an unknown but slowly changing effective field that can substantially reduce the ability to predict the system dynamics. A possible strategy to mitigate this effect is to carry out a quantum measurement which allows for an estimation of the unknown reservoir field by controlled manipulation and measurement of the qubit. A precise estimation of the field acting on the large Hilbert space of the reservoir requires, however, many repetitions of the procedure: this constitutes a major limitation since in almost all cases of interest projective measurements on the qubit are slow [61] and in turn will limit the accuracy of the estimation that can be achieved before the reservoir field changes.

In this work, we propose a new method for estimating an unknown quantum field associated with a mesoscopic spin ensemble. By using an incoherent version of the *quantum phase estimation algorithm*, [109, 142] we show that the number of qubit measurements scale linearly with the number of significant digits of the estimation. We only assume the availability of single qubit operations such as preparation of a known qubit state, rotations in the xy-plane, and measurement, of which only rotations need to be fast. The estimation procedure that we describe would suppress the dephasing of the qubit induced by the reservoir; indeed, interaction with the estimated field leads to coherent unitary evolution that could be used for quantum control of the qubit. If the measurement of the reservoir observable is sufficiently fast and strong, it may in turn suppress the free evolution of the reservoir in a way that is reminiscent of quantum Zeno effect.

After presenting a detailed description of the measurement procedure and discussing its performance and limitations, we focus on a specific application of the procedure for the case of a single quantum dot (QD) electron spin interacting with the mesoscopic

nuclear spin ensemble defined by the QD. It is by now well known that the major source of decoherence for the electron-spin qubits in QDs [122] is the hyperfine interaction between the spins of the lattice nuclei and the electron [103, 134, 162, 38, 66, 46, 48]. A particular feature of the hyperfine-related dephasing is the long correlation time (t_c) associated with nuclear spins. This enables techniques such as spin-echo to greatly suppress the dephasing [151]. In [38] it was suggested to measure the nuclear field to reduce electron spin decoherence times; precise knowledge of the instantaneous value of the field would even allow for controlled unitary operations. For example, knowledge of the field in adjacent QDs yields an effective field gradient that could be used in recently proposed quantum computing approaches with pairs of electron spins [179]. Moreover, with sufficient control, the collective spin of the nuclei in a QD may be used as a highly coherent qubit-implementation in its own right [183, 181, 180].

5.1 Phase estimation

In the following we consider an indirect measurement scheme in which the system under investigation is brought into interaction with a probe spin (a two-level system in our case) in a suitably prepared state. Measuring the probe spin after a given interaction time t yields information about the state of the system. We assume the mesoscopic system evolves only slowly compared to the procedure, and further that the measurement does not directly perturb the system. In essence, we are performing a series of quantum non-demolition (QND) measurements on the system with the probe spin.

We consider an interaction Hamiltonian of the form

$$H_{\text{int}} = \hbar A_z \otimes S_z \tag{5.1}$$

which lends itself easily to a measurement of the observable A_z. The QND requirement is

satisfied for $[H_{\rm int}, H_{\rm bath}] \to 0$. The applicability of $H_{\rm int}$ in situations of physical interest is discussed in Sec. 5.5. Given this interaction, the strategy to measure A_z is in close analogy to the so-called Ramsey interferometry approach, which we now briefly review.

For example, an atomic transition has a fixed, scalar value for A_z which corresponds to the transition frequency. By measuring A_z as well as possible in a given time period, the measurement apparatus can be locked to the fixed value, as happens in atomic clocks. The probe spin S is prepared in a state $|+\rangle = (|\uparrow\rangle + |\downarrow\rangle)/\sqrt{2}$. It will undergo evolution under H according to $U_t = \exp(-itA_zS_z)$. After an interaction time t, the probe spin's state will be

$$\cos(\Omega t)|+\rangle + i\sin(\Omega t)|-\rangle \tag{5.2}$$

where $\Omega = A_z/2$ is the precession frequency for the probe spin. A measurement of the spin in the $|\pm\rangle$ basis yields a probability $\cos^2(\Omega t)$ of being in the $|+\rangle$ state. Accumulating the results of many such measurements allows one to estimate the value for Ω (and therefore A_z). In general, the best estimate is limited by interaction time: for an expected uncertainty in A_z of Δ_0 and an appropriate choice of t, M measurements with fixed interaction times $1/\Delta_0$ can estimate A_z to no better than $\sim \Delta_0/\sqrt{M}$ (see [198] and references therein).

In our scenario, the situation is slightly different in that A_z is now a quantum variable. For a state $|s\rangle$ in the Hilbert space of the system $\mathcal{H}$ which is an eigenstate of A_z with eigenvalue $2\Omega_s$, the coupling induces oscillations:

$$U_t|s\rangle|+\rangle = |s\rangle\left[\cos(\Omega_s t)|+\rangle + i\sin(\Omega_s t)|-\rangle\right] \ . \tag{5.3}$$

Thus, the probability to measure the probe spin in state $|+\rangle$ given that the system is in a state $|s\rangle$ is $p(+|s) = \cos^2(\Omega_s t)$ at time t, providing information about which eigenvalue of A_z is realized. Comparing Eq. (5.2) to Eq. (5.3) indicates that the same techniques used in atomic clocks (Ramsey interferometry) could be used in this scenario to measure Ω_s

and thus project the bath in some eigenstate of A_z with an eigenvalue of Ω_s to within the uncertainty of the measurement.

Beyond the Ramsey approach, there are several ways to extract this information, which differ in the choice of interaction times t_j and the subsequent measurements. The general results on quantum metrology of [81] show, however, that the standard Ramsey scheme with fixed interaction time t is already optimal in that the scaling of the final variance with the inverse of the total interaction time cannot be improved without using entangled probe states. Nevertheless, the Ramsey scheme will not be the most suitable in all circumstances. For example, we have assumed so far that preparation and measurement of the probe spin is fast when compared to $1/\Delta_0$. However, in many situations with single quantum systems, this assumption is no longer true, and it then becomes desirable to minimize the number of preparation/measurement steps in the scheme.

5.2 The measurement scheme

We now show that by varying the interaction time and the final measurements such that each step yields the maximum information about Ω_s, we can obtain the same accuracy as standard Ramsey techniques with a similar interaction time, but only *logarithmic* number of probe spin preparations and measurements. As a trivial case, if A_z had eigenvalues 0 and 1 only, then measuring the probe in the $\pm$-basis after an interaction time $t_1 = \pi$, we find $+(-)$ with certainty, if the system are in an $A_z = 0(1)$-eigenstate; if they were initially in a superposition, measuring the probe projects the system to the corresponding eigenspaces. We can extend this simple example (in the spirit of the quantum phase estimation algorithm [109, 142] and its application to the measurement of a classical field [188]) to implement an A_z-measurement by successively determining the binary digits of the eigenvalue. We start

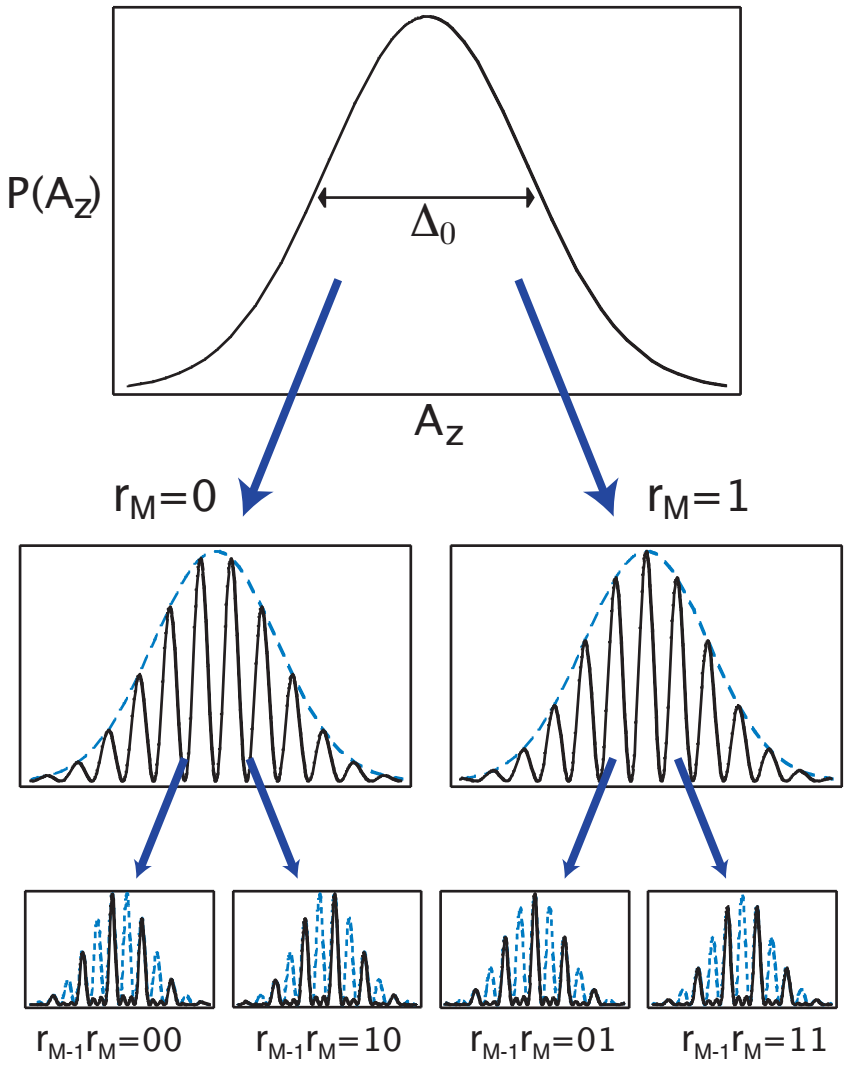

Figure 5.1: Illustration of the first two steps of the measurement procedure. The original distribution $P(A_z)$, with rms width Δ_0 is shown at the top. After the first measurement, with result $r_M = 0, 1$, the conditional distribution (middle plots) reflects the knowledge of the least significant bit. The next measurement result, r_{M-1}, further reduces the distribution (bottom plots).

with the ideal case, then generalize to a more realistic scenario.

5.2.1 Ideal case

If all the eigenvalues of A_z are an integer multiple of some known number α and bounded by $2^M\alpha$, then this procedure yields a perfect A_z-measurement in M steps: let us write all eigenvalues as $2\Omega_s = \alpha 2^M \sum_{l=1}^{M} s_l 2^{-l}$. The sum we denote by s and also use the notation $s = 0.s_1 s_2 \dots s_M$. Starting now with an interaction time $t_1 = \frac{\pi}{\alpha}$, we have $\Omega_s t_1 = s_M \frac{\pi}{2} \bmod \pi$. Hence the state of the probe electron is flipped if and only if $s_M = 1$. Therefore measuring the probe electron in state $+(-)$ projects the nuclei to the subspace of even(odd) multiples of α (see Fig. 5.1). We denote the result of the first measurement by $r_M = 0(1)$ if the outcome was "$+(-)$". All the higher digits have no effect on the measurement result since they induce rotations by an integer multiple of π which have no effect on the probabilities $p(\pm|s)$.

To measure the higher digits, we reduce the interaction time by half in each subsequent step: $t_{j+1} = 2^{-j} t_1$ until we reach $t_M = \frac{\pi}{\alpha}$ in the final and shortest step. For $j > 1$ the rotation angle $\Omega_s t_j \pmod{\pi}$ in the jth step does not only depend on the jth binary digit of s but also on the previous digits (which have already been measured, giving results $r_{M+1-l} = s_{M+1-l}, l = 1, \dots, j-1$). The angle $\Omega_s t_j \pmod{\pi}$ is given by $s_{M+1-j}\frac{\pi}{2} + \varphi_j$ with $\varphi_j = \frac{\pi}{2}\sum_{l=1}^{j-1} r_{M+1-l} 2^{l-j}$, where we have used the results r_l already obtained. This over-rotation by the angle φ_j can be taken into account in the choice of the measurement basis for the jth step: if the jth measurement is performed in a *rotated basis* $|\pm_j\rangle$ that is determined by the previous results r_l, namely

$$|+_j\rangle := \cos\varphi_j|+\rangle - i\sin\varphi_j|-\rangle, \tag{5.4a}$$

$$|-_j\rangle := \sin\varphi_j|+\rangle + i\cos\varphi_j|-\rangle, \tag{5.4b}$$

then the jth measurement yields "+" ($r_{M+1-j} = 0$) if $s_{M+1-j} = 0$ and "−" ($r_{M+1-j} = 1$) otherwise. Thus, after M measurements we obtain $r_l = s_l, \forall l = 1, \ldots, M$ and have performed a complete measurement of A_z (where the number M of probe particles used is the smallest integer such that $2^M \geq A_z/\alpha$).

Before proceeding, we note that the proposed scheme is nothing but an "incoherent" implementation of the quantum phase estimation algorithm: As originally proposed, this algorithm allows measurement of the eigenvalue of a unitary U by preparing M qubits (the control-register) in the state $|+\rangle^{\otimes M}$ (i.e., the equal superposition of all computational basis states $|j\rangle, j = 0, \ldots, 2^M - 1$) and performing controlled-$U^{2^{j-1}}$ gates between the jth qubit and an additional register prepared in an eigenstate $|s\rangle$ of U with $U|s\rangle = e^{i2\pi s}|s\rangle$. The controlled-$U$ gates let each computational basis state acquire a s-dependent phase: $|l\rangle \mapsto e^{i2\pi ls}|l\rangle$. Then the inverse quantum Fourier transformation (QFT) is performed on the control register, which is then measured in the computational basis, yielding the binary digits of s. Performing the QFT is still a forbidding task, but not necessary here: the sequence of measurements in the rotated basis $|\pm_j\rangle$ described above is in fact an implementation of the combination of QFT and measurement into one step. This was previously suggested in different contexts [84, 148, 187].

5.2.2 Realistic case

In general, there is no known α such that all eigenvalues s of A_z are integer multiples of α. Nevertheless, as discussed below, the above procedure can still produce a very accurate measurement of A_z if sufficiently many digits are measured. Now we evaluate the performance of the proposed measurement scheme in the realistic case of non-integer eigenvalues. Since here we are interested in the fundamental limits of the scheme, we will for now assume all operations on the probe qubit (state preparation, measurement, and

timing) to be exact; the effect of these imperfection is considered in Sec. 5.4. Without loss of generality, let A and 0 denote the largest and smallest eigenvalues of A_z, respectively [1] and choose $\alpha = 2A$ such that the eigenvalues of A_z/α are all $\in [0, 1/2]$. These are the eigenvalues s we measure in the following.

The function from which all relevant properties of our strategy can be calculated is the conditional probability $p_M(R|s)$ to obtain (after measuring M electrons) a result $R = 0.r_1 r_2 \dots r_M$ given that the system was prepared in an eigenstate with eigenvalue s. The probability to measure R is given by the product of the probabilities to measure r_{M+1-j} in the jth step, which is $\cos^2(\Omega_s t_j - \varphi_j + r_{M+1-j}\frac{\pi}{2}) = \cos^2(\pi[s-R]2^{M-j})$. Hence

$$p_M(R|s) = \prod_{k=0}^{M-1} \cos^2(\pi[s-R]2^k), \tag{5.5}$$

see also [188]. This formula can be simplified by repeatedly using $2\sin x = \sin(x/2)\cos(x/2)$ to give

$$p_M(R|s) = \left(\frac{\sin(2^M\pi[s-R])}{2^M \sin(\pi[s-R])}\right)^2. \tag{5.6}$$

Assume the nuclei are initially prepared in a state ρ with prior probability $p(s)$ to find them in the eigenspace belonging to the eigenvalue s. After the measurement, we can update this distribution given our measurement result. We obtain, according to Bayes' formula:

$$p_M(s|R) = \frac{p_M(R|s)p(s)}{\sum_s p_M(R|s)p(s)}, \tag{5.7}$$

with expectation value denoted by $\bar{s}_R$.

[1] In practice one may want to make use of prior knowledge about the state of the system to reduce the interval of possible eigenvalues that need to be sampled. Hence A may be understood as an effective maximal eigenvalue given, e.g., by the expectation value of A_z plus f standard deviations. The values outside this range will not be measured correctly by the schemes discussed, but we assume f to be chosen sufficiently large for this effect to be smaller than other uncertainties.

5.3 Performance of the scheme

As the figure of merit for the performance of the measurement scheme we take the improvement of the average uncertainty in A_z of the updated distribution

$$\overline{\Delta A_{z,\mathrm{est}}}^{(M)} := \sum_R p_M(R) \sqrt{\sum_s (s-\bar{s}_R)^2 p_M(s|R)} \tag{5.8}$$

over the initial uncertainty $\Delta_0 = \Delta A_z^{(0)}$. An upper bound to $\overline{\Delta A_{z,\mathrm{est}}}^{(M)}$ is given by the square root of the average variance $\overline{V}$

$$\overline{V}_M := \sum_R p_M(R) \sum_s (s-\bar{s}_R)^2 p_M(s|R), \tag{5.9}$$

as easily checked by the Cauchy-Schwarz inequality. We now show that $\overline{V}_M \leq 2^{-M}$. We replace $\bar{s}_R \to \tilde{R} = \min\{R, 1-R\}$; we can use any such replacement to obtain an upper bound, as the expectation value $\bar{x} = \sum_x p(x)x$ minimizes $v(y) = \sum_x p(x)(x-y)^2$. This choice means that measurement results $R > 1/2$ are interpreted as $1-R$, which is appropriate since the scheme does not distinguish the numbers $s = \delta$ and $s' = 1-\delta$ and due to the choice of α only $s \in [0, 1/2]$ occur. Thus

$$\overline{V}_M \;\leq\; \sum_s p(s) \sum_R (s-\tilde{R})^2 p_M(R|s) =: \sum_s p(s) \overline{V}_M(s).$$

The terms $\overline{V}_M(s)$ can be shown[2] to be $\leq b_V\, 2^{-M}$ with $b_V = (1+2^{-M})/2$. This means that performing M measurements yields a state with A_z-uncertainty $\Delta A_{z,\mathrm{est}} \leq \alpha 2^{-M/2}$. For example, we need about 13 interactions with the probe spin to reach the 1%-level in $\Delta A_{z,\mathrm{est}}/\alpha$ and about 7 more for every additional factor of 10.

The overall procedure requires a total time $T_M = \sum_{j=1}^{M}(t_j + \tau_m) = 2t_1(1 - 2^{-M}) + Mt_m$, which is an interaction time (determined mainly by the time $t_1 = \frac{\pi}{\alpha}2^M =$

[2]For this we make use of Eq. (5.6) and $(\sin x)/x \geq 1 - \pi^{-1}|x|$ (for $|x| \leq \pi$) to bound all terms of the sum over R.

$\pi(2f\Delta_0)^{-1}2^M$ needed for the least significant digit probed) and the time to make M measurements (τ_m is the time to make a single measurement). We obtain for the average uncertainty an upper bound in terms of the interaction time $T_{\rm int} = T_M - M\tau_m$ needed:

$$\frac{\Delta A_{z,\rm est}}{\Delta_0} \leq \sqrt{\frac{\pi f}{\Delta_0 T_{\rm int}}}. \tag{5.10}$$

Immediately the similarity with standard atomic clock approaches is apparent, as the uncertainty decreases with the square root of the interaction time. However, while for an atomic clock scheme, in which the interaction time per measurement is kept fixed to $\sim \pi/(f\Delta_0)$, the total time to reach the precision of Eq. (5.10) is $T_M^{\rm r} = 2t_1 + \tau_m 2^M$. For our method the measurement time is reduced dramatically by a time $T_M^{\rm r} - T_M = \tau_m(2^M - M)$. In this manner our approach requires a polynomial, rather than exponential, number of measurements for a given accuracy, though the overall interaction time is the same for both techniques.

It may be remarked that even the scaling in interaction time differs significantly if other figures of merit are considered. For example, our scheme provides a *square-root speed-up* in $T_{\rm int}$ over the standard Ramsey scheme if the aim is to maximize the information gain or to minimize the confidence interval [129].

5.4 Errors and Fluctuations in A_z

Up until now we have considered an idealized situation in which the value of A_z does not change over the course of the measurement and in which preparation and measurement of the probe system work with unit fidelity. Let us now investigate the robustness of our scheme in the presence of these errors.

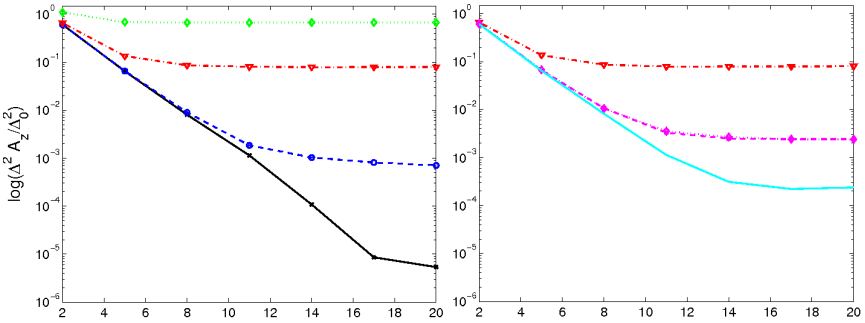

Figure 5.2: Estimation in the presence of preparation and measurement error p: (A) improvement $\Delta A_{z,\mathrm{est}}/\Delta_0$ is plotted versus number M of binary digits measured for different error rates: $p = 0$ (solid black), $p = 0.0001$ (dashed blue), $p = 0.01$ (dash-dotted red), and $p = 0.1$ (dotted green). (B) The benefit of simple error correction for $p = 0.01$: no EC (dash-dotted red); strategy I: 3 repetitions per digit, use majority result (either for all digits or only for leading $M/2$ digits) (purple dashed, dotted); strategy II: increase number of repetitions for more significant digits (7 repetitions for leading $M/8$ digits, 5 for next $M/8$, and 3 for next $M/4$) (purple solid).

5.4.1 Preparation and Measurement Errors

By relying upon a small number of measurements, the scheme we described becomes more susceptible to preparation and measurement errors. An error in the determination of the kth digit leads to an increase of the error probability in the subsequent digits. This error amplification leads to scaling of final error of $\sqrt{p}$, where p is the probability of incurring a preparation or measurement error in a single step. We confirm this with Monte Carlo simulations of the measurement procedure (Fig. 5.2A), leading to an asymptotic bound:

$$\Delta A_{z,\mathrm{est}} \leq (2f\Delta_0)\sqrt{p}. \tag{5.11}$$

Standard error correcting (EC) techniques can be used to overcome this problem. E.g., by performing three measurement for each digit and using majority vote, the effective probability of error can be reduced to $\sim 3p^2$ – at the expense of tripling the interaction time and number of measurements. While this may look like a significant overhead, it should be noted that the scheme can be significantly improved: the least significant digits

do not require any EC. For them, the scheme gives noisy results even for error rate $p = 0$ due to the undetermined digits of A_z, this does not affect the most significant $M/2$ digits. This indicates that it may be enough to apply EC for the leading digits.

As can be seen from Fig. 5.2B, this simple EC strategy provides a significant improvement in the asymptotic ΔA_z. This is hardly changed, when EC is applied only to the leading half of the digits. Thus only twice as many measurements (and an additional interaction time $\sim 2^{M/2+2}$ which is $\ll T_M$) is needed for an order-of-magnitude improvement in ΔA_z. By repeating the measurement of more important digits even more often, the effect of technical errors can be reduced even further, as confirmed by Monte Carlo simulations (Fig. 5.2B). We also note that further improvements (beyond M digits) can be achieved by this technique. In essence, choosing a digital approach to error correction for our digital technique yeilds substantially better performance than adapting the digital technique to an analog approach.

5.4.2 Estimation of bath decorrelation errors

In practice, internal bath dynamics will lead to fluctuations in A_z, such that $A_z(t) \neq A_z(t')$ for times t and t' that are sufficiently different. Furthermore, apparatus errors, as outlined above, lead to errors in our measurement procedure. We will assume that the variations of A_z are slow over short time intervals, allowing us to approximate the M bit measurement process as a continuous measurement over the time T_M with some additional noise with variance $\approx \Delta A_{z,\mathrm{est}}(M)^2 \ll \Delta_0^2$. Then we will find the expected difference in our measurement result and the value of A_z at a later time.

Under the above approximations the value of the kth such measurement (a com-

plete set of M bits taking a time T_M and ending at time t_k) is

$$m_k = \frac{1}{T_M}\int_{t_k-T_M}^{t_k} A_z(t)dt + G_k \tag{5.12}$$

where the noise from measurement is incorporated in the stochastic noise variable G_k with $\langle G_k G_{k'}\rangle \approx \delta_{kk'}\Delta A_{z,\mathrm{est}}(M)^2$. We can estimate A_z at a later time, and find the variance of this estimate from the actual value:

$$\begin{aligned}\bar{V}_M(t>t_k) &= \langle [m_k - A_z(t)]^2\rangle \\ &= \langle G_k^2\rangle + \Delta_0^2 + \frac{1}{2T_M^2}\int_{t_k-T_M}^{t_k}\int_{t_k-T_M}^{t_k}\langle\{A_z(t'),A_z(t'')\}_+\rangle dt''dt' \\ &\quad -\frac{1}{T_M}\int_{t_k-T_M}^{t_k}\langle\{A_z(t'),A_z(t)\}_+\rangle dt'\end{aligned}$$

If we assume A_z is a Gaussian variable with zero mean, described by a spectral function $S(\omega)$ (i.e., $\langle A_z(t)A_z(t+\tau)\rangle = \int_{-\infty}^{\infty} S(\omega)e^{i\omega\tau}d\omega$), then

$$\begin{aligned}\bar{V}_M(t) &= \Delta A_{z,\mathrm{est}}(M)^2 + \Delta_0^2 + \frac{1}{T_M^2}\int_{-\infty}^{\infty} S(\omega)\frac{\sin^2(T_M\omega/2)}{(\omega/2)^2}d\omega \\ &\quad -\int_{-\infty}^{\infty} S(\omega)\frac{\sin[(t-t_k+T_M)\omega]-\sin[(t-t_k)\omega]}{T_M\omega/2}d\omega\end{aligned}$$

For A_z that fluctuates slowly in time and corresponds to a non-Markovian, low frequency noise, the second moment of $S(\omega)$ converges. We define:

$$\frac{1}{t_c^2} = \frac{1}{\langle A_z^2\rangle}\int_{-\infty}^{\infty} S(\omega)\omega^2 d\omega\ . \tag{5.13}$$

When $T_M, t-t_k+T_M \ll t_c$, we may expand the sine terms in the integrals. Taking $t = t_k + T_M$, the expected variance to order $(T_M/t_c)^2$ is

$$\bar{V}_M(t) \approx \Delta A_{z,\mathrm{est}}(M)^2 + \Delta_0^2\left[\frac{T_M}{t_c}\right]^2\left(\frac{7}{3}-\frac{1}{12}\right) \tag{5.14}$$

As an example case, we consider as realistic parameters $t_c \approx 1$ms and $T_M = 16$ μs with $\Delta A_{z,\mathrm{est}}^2/\Delta_0^2 = 0.025^2$. These parameter choices are described in detail in Section 5.5. We

find that our variance 16μs *after* the measurement is approximately $0.035^2\Delta_0^2$ with equal contributions from the measurement noise and from the bath decorrelation. Substantially faster decorrelation would dominate the noise in the estimate, and render our technique unusable.

In the limit of slow decorrelation, this approach would allow one to use the (random) field A_z to perform a controlled unitary of the form $\exp(-im_k S_z \tau)$ at a time t, with a fidelity

$$F = \exp(-\langle(\int_{t-\tau}^{t} A_z(t')dt' - m_k)^2\rangle/4) \tag{5.15}$$

For example, a π rotation around the probe spins' z axis would have a fidelity $\approx 1 - \bar{V}_M(t)\pi^2/\Delta_0^2$, or 0.998 for the above parameters.

We remark that this approach for estimation in the presence of bath fluctuations is not optimal (Kalman filtering [98] would be more appropriate for making an estimation of A_z using the measurement results). Furthermore, it does not account for the non-linear aspects of our measurement procedure, nor does it incorporate any effect of the measurement on the *evolution* of the bath (e.g., quantum Zeno effect). More detailed investigations of these aspects of the process should be considered in an optimal control setting. Nonetheless, our simple analysis above indicates that slow decorrelation of the bath will lead to modest additional error in the estimate of A_z.

5.5 Example: Estimating collective nuclear spin in a quantum dot

Let us now apply these general results to the problem of estimating the collective spin of the lattice nuclei in a QD. The interaction of a single electron spin in a QD with the

spins of the lattice nuclei $\vec{I}_j$ is described by the Fermi contact term [162]

$$\vec{S} \cdot \sum_j \alpha_j \vec{I}_j, \tag{5.16}$$

where the sum in Eq. (5.16) runs over all the N lattice nuclei. The α_j are constants describing the coupling of the jth nuclear spin with the electron. They are proportional to the modulus squared of the electron wavefunction at the location of the jth nucleus and are normalized such that $\sum_j \alpha_j I^{(j)} = A$, which denotes the hyperfine coupling strength.

Due to the small size of the nuclear Zeeman energies, the nuclei are typically in a highly mixed state even at dilution refrigerator temperatures. This implies that the electron experiences an effective magnetic field (Overhauser field, $\vec{B}_{\rm nuc}$) with large variance, reducing the fidelity of quantum memory and quantum gates. This reduction arises both from the inhomogeneous nature of the field ($\vec{B}_{\rm nuc}$ varies from dot to dot) [118] and the variation of $\vec{B}_{\rm nuc}$ over time due to nuclear-spin dynamics (even a single electron experiences different field strengths over time, implying loss of fidelity due to time-ensemble averaging).

In a large external magnetic field in z-direction the spin flips described by the x and y terms are suppressed and – in the interaction picture and the rotating wave approximation – the relevant Hamiltonian is of the type given in Eq. (5.1), where A_z is now the collective nuclear spin operator

$$\hat{A}_z = \sum_{j=1}^{N} \alpha_j I_z^{(j)}, \tag{5.17}$$

which gives the projection of the Overhauser field along the external field axis by $B_{{\rm nuc},z} = \hbar A_z / g^*$.

Many ways to realize single qubit operations such as spin rotations and measurement have been proposed for QDs (see, e.g., [26] for a recent review) and while experimentally still challenging, great progress has been reported recently [61, 151].

For GaAs and InAs QDs in the single electron regime, $A \sim 50 - 200{\rm ns}^{-1}$ and

$N \sim 10^4 - 10^6$. The uncertainty $\Delta_0^2 = \langle \hat{A}_z^2 \rangle - \langle \hat{A}_z \rangle^2 = (T_2^*)^{-2}$ determines the inhomogeneous dephasing time T_2^* [38]. Especially at low polarization P, this uncertainty is large $\Delta_0^2 \approx A^2(1-P^2)/N$, and without correction $H_{\rm zz}$ leads to fast inhomogeneous dephasing of electron spin qubits: $T_2^* \gtrsim 10$ ns has been observed [14, 96, 112]. However, as $\hat{A}_z$ is slowly varying [134, 103, 151], it may be estimated, thereby reducing the uncertainty in its value and the corresponding dephasing. This is expected to be particularly effective, when combining estimation with recent progress in polarizing the nuclear spin ensemble [14, 59, 115].

In a QD system such as [61], with $\tau_m \simeq 1\mu$s and for $1/\Delta_0 \simeq 10$ns we can estimate 8 digits ($M = 8$) (improving $\Delta A_{z,\rm est}$ by a factor of at least 16) in a total time $T_M = 16\mu$s. In contrast, a standard atomic clock measurement scheme would require a time $\simeq 280\mu$s.

We now consider limits to the estimation process, focusing on expected variations of $\hat{A}_z$ due to nuclear spin exchange and preparation and measurement errors. Nuclear spin exchange, in which two nuclei switch spin states, may occur directly by dipole-dipole interactions or indirectly via virtual electron spin flips. Such flips lead to variations of $\hat{A}_z$ as spins i and j may have $\alpha_i \neq \alpha_j$.

The dipole-dipole process, with a $1/r^3$ scaling, may be approximated by a diffusive process at length scales substantially longer than the lattice spacing [168, 48]. The length scale for a spin at site i to a site j such that $\alpha_j \approx \alpha_i$ is not satisfied is on the order of the QD radius (5-50 nm); for diffusion constants appropriate for GaAs [146], the time scale for a change of $\hat{A}_z$ comparable to $\Delta \hat{A}_z$ by this process is $\sim 0.01 - 10$s.

However, nuclear spin exchange mediated by virtual electron spin flips may be faster. This process is the first correction to the rotating wave approximation, and is due to the (heretofore neglected) terms in the contact interaction, $H_{\rm ff} = \frac{\hbar}{2}(A_+ S_- + A_- S_+)$, which are suppressed to first order by the electron Larmor precession frequency ϵ_z. These

have been considered in detail elsewhere [134, 38, 165, 203, 47, 184]. Using perturbation theory to fourth order, the estimated decorrelation time for $\hat{A}_z$ is $t_c^{-1} = A^2/(\epsilon_z N^{3/2})$, giving values $0.1 - 100\text{ms}^{-1}$ for our parameter range [184]. Taking $t_c = 1$ ms, we may estimate the optimal number of digits to measure. Using Eq. (5.14), the best measurement time is given by $T_M \sim t_c/2^{M/2}$ and for the values used above, $M \approx 10 - 11$ is optimal. We note as a direct corollary that our measurement scheme provides a sensitive measure of the nuclear spin dynamics on nanometer length scales.

We now consider implications of these results for improving the performance of nuclear spin ensembles, both as quantum memory [181] and as a qubit [180]. The dominant error mechanism is the same as for other spin-qubit schemes in QDs: uncertainty in $\hat{A}_z$. The proposed measurement scheme alleviates this problem. However, the nuclear spin ensembles operate in a subspace of collective states $|0\rangle$ and $|1\rangle$, where the first is a "dark state", characterized by $\hat{A}_-|0\rangle = 0$ (and the second is $\propto \hat{A}_+|0\rangle$, where $A_\pm = \sum_j \alpha_j I_\pm^{(j)}$). Thus $|0\rangle$ is an $\hat{A}_-$ eigenstate and cannot be an $\hat{A}_z$ eigenstate when $\alpha_k \neq$ const (except for full polarization). Therefore, the measurement [which essentially projects to certain A_z-"eigenspaces" ($A_z \in [a - \Delta a, a + \Delta a]$)] moves the system out of the computational space, leading to leakage errors. The incommensurate requirements of measuring $\hat{A}_z$ and using an $\hat{A}_-$ eigenstate place a additional restriction on the precision of the measurement. The optimal number of digits can be estimated in perturbation theory, using an interaction time $T_{\text{int}} \approx 2t_1$ and numerical results [181] on the polarization dependence of Δ_0. We find that for high polarization $P > 90\%$ a relative error of $\Delta a/a \lesssim 1\%$ is achievable.

5.6 Conclusions

We have shown that a measurement approach based on quantum phase estimation can accurately measure a slowly varying mesoscopic environment coupled to a qubit via a pure dephasing Hamiltonian. By letting a qubit interact for a sequence of well controlled times and measuring its state after the interaction, the value of the dephasing variable can be determined, thus reducing significantly the dephasing rate.

The procedure requires fast single qubit rotations, but can tolerate realistically slow qubit measurements, since the phase estimation approach minimizes the number of measurements. Limitations due to measurement and preparation errors may be overcome by combining our approach with standard error correction techniques. Fluctuations in the environment can also be tolerated, and our measurement still provides the basis for a good estimate, if the decorrelation time of the environment is not too short.

In view of the implementation of our scheme, we have considered the hyperfine coupling of an electron spin in a quantum dot to the nuclear spin ensemble Our calculations show that the Overhauser field in a quantum dot can be accurately measured in times shorter that the nuclear decorrelation time by shuttling suitably prepared electrons through the dot. Given recent advances in electron measurement and control [61, 151] this protocol could be used to alleviate the effect of hyperfine decoherence of electron spin qubits and allow for detailed study of the nuclear spin dynamics in quantum dots. Our approach complements other approaches to measuring the Overhauser field in a quantum dot that have recently been explored [110, 176].

While we discussed a single electron in a single quantum dot, the method can also be applied, with modification to preparation and measurement procedures [3], to the case

[3] In the strong field case a two-level approximation for the spin system is appropriate [39]. Preparing superpositions in the $S_z = 0$ subspace such as the singlet, and measuring in this basis as well [151], the scheme would measure the z-component of the nuclear spin difference between the dots. To measure the

of two electrons in a double dot [112, 96, 39]. We expect that this technique may find application in other systems with long measurement times and slowly varying mesoscopic environments.

J.M.T. would like thank the quantum photonics group at ETH for their hospitality. The authors thank Ignacio Cirac and Guifré Vidal for sharing their notes on the performance of the QFT scheme for different figures of merit. The work at ETH was supported by NCCR Nanoscience, at Harvard by ARO, NSF, Alfred P. Sloan Foundation, and David and Lucile Packard Foundation, and at Ames by the NSF Career Grant ECS-0237925, and at MPQ by SFB 631.

total Overhauser field, superpositions of the $S_z \neq 0$ triplet states have to be used.

Chapter 6

Relaxation, dephasing, and quantum control of electron spins in double quantum dots

J. M. Taylor[1], J. R. Petta[1], A. C. Johnson[1], A. Yacoby[2], C. M. Marcus,[1]
M. D. Lukin[1], M. P. Hanson[3] and A. C. Gossard[3]

[1]Department of Physics, Harvard University, 17 Oxford St., Cambridge, MA 02138 USA
[2]Department of Condensed Matter Physics, Weizmann Institute of Science, Rehovot 76100, Israel
[3]Materials Department, University of California, Santa Barbara, California 93106 USA

We present a detailed theory for electron spin dynamics in two-electron double dot systems that was used to guide and analyze recent experimental demonstrations of the quantum manipulation of two-electron spin states in double quantum dots using electrically controlled exchange interactions. The theory treats both charge and spin degrees of freedom on an equal basis. Specifically, we analyze the relaxation and dephasing mechanisms that are relevant to experiments and discuss practical approaches for quantum control of two-electron system. We show that both charge and spin dephasing play important roles in the dynamics of the two-spin system, but neither represents a fundamental limit for electrical control of spin degrees of freedom in semiconductor quantum bits.
This chapter is reproduced with some modification from Petta et al.,"Coherent Maniuplation of Coupled Electron Spins in Semiconductor Quantum Dots" Science 309, 2180 (2005). Reprinted with permission from AAAS.

Electron spins in quantum dots represent a promising system for studying mesoscopic physics, developing elements for spintronics [7], and creating building blocks for quantum information processing [122, 93, 179]. In the field of quantum information, confined electron spins have been suggested as potential realization of a quantum bit, due to their potential for long coherence times [105, 104, 82]. However, the deleterious effects of hyperfine coupling to lattice nuclear spins [164, 21, 134, 103, 63, 45, 38, 203, 47], as found in experiments [14, 96, 112, 151], severly limit the phase coherence of electron spins. Thus, it is important to understand dynamics of electron spin coupled to nuclei and to develop corresponding quantum control techniques to mitigate this coupling.

Recent experiments by our group explored coherent spin manipulation of electron spins to observe and suppress the hyperfine interaction [96, 151]. In this chapter, we present a detailed theory describing coherent properties of coupled electrons in double quantum dots, that was used to guide our experiments and analyze experimental results. The effects of hyperfine interactions, external magnetic field, exchange terms and charge interactions are combined into a unified theory. Details of the experimental approach (published more completely in in Ref. [151]) are included, with headings in italic, to illustrate the implementation of these theoretical ideas.

Our approach relies upon an approximation based on the separation of time scales between electron spin and nuclear spin degrees of freedom. In particular, the time scales governing nuclear spin evolutions are slower than most relevant electron spin processes. This allows us to treat the nuclear environment using a quasi-static approximation (QSA) [164, 134]. In this model, the nuclear configuration is fixed for any given experimental run, but changes randomly on the time scale over which different runs are integrated over to yield a data point in the experiment. The first corrections to this approximation, where experimentally relevant, are included.

In what follows, we start by extending the theory of the previous chapters to the case of a double quantum dot, where electronic control plays an important role. We then consider the role of charge dephasing and charge-based decay in experiments involving so-called spin blockade, in which a simultaneous spin flip and charge transition is required for electrons to tunnel from one dot to another [96]. Consistent with the experiments, we find that blockade is reduced near zero magnetic field over a range set by the average magnitude of the random Overhauser (nuclear) field. We then consider the effect of fast control of the local electrostatic potentials of double quantum dots, and show how this may be used to perform exchange gates [122, 21, 161], and to prepare and measure two-spin entangled states [178, 151]. Various limitations to the preparation, manipulation, and measurement techniques, due to nuclear spins, phonons, and classical noise sources, are considered.

Before proceeding we note that theories which explicitly include quantum mechanical state and evolution effects of the nuclear spins both within and beyond QSA have been considered by several authors (Refs. [21, 103, 38, 165, 39, 199, 203, 47]). Dephasing, decoherence, and gating error in double quantum dots have also been investigated previously [39, 90, 110]; the present work develops the theory behind quantum control techniques used in experiments, connecting the previous general theoretical treatments to experimental observations.

6.1 Electron spins in a double quantum dot

In the previous chapters, we focused entirely upon the case of a single electron in a quantum dot confined to the lowest energy orbital state of the dot. We start by detailing how to isolate and measure two electrons in a double quantum dot. We then extend the single electron theoretical model to describe the case of two electrons in adjacent, coupled quantum

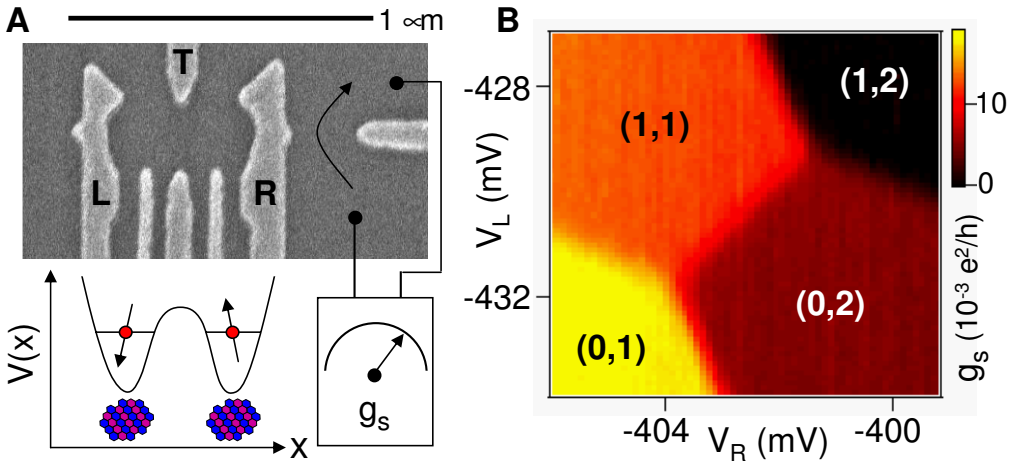

Figure 6.1: (A) Scanning electron micrograph of a sample identical to the one measured, consisting of electrostatic gates on the surface of a two-dimensional electron gas. Voltages on gates L and R control the number of electrons in the left and right dots. Gate T is used to adjust the interdot tunnel coupling. The quantum point contact conductance, g_s, is sensitive primarily to the number of electrons in the right dot. (B) g_s measured as a function of V_L and V_R reflects the double dot charge stability diagram (a background slope has been subtracted). Charge states are labeled (m,n) where m (n) is the number of electrons in the left (right) dot. Each charge state gives a distinct reading of g_s.

dots, first by considering only charge-related couplings, then including spin couplings. The relevant states are separated electron states, in which one electron is in each quantum dot, and double-occupied states, with two electrons in one of the two dots.

6.1.1 *Isolating and measuring two electrons*

Gate-defined double quantum dot devices are fabricated using a GaAs/AlGaAs heterostructure grown by molecular beam epitaxy with a two-dimensional electron gas (2DEG) 100 nm below the surface. The 2DEG density is $\sim 2 \times 10^{11}$ cm^2. When biased with negative voltages, the patterned gates create a double- well potential (Fig. 6.1A). Tunnel barriers (controlled by voltages V_L and V_R) connect each dot to adjacent reservoirs, allowing electrons to be transferred into the dots. Interdot tunneling t (at a rate set by voltage V_T) allows electrons to be moved between dots when the detuning parameter

$\epsilon \propto V_R - V_L$ is adjusted. Measurements are performed in a dilution refrigerator with electron temperature $T_e \sim 135$ mK, determined from Coulomb blockade peak widths. Gates L and R are connected via low-temperature bias tees to high-bandwidth coaxial lines allowing rapid ($\sim$ 1 ns) pulsing of these gates [1]. High-frequency manipulation of a single electron, demonstrating the GHz bandwidth of this set-up, was reported in Ref. [150].

Quantum point contact (QPC) sensors fabricated next to each dot serve as local electrometers [72, 61], showing a few-percent reduction of conductance when a single charge is added to the adjacent dot. Figure 6.1B shows the conductance, g_s, of the right QPC sensor as a function of V_L and V_R near the two-electron regime. Each charge state gives a distinct value of g_s, decreasing each time an electron is added to the system, or when an electron is transferred from the left dot to the right dot. Labels (m,n) in each region indicate the absolute number of electrons confined on the (left, right) dot in the ground state. We focus on transitions involving (0,2) and (1,1) two-electron states, where previous experiments have demonstrated spin selective tunneling [152, 96, 143, 150].

6.1.2 Orbital Hamiltonian for a double dot

As both (2,0) and (0,2) charge configurations have two electrons sharing the same dot, the electron wavefunction overlap is large, and the exchange interaction leads to an energy splitting of the orbitally antisymmetric (and spin symmetric) triplet states ($|T_+\rangle = |\uparrow\uparrow\rangle, |T_0\rangle = (|\uparrow\downarrow\rangle + |\downarrow\uparrow\rangle)/\sqrt{2}, |T_-\rangle = |\downarrow\downarrow\rangle$) from the orbitally symmetric singlet state ($|S\rangle = (|\uparrow\downarrow\rangle - |\downarrow\uparrow\rangle)/\sqrt{2}$), with an energy gap $J_{(2,0)}$ for (2,0). The same occurs for (0,2). In contrast, the state with one electron in each quantum dot has little overlap between the two electrons, and a much smaller exchange energy J. By controlling the relative potentials of the two

[1] Except where noted, a Tektronix AWG520 pulse generator with a 1 ns minimum pulse width is used for fast gate control. Sample response to fast pulses is checked by measuring g_s with pulses applied individually to gates L and R. A doubling of the charge stability diagram is observed for pulses widths down to 1 ns [61].

quantum dots using electrostatic potentials applied, e.g., changing ϵ with external gates, the ground state can be changed from one of the doubly occupied states to one of the separated electron states. We note before proceeding that this approach is similar to a double well Hubbard model of the double-dot. In particular, we include doubly occupied states while neglecting any higher orbital states, appropriate if we assume $J_{(0,2)}, J_{(2,0)} \approx J_2 < \upsilon$, where υ is the orbital level spacing of a single quantum dot. A more detailed, Hund-Mulliken analysis would also include the intrinsic exchange interaction for the separated spin states. See Ref. [21] for details of the Hund-Mulliken approach in double quantum dots.

We consider two quantum dots with sufficient overlap to allow electrons on one dot to quantum mechanically tunnel to the other dot with a matrix element t. This allows for electrons to transfer from the (2,0) and (0,2) singlet states to the (1,1) singlet state, and similarly for the triplet states. The finite exchange energy of the (2,0) and (0,2) configurations means that the triplet states transition to different charge states at much larger values of $|\epsilon|$. The corresponding level structure is given in Fig. 6.2c.

We can model the overall system with separate orbital Hamiltonians for the singlet states and triplet states. Written in the basis $\{|(1,1)S\rangle, |(2,0)S\rangle, |(0,2)S\rangle\}$ for the singlets,

$$H_S = \begin{pmatrix} 0 & t_l & t_r \\ t_l^* & \epsilon + E_c & 0 \\ t_r^* & 0 & -\epsilon \end{pmatrix} . \tag{6.1}$$

Here $t_l = t_r = t$ is the tunnel coupling between left and right dots, and is assumed to be symmetric and real. For the triplets, a similar Hamiltonian is found, but with additional

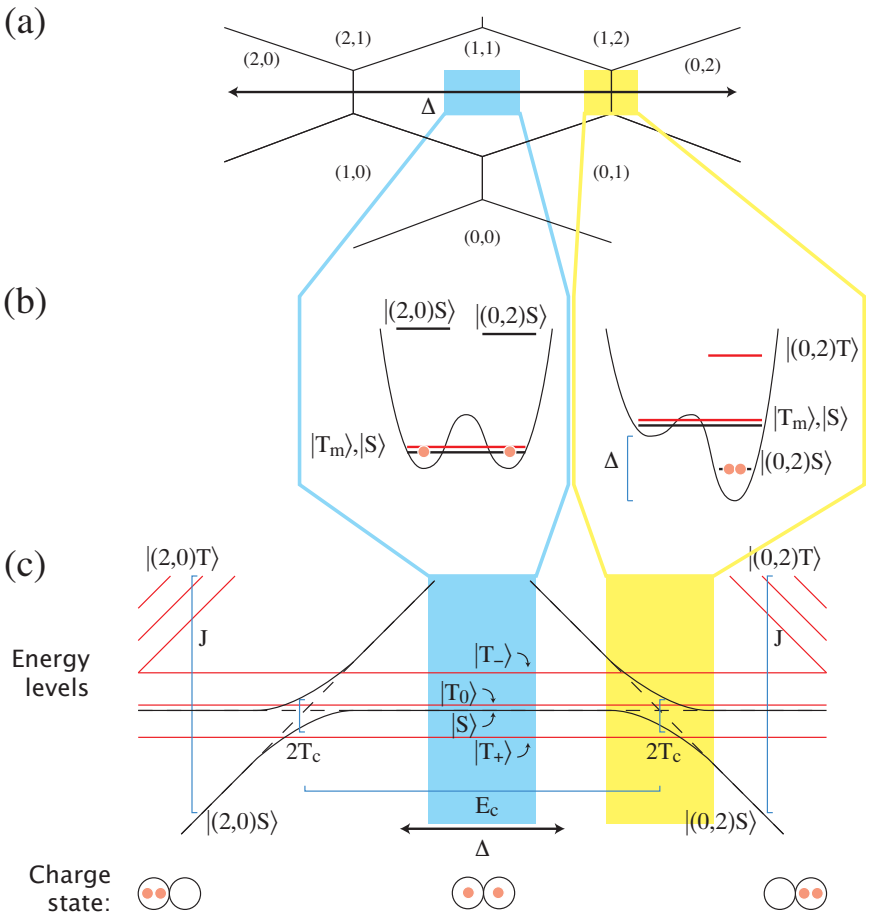

Figure 6.2: (a) Charge stability diagram for a double dot system. Electron numbers are given in (n_l, n_r) notation. The detuning axis is shown, with ϵ parameterizing it, and the far detuned regime (light blue) and charge transition (yellow) are shown. (b) The blue (left) and yellow (right) regions as double-well potentials along one axis (x) with tight confinement in the other two axes (i.e., y and z). In the left, the (1,1) charge states are the ground state, while in the right, (0,2) can be the ground state. Triplet states are indicated in red, while electron charges are indicated in orange. (c) Energy level structure of the double dot system. The far detuned regime is in light blue, and the charge transition is in light yellow. The charge state of the lowest energy state as a function of ϵ is given diagrammatically; from left to right, it is (2,0), (1,1), and (0,2). $\epsilon = -E_c/2$, where E_c is the charging energy of a single dot, is at the middle of the graph. The three triplet states of (1,1) are shown (in red) split by Zeeman energy to easily distinguish them from the singlet state $|S\rangle$.

energy terms $J_{(2,0)}$ and $J_{(0,2)}$.[2] In the basis $\{|(1,1)T\rangle, |(2,0)T\rangle, |(0,2)T\rangle\}$,

$$H_T = \begin{pmatrix} 0 & t_l & t_r \\ t_l^* & \epsilon + E_c + J_{(2,0)} & 0 \\ t_r^* & 0 & -\epsilon + J_{(0,2)} \end{pmatrix} . \tag{6.2}$$

Exact solutions are shown in Fig. 6.3.

When $-E_c - J \ll \epsilon \ll J$ (setting $J_{(2,0)} = J_{(0,2)} = J$), the doubly occupied charge states, (2,0) and (0,2) triplet states are never populated and can be integrated out by renormalization of the low energy states of remaining subspace. While this may be formally accomplished by finding an energy-dependent effective Hamiltonian [6], we expand only to zeroth order in the energy dependence. For the remainder of this chapter, we will no longer refer to spin and orbital states separately, instead reserving the designations $|S\rangle$ and $|T_m\rangle$ strictly for the (1,1) charge subspace, while refering to the doubly-occupied states as, e.g., $|(0,2)S\rangle$.

One regime of interest corresponds to $|\epsilon + E_c/2| \ll E_c/2$, where both doubly occupied states $|(0,2)S\rangle, |(2,0)S\rangle$ may be eliminated from the problem by the above renormalization. We denote this the far-detuned regime, where the states $|S\rangle, |T_0\rangle$ are near-degenerate and the system is far from the (1,1) to (0,2) charge transition. Inclusion of the effect of doubly occupied states leads to a small energy gap between $|S\rangle$ and the triplet $|T_m\rangle$, which we find to be $J \lesssim 10$ neV for the parameters used above.

However, when $\epsilon \gtrsim -t$, we can no longer consider the state $|(0,2)S\rangle$ a high energy state and thus removable by renormalization. It becomes appropriate to explicitly include this additional state, $|(0,2)S\rangle$. Our small parameter will be ϵ. The Hamiltonian near the

[2] An additional correction, $J_{(1,1)} (\neq J)$ consists only of corrections to the (1,1) state's exchange energy from higher energy states. We estimate this to be negligble, it and will be neglected in the following analysis.

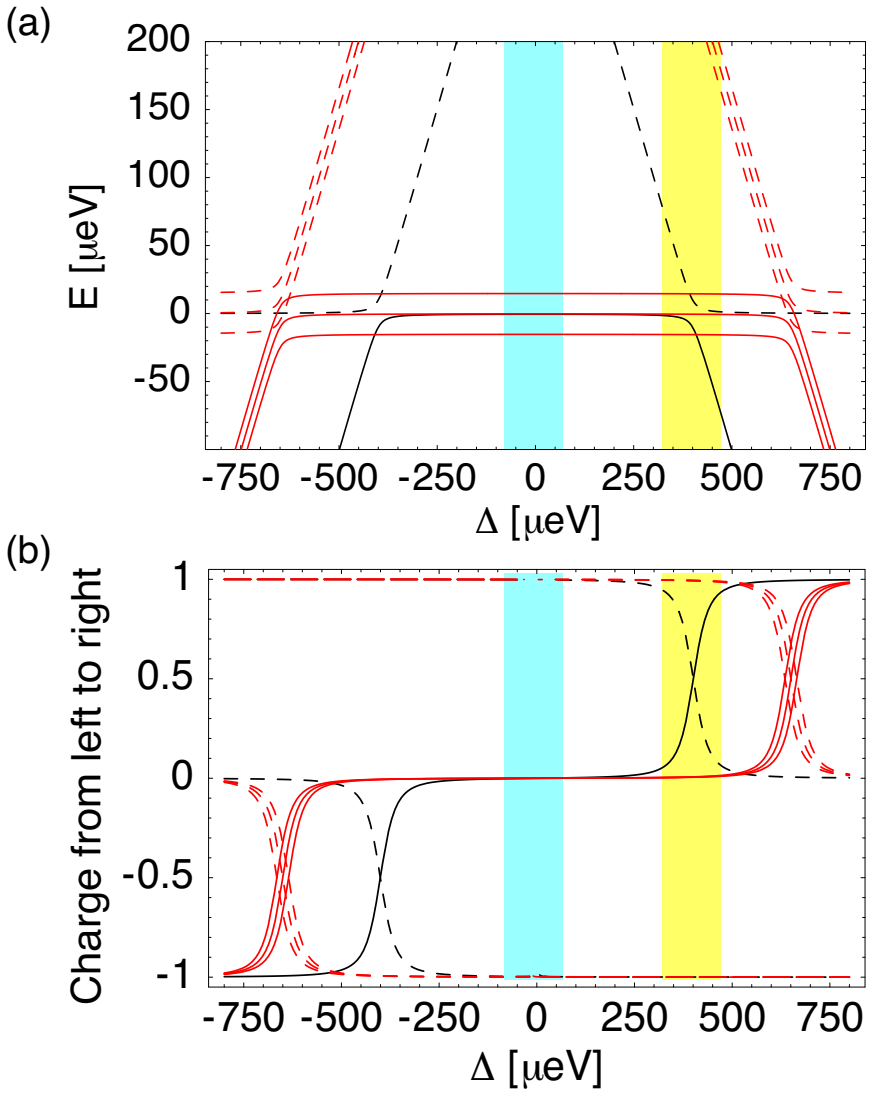

Figure 6.3: (a) Exact solution of the total Hamiltonian, $H = H_S + H_T$. Parameters are charging energy $E_c = 0.8$ meV, tunnel coupling $t = 20$ μeV, single dot exchange $J_{(2,0)} = J_{(0,2)} = 0.5$ meV, and a small magnetic field with Zeeman energy $E_z = \hbar\gamma_e B_{\text{ext}} = 15$ μeV. Singlet orbitals are black, triplet orbitals are red. The higher energy states that will be renormalized are given with dashed lines. The far detuned (light blue) and charge transition (yellow) regimes are indicated. (b) Corresponding charge expectation; -1 indicates two charges on the left, +1 indicates two charges on the right. The expected charge transitions are observed to occur at different detuning parameters ϵ for the singlet (black) and triplet (red) states. The far detuned (light blue) and charge transition (yellow) regimes are indicated.

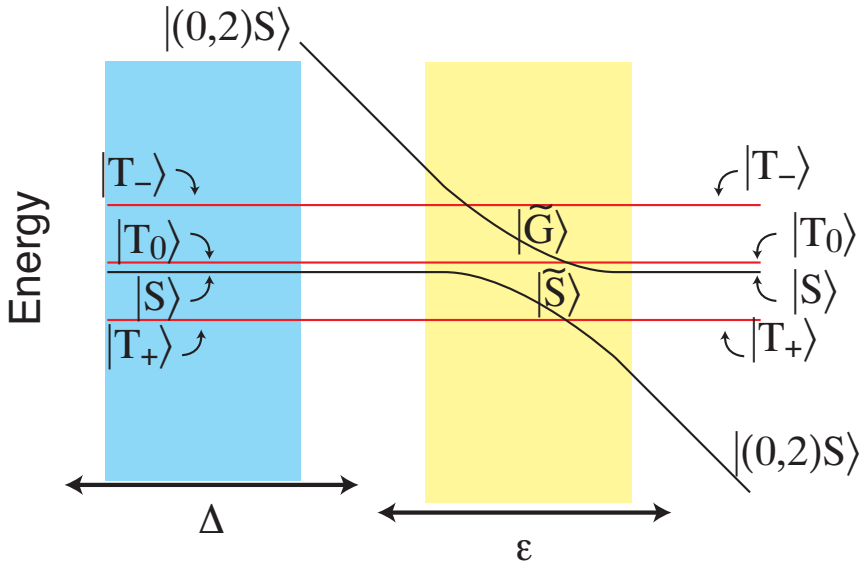

Figure 6.4: Zoomed-in view from Fig. 6.2c of the low energy states in the parameter ranges of interest: far detuned (light blue) and near the charge transition (yellow).

charge transition

$$H_{11-02} = -\epsilon|(0,2)S\rangle\langle(0,2)S| + t(|S\rangle\langle(0,2)S| + |(0,2)S\rangle\langle S|) \tag{6.3}$$

The related experiments (Refs. [96, 151]) are performed near the (1,1) to (0,2) charge transition.

The Hamiltonian of Eqn. 6.3 can be understood by considering the avoided crossing between $|S\rangle$ and $|(0,2)S\rangle$ near $\epsilon = 0$. In particular, for a slowly varying or time-independent Hamiltonian, the eigenstates are given by

$$|\tilde{S}\rangle = \cos\theta|S\rangle + \sin\theta|(0,2)S\rangle \tag{6.4}$$

$$|\tilde{G}\rangle = -\sin\theta|S\rangle + \cos\theta|(0,2)S\rangle \ . \tag{6.5}$$

We introduce the tilde states as the adiabatic states, with $|\tilde{G}\rangle$ the higher energy state. The

adiabatic angle is $\theta = \arctan(\frac{2t}{\epsilon - \sqrt{4|t|^2+\epsilon^2}})$, and the energies of the two states are

$$E_{\tilde{S}} = -\frac{t}{2}\tan(\theta) \tag{6.6}$$

$$E_{\tilde{G}} = \frac{t}{2}\tan(\pi/2-\theta) \text{ ..} \tag{6.7}$$

When $\epsilon \ll -|t|$, $\theta \to 0$, the eigenstates become $|\tilde{S}\rangle \to |S\rangle, |\tilde{G}\rangle \to |(0,2)S\rangle$. For $\epsilon \gg |t|$, $\theta \to \pi/2$, and the eigenstates are switched, with $|\tilde{S}\rangle \to |(0,2)S\rangle$ and $|\tilde{G}\rangle \to |S\rangle$.

As an indication of what is to come, we remark that change of ϵ allows for adiabatic passage between the near degenerate spin states $|S\rangle, |T_m\rangle$ (far detuned regime) to past the charge transition, with $|(0,2)S\rangle$ as the ground state ($\epsilon \gg |t|$). This adiabatic passage can be used for singlet generation and detection. In addition, $|\tilde{S}\rangle$ has an energy difference when compared to the $|T_m\rangle$ triplet subspace of $J(\epsilon) = E_{\tilde{S}}(\epsilon)$. Therefore, an adiabatic pulse moving from the far detuned regime to near the charge transition and back by control of ϵ induces a relative phase between $|S\rangle$ and $|T_m\rangle$ states of angle $\theta = \int dt\ J(\epsilon(t))/\hbar$. This is effectively an exchange gate [122, 21] of angle θ.

One possible correction to the above analysis comes from inclusion of the doubly-occupied triplet states and the (2,0) singlet state. This leads to an additional term,

$$V = E'_T \sum_m |T_m\rangle\langle T_m| + E'_S |S\rangle\langle S| \tag{6.8}$$

where

$$E'_S = \frac{-|t|^2}{E_c+\epsilon} \approx E_S(\epsilon = -E_c)/4 + \frac{|t|^2}{E_c^2}\epsilon + O((\epsilon/E_c)^2)$$

$$E'_T = \frac{-|t|^2}{E_c+J+\epsilon} + \frac{-|t|^2}{J-\epsilon} \approx E_T(\epsilon = -E_c)/4 + \left[\frac{|t|^2}{(E_c+J)^2} - \frac{|t|^2}{J^2}\right]\epsilon + O((\epsilon/J)^2)$$

These are comparable in magnitude to the far-detuned regime's exchange, i.e., $E'_S, E'_T \lesssim 10$ neV. We will neglect it in what follows.

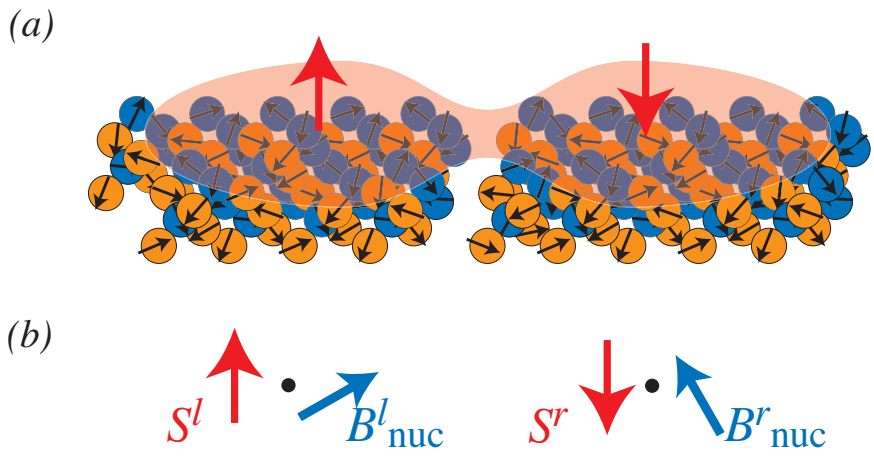

Figure 6.5: A double quantum dot in the (1,1) configuration. (a) Schematic of the two-electron wavefunction in the far detuned regime interacting with lattice nuclear spins. (b) Electron spins in the left and right dots interacting with their respective effective nuclear fields in the quasi-static approximation.

6.1.3 Two-electron spin Hamiltonian for a double dot

We now add spin couplings to the double dot system, including both Zeeman interactions and hyperfine contact coupling. Two effective Hamiltonians, one for the far detuned regime and one appropriate near the charge transition, are developed. Our approach is similar to that of Ref. [39], and we include it here for completeness. The spin interactions in a double quantum dot for the states $|T_m\rangle, |\tilde{S}\rangle$ may be written for $\theta \ll 1$ (i.e., the far detuned regime) as

$$H_{\text{hf,tot}} = H^l_{\text{hf,eff}} + H^r_{\text{hf,eff}} - J(\epsilon)|S\rangle\langle S| \tag{6.9}$$

$$= \hbar\gamma_e[(\vec{B}_{\text{ext}} + \vec{B}_{\text{nuc,l}}) \cdot \hat{\vec{S}}^l + (\vec{B}_{\text{ext}} + \vec{B}_{\text{nuc,r}}) \cdot \hat{\vec{S}}^r] - J|S\rangle\langle S| \tag{6.10}$$

where l and r refer to left and right dot, respectively, and the nuclear fields are determined by the ground orbital state envelope wavefunctions of the single dot Hamiltonians (see Fig. 6.5).

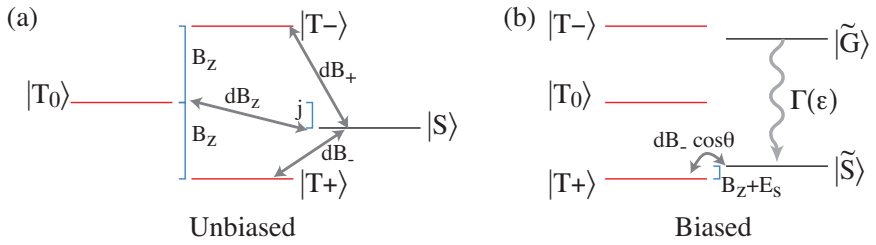

Figure 6.6: (a) Levels in the far detuned regime including all couplings of Eqn. 6.12. (b) Levels near the charge transition; the $|T_+\rangle \leftrightarrow |\tilde{S}\rangle$ is near resonance, with the coupling between $|T_+\rangle$ and $|\tilde{S}\rangle$ indicated, as per Eqn. 6.14.

Reordering terms simplifies the expression:

$$H_{\text{hf,tot}} = \hbar\gamma_e[\vec{B}\cdot(\hat{\vec{S}}^l + \hat{\vec{S}}^r) + d\vec{B}\cdot(\hat{\vec{S}}^l - \hat{\vec{S}}^r)] - J(\epsilon)|S\rangle\langle S| \tag{6.11}$$

with an average field $\vec{B} = \vec{B}_{\text{ext}} + \frac{\vec{B}_{\text{nuc,l}}+\vec{B}_{\text{nuc,r}}}{2}$ and difference field $d\vec{B} = (\vec{B}_{\text{nuc,l}} - \vec{B}_{\text{nuc,r}})/2$. The form of Eqn. 6.11 indicates that terms with $\vec{B}$ and $J(\epsilon)$ are diagonal in total spin and spin projection along $\vec{B}$, creating a natural set of singlet and triplet states. However, the term with $d\vec{B}$ breaks total spin symmetry, and couples the singlet to the triplet states.

We can now write Eqn. 6.11 in matrix form in the basis $\{|T_+\rangle, |T_0\rangle, |T_-\rangle, |S\rangle\}$,

$$H = \hbar\gamma_e \begin{pmatrix} B_z & 0 & 0 & \frac{dB_x - idB_y}{\sqrt{2}} \\ 0 & 0 & 0 & -dB_z \\ 0 & 0 & -B_z & \frac{-dB_x - idB_y}{\sqrt{2}} \\ \frac{dB_x + idB_y}{\sqrt{2}} & -dB_z & \frac{-dB_x + idB_y}{\sqrt{2}} & -J(\epsilon)/\gamma_e \end{pmatrix} \tag{6.12}$$

The corresponding level structure is given in Fig. 6.6a. We have implicitly assumed the QSA in writing this Hamiltonian by defining the axis of spin up and down as $\vec{B}$, which is a sum of the external field and the average nuclear field. If the nuclear field fluctuates, those terms will contribute by coupling different triplet states together. However, those terms only effect the observable behavior of the system when going beyond the quasi-static approximation.

At zero external magnetic field all states couple to the singlet, and solving the dynamics require diagonalizing the 4-by-4 matrix of Eqn. 6.12. However, at finite magnetic field, a large Zeeman splitting (which sets $B_z \gg B_{\rm nuc}$) allows us to separate the system. The far detuned regime only has transitions between the $m_s = 0$ states; in this basis ($\{|T_0\rangle, |S\rangle\}$), the matrix becomes

$$H_{m_s=0} = \hbar\gamma_e \begin{pmatrix} 0 & -dB_z \\ -dB_z & -J(\epsilon)/\gamma_e \end{pmatrix}. \tag{6.13}$$

This two-level system has appropriately straightforward dynamics, and we investigate it in some detail below.

Near the charge transition and at finite magnetic field, another coupling can occur, this time between $|T_+\rangle$ and $|\tilde{S}\rangle$. This resonance corresponds to the adiabatic singlet $|\tilde{S}\rangle$ having an exchange energy $-J$ close to the Zeeman-split triplet's Zeeman energy, $E_z = -\gamma B_z$. Written in the basis $\{|T_+\rangle, |\tilde{S}\rangle\}$, the Hamiltonian is

$$H_{\rm flip-flop} = \hbar\gamma_e \begin{pmatrix} B_z & \frac{dB_x - idB_y}{\sqrt{2}}\cos\theta \\ \frac{dB_x + idB_y}{\sqrt{2}}\cos\theta & -J(\epsilon)/\gamma_e \end{pmatrix}. \tag{6.14}$$

We have subscripted Eqn. 6.14 with "flip-flop" indicating that flips between $|\tilde{S}\rangle$ and $|T_+\rangle$ result in the flipping of a nuclear spin, as can be seen by identifying $dB_+ = dB_x + idB_y = (\hat{B}_{\rm nuc,l,+} - \hat{B}_{\rm nuc,r,+})/2$.

Because the $\tilde{S}$–T_+ resonance leads to spin flips and eventual polarization of the nuclear field, the QSA will not be valid if appreciable change of field occurs, and the overall dynamics may go beyond the approximation. This has been examined experimentally [143] and theoretically [181, 65] for some specific cases, and is discussed in Chapter 7. While the discussion to follow mentions this resonance, it will focus on the zero field mixing of Eqn. 6.11 and the far detuned regime's finite field mixing of Eqn. 6.13. We remark that Eqns. 6.13 and 6.14 have been previously derived outside of the QSA [39].

We have now established that in the far detuned regime, the relevant spin interactions are limited to dynamics within the singlet-triplet subspace and determined by the Hamiltonian in Eqn. 6.13. Similarly, near the charge transition a resonance between $|S\rangle$ and $|T_+\rangle$ may be observed; as this resonance allows for nuclear spin polarization, it may only be partially described by the QSA, and we do not consider its dynamics in detail. However, we note that in the absence of nuclear spin polarization the resonance occurs when the Zeeman splitting of the external field equals the exchange energy, j. Thus, if the Zeeman energy is known, measuring the position of the splitting gives a map between external parameters and the actual exchange energy.

6.1.4 *Voltage-controlled exchange*

The relative energy detuning, ϵ, of the (0,2) and (1,1) charge states can be rapidly controlled by applying calibrated voltage pulses to gates L and R (see Fig. 6.7B). For $\epsilon > 0$, the ground state charge configuration is (0,2). Tight confinement in (0,2) favors a spin-singlet configuration, denoted (0,2)S. As note above, the corresponding (0,2) triplet states are energetically inaccessible, lying $J_2 \sim 400$ μeV above (0,2)S, and are neglected in the following discussion. For ϵ ¡ 0 the ground state configuration is (1,1). In this case, four spin states are accessible: the singlet ($S = 0$), denoted S (suppressing the (1,1) label), and three triplets ($S = 1$), denoted T_-, T_0, T_+ corresponding to $m_s = -1, 0, +1$.

In the absence of interdot tunneling, the two spins in the (1,1) configuration are independent, i.e., S, T_0, and $T_\pm$ are degenerate. At finite magnetic fields, S and T_0 are degenerate. When interdot tunneling is present, the (0,2) and (1,1) charge states hybridize, which results in an exchange splitting $J(\epsilon)$ between the S and T_0 spin states of (1,1) that depends on detuning (Fig. 6.7B). Near zero detuning, exchange $J(\epsilon \rightarrow 0)$ becomes large (equal to the tunnel coupling, t); for large negative detuning, $\epsilon \ll -t$, exchange vanishes,

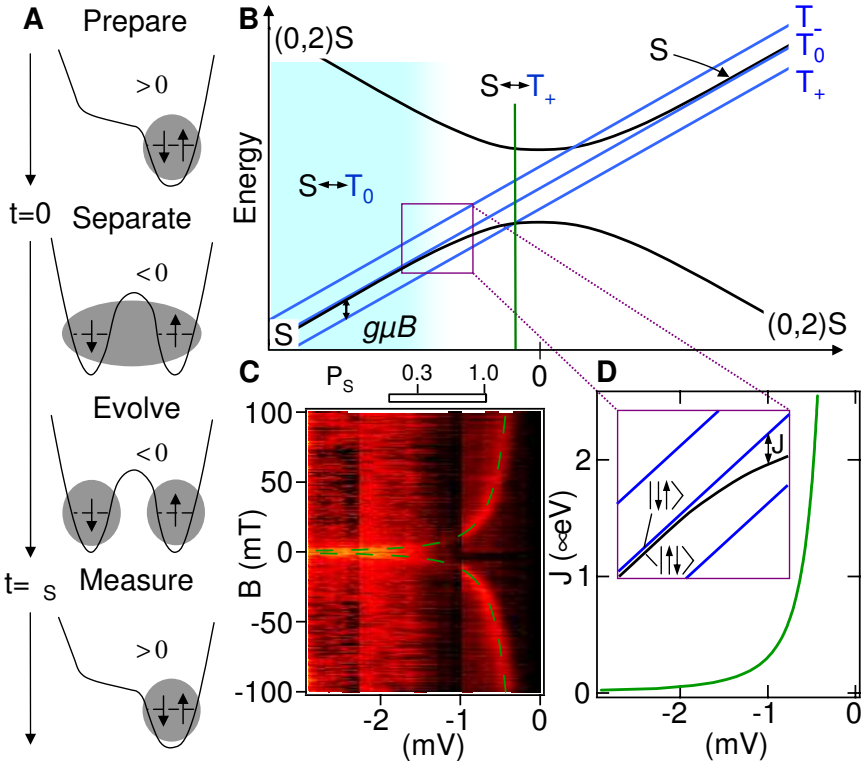

Figure 6.7: (A) The control cycle for experiments generally consists of preparation, singlet separation, evolution of various kinds, and projection onto the (0,2) singlet state (measurement). Projective measurement is based on the spin-blockaded transition of T states onto (0,2)S, while S states proceed freely (see text for notation), allowing S to be distinguished from T by the charge sensor during the measurement step. (B) Energy diagram near the (1,1) to (0,2) charge transition. Magnetic field splits T states by the Zeeman energy. At the $S - T_0$ degeneracy (light blue region) and the S-T+ degeneracy (green line), hyperfine fields drive evolution between S and respective T states. (C) Singlet probability P_S after τ_S = 200ns, as a function of detuning ϵ and magnetic field B maps out degeneracies of $S - T_0$ ($\epsilon \lesssim$ -1.2 mV) and $S - T_+$ (dashed green curve). (D) Dependence of exchange on detuning, extracted from fit of along the $S - T_+$ $J(\epsilon) = g^*\mu_B B$ resonance assuming $g^* = -0.44$ (dashed curve in (C)). Inset: For , $J(\epsilon) \gg g^*\mu_B B_{\rm nuc}$ eigenstates S and T_0 are split by $J(\epsilon)$. At large negative detuning $J(\epsilon) \ll g^*\mu_B B_{\rm nuc}$, S and T are mixed by hyperfine fields, but eigenstates $\uparrow\downarrow$ and $\downarrow\uparrow$ are not.

$J(\epsilon) \to 0$, and the spins again become independent. Except where noted, a perpendicular magnetic field $B = 100$ mT is used to split off the $T_\pm$ states from T_0 by the Zeeman energy, $E_Z = \pm g^* \mu_B B \sim 2.5$ μeV ($g^* = -0.44$ is the electron g-factor in GaAs; μ_B is the Bohr magneton). The split-off T_+ state crosses the hybridized singlet S when $J(\epsilon) = g^* \mu_B B$ (vertical green line in Fig. 6.7B), allowing $J(\epsilon)$ to be readily measured, as discussed below.

In all measurements a cyclical pulse sequence is used (see Fig. 6.7A for a schematic representation). A pulse transfers the (0,2)S state into the spatially separated (1,1) singlet state, S. The singlet state is manipulated using various control techniques (discussed below). After manipulation, the resulting (1,1) spin state is projected back onto (0,2)S for a measurement of the singlet probability, P_S. P_S is measured using the QPC: the T states of (1,1) remain in a spin-blocked configuration, while the S state tunnels directly to (0,2)S. This spin-to-charge conversion readout is based on the same mechanism that results in rectification in dc transport found in similar devices [143, 150]. The majority of the duty cycle is spent in the measurement configuration ($\epsilon > 0$), so that the slow (time-averaged) measurement of the QPC conductance reflects the charge configuration during the measurement phase [152, 96].

Even though we can coherently control and measure two-electron spin states electrically, the local solid state environment remains critically important. For our device, each electron is coupled to roughly 10^6 GaAs nuclei through the hyperfine interaction. The hyperfine interaction results in an effective random magnetic field with magnitude [96, 147, 14]. These random hyperfine fields evolve slowly ($> 10\mu$s) relative to typical pulse sequence periods and result in spin dephasing, thereby coupling two-electron spin states [164, 21, 103, 134, 45, 38]. At large negative detuning, where $J(\epsilon) < g^* \mu_B B_{\rm nuc}$, these effective fields mix S and T states.

6.2 Nuclear-spin-mediated relaxation in double dots

In this section we consider what occurs past the charge transition, when the ground state of the system is $|(0,2)S\rangle$ and the low-lying excited states are the (1,1) states, $\{|S\rangle, |T_m\rangle\}$. This situation occurs in dc transport when the system is in the spin blockade regime, where transitions from $|T_m\rangle$ to $|(0,2)S\rangle$ are suppressed because they require both a spin and charge transition.

Several groups[87, 61, 114] have studied spin relaxation between Zeeman split spin states at high magnetic field ($B >$4 T). The measured relaxation rates were found to scale as B^4, consistent with a spin-orbit mediated spin relaxation process[82]. Similarly, measurements of relaxation of triplet states to the singlet when $J \gg \gamma_e B_{\rm nuc}$ (i.e., when the effect of nuclei is small) indicate long lifetimes, likely limited by similar spin-orbit mediated mechanisms[75]. On the other hand, at low field and small exchange, when the splitting between spin states becomes comparable to $B_{\rm nuc}$, the hyperfine interaction dramatically increases the spin relaxation rate. Previous theoretical work for two electron systems has focused on triplet and singlet decay of two-electron states in a single quantum dot [64]; in contrast, the present analysis deals with a double quantum dot system where the electrons can be well separated. Contrary to more general spin blockade calculations[97] and experiments, the present work is focused entirely on the rate limiting step of blockade: the spin flip followed by charge transition within the double quantum dot. Recent experiments have measured spin relaxation between nearly degenerate singlet and triplet spin states in this regime [96]. Experimental techniques are discussed in Ref. [152], and a full analysis of the field and energy dependence of the relaxation rate is discussed in Ref. [96] (and reprinted in Appendix D). We only briefly outline the experiment here.

Experiments are performed near the two-electron regime with very weak tunnel

coupling. In contrast to the above discussion, t is slower than the pulse rise times ($t \ll 1\mu$ eV). Pulsed-gate techniques are used to change the charge occupancy from (0,1) to (1,1) to (0,2) and back to (0,1). In the (1,1) charge configuration with weak interdot tunnel coupling the $|S\rangle$ and $|T_m\rangle$ states are nearly degenerate. Shifting the gates from (0,1) to (1,1) creates a mixture of all four states, $|S\rangle, |T_{m=-1,0,1}\rangle$ by loading an electron from a nearby Fermi sea. Then, the system is rapidly (non-adiabatic with respect to tunnel coupling t) shifted to the (0,2) regime, with $|(0,2)S\rangle$ as the ground state. In this rapid shift procedure, the singlet $|S\rangle$ does not adiabatically follow to the doubly-occupied singlet $|(0,2)S\rangle$, but instead follows the Zener branch of the avoided crossing and stays in $|S\rangle$, as is illustrated in Fig. 6.8.

Due to Pauli exclusion, $|T_m\rangle$ to $|(0,2)S\rangle$ transitions are spin blocked, and require spin relaxation to occur. By measuring this transition probability as a function of the time when past the charge transition a spin relaxation time can be deduced. Charge state occupancies are directly measured using a local quantum point contact charge detector. We found that the decay rate from (1,1) to (0,2) occurred a factor of 1000 times faster within a few mT of zero field. Essentially, the nuclear field leads to mixing of the four (1,1) states. In the absence of nuclei (and other spin mixing mechanisms), only the singlet (1,1) state ($|S\rangle$) decays to the state $|(0,2)S\rangle$; in their presence, all four states can decay.

We now use the theory developed in the preceding sections to discuss the experiment. The experiment consisted of starting the system in the far detuned regime, where coupling to the leads resulted in filling (with equal probability) one of the four low-energy states of the far detuned regime's states, $|T_m\rangle, |S\rangle$. A non-adiabatic shift past the charge transition puts the system out of equilibrium. The system is allowed to relax to the ground state $|(0,2)S\rangle$ for a controlled time, and the charge state measured by use of a nearby electrometer, such as a quantum point contact (QPC). It was found that at zero magnetic field, exponential decay of the (1,1) states to the state $|(0,2)S\rangle$ occurs, but as field grows

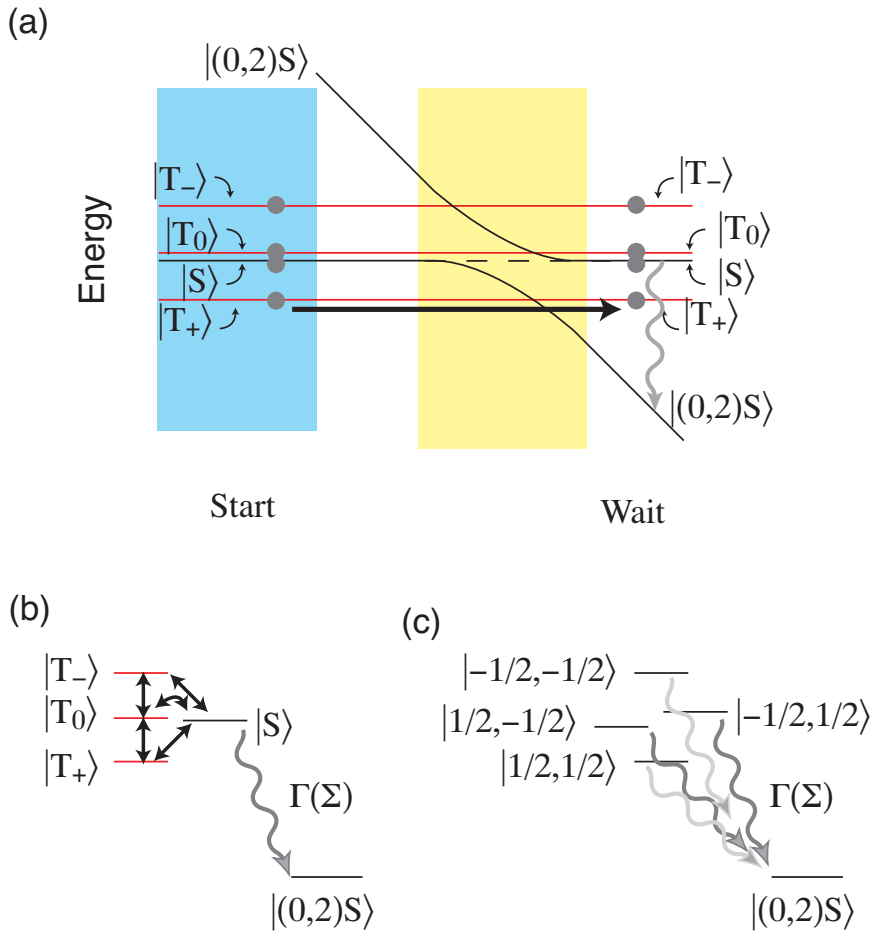

Figure 6.8: (a) Energy level structure as a function of detuning. Coupling to a Fermi sea with $k_bT \gg \gamma_e|B_{\text{ext}}|$ leads to equal filling of all four low energy states in the far detuned regime (labelled start). Then ϵ is changed rapidly with respect to the tunnel coupling, leading to all four spin states still in the (1,1) charge configuration. The time spent waiting in this configuration results in slow decay of the metastable (1,1) states to the $|(0,2)S\rangle$ state. (b) Nuclear spins couple between the eigenstates of exchange, and slow inelastic decay at a rate Γ proceeds from $|S\rangle$ to $|(0,2)S\rangle$. (c) The same process, but for the eigenstates of the double dot Hamiltonian. The $m_s = 0$ states are equal superpositions of $|S\rangle$ and decay rapidly to $|(0,2)S\rangle$, while the $|m_s| = 1$ states are only weakly mixed at large magnetic field with the $|S\rangle$, resulting in slow decay to $|(0,2)S\rangle$.

beyond $B_{\rm nuc}$, double exponential behavior is observed. This behavior may be described by the above theory as follows.

Past the charge transition, when the adiabatic basis $|\tilde{S}\rangle, |\tilde{G}\rangle$ is an appropriate representation of the system, it is possible for the system to experience inelastic decay from the excited state $|\tilde{G}\rangle$ to the ground state $|\tilde{S}\rangle$ via charge coupling, e.g., to phonons. The energy gap is $\mathcal{E} = E_{\tilde{G}} - E_{\tilde{S}} = \sqrt{\epsilon^2 + 4|t|^2}$. Inelastic decay near a charge transition in a double quantum dot has been investigated in great detail [74, 15, 16], and we do not seek to reproduce those results. Instead, we note that the decay from the excited state $|\tilde{G}\rangle$ to the ground state $|\tilde{S}\rangle$ is well described by a smoothly varying, energy-dependent decay rate $\Gamma_{ph}(\mathcal{E})$. Incoherent population of $|\tilde{G}\rangle$ by absorption of a thermal phonon is suppressed as long as $2t > k_b T$, which is satisfied for $t = 0.01$ meV and $T = 100$ mK. Other charge-based dephasing and relaxation mechanisms, such as co-tunneling and other couplings to the leads (nearby Fermi seas), may be controlled by closing off the quantum point contact barriers separating the dots from the leads. When tunneling is important, this system can exhibit spin-blockade; a theory describing this effect is given in Ref. [97].

We can combine the coherent spin precession and charge dynamics with the charge-based decay and dephasing mechanisms to investigate relaxation of $|T_m\rangle$ states to the state $|\tilde{S}\rangle$. Of particular interest is the regime past the charge transition, $\epsilon \gg t$, where $|\tilde{G}\rangle \approx |S\rangle$ becomes nearly degenerate with $|T_0\rangle$, as was studied in the experiment of Ref. [96]. An effective five-level system is formed with the levels $\{|T_+\rangle, |T_0\rangle, |T_-\rangle, |S\rangle\}$ described by the spin Hamiltonian of Eqn. 6.12, while inelastic decay from $|S\rangle$ to $|(0,2)S\rangle$ (the fifth level) is possible at a rate $\Gamma(\mathcal{E})$, as shown in Fig. 6.8b.

To analyze this process, we start with the Louivillian superoperator that describes

inelastic tunneling:

$$\begin{aligned}\dot{\rho} &= i[\rho, H/\hbar] + \Gamma(\mathcal{E})/2\Big[|S\rangle\langle S|\rho + \rho|S\rangle\langle S| \\ &\quad -2|(0,2)S\rangle\langle S|\rho|S\rangle\langle(0,2)S|\Big] \end{aligned} \tag{6.15}$$

where

$$H = \hbar\gamma_e[\vec{B}^l \cdot \hat{\vec{S}}^l + \vec{B}^r \cdot \hat{\vec{S}}^r]_{(1,1)} - \hbar\mathcal{E}|(0,2)S\rangle\langle(0,2)S| \ . \tag{6.16}$$

l and r indicate left and right spins for the (1,1) charge space. Assuming the nuclear field is quasi-static (QSA), we can diagonalize H. The eigenstates are the ground state, $|(0,2)S\rangle$, and (1,1) states with spin aligned and anti-aligned with the local magnetic fields, $\vec{B}^{l,r} = \vec{B}_{\rm ext} + \vec{B}^{l,r}_{\rm nuc}$. We write these eigenstates as $|s,s'\rangle = |s\rangle_l \otimes |s\rangle_r$, where $s, s' = \pm 1/2$ are the eigenvalues of the spin projection on the fields of the l and r dots, respectively. The eigenvalue for $|(0,2)S\rangle$ is $E_G = -\mathcal{E}$ and the other four eigenstates $|s,s'\rangle$ have energy

$$E_{s,s'} = s\gamma_e|B^l| + s'\gamma_e|B^r| \ . \tag{6.17}$$

By considering decay from the energy eigenstates of the nuclear field, $|s,s'\rangle$ to $|(0,2)S\rangle$, we may eliminate rapidly varying phase terms, e.g., $|1/2,-1/2\rangle\langle -1/2,1/2|$. This requires that the inelastic decay mechanism, $\Gamma(\mathcal{E})$, be slow in comparison to the electrons' Larmor precession in the nuclear field, Ω. In this limit, each state $|s,s'\rangle$ decays to $|(0,2)S\rangle$ with a rate given by $\Gamma(\mathcal{E})|\langle s,s'|(0,2)S\rangle|^2$, as indicated in Fig. 6.8c. A detailed analysis is given in appendix C.1. For convenience, we write $c_{s,s'} = \langle s,s'|(0,2)S\rangle$.

In the context of Ref. [96], we can find analytical expressions for the time evolution of the density matrix of an initial form $\rho(t=0) = \sum_{s,s'} |s,s'\rangle\langle s,s'|/4$. This initial state corresponds to a mixture of the four (1,1) spin states. The charge measurement distinguishes only between (1,1) states and $|(0,2)S\rangle$; accordingly, we evaluate the evolution of the projector for the (1,1) subspace $P_{11} = \sum_{s,s'} |s,s'\rangle\langle s,s'|$. In particular,

$$P_{11}(t) = e^{-\Gamma(\mathcal{E})|c_{++}|^2 t}/2 + e^{-\Gamma(\mathcal{E})|c_{+-}|^2 t}/2 \tag{6.18}$$

The actual experimental signal is the integrated charge difference, given by

$$M(t) = \int_0^t P_{11}(t')dt' \tag{6.19}$$

Finally, we must average over possible initial nuclear spin configurations to find the measured signal. This means evaluating $\langle P_{11}(t)\rangle_{\rm nuc}$, a difficult task in general. However,

$$\langle P_{11}(t)\rangle_{\rm nuc} \approx e^{-\Gamma(\mathcal{E})\langle|c_{++}|^2\rangle_{\rm nuc}t}/2 + e^{-\Gamma(\mathcal{E})\langle|c_{+-}|^2\rangle_{\rm nuc}t}/2\ . \tag{6.20}$$

In this approximation, we replace the average of the exponents with the average values for the coefficients $|c_{++}|^2, |c_{+-}|^2$. The validity of this approximation can be checked with numerical integration, and for the range of parameters presented here the approximation holds to better than 1%.

The mean values of the coefficients $|c_{++}|^2, |c_{+-}|^2$ are in turn straightforward to calculate approximately (as done in Ref. [96], supplemental information[3]), giving

$$\Gamma_{+-} = \Gamma(\mathcal{E})\langle|c_{+-}|^2\rangle_{\rm nuc} = \frac{\Gamma(\mathcal{E})}{4}(1 + I_l I_r) \tag{6.21}$$

$$\Gamma_{++} = \Gamma(\mathcal{E})\langle|c_{++}|^2\rangle_{\rm nuc} = \frac{\Gamma(\mathcal{E})}{4}(1 - I_l I_r) \tag{6.22}$$

with

$$I_l = \frac{1}{\sqrt{[1 + 3(\frac{B_{{\rm nuc},l}}{B_{\rm ext}})^2]}} \tag{6.23}$$

and similarly for I_r. We plot the product $I_l I_r$, found in both Eqns. 6.21-6.22, as a function of external magnetic field for increasing difference in dot sizes in Fig. 6.9. This indicates that the effective decay rates are largely independent of the ratio of dot sizes, relying only on the average effective nuclear field, $B_{\rm nuc} = (B_{{\rm nuc},l} + B_{{\rm nuc},r})/2$.

We find that past the charge transition with $\epsilon \gg |t|$ the states $|S\rangle$ and $|T_0\rangle$ decay to $|(0,2)S\rangle$ with a lifetime Γ_{+-}^{-1}, while the two $|m_s| = 1$ triplet states have a lifetime

[3] In contrast to Ref. [96], where $B_{\rm nuc} = \sqrt{\langle|\hat{\vec{B}}_{\rm nuc}|^2\rangle}$, we define $B_{\rm nuc} = \sqrt{\langle|\hat{\vec{B}}_{\rm nuc}|^2\rangle/3}$.

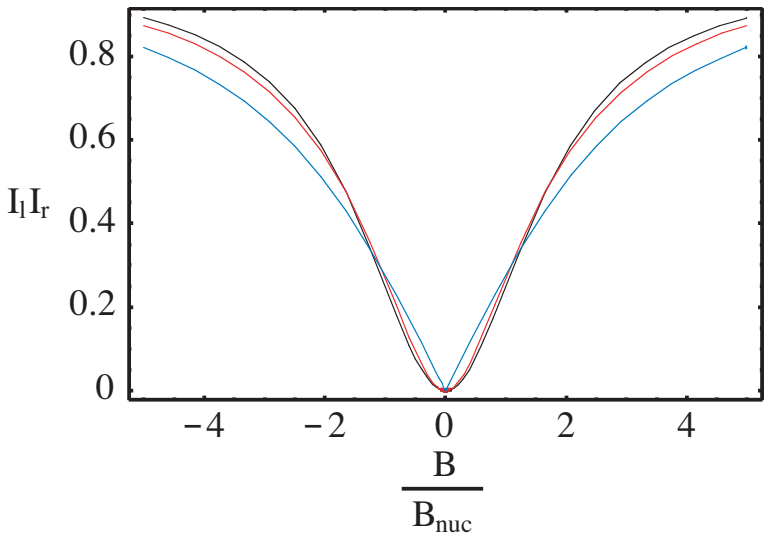

Figure 6.9: The product $I_l I_r$ as a function of external magnetic field B in units of average nuclear field, $B_{\rm nuc} = (B_{{\rm nuc},l} + B_{{\rm nuc},l})/2$. Several ratios of dot nuclear fields, $r = B_{{\rm nuc},l}/B_{{\rm nuc},r}$ are considered: $r = 1$ (black), $r = 1/3$ (red) and $r = 0$ (blue). Cusp behavior near zero field is found in the limit of highly inhomogeneous dot field strengths.

Γ_{++}^{-1}. At finite magnetic field, $\Gamma_{+-} \gg \Gamma_{++}$, and we can call the states of the $|m_s| = 1$ subspace "metastable". The metastability allows for charge-based measurement to distinguish between $\{|S\rangle, |T_0\rangle\}$ and $|T_\pm\rangle$ subspaces: by using a nearby charge sensor, the decay of $|S\rangle, |T_0\rangle$ may be detected long before $|T_\pm\rangle$ has finite probability of decay in the weak tunneling limit. This indicates that, while at zero field decay of the (1,1) states to the state $|(0,2)S\rangle$ is governed by a single exponential, a double-exponential behavior appears as $B > B_{\rm nuc}$ is satisfied, in direct confirmation of the results of Ref. [96]. The double exponential behavior is shown in Fig. 6.10.

In the context of spin blockade, contrary to expectation, the blockade is contributed to solely by the $|m_s| = 1$ triplet states. In particular, spin blockade is charge transport at finite bias through, for example, the charge states $(0,1) \to (1,1) \to (0,2)$. For biases between left and right leads that are less than J only the four (1,1) spin states and the state $|(0,2)S\rangle$ are necessary for understanding the process. An electron (of arbitrary spin)

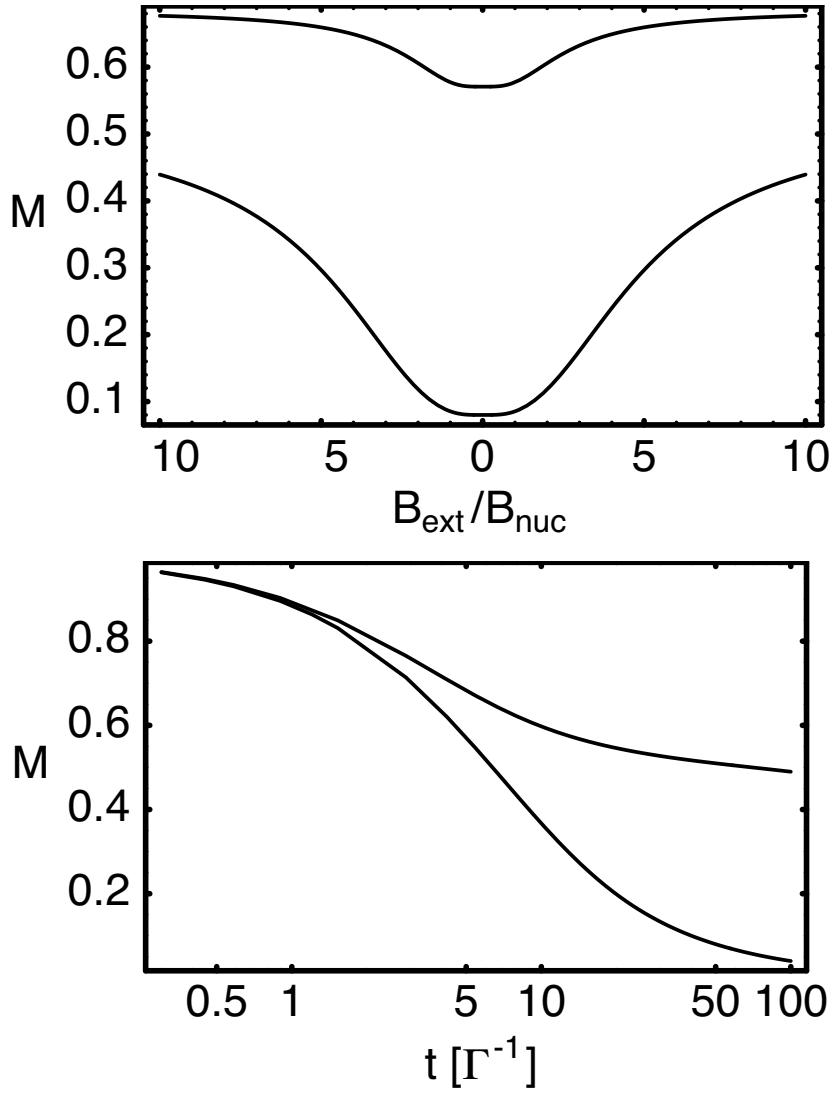

Figure 6.10: (a) The signal $M(t)$ (Eqn. 6.19) for $t = 5\ \Gamma(\mathcal{E})^{-1}$ (top) and $50\ \Gamma(\mathcal{E})^{-1}$ (bottom) as a function of external magnetic field. (b) Log-linear plot of $M(t)$ for $B = 0$ (bottom) and $B = 30B_{\rm nuc}$ (top). Double exponential behavior is observed for the latter case.

loads from the left lead, creating with equal probability any of the states $|s, s'\rangle$. This then tunnels with a rate Γ_{+-} or Γ_{++} to the state $|(0,2)S\rangle$, after which the extra electron on the right tunnels into the leads, and the cycle repeats anew. The average current through the device is dominated by the slowest rate, which in the absence of cotunneling, is Γ_{++}. In other words, loading into a spin-aligned state $|s, s\rangle$ prevents further charge transport until it decays, with rate Γ_{++}, or is replaced from the leads by a cotunneling process.

The measurements by Johnson *et al.* demonstrate that the transition probability from (1,1) to $|(0,2)S\rangle$ depends strongly on both magnetic field and detuning [96]. Our theoretical model, which accounts for hyperfine mixing coupled with inelastic decay agrees well with experimental results for timescales less than 1 ms. The discrepancy between experiment and theory for longer times suggests that other spin relaxation processes may become important above 1 ms (spin-orbit).

6.3 Quantum control of two electron spin states

We now analyze how time-dependent control of gate parameters (e.g., ϵ) may be used to control electron spin in double quantum dots. Of particular interest are methods for probing the hyperfine interation more directly than in the previous section. The new techniques we use are primarily rapid adiabatic passage and slow adiabatic passage. Rapid adiabatic passage (RAP) can prepare a separated, two-spin entangled state ($|S\rangle$ in the far detuned regime), and when reversed, allows a projective measurement that distinguishes the state $|S\rangle$ from the triplet states, $|T_m\rangle$. A similar technique used at large external magnetic field, slow adiabatic passage (SAP), instead prepares and measures eigenstates of the nuclear field, $|s, -s\rangle$.

Rapid adiabatic passage is used to measure the time-resolved dephasing due to

nuclei for two electron spin states. Slow adiabatic passage is used to probe in a time-resolved fashion gate control of the exchange interaction. We connect these techniques with the experiments in Ref. [151] and estimate their performance.

6.3.1 Spin-to-charge conversion for preparation and measurement

Adiabatic passage from $\epsilon \ll -t$ to $\epsilon \gg t$ maps the far detuned regime states $|S\rangle, |T_m\rangle$ to the states past the charge transition $|(0,2)S\rangle, |T_m\rangle$, allowing for a charge measurement to distinguish between these results [178, 151]. In the quantum optics literature, when adiabatic transfer of states is fast with respect to the relevant dephasing (nuclear spin-induced mixing, in our case), it is called "rapid adiabatic passage" (RAP) and we adopt that terminology here.

When the change of detuning, ϵ, is adiabatic with respect to tunnel coupling, t, but much faster than $\gamma_e B_{\rm nuc}$ (the hyperfine coupling), the adiabatic passage is independent of the nuclear dynamics. For example, starting past the charge transition with the state $|(0,2)S\rangle (= |\tilde{S}\rangle)$ and $\epsilon \gg t$ and using RAP to the far detuned regime causes adiabatic following to the state $|S\rangle$. This prepares a separated, entangled spin state. The procedure is shown in Fig. 6.11a.

The reverse procedure may be used to convert the singlet state to the charge state (0,2) while the triplet remains in (1,1). Then, charge measurement distinguishes singlet versus triplet. Specifically, if we start with some superposition in the far detuned regime, $|\psi\rangle = c_S|S\rangle + \sum_m c_m|T_m\rangle$ where c_S, c_m are quantum amplitudes, after RAP past the charge transition, with $\epsilon \gg t$, the state is $|\psi'\rangle = c_S e^{i\phi}|(0,2)S\rangle + \sum_m c_m|T_m\rangle$, where ϕ is the adiabatic phase accumulated. Recalling that $|(0,2)S\rangle$ is in the (0,2) charge subspace, while $|T_m\rangle$ states are in the (1,1) subspace, a nearby electrometer may distinguish between these two results, performing a projective measurement that leaves the $|T_m\rangle$ subspace untouched.

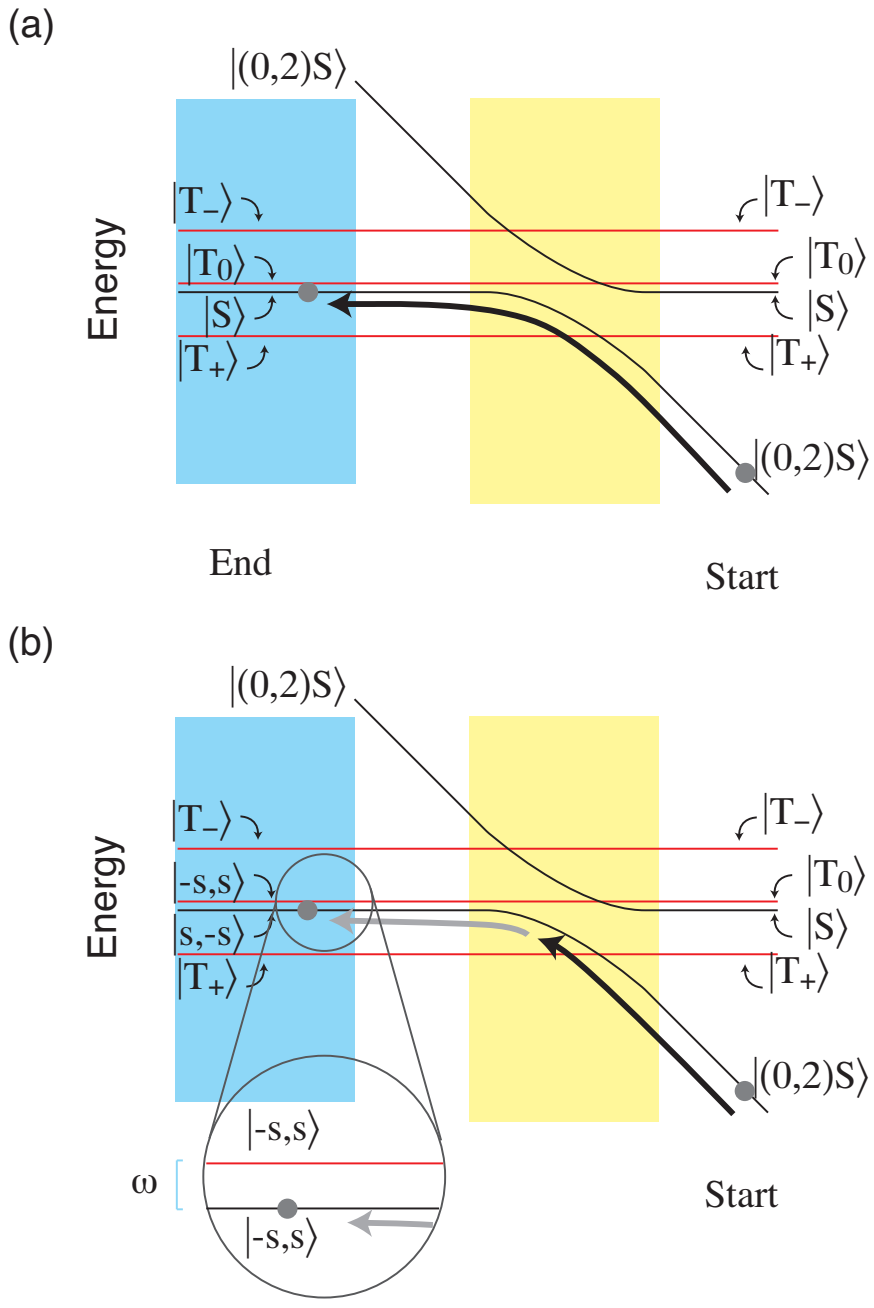

Figure 6.11: (a) Rapid-adiabatic passage: starting in the state $|(0,2)S\rangle$, the detuning is changed from $\epsilon \gg t$ to $\epsilon \ll -t$, fast with respect to the nuclear energy scale, $\gamma_e B_{\text{nuc}}$. (b) Slow adiabatic passage: as above, but once the system is past the $S - T_+$ degeneracy point, the change of ϵ is made slow with respect to the nuclear energy scale. The zoomed-in section shows the current nuclear energy splitting ($\hat{\omega}$) and the nuclear field eigenstates, $|s,-s\rangle$ and $|-s,s\rangle$. Both procedures may be reversed to transfer either $|S\rangle$ (RAP) or $|s,-s\rangle$ (SAP) to $|(0,2)S\rangle$ while keeping the other states within the (1,1) charge configuration, allowing for charge-based measurement of the system.

Furthermore this measurement is independent of the adiabatic phase.

In contrast, if the change of ϵ is slow with respect to nuclei, adiabatic passage follows to eigenstates of the hyperfine interaction. For simplicity, we assume that RAP is used between the charge transition to just past the $S-T_+$ resonance of Eqn. 6.14, such that we may neglect transfer between the S and T_+ states (see also Fig. 6.12b. This requires an external magnetic field $|B_{\rm ext}| \gg B_{\rm nuc}$. Continuing from this ($\epsilon < -t$) point to the far detuned regime, ϵ is changed slowly with respect to Ω. Accordingly, adiabatic passage proceeds into eigenstates of the *nuclear* field, $|s,-s\rangle$, as shown in Fig. 6.11b. These are the product spin states, with one spin up and the other down with respect to magnetic field. This technique may be called slow adiabatic passage (SAP).

Before (for RAP) the mapping was $|S\rangle \leftrightarrow e^{i\phi}|(0,2)S\rangle, |T_m\rangle \leftrightarrow |T_m\rangle$, leaving the triplet states unperturbed. For SAP, the mapping is

$$\begin{cases} |(0,2)S\rangle & \leftrightarrow & e^{i\phi}|s,-s\rangle \\ |T_0\rangle & \leftrightarrow & e^{i\phi'}|-s,s\rangle \\ |T_{\pm 1}\rangle & \leftrightarrow & |T_{\pm 1}\rangle \end{cases} \tag{6.24}$$

It is always the current, lowest energy eigenstate of the nuclear field that $|(0,2)S\rangle$ maps to. That is, we choose s such that $E_{s,-s} < E_{-s,s}$, with $E_{s,-s} = s\gamma_e(B^l_{{\rm nuc},z} - B^r_{{\rm nuc},z})$, (see Section 6.2, Eqn. 6.17, evaluated at large external magnetic field). We remark that SAP allows for deterministic preparation and measurement of states rotated $\pi/2$ with respect to $|S\rangle, |T_0\rangle$ without direct knowledge of which states they correspond to for each realization.

We now examine the adiabaticity condition for slow adiabatic passage. In SAP, ϵ is changed at a constant rate to approach the far detuned regime (point S). Using the approximate relation $j(\epsilon) = 4T_C^2/\epsilon$, the adiabaticity condition is that $\hbar\dot{j} \ll (\hbar\omega)^2$ in the range of ϵ where $j(\epsilon) \lesssim \Omega$ (the current nuclear field gradient's frequency is given by ω). This can be rewritten $\hbar\dot{\epsilon}\frac{T_C^2}{\epsilon^2} \ll (\hbar\omega)^2$; for $T_c \simeq 5$ μeV, and $\epsilon \in [50, 550]$ μeV, the required

time to make the 500 μeV change, τ, gives $\hbar\dot{\epsilon} = \frac{\hbar}{\tau}500$ μeV, and roughly, $\hbar\dot{\epsilon}\frac{T_C^2}{\epsilon^2} = \frac{\hbar}{\tau} \times 50$ neV. In units of time, $\hbar^2(\tau \times 13$ ns). For $\tau = 1000$ ns, the adiabaticity requirement is that the current value of $1/|\omega| \lesssim 3 \times \sqrt{1000 \times 13}$ ns = 300 ns. For the nuclear fields in lateral quantum dots such as those of Ref. [96] (each dot with a $T_2^* = 10$ ns), the probability of $1/|\omega| > 300$ ns is

$$P(|\omega| < 3\ \mu\mathrm{s}^{-1}) = 2\int_0^{3\ \mu\mathrm{s}^{-1}} d\nu\ \frac{e^{-(\nu T_2^*)^2}}{\sqrt{\pi (T_2^*)^{-2}}} \tag{6.25}$$

This gives an error probability of 3% for 300 ns rise time, that is, every 1 in 30 experimental runs, the nuclear gradient will be too small for the adiabatic filling of $|\pm\rangle$ to occur.

We can ask the effect of finite, residual exchange energy j_{res} at the S point. Finite j leads to filling of a superposition of $|s, -s\rangle$ and $|-s, s\rangle$:

$$\cos(\phi)|s, -s\rangle - \sin(\phi)|-s, s\rangle\ , \tag{6.26}$$

where the value of s is, as above, determined by the current value of ω and $\phi = \arctan[j_{\mathrm{res}}/(\sqrt{j_{\mathrm{res}}^2 + \omega^2} + |\omega|)]$ is the adiabatic angle. The resulting loss of contrast will be $\sin^2(\phi) \simeq (j/2\omega)^2$. For residual $j_{\mathrm{res}} \sim 0.1\ \Omega$, the error is less than 1%. For $j_{\mathrm{res}} \sim 0.25\ \Omega$ the error is order 2%. The role of residual nuclear fields during the exchange gate is evaluated elsewhere [182].

6.3.2 Probing the nuclear field by electron spin measurement

We now consider how adiabatic passage can be used to probe the dephasing of a spin-singlet state. This relates directly to a critical question in quantum information science: how long can two electron spins remain entangled when the electrons are spatially separated on a GaAs chip. In our model, variations in the local nuclear environment cause the spatially separated electrons to experience distinct local magnetic fields, and hence precess at different rates, mixing the singlet and triplet states. If many measurements are taken to determine the probability of remaining a singlet, the time-ensemble-averaging leads

to an observable dephasing of the singlet state (T_2^*) [151].

To evaluate the effects of nuclei on this process, we will calculate the autocorrelation function $A_{SS}(t) = |\langle S(t)|S(0)\rangle|^2$ for the far detuned regime. This autocorrelation function has been evaluated for quantum chemistry [164], and the integrals encountered here solved in that work. We also note that the single dot case has been considered in Refs. [134, 103].

We start by evaluating the evolution operation $U(t)$, where the Schrodinger picture $|S(t)\rangle = U(t)|S\rangle$. Taking $J \to 0$ for the far detuned regime, we solve analytically the equation of motion any spin state of the (1,1) subspace. In particular, we take the Hamiltonian of Eqn. 6.10 and write it in the form two effective fields, each acting separately on one spin. The evolution operator, $U(t) = \exp(-iHt/\hbar)$ can be factorized as $U(t) = U_l(t) \otimes U_r(t)$, where

$$U_i(t) = \exp(-i\gamma_e t[\vec{B} + \vec{B}_{\mathrm{nuc},i}] \cdot \vec{S}_i) \tag{6.27}$$

acts only on the spin in dot i. As each is spin 1/2, we may take advantage of the algebra of Pauli operators, and using $\exp(i\phi(2\vec{n} \cdot \vec{S})) = \cos(\phi) + i(2\vec{n} \cdot \vec{S})\sin(\phi)$ for $|n| = 1$, write

$$U_i(t) = \cos(\omega_i t)1 - 2i\vec{n}_i \cdot \vec{S}_i \sin(\omega_i t) \tag{6.28}$$

where $\omega_i = \gamma_e|\vec{B} + \vec{B}_{\mathrm{nuc},i}|/2$ and $\vec{n}_i = (x_i, y_i, z_i) \propto \vec{B} + \vec{B}_{\mathrm{nuc},i}$ is of length 1.

If the system is prepared by RAP in the state $|S(t=0)\rangle = (|\uparrow\downarrow\rangle - |\downarrow\uparrow\rangle)/\sqrt{2}$, and subsequently measured using RAP to distinguish the singlet and triplet subspaces, the measurement probes the state's autocorrelation function, i.e., the probability of remaining a singlet after a time t. The autocorrelation function is a function of t and external magnetic field, B:

$$\begin{aligned} A_{SS}(t,B) &= |\langle S(t)|S(t=0)\rangle|^2 \\ &= |\cos(\omega_l t)\cos(\omega_r t) + \vec{n}_l \cdot \vec{n}_r \sin(\omega_l t)\sin(\omega_r t)|^2 \end{aligned} \tag{6.29}$$

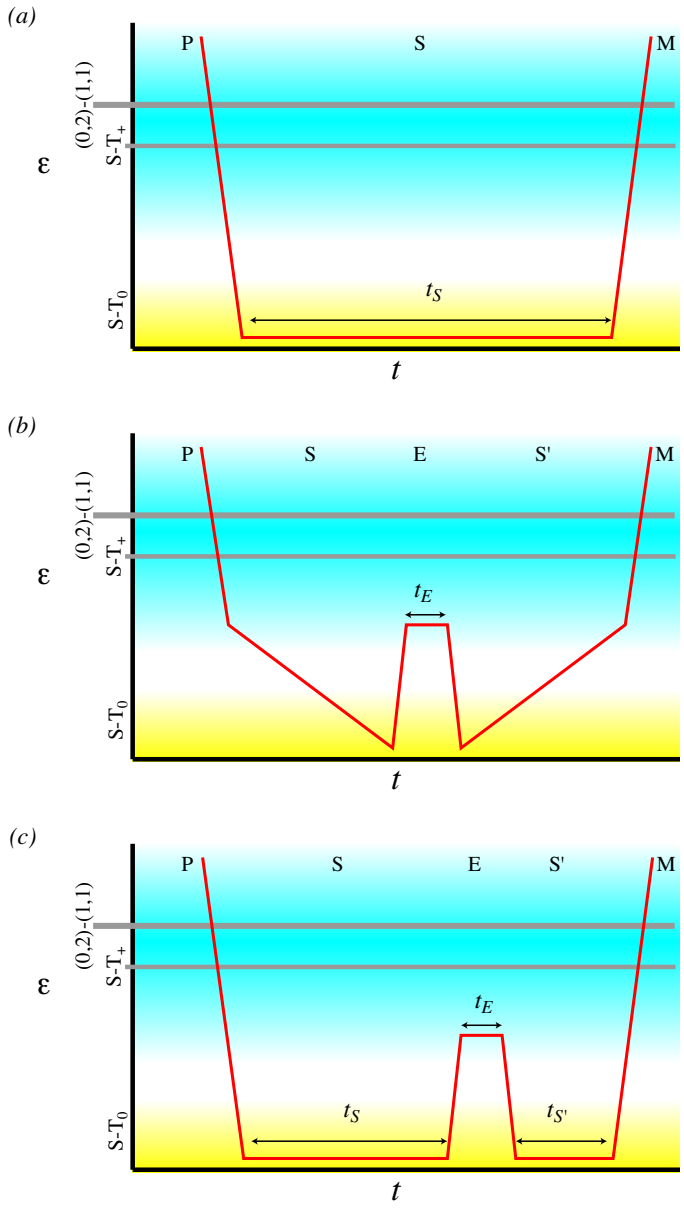

Figure 6.12: Pulse sequences: detuning parameter ϵ versus time, for (a) RAP for measurement of the singlet autocorrelation function, (b) SAP for the exchange-gate sequence, and (c) the singlet-triplet echo sequence. Blue is the charge transition region, while yellow is the far detuned regime. The charge degeneracy point (the crossing from (1,1) to (0,2)) and the degeneracy between $|\tilde{S}\rangle$ and $|T_+\rangle$ (when $j(\epsilon) = \gamma_e |B_{\text{ext}}|$) are shown for reference.

To obtain the signal in the quasi-static approximation, Eqn. 6.29 must be averaged over the different possible nuclear field values.

The signal expected at zero magnetic field may be evaluated now. When $\vec{B} = 0$, the properties of $\vec{n}_i$ within the QSA are described by $\langle n_{i,\mu} n_{j,\nu} \rangle = \delta_{ij}\delta_{\mu\nu}/3$. Averaging over nuclei, the signal is

$$\begin{aligned} A_{SS}(t,0) &= \langle \cos^2(\omega_l t)\rangle_{\rm nuc} \langle \cos^2(\omega_r t)\rangle_{\rm nuc} + \\ &\quad \frac{1}{3}\langle \sin^2(\omega_l t)\rangle_{\rm nuc} \langle \sin^2(\omega_r t)\rangle_{\rm nuc} \end{aligned} \tag{6.30}$$

where

$$\begin{aligned} \langle \cos^2(\omega_i t)\rangle_{\rm nuc} &= \frac{1}{2}[1 + e^{-\frac{1}{2}(t/T_{2,i}^*)^2}(1 - (t/T_{2,i}^*)^2)] \ , \\ \langle \sin^2(\omega_i t)\rangle_{\rm nuc} &= \frac{1}{2}[1 - e^{-\frac{1}{2}(t/T_{2,i}^*)^2}(1 - (t/T_{2,i}^*)^2)] \ . \end{aligned}$$

We recall that $T_{2,i}^* = (\gamma_e B_{{\rm nuc},i})^{-1}$. A distinct difference of this model from other dephasing mechanisms is the order 10% overshoot of the decay at short times, and the asymptoptic approach of $A_{SS}(t \gg T_2^*, 0)$ to 1/3. A classical master equation would exhibit neither of these features; they are unique identifiers of the quasi-static regime, in which different coherent dynamics are averaged over many realizations. Numerically we find that the qualitative behavior of $A_{SS}(t,0)$ (overshoot and saturation at 1/3) does not depend on $B_{{\rm nuc},l}/B_{{\rm nuc},r}$ for variations of up to 50%.

Another regime of interest is when the external field is much larger than the effective nuclear fields ($|\vec{B}| \gg B_{{\rm nuc},i}$). Spin-flip terms are highly suppressed and the system is restricted to two levels, $|S\rangle$ and the $m_s = 0$ triplet, $|T_0\rangle = (|\uparrow\downarrow\rangle + |\downarrow\uparrow\rangle)/\sqrt{2}$. This is described by the Hamiltonian of Eqn. 6.13. This effective two-level system's evolution operator is straightforward to evaluate, again using the algebra of Pauli operators, but now for the psuedo-spin of $|S\rangle$ and $|T_0\rangle$ (for example, $\sigma_z = |T_0\rangle\langle T_0| - |S\rangle\langle S|$). Working with

$j = 0$, the singlet autocorrelation function before averaging within the QSA is

$$|\langle S(t)|S(0)\rangle|^2 = \cos^2(\omega_B t) \ , \tag{6.31}$$

with $\hat{\omega} = \frac{\gamma_e}{2}(B_{\mathrm{nuc},l,z} - B_{\mathrm{nuc},r,z})$. Using the QSA, the variable $\hat{\omega}$ may be considered as a random (stochastic) gaussian-distributed variable of rms width $\sigma_\omega = 1/\sqrt{2}T^*_{2,\mathrm{eff}} = \frac{1}{2}\sqrt{(T^*_{2,l})^{-2} + (T^*_{2,r})^{-2}}$.

When both dots are of equal size, $T^*_{2,\mathrm{eff}}$ is the single-dot time-ensemble-averaged dephasing time, as described in Section 1.3.2. The signal may be averaged over all initial nuclear field configurations, to give

$$A_{SS}(t, B \gg B_{\mathrm{nuc}}) = \langle \cos^2(\hat{\omega}t)\rangle = \frac{1}{2}[1 + e^{-(t/T^*_{2,\mathrm{eff}})^2}] \tag{6.32}$$

as the expected signal in the QSA. Qualitatively, the decay of the autocorrelation function A_{SS} due to the nuclear field is described by Gaussian decay with a timescale $T^*_{2,\mathrm{eff}}$. Similar to the case of zero magnetic field, the behavior of this autocorrelation function is independent of variations in dot size up to $\simeq 50\%$.

The logical qubit.

With the $T_\pm$ states split off by an applied field $B \gg B_{\mathrm{nuc}}$, the states S and T_0 form an effective two-level system (or qubit). To facilitate the following discussion, we define a Bloch sphere for the $S-T$ two-level system that has S and T_0 at the north and south poles (z axis) and the eigenstates of the instantaneous nuclear fields within this subspace, $\uparrow\downarrow$ and $\downarrow\uparrow$, as the poles along the x axis (see Fig. 6.13A).

6.3.3 *Dephasing of the separated singlet.*

The pulse sequence described in Fig. 6.13A is used to measure the dephasing of the separated singlet state as a function of the time τ_S that the system is held at large detuning (with $J(\epsilon) < g^*\mu_B B_{\mathrm{nuc}}$). This time is a T_2^* time (the star indicates an average over many

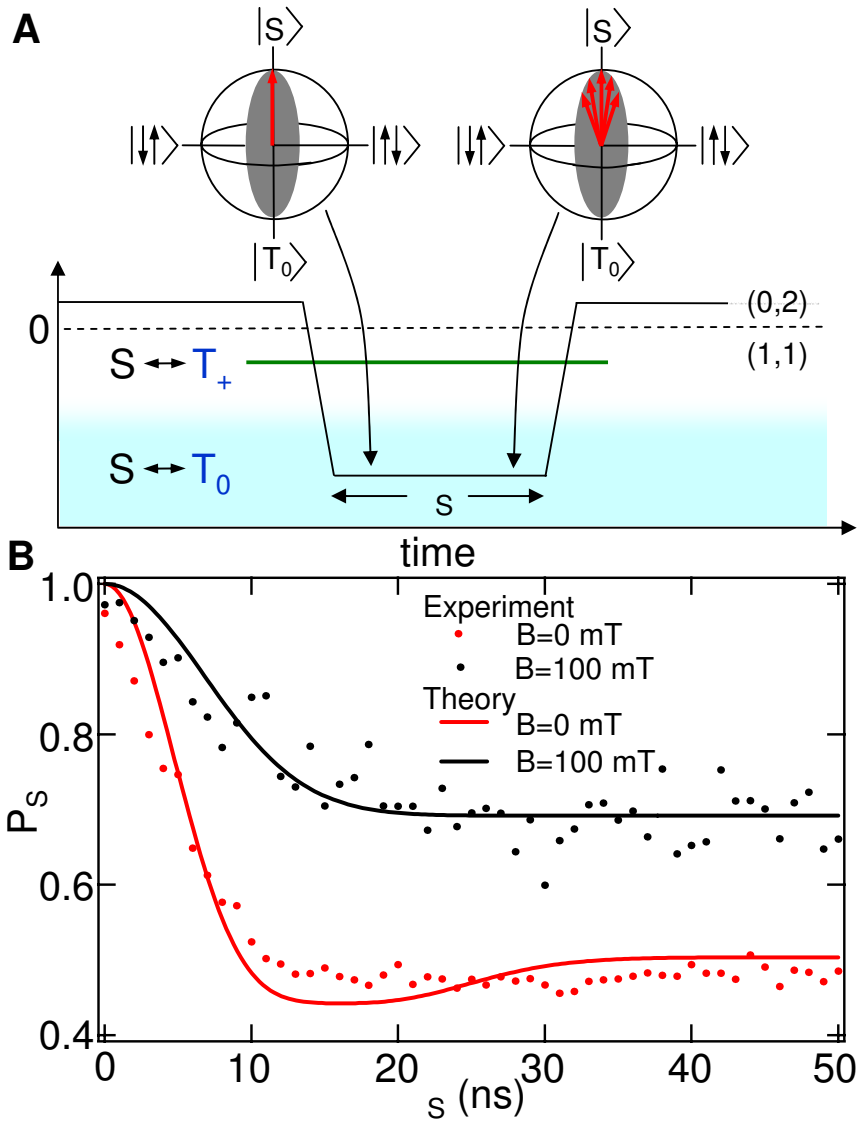

Figure 6.13: (A) Pulse sequence used to measure T_2^*. The system is initialized into (0,2)S and transferred by rapid adiabatic passage to the spatially separated S state (see text). With $T_\pm$ separated by Zeeman field, S and T_0 mix at large detuning (light blue region), where hyperfine fields drive rotations about the x axis in the Bloch sphere. After a separation time τ_S, the state is projected onto (0,2)S. (B) Singlet probability, P_S, measured using the calibrated QPC charge sensor, as a function of τ_S at 100 mT (black curve) and 0 mT (red curve). For $\tau_S \ll T_2^*$, the singlet state does not have ample time to dephase, and P_S ~0. For $\tau_S \gg T_2^*$, P_S ~0.7 at 100 mT and P_S ~0.5 at 0 mT. Semiclassical model of dephasing due to hyperfine coupling [164] predicts $P_S \sim 1/2$ at high field and P_S ~1/3 at zero field. Fits of the model (solid curves), including a parameter adjusting measurement contrast, give T_2^*=10ns and $B_{\rm nuc} = 2.3$ mT.

experimental runs), as relative phase evolution of the separated spins can convert the initial singlet into a triplet, which will not be able to return to (0,2)S. The (0,2)S initial state is prepared each cycle by allowing tunneling to the reservoir with (0,2)S below the Fermi level of the leads, and the (0,2) triplets above. Through a process in which an electron is exchanged with the leads, (0,2)S is prepared. The state is then separated into (1,1) using rapid adiabatic passage, where ϵ is swept from a positive value to a large negative value quickly ($\sim$1 ns) relative to the nuclear mixing time, $\sim \hbar/(g^*\mu_B B_{\rm nuc})$ but slowly compared to the tunnel splitting of the hybridized charge states $\sim \hbar/J(0)$. This yields a separated singlet, S. Following a separation time τ_S the state is projected back onto (0,2)S, again using rapid adiabatic passage, and the system is held at the measurement point for a time $\tau_M \sim$ 5-10 μs $< T_1$.

The average singlet probability measured after a separation time of 200 ns, $P_S(\epsilon,B,\tau_S = 200\text{ns})$, is shown in Fig. 6.7C as a function of detuning at the separation point and applied field [4]. Evident in the data is a funnel-shaped feature where S and T_+ cross (vertical green line in Fig. 6.7B) and are rapidly mixed by hyperfine fields. The degeneracy occurs at $J(\epsilon) = g^*\mu_B B$, allowing $J(\epsilon)$ to be measured (Fig. 6.7D) by mapping the location of this feature in $P_S(\epsilon, B)$. At larger detuning, where $J(\epsilon) < g^*\mu_B B_{\rm nuc}$, the S and T states approach degeneracy and are susceptible to hyperfine mixing, which reduces P_S (light blue area of Fig. 6.7B). When all three degenerate triplet states can mix with S at large detuning, which further reduces P_S compared to the finite field case.

For applications involving the manipulation of entangled pairs of electrons, a relevant question is how long the electrons can be spatially separated before losing phase coherence. We measure this time by varying the singlet separation time τ_S. The time evo-

[4]The separation detuning can be changed by keeping pulse displacements fixed and sweeping the measurement point detuning using dc gates, or by keeping the measurement point fixed and changing pulse parameters.

lution of the average singlet return probability, $P_S(\tau_S)$, measured using the pulse sequence in Fig. 6.13A with ϵ = -6 mV, is shown in Fig. 6.13B. As τ_S increases, P_S decreases from $\sim$1 on a 10 ns timescale, saturating after 20 ns to $P_S \sim 0.5$ (0.7) for B= 0 (100) mT. A semi-classical model of dephasing of the separated singlet was investigated in [164]. It assumes independent quasistatic nuclear fields acting on the two spins [134] and ideal measurement contrast, and yields Gaussian-like decay from $P_S(\tau_S = 0) = 1$ on a timescale to long-time saturating values $P_S(\tau_S \gg T_2^*) = 1/3$ for $B \ll B_{\rm nuc}$ and $P_S(\tau_S \gg T_2^*) = 1/2$ at $B \gg B_{\rm nuc}$. The field dependence reflects the lifting of the triplet degeneracy with external field. Fits to the measured $P_S(\tau_S)$ yield $T_2^* = 10 \pm 1$ ns, corresponding to $B_{\rm nuc} = 2.3$ mT, consistent with previous measurements [96, 14]. An observed $\sim$40% reduction of contrast is treated as a fit parameter. The predicted weak overshoot of P_S for $B = 0$, a remnant of Rabi oscillations [164], is not seen in these data.

As shown above, the singlet state autocorrelation functions we find using the quasi-static approximation agree well with experiment. In particular, experiments measured a gaussian decay of the spin singlet state with a characteristic timescale $T_2^*\sim$10 ns, which agrees with simple estimates of T_2^* based on sample size and GaAs hyperfine coupling parameters. In addition, the field dependence observed in experiment is in good agreement with theory. However, the long τ_S predictions for A_{SS} at both small and large external magnetic field are off by nearly a factor of two. This discrepancy can be explained by reduced measurement contrast due, e.g., to coupling to the nearby Fermi seas. Fast readout of the charge state may improve the measurement efficiency of this setup [61].

6.3.4 Probing the exchange gate through adiabatic techniques

We now indicate how *slow* adiabatic passage at large external magnetic field allows measurement of the results of an exchange gate. In particular, SAP allows for preparation

and measurement of the individual spin eigenstates, $|1/2,-1/2\rangle$ and $|-1/2,1/2\rangle$. An exchange gate leads to partial rotation between these states, where the rotation angle is given by the product of the exchange energy during the gate, j, and the time the exchange energy is non-zero, t_E. Finally, reversing SAP takes the lower energy eigenstate ($|s,-s\rangle$) back to $|(0,2)S\rangle$ while the higher energy eigenstate ($|-s,s\rangle$) is mapped to $|T_0\rangle$, a (1,1) charge state. The final measurement determines whether the final state is the same as the initial state (the (0,2) result) or has changed to the state with the two spins exchanged (the (1,1) result). Thus, preparing the state $|1/2,-1/2\rangle$ and measuring in the same basis distinguishes the results of the exchange-based rotation of the two-spin state. For example, when the probability is 50% for either measurement result, a $\sqrt{\text{SWAP}}$ gate has been performed. When the probability goes to 100% of recovering the higher energy eigenstate (measuring (1,1)), a complete swap of the two spins has occurred (SWAP).

To explain the experiments in more detail, we start by considering the the role of the nuclear field in the procedure. By preparing the system in a state $|s,-s\rangle$ and measuring in the $|s,-s\rangle, |-s,s\rangle$ basis (individual spin basis) the stochastic nature of the hyperfine field does not play a role in the measurement within the QSA. In the $|s,-s\rangle, |-s,s\rangle$ basis, SAP loads into the current lower energy eigenstate of the nuclear spin system, which is $|s,-s\rangle$ and $s=\pm 1/2$ is determined by the current sign of $\hat{\omega}$. After preparing this state, we perform the resonant exchange gate of angle $\theta_E = Jt/\hbar$ where t is the time spent waiting with exchange energy J. This leads to a rotation of the state $|s,-s\rangle$ to

$$|s,-s\rangle \rightarrow \cos(\theta_E/2)|s,-s\rangle - i\sin(\theta_E/2)|-s,s\rangle \ . \tag{6.33}$$

The resulting oscillations demonstrate coherent swap operations, where $\sqrt{\text{SWAP}}$ is a maximally entangling operation; in addition, it operates in a basis rotated $\pi/2$ from the singlet-triplet measurements of the previous section. The measured signal corresponds to the

probability of returning to the lower energy eigenstate, and is given by

$$A_{s,-s}(t) = ||s,-s(t)\rangle\langle s,-s||^2 \quad (6.34)$$

$$= \cos^2(\theta_E/2) \; . \quad (6.35)$$

If the exchange term $j \leq \Omega$, then additional effects due to nuclei would be observed; we evaluate these below.

For comparison, if the final pulse (S' to M) were to occur in the rapid adiabatic regime, this would measure in the $|S\rangle, |T_0\rangle$ basis (singlet-triplet), and while each term would go to either singlet or triplet, the inability to know which state we started in, combined with the system changing from starting in $|s,-s\rangle$ to $|-s,s\rangle$ as the sign of the nuclear field gradient, i.e., $\hat{\omega}$, changes, leads to a total signal with zero contrast when averaged over long times (just 50% triplet and 50% singlet).

We emphasize that the combination of RAP for preparation (prepares $|S\rangle$), SAP for preparation (prepares lower energy eigenstate of the nuclear field, $|\pm\rangle$), RAP for measurement (spin-to-charge in $|S\rangle, |T_0\rangle$ basis) and SAP for measurement (spin-to-charge in current eigenstates of the nuclear field, $|\pm\rangle$), when combined with the exchange gate (rotations of $|\pm\rangle$ to $|\pm\rangle + i|\mp\rangle$) allows for full state tomography in the $|S\rangle, |T_0\rangle$ subspace.

6.3.5 *Spin SWAP and Rabi oscillations in the $\uparrow\downarrow$, basis*

Experiments measured the probability of staying in the lower energy eigenstate, $A_{s,-s}$ as a function of both detuning and exchange time, t_E. Clear oscillations in $A_{s,-s}$ were observed, indicating coherent spin rotations. The dependence of $A_{s,-s}$ on ϵ and t_E was consistent with theoretical predictions calculated using a calibration curve of $j(\epsilon)$ obtained by measuring the S-T_+ resonance condition as a function of Zeeman energy splitting. In the experiments, a contrast of $\sim$45% was obtained. The fastest π-pulse time achieved using

this setup was ∼350 ps. These experiments demonstrated that fast electrical control of $J(\epsilon)$ can be used to coherently manipulate two-electron spin states in the double dot.

By initializing from (0,2)S using slow ramping of detuning, the (1,1) system can be initialized into the ground state of the nuclear field (defined as $\uparrow\downarrow$, see Fig. 6.7D, inset) instead of the singlet state, S. This initialization scheme is illustrated in Fig. 6.14A: after preparing (0,2)S (as described above) detuning is swept to $\epsilon < 0$ slowly relative to tunnel splitting but quickly relative to the nuclear mixing time through the $S - T_+$ degeneracy. The system is then ramped slowly compared to the nuclear mixing time ($\tau_A \sim 1\ \mu\text{s} \gg T_2^*$) to large negative detuning. This slow lowering of J(ϵ) leads to adiabatic following of the initial state S into the state $\uparrow\downarrow$, the ground state of the Hamiltonian with $J = 0$ [5]. Readout follows the same steps in reverse: ramping slowly out of the large detuning region unloads $\uparrow\downarrow$ to S and $\downarrow\uparrow$ to T_0. Then, moving quickly though $S - T_+$ degeneracy and finally projecting onto (0,2)S measures the fraction that was in the state $\uparrow\downarrow$ prior to readout. Once initialized in $\uparrow\downarrow$, the application of a finite exchange J(ϵ) for a time τ_E rotates the spin state about the z axis of the Bloch sphere, in the plane containing $\uparrow\downarrow$ and $\downarrow\uparrow$, through an angle $\phi = J(\epsilon)\tau_E/\hbar$. The case $J(\epsilon)\tau_E/\hbar = \pi$ constitutes a SWAP operation, rotating the state $\uparrow\downarrow$ into the state $\downarrow\uparrow$.

Figure 6.14B shows $P_S(\epsilon, \tau_E)$ oscillating as both a function of τ_E and ϵ with minima of the singlet probability corresponding to $J = \pi$, 3π, 5π,.... The inset shows theoretical predictions $P_S = \{1 + \cos[J(\epsilon)\tau_E/\hbar]\}/2$ using values for $J(\epsilon)$ obtained independently from the $S - T_+$ resonance measurement as in Fig. 6.7C. In Fig. 6.14C we plot exchange oscillations at the four values of detuning marked by the dashed lines in Fig. 6.14B. Data are fit using an exponentially damped cosine with offset, amplitude, decay time, and phase as fit

[5] We have verified that the system is in the ground state of the nuclear fields by varying the pulse parameters τ_S and $\tau_{S'}$. No dependence on these parameters is observed when varied as in the singlet-triplet spin echo measurements.

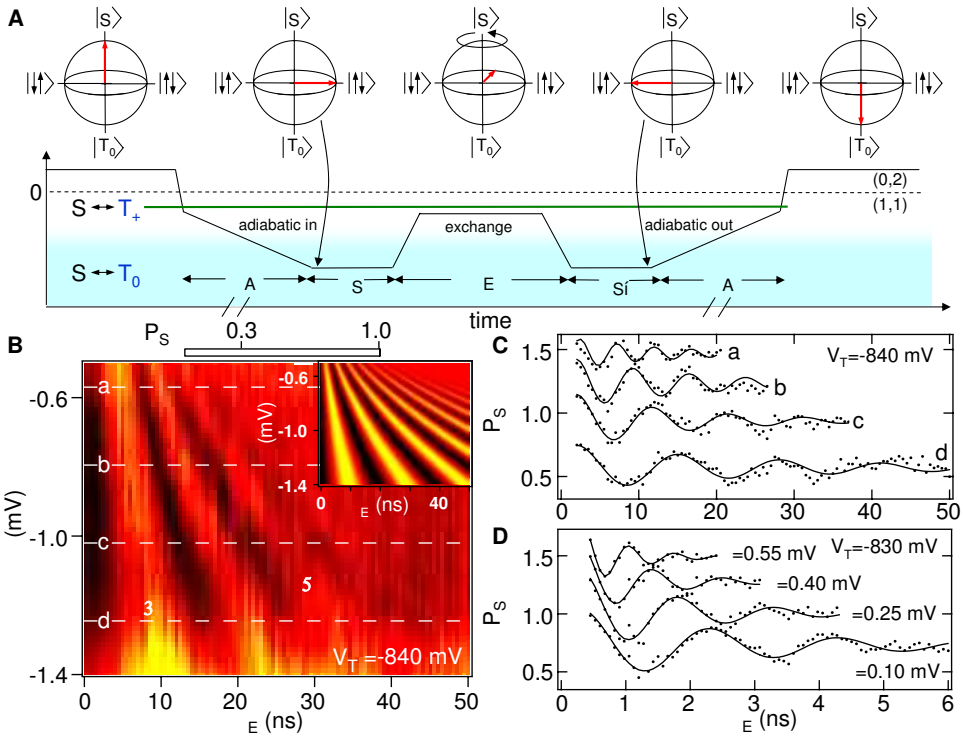

Figure 6.14: (A) Pulse sequence demonstrating exchange control. After initializing into (0,2)S, detuning ϵ is swept adiabatically with respect to tunnel coupling through the $S-T_+$ resonance (quickly relative to $S-T_+$ mixing) , followed by a slow ramp ($\tau_A \sim 1$ μs) to large detuning, loading the system in the ground state of the nuclear fields $\uparrow\downarrow$. An exchange pulse of duration τ_E rotates the system about the z axis in the Bloch sphere from $\uparrow\downarrow$ to $\downarrow\uparrow$. Reversing the slow adiabatic passage allows the projection onto (0,2)S to distinguish states $\uparrow\downarrow$ and $\downarrow\uparrow$ after time τ_E. Typically, τ_S=$\tau_{S'}$=50 ns. (B) P_S as a function of detuning and τ_E. The z-axis rotation angle $\phi = J(\epsilon)\tau_E/\hbar$ results in oscillations in P_S as a function of both ϵ and τ_E. Inset: Model of P_S using $J(\epsilon)$ extracted from $S-T_+$ resonance condition assuming $g^* = -0.44$ and ideal measurement contrast (from 0 to 1). (C) Rabi oscillations measured in P_S at four values of detuning indicated by the dashed lines in (B). Fits to exponentially damped cosine function with amplitude, phase, and decay time as free parameters (solid curves). Curves are offset by 0.3 for clarity. (D) Faster Rabi oscillations are obtained by increasing tunnel coupling and by increasing detuning to positive values, resulting in π-pulse time of $\sim$300 ps.

parameters. To achieve faster π-pulse times, $J(\epsilon)$ can be increased by setting V_T to increase interdot tunnel coupling and by moving to less negative (or even positive) detunings during the exchange pulse (Fig. 6.14D). The fastest π-pulse time obtained using these methods is ~ 300 ps [6].

We note that the observed decay time of Rabi oscillations is proportional to the Rabi period, suggesting that dephasing scales with the value of $J(\epsilon)$ during the exchange pulse, and may reflect gate noise during the τ_E interval. The contrast ($\sim$45%) seen in Figs. 6.14B,C is consistent with the contrast obtained in the singlet separation measurement of T_2^*.

6.3.6 Errors in exchange gates

The primary error in exchange gates is likely due to charge-based dephasing and is directly related to the parametric dependence of the exchange energy, J, on gate voltages near the charge transition. In addition, other errors are possible due to the stochastic nature of the nuclear field. For example, there is the possibility that the current value of the field gradient frequency, $\hat{\omega}$, is sufficiently small to make the initial and final transfer stages non-adiabatic. Also, the gradient can flip sign in the course of the experiment. Finally, finite residual exchange interaction during SAP reduces effectiveness. We consider each of these in turn below.

In the far detuned regime, the energy gap between the (1,1) singlet/triplet space and higher orbital states, as well as (2,0) and (0,2) charge states, is large (of order υ, the orbital level spacing of a single dot, and $E_c/2$, the single dot charging energy, respectively). At dilution refrigerator temperatures, this energy gap is many times greater than $k_b T$, and absorption of a quanta of energy from the environment leading to incoherent excitation

[6] Two synchronized Tektronix AWG710B pulse generators are used for the fast Rabi measurements.

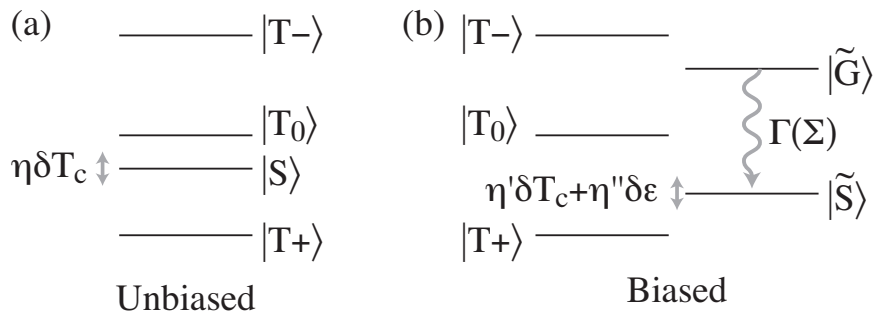

Figure 6.15: Level structures of the double dot system in the (a) far detuned regime, with charge dephasing shown, and (b) near the charge transition with charge-based decay and dephasing.

may be neglected. Also in this regime, the residual exchange splitting is both numerically small and insensitive to first order fluctuations in detuning, ϵ, leading to little charge-based dephasing due to differential coupling of the $|S\rangle$ state to the doubly occupied states when compared to the $|T_m\rangle$ states' couplings to doubly occupied states. The system remains sensitive to charge-based dephasing up to second order due variations in the tunnel coupling, t. If we can write variations of t from the mean as δt, its correlation function is given generally by

$$\langle \delta t(u+\tau)\delta t(u)\rangle = \hbar^2 \int d\omega \; S_t(\omega) e^{i\omega\tau} \; . \tag{6.36}$$

The corresponding phase noise term in the Hamiltonian is $V_{11} = \eta\delta t(u)(\sum_m |T_m\rangle\langle T_m| - |S\rangle\langle S|)/2$ where $\eta = \frac{8tJ}{E_c^2} \lesssim 10^{-3}$, again using $E_c = 5$ meV, $J = 0.3$ meV, and $\langle t\rangle = 0.01$ meV.

As an example, a coherence between the $|S\rangle$ and $|T_m\rangle$ subspace in the far detuned regime could be expected to decay due to the noise on t according to

$$\langle e^{-\frac{i\eta}{\hbar}\int_0^\tau du'\delta t(u')}\rangle = \exp(-\eta^2 \int d\omega \; S_t(\omega) \frac{\sin^2(\tau\omega/2)}{(\omega/2)^2}) \tag{6.37}$$

While we consider a variety of noise sources in Appendix C.2, it is instructive here to take the case of white noise spectrum with $S_t = \gamma_0/2\pi$. It leads to exponential decay of

coherences between $|S\rangle$ and states of the $|T_m\rangle$ subspace with a constant $\gamma_t = \eta^2\gamma_0$. In general, as $\eta \ll 1$, this decay will be negligible.

The charge transition will have stronger dephasing when compared with the far detuned regime. In addition to inelastic decay of the excited adiabatic state to the ground adiabatic state, the system is susceptible to fluctuations in both ϵ and t, as J is potentially large and strongly dependent on gate parameters. In so far as the power spectra associated with t and ϵ have no appreciable spectral components at frequencies of order $\mathcal{E}$, the excitation/relaxation terms between $|\tilde{G}\rangle$ and $|\tilde{S}\rangle$ may be neglected. Then we may restrict considerations to dephasing of coherence between the subspace of $|T_m\rangle$ and the state $|\tilde{S}\rangle$, and write the effective Hamiltonian as

$$V_{11-02} = [\eta'\delta t(\tau) + \eta''\delta\epsilon(\tau)][\sum_m |T_m\rangle\langle T_m| - |\tilde{S}\rangle\langle\tilde{S}|]/2 \tag{6.38}$$

with $\eta' = \frac{2t}{\epsilon/2+\mathcal{E}}$ and $\eta'' = \frac{1}{2}(1+\frac{\epsilon}{\epsilon/2+\mathcal{E}})$. The accompanying noise is given again by Eqn. 6.37, but with $\eta = \sqrt{(\eta')^2 + (\eta'')^2}$ and the power spectrum replaced with

$$S_{11-02}(\omega) = \left(\frac{\eta'}{\eta}\right)^2 S_t(\omega) + \left(\frac{\eta''}{\eta}\right)^2 S_\epsilon(\omega) \tag{6.39}$$

While η' may be small ($\eta \ll 1$), near the charge transition η'' is of order unity. This indicates that noise in the detuning parameter ϵ has significant repercussions for coherences between singlet and triplet states during exchange gate operation.

We consider charge-based dephasing for the exchange gate according to Eqn. 6.37. In all cases we assume the spectral function has a high-frequency cutoff γ such that $\gamma \ll J$. This assumption prevents dephasing noise from producing population changes (relaxation) due to energy conservation. Additionally, we rewrite the expected probability of maintaining phase coherence (Eqn. 6.37) as

$$\exp(-\eta^2 P) \tag{6.40}$$

where $P = \int d\omega\ S(\omega)\frac{\sin^2(\tau_E\omega/2)}{(\omega/2)^2}$ is set by the spectral function and the time of the exchange gate, τ_E. This allows separation of the interaction strength (η) and the noise spectrum. Each spectrum considered has a normalization parameter ν such that $S(\omega)$ has units of inverse time.

We note that in general, the number of observable exchange oscillations will be limited by these dephasing processes. By finding $T_2 = P^{-1}(\eta^{-2})$ the observable number of oscillations goes as $T_2 J/\hbar$. When, for example, $S(\omega) = \Gamma/2\pi$, we may easily invert $P(t)$ and find $T_2 = \eta^{-2}/\Gamma$.

Comparing the behavior of the ohmic and super-ohmic cases to the $1/f$ case (see Appendix C.2), the limiting value of P for the super-ohmic case and the power law tail of the ohmic decay indicates that for small coupling parameter η, the super-exponential $1/f$ terms (going as a gaussian) will dominate at long times. For very short interaction times, all three will be less than the white noise contribution, which goes linearly in time. The different behaviors are shown in Fig. 6.16. Comparing to Ref. [151], it seems likely that 1/f and white noise terms contribute most to the observed decay of oscillations in the experiment.

This indicates that electrical control of exchange interactions in double dot systems may be relatively robust with respect to nuclear spin degrees of freedom. However, during the exchange gate, the system is susceptible to charge-related dephasing. The observed decay of oscillations of Ref. [151], in which the decay rate appears to match the exchange energy such that the number of exchange oscillations observed is independent of the detuning, is qualitatively similar to the behavior of oscillations in the presence of sub-ohmic noise. A more detailed experimental analysis of the noise will be required before a direct comparison between experiment and theory will be possible.

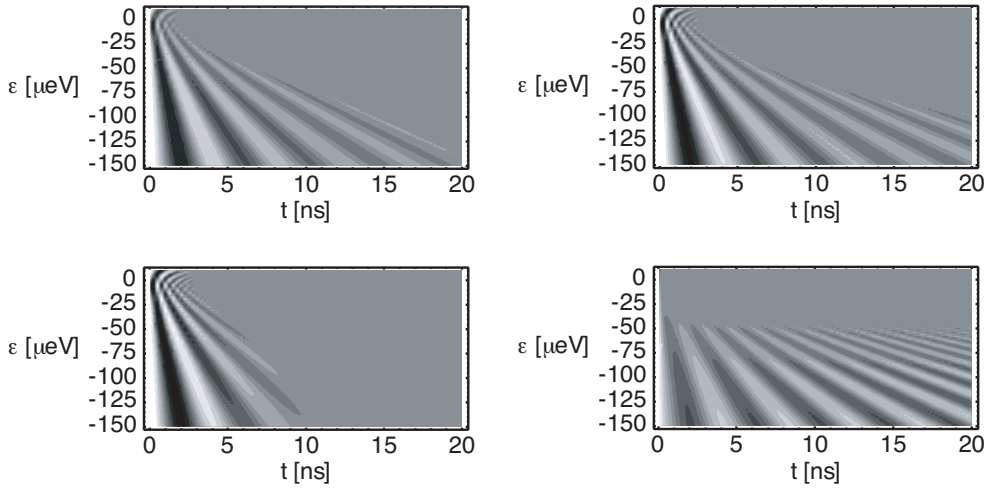

Figure 6.16: Decay of exchange oscillations for the four scenarios (clockwise from lower left): white noise, $1/f$, ohmic, and super-ohmic (ω^2). White corresponds to probability 1 of ending in the initial state $|s, -s\rangle$ after exchange interaction is on for a time τ_E (bottom axis), while black is probabiliy 0 of ending in the initial state. Tunnel coupling is taken to be 10 μeV, and the spectral density (ν) is chosen for similar behavior near $\epsilon = 50$ μeV. Note that $1/f$ terms increase decay in the slow oscillation limit, while increasing powers of ω (white noise=0, ohmic = 1, super-ohmic = 2) lead to more oscillations for smaller exchange energies.

6.4 Exchange gates and echo techniques

The techniques of rapid adiabatic passage, slow adiabatic passage, and time-resolved control of the exchange interaction in the previous section have far reaching consequences. In this section, we consider how exchange gates can undo the effect of the quasi-static nuclear field, greatly reducing the deleritous effects of nuclear spins on electron spin coherences.

6.4.1 Spin-echo in the singlet-triplet basis

Since the nuclear fields vary slowly on timescales compared to a typical pulse cycle time, a spin-echo pulse sequence can be used to refocus the spin singlet state. A spin-echo pulse sequence based on fast electrical control of the exchange interaction was demonstrated in Ref. [151]. The experiment starts by using RAP to transfer $|(0,2)S\rangle$ to $|S\rangle$, preparing a separated singlet pair of electron spins. As demonstrated in the T_2^* experiment, the hyperfine interaction mixes the singlet and triplet states on a 10 ns time scale. After a separation time t_S, a π exchange pulse (SWAP) is performed by adjusting the detuning to a region with a finite exchange energy. The exchange energy is then set to zero by moving to the far detuned regime for a time $t_{S'}$, during which the singlet state refocuses.

The dephasing due to hyperfine interactions occurs by producing a relative, unknown phase between $|\uparrow\downarrow\rangle$ and $|\downarrow\uparrow\rangle$. Switching between these two states via exchange gates will produce an echo (recovery of the original state, $|S\rangle$) if the waiting time before and after the SWAP operation is the same. In other words, the pseudo-spin of $|S\rangle$ and $|T_0\rangle$ (the $m_s = 0$ subspace) is amenable to echo techniques using exchange interactions.

We will use the pulse sequence of Fig. 6.12c. In the far detuned regime at finite field, $|S\rangle$ and $|T_0\rangle$ mix due to nuclei, as per the Hamiltonian of Eqn. 6.13. This mixing is

driven by a relative constant, but unknown, energy, corresponding to the current value of

$$\hbar\hat{\omega} = g^*\mu_B(\hat{B}_{\mathrm{nuc},l,z} - \hat{B}_{\mathrm{nuc},r,z}) \ . \tag{6.41}$$

It is convenient to rewrite the Hamiltonian (Eqn. 6.13) using Pauli matrices with states $|S\rangle, |T_0\rangle$ as a psuedo-spin, in our logical basis defined above (recall that $\sigma_z = |T_0\rangle\langle T_0| - |S\rangle\langle S|$). For these two states, the effect of nuclei is given by the effective Hamiltonian

$$H_{eff} = \hbar\hat{\omega}\hat{\sigma}_x/2 \ . \tag{6.42}$$

For example, using the T_2^* pulse sequence (Fig. 6.12a), the probability of ending in the singlet as a function of τ_S is

$$\mathrm{Tr}_{\mathrm{nuc}}\left[\left|\langle 0|e^{-i\tau_S\hat{\omega}\hat{\sigma}_x/2}|0\rangle\right|^2\right] \ . \tag{6.43}$$

If the system starts in the $|S\rangle$ state, evolution of the system is governed by the propagator $U_{\mathrm{nuc}}(t) = e^{-it\hat{\omega}\hat{\sigma}_x/2}$, and measurement yields the probability of returning to the singlet state. This is immediately evaluated to give $\mathrm{Tr}_{\mathrm{nuc}}[|\cos(\hat{\omega}\tau_S/2)|^2] = \frac{1}{2}[1 + \exp(-\langle\omega^2\rangle\tau_S^2/2)]$. As should be expected, this duplicates the result of the previous section.

Now, we consider how this result changes with the more complex sequence given by Fig. 6.12c, in particular its dependence on τ_E and $\tau_{S'}$. If $\tau_E = 0$, then nothing has changed from before, except now the system evolves according to $U_{\mathrm{nuc}}(\tau_{S'})U_{\mathrm{nuc}}(\tau_S) = U_{\mathrm{nuc}}(\tau_S + \tau_{S'})$. However, what happens with finite τ_E?

For our reduced two-level system, when $\tau_E \neq 0$ the effective Hamiltonian during this stage is given by

$$H_{eff,E} = \hbar\hat{\omega}\hat{\sigma}_x/2 + J(\epsilon_E)\hat{\sigma}_z/2 \ . \tag{6.44}$$

Taking the turn-on of finite J to be instananeous, the total evolution operator is

$$U(\tau_{S'}, \tau_E, \tau_S) = U_{\mathrm{nuc}}(\tau_{S'})\exp(-iH_{eff,E}\tau_E/\hbar)U_{\mathrm{nuc}}(\tau_S) \ . \tag{6.45}$$

When the exchange energy for the middle point satisfies $J(\epsilon_E) \gg \gamma_e B_{\rm nuc}$, we approximate the middle term of the evolution operator by $U_E(\tau_E) \approx \exp(-i\tau_E J(\epsilon_E)\hat{\sigma}_z/2\hbar)$.

At the end of the pulse sequence, the probability of returning to the state $|(0,2)S\rangle$ (C) is given by

$$C = \mathrm{Tr}_{\rm nuc}\left[\left|\langle 0|e^{-i\tau_{S'}\hat{\omega}\hat{\sigma}_x/2}e^{-i\tau_E J(\epsilon_E)\hat{\sigma}_z/2\hbar}e^{-i\tau_S\hat{\omega}\hat{\sigma}_x/2}|0\rangle\right|^2\right] . \tag{6.46}$$

To see the analogy between this evolution and a spin echo experiment, we insert unity after the initial ket, i.e., $|0\rangle = e^{iJ(\epsilon_E)\hat{\sigma}_z/2\hbar}e^{-iJ(\epsilon_E)(-1)/2\hbar}|0\rangle$, as 0 is the -1 eigenstate of σ_z. The overall phase is irrelevant due to the absolute value terms, and so we rewrite the above as

$$C = \mathrm{Tr}_{\rm nuc}\left[\left|\langle 0|e^{-i\tau_{S'}\hat{\omega}\hat{\sigma}_x/2}\left(e^{-i\tau_E J(\epsilon_E)\hat{\sigma}_z/2\hbar}e^{-i\tau_S\hat{\omega}\hat{\sigma}_x/2}e^{i\tau_E J(\epsilon_E)\hat{\sigma}_z/2\hbar}\right)|0\rangle\right|^2\right] . \tag{6.47}$$

The term in parenthesis, an exchange gate, is a rotation of angle $\theta_E = \tau_E J(\epsilon_E)/\hbar$ about the z axis of the psuedo-spin. It acts on the operator $U_{nuc}(\tau_S) = e^{-i\tau_S\hat{\omega}\hat{\sigma}_x/2}$, flipping the sign of the σ_x operator when $\theta_E = \pi$ (SWAP).

We can probe its effects by analogy with standard spin echo. For example, when $\theta_E = \pi$, we get $C = \frac{1}{2}[1 + \exp(-\langle\omega^2\rangle(\tau_S - \tau_{S'})^2/2)]$. This means the dephasing due to nuclei in the first half of the sequence is exactly undone when the rephasing time is equal ($\tau_S = \tau_{S'}$). For fixed $\tau_S + \tau_{S'}$, the probability of returning to the singlet state as a function of $\tau_S - \tau_{S'}$ and τ_E should exhibit 50% mixing expected for dephasing when $|\tau_S - \tau_{S'}| > T_2^*$, and when $\tau_E J/\hbar$ is not an odd integer multiple of π. For example, setting $\tau_S + \tau_{S'} = 100$ ns, and using ϵ_E such that $J(\epsilon_E) = \hbar\gamma_e(20\text{ mT})$, the probability exhibits this behavior (as shown in Fig. 6.17).

In practice, the instantaneous approximation breaks down in realistic situations, as does the $J \gg \gamma_e B_{\rm nuc}$ assumption. The former is easily fixed by noting that such a "Rabi" type pulse only has sensitivity to the integrated area, i.e., $\theta = \int J(\epsilon(t))dt$. The latter requires working with finite $\tau_E\Omega$. This effect has been considered in detail elsewhere [182].

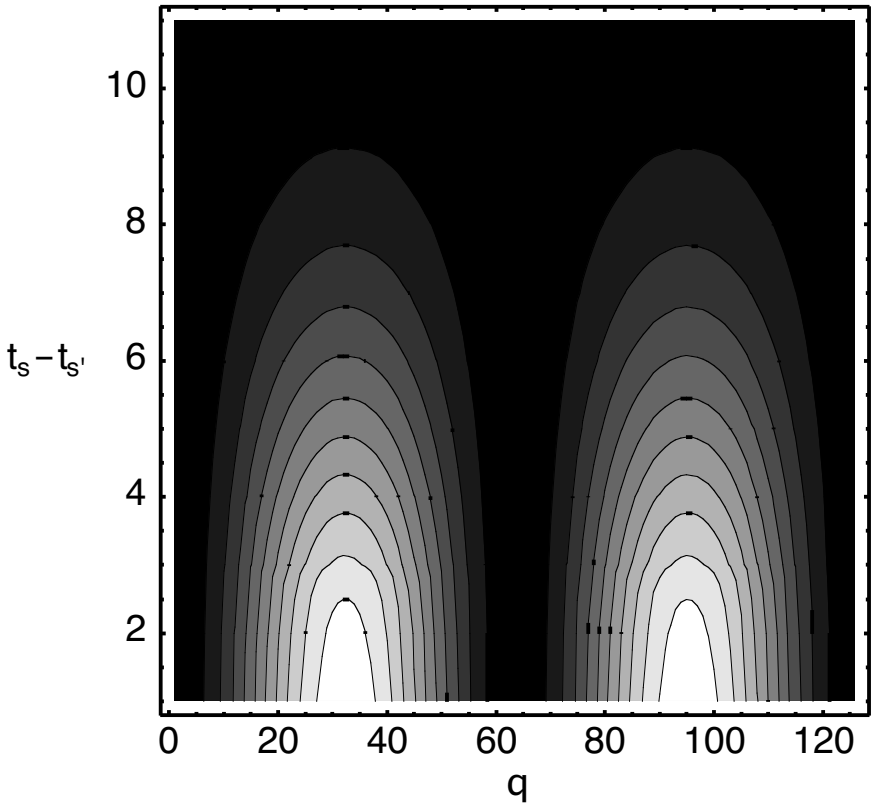

Figure 6.17: Expected signal (probability of returning to the singlet state) using the pulse sequence in Fig. 6.12c for fixed $\tau_S + \tau_{S'}$ and as a function of $\tau_S - \tau_{S'}$ and τ_E. The exchange energy j is taken to be 1.5 μeV. White indicates probability 1 that we end in (1,1)S; black is probability 1/2 that we end in (1,1)S.

6.4.2 *Singlet-triplet spin echo: experiment*

Voltage controlled exchange provides a means of refocusing the separated singlet to undo dephasing due to the local hyperfine fields. The pulse sequence is shown in Fig. 6.18A and is similar to refocusing sequences used in NMR [168, 191]. The separated singlet, S, will dephase at large negative detuning ($J(\epsilon) \sim 0$) due to local hyperfine fields after a separation time τ_S. In the Bloch sphere representation, hyperfine dephasing results in a rotation by a random, nuclear-field-dependent angle about the x axis. Thus in each given run the Bloch vector rotates by a random amount about the x axis. The dephased (1,1) state can be refocused to S by applying a pulse of finite exchange J(ϵ) for a time τ_E, where $J(\epsilon)\tau_E/\hbar = \pi$, 3π, 5π,..., which rotates the Bloch vector around the z axis by an angle π, 3π, 5π,..., and waiting for a time $\tau_{S'} = \tau_S$.

The singlet probability $P_S(\epsilon, \tau_E)$ measured using the spin-echo sequence (Fig. 6.18A) is shown as a function of detuning and τ_E in Fig. 6.18B. Singlet recoveries (black regions) are observed for π, 3π, and 5π exchange pulses. A plot of the theoretical prediction $P_S = \{3-\cos[J(\epsilon)\tau_E/\hbar]\}/4$ (Fig. 6.18B, inset) using values for $J(\epsilon)$ measured independently from the $S-T_+$ resonance condition compares well with experiment. We note greater noise in these data than in Fig. 6.14. We speculate that this noise, which is ~ 100 times noisier than the QPC sensor readout instrument noise, is likely due to slow fluctuations in the nuclear system. Noise from a possibly similar origin was recently observed in dc transport through a double quantum dot system [112]. Figure 6.18C shows P_S (red) as function of the difference in dephasing and rephasing times, $\tau_S - \tau_{S'}$, for increasing values of the total time spent at large detuning, $\tau_S + \tau_{S'}$, averaged over 10 data sets. The finite saturation value for P_S reflects the reduced measurement contrast. Differences in τ_S and $\tau_{S'}$ result in imperfect refocusing and decrease the recovery amplitude on a characteristic timescale $\tau_S - \tau_{S'} = T_2^*$.

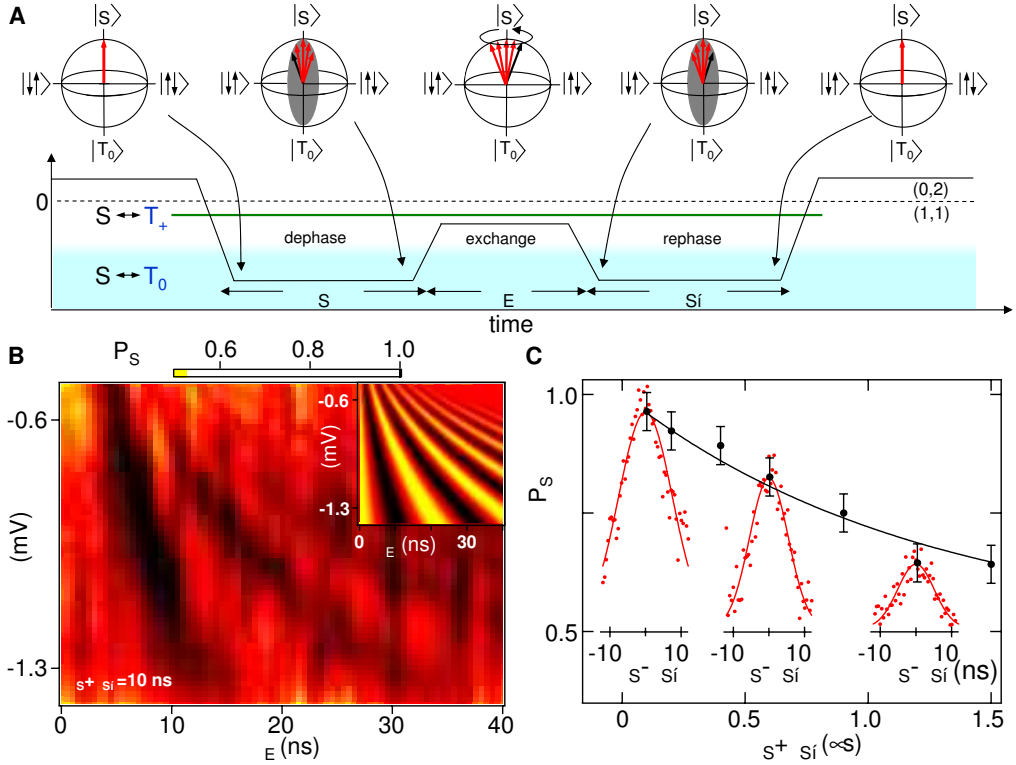

Figure 6.18: (A) Spin echo pulse sequence. System is initialized in (0,2)S and transferred to S by rapid adiabatic passage. After a time τ_S at large negative detuning, S has dephased into a mixture of S and T_0 due to hyperfine interactions. A z axis π-pulse is performed by making detuning less negative, moving to a region with sizable $J(\epsilon)$ for a time τ_E. Pulsing back to negative detunings for a time $\tau_{S'} = \tau_S$ refocuses the spin singlet. (B) P_S as a function of detuning and τ_E. The z-axis rotation angle $\phi = J(\epsilon)\tau_E/\hbar$ results in oscillations in P_S as a function of both ϵ and τ_E. Inset: Model of P_S using $J(\epsilon)$ extracted from the $S - T_+$ resonance condition assuming $g^* = -0.44$ and ideal measurement contrast (from 0.5 to 1). (C) Echo recovery amplitude, P_S, plotted as a function of $\tau_S - \tau_{S'}$ for increasing $\tau_S + \tau_{S'}$ (red points), along with fits to a Gaussian with adjustable height and width. Best fit width gives $T_2^* = 9$ ns, consistent with the value T_2^*= 10 ns obtained from singlet decay measurements (Fig. 6.13B). Best fit heights (black points) along with exponential fit to the peak height decay (black curve) give a lower bound on the coherence time T_2 of 1.2 μs.

For each value of $\tau_S + \tau_{S'}$, the data are fit to a Gaussian form giving $T_2^* = 9 \pm 2$ ns, consistent with measurements of the singlet decay discussed above. The best fit heights for each $\tau_S + \tau_{S'}$ time are plotted as the black data points in Fig. 6.18C. A fit to an exponential decay with an adjustable offset to correct for the finite measurement contrast gives a characteristic coherence time of 1.2 μs, which sets a lower bound on T_2. Comparing measured values of T_2^* and this bound on T_2, we note that a simple spin echo sequence extends the coherence time of a spatially separated singlet by more than a factor of 100. We find that two spin echo pulse sequences applied in series (Carr-Purcell) extends the bound on T_2 by at least another factor of two. The coherence time of our qubit using the simple spin echo sequence exceeds the SWAP operation time by a factor of ~ 8000. We note that since the echo sequence relies on gate-voltage control of $J(\epsilon)$, it is susceptible to charge dephasing during the exchange pulse. The interplay between charge dephasing during the exchange pulse and dephasing due to nuclear processes warrants further investigation [39].

6.4.3 Probing nuclear spin dynamics through echo techniques

So far the analysis has worked entirely within the QSA. However, the echo sequence in principle reveals higher order dynamical information about the nuclear field and other noise sources. Rewriting the Hamiltonian as $H = \hbar\Omega\hat{A}_z(t)\sigma_x/2$ where $\hat{A}_z = \hat{A}_{z,l} - \hat{A}_{z,r}$ is the renomalized difference of the two nuclear operators of each dot, and has the spectral function

$$\langle \hat{A}_z(t)\hat{A}_z(t')\rangle = \int d\nu \; S(\nu)e^{i\nu(t-t')} \; , \tag{6.48}$$

allows a large range of possible noise sources and correlation functions to be considered. Assuming (for the moment) that the exchange gate is of high fidelity and insensitive to the

current value of $\omega = \Omega \hat{A}_z$, the measured result of the echo sequence is given by

$$\begin{aligned} C &= |\langle 0_L| \exp(i \int_{t_S}^{t_S+t_{S'}} \Omega \hat{A}_z(t) dt \sigma_x/2 \\ &\quad -i \int_0^{t_S} \Omega \hat{A}_z(t) dt \sigma_x/2) |0_L\rangle|^2 \qquad (6.49) \\ &= \cos^2[(\int_{t_S}^{t_S+t_{S'}} \Omega \hat{A}_z(t) dt + \int_0^{t_S} \Omega \hat{A}_z(t) dt)/2] \qquad (6.50) \\ &= \frac{1}{4}[e^{-i\Omega\Xi} + e^{i\Omega\Xi} + 2] \qquad (6.51) \\ &= \frac{1}{2}[e^{-\Omega^2\langle\Xi^2\rangle/2} + 1] \qquad (6.52) \end{aligned}$$

where $\Xi = \int_{t_S}^{t_S+t_{S'}} \hat{A}_z(t) dt + \int_0^{t_S} \hat{A}_z(t) dt$. The second moment of Ξ is

$$\langle \Xi^2 \rangle = \langle \Xi_{S'}^2 \rangle + \langle \Xi_S^2 \rangle - 2\langle \Xi_{S'} \Xi_S \rangle \qquad (6.53)$$

with $\langle \Xi_{S'}^2 \rangle = \int d\nu \; S(\nu) \frac{4}{\nu^2} \sin^2(t_{S'}\nu/2) \simeq (t_{S'}/T_2^*)^2$ and similarly for Ξ_S. The cross term, corresponding to the correlations between the two frequencies, is

$$2\langle \Xi_{S'} \Xi_S \rangle = \int d\nu \; S(\nu) \frac{\sin(t_S\nu/2)\sin(t_{S'}\nu/2)}{(\nu/2)^2} e^{i(t_S+t_{S'})\nu/2} \; . \qquad (6.54)$$

Finally, when $t_S = t_{S'}$, the second moment is

$$\langle \Xi^2 \rangle = 2 \int d\nu \; S(\nu) \frac{\sin^2(t_S\nu/2)}{(\nu/2)^2} [1 - e^{it_S\nu}] \; . \qquad (6.55)$$

For low frequency noise, with cutoff $\gamma \simeq [\int d\nu \; \nu^2 S(\nu)]^{1/2} \ll 1/t_S$, we obtain $\langle \Xi^2 \rangle \simeq 2(t_S)^2 \times (t_S\gamma)^2$, or decay in the total wait time $2t_S$ with an effective time constant

$$T_{2,SE} = 8^{1/4} (T_2^*/\gamma)^{1/2} \; . \qquad (6.56)$$

Our evaluation has implicitly assumed that above the cutoff, γ, $S(\omega)$ dies off at least as $1/\omega^3$. As indicated in Appendix A, this is appropriate for interaction times on the order of microseconds—initial decay of the nuclear spin correlation function is quadratic. For longer interaction times, different decay (going as $\exp(-t^3)$ would be observed.

Our predicted decay is consistent with the experiments of Ref. [151]. In appendix A we derive γ due to electron spin-mediated nuclear spin exchange to be of order 10 ms^{-1}, giving $T_{2,SE} = 2$ μs. However, addition exponential decay could be observed if the high frequency cut-off assumed above has a too-slow decay, going as $\omega^{-2-\epsilon}$ with $\epsilon < 1$. Furthermore, higher order pulse sequences, such as Carr-Purcell, will likely allow for extensions of the echo signal to substanially longer times.

The experiments discussed in the previous sections demonstrate that the hyperfine interaction is efficient at dephasing an intially prepared spin singlet state on a 10 ns timescale. By using a simple spin-echo pulse sequence, this bare dephasing time was extended by over a factor of 100, to times $T_2 > 1.2\mu$s. Further experimental effort will be required to fully map out the nuclear correlation function and extend the lower bound on electron spin coherence times.

6.5 Conclusions

We have shown how a model combining charge and spin interactions for two-electrons in a double quantum dot effectively describes the experimental results of Refs. [96, 151]. By starting with the case of a single electron in a single dot, we developed the quasi-static approximation, and considered its applicability to describing current experimental results.

The spin interactions with nuclear spins are extended to the double dot case, and two regimes emerge: the far detuned regime, in which two electrons are in separate dots and interact with independent nuclear fields, and the charge transition, in which the two electrons may transition from a separated orbital state to a doubly-occupied, single-dot state.

This model was used to describe spin blockade, and we found spin blockade is broken by interactions with nuclei near zero magnetic field, explaining the experimental results of Johnson *et al.* (Ref. [96]). A striking magnetic field dependance is derived, consistent with observed experimental behavior. This indicates that the dominant mechanism for spin blockade at finite magnetic field is trapping of the $m_s = \pm 1$ separated spin states, as their mixing with the charge-transition-allowed singlet $|G\rangle$ is suppressed by finite Zeeman splitting. Observation of the breaking of spin blockade near zero field provides a sensitive measure of the magnitude of the random nuclear-spin-induced magnetic field.

Time-domain control of local potentials, achieved through manipulation of electrostatic depletion gates, provides powerful mechanisms for preparing and measuring spin singlets, as well as eigenstates of the nuclear field. These techniques have been exploited by Petta *et al.* to measure the effective dephasing of a two-spin entangled state, and to probe via coherent oscillations in the $m_s = 0$ two-spin subspace the exchange interaction as controlled by gate voltages [151]. Limiting mechanisms for such oscillations, due to charge fluctuations of indeterminate nature, are considered for a variety of environmental noise spectra.

Finally, we analyzed how controlled exchange interactions can protect the electron spin from the deleritous effect of nuclear spins by working within a two-spin subspace, putting in specific terms protocols previously concieved more generally. We expect the limiting mechanism for the rephasing of the two-spin states comes from corrections to the quasi-static approximation, and as such, spin-echo experiments provide a useful measure of the validity of this approximation.

The authors would like to thank H.-A. Engel, W. Dür, P. Zoller, G. Burkard, and D. Loss for helpful discussions. This work was supported by ARO, NSF, Alfred P. Sloan Foundation, David and Lucile Packard Foundation. For the experiments, we ac-

knowledge useful discussions with Sankar Das Sarma, Hans-Andreas Engel, Xuedong Hu, Daniel Loss, Emmanuel Rashba, and Peter Zoller. Funding was provided through the ARO under DAAD55-98-1-0270 and DAAD19-02-1-0070, the DARPA-QuIST program, the NSF under DMR-0072777, the NSF Career Program, the Harvard Center for Nanoscale Systems, and the Sloan and Packard Foundations.

Chapter 7

Electronic pumping of nuclear spin polarization in a double quantum dot

J. M. Taylor[1], J. R. Petta[1], A. C. Johnson[1], E. A. Laird[1], A. Yacoby[2], M. D. Lukin[1], and C. M. Marcus[1]

[1]Department of Physics, Harvard University, 17 Oxford St., Cambridge, MA 02138
[2]Department of Condensed Matter Physics, Weizmann Institute of Science, Rehovot 76100, Israel

We investigate the controlled polarization of nuclear spins in a double quantum dot by pulsed control of the exchange interaction between two electron spins. We develop a nuclear spin pumping technique and use it to achieve substantial non-equilibrium polarization of the nuclear spins. Furthermore, the single spin-flip process is investigated,allowing for a detailed understanding of the polarization process over a wide range of time scales.

Nuclear spins interacting with electron spins in the solid-state has long been a topic of investigation, from early electron spin-nuclear spin double resonance (ENDOR) experiments [131] to spin-dephasing and relaxation in bulk semiconductors [132]. More recently, advances in fabrication technology and a new theoretical impetus to examine

single electron spin systems from a quantum information science perspective has led to the development of few electron, few quantum dot systems [33, 75, 189, 150]. For these systems, spin interactions between the electron spin and the lattice nuclear spins (such as the Gallium and Arsenide nuclei comprising the semiconductor) lead to substantial dephasing of electron spin states, as observed in recent experiments [14, 151]. However, to date there have been few experimental investigations into the back-action of electron spins upon the nuclear spins of the lattice. Optical studies of self-assembled quantum dots and transport studies in vertical quantum dot structures indicate that substantial polarizations of nuclear spins may be induced, far beyond what might be expected from standard cross-relaxation experiments such as ENDOR [77, 143].

In this work, we investigate the controlled polarization of nuclear spins in a double quantum dot by pulsed control of the exchange interaction between two electron spins. Our approach builds upon techniques developed by our group for previous experiments [96, 151], in which pairs of electron spins are reliable initalized into a singlet state, then brought into interaction with nuclear spins by reducing their exchange energy. Finally, spin-to-charge conversion and nearby electrometers allow for readout of the the results of each controlled interaction.

In more specific terms, we have a means for preparing and measuring separated singlets of electron spin, $|(1,1)S\rangle$. Of particular interest is nuclear-spin mediated mixing between $|(1,1)S\rangle$ and the lowest energy Zeeman-split state of the triplet, $|(1,1)T_-\rangle$. This mixing occurs when the Zeeman energy matches the exchange energy of the double dot. Finding the electrons in the singlet after interaction indicates that the electron spin state remained a singlet; otherwise, an electron spin had to have flipped down. Spin conservation requires that each electron spin flip is accompanied by a simultaneous nuclear spin flip. By cycling the electrons many times, a substantial nuclear spin polarization can be established.

We investigate both time-dynamics of the spin flip process and the limits to polarization.

7.1 Experimental setup

Experiments were performed in a dilution refridgerator with an electron temperature $\sim$ 135 mK. A double quantum dot was formed by charging depletion gates on the surface of a two-dimensional electron gas heterostructure (Fig. 7.1a). A nearby quantum point contact, operated near the first conductance plateau, has a conductance g that depends upon the local electric field produced by the electrons in the double quantum dot. Thus, the conductance g through the QPC is a direct measure of the charge state of the double dot system. This approach has been detailed in Refs. [150, 152, 96, 151]. Additionally, a superconducting magnet produced a controlled perpendicular external magnetic field, $B_{\rm ext}$.

The double dot system was depleted to the two-electron regime. The absence of charge transitions, indicating that no electrons are in the system) was confirmed by measuring the QPC conductance to large and negative voltages in both V_L and V_R [150, 152]. The total electron number in the double dot was controlled by changing $V_L + V_R$, while the difference, $V_{\rm diag} = V_L - V_R$, determined the relative number of electrons in the left quantum dot versus the right quantum dot. The QPC conductance, corrected for linear coupling to the gates L and R, is shown in Fig. 7.1b near the charge transition from one electron in each dot (1,1) to two electrons on the right (0,2).

The low energy states of the two-electron system near the charge transition consists of two singlets, $|(1,1)S\rangle$ and $|(0,2)S\rangle$, and a triplet, $|(1,1)T_{0,\pm}\rangle$, where S indicates a singlet spin state (Fig. 7.1c and also Chapter 6). When $V_{\rm diag}$ is above the transition, the ground state of the system is (0,2)S. The next (0,2) excited state, a triplet, was measured to have

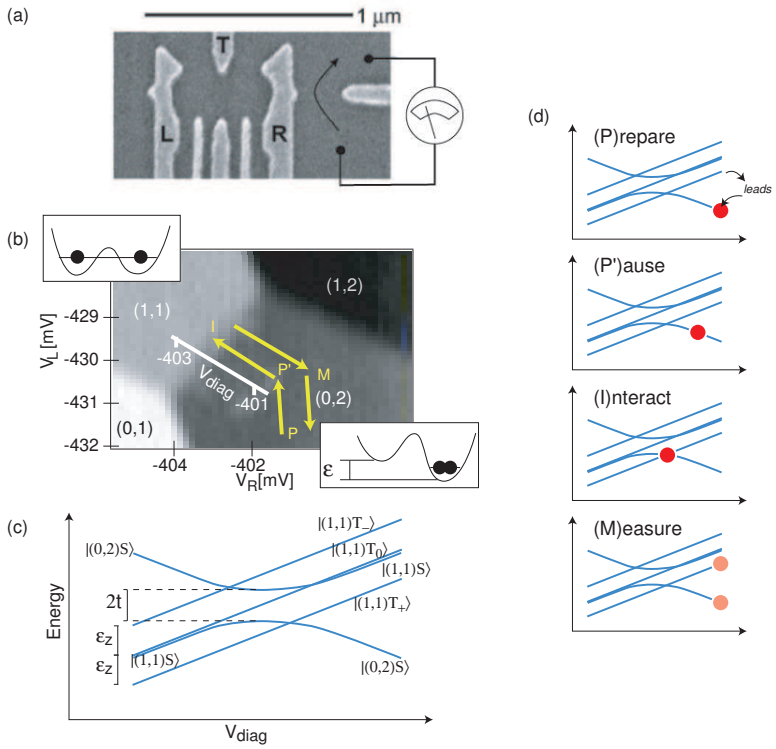

Figure 7.1: Schematic of the experimental setup (a) Electron micrograph of the double dot. The metallic gates (gray) confine electrons in the double dot, while current through a quantum point contact (black arrow) allows direct measurement of the electrostatic configuration of the double-dot system. (b) Charging energy diagram as a function of left (V_L) and right (V_R) gate voltages. Electron numbers in left and right dots are given as (n_L, n_R). During pulse sequences, the gate voltages are controlled together, along the line labelled $V_{\rm diag}$. Increasing $V_{\rm diag}$ leads to a transition from one electron in each dot (shown upper left) to two electrons on the right (lower right); the energy difference between these two states is ϵ. (c) Low energy spin states of the double dot system in the two-electron regime. An avoided crossing occurs between the ground state of the two-electron single dot state $|(0,2)S\rangle$, and the one-electron per dot state $|(1,1)S\rangle$. The triplet of the (1,1), corresponding to the antisymmetric orbital state (shown split by Zeeman energy), has its avoided crossing at a much larger value of $V_{\rm diag}$, corresponding to the introduction of a spin triplet state of (0,2). (d) The pulse sequence used in the experiments. The system is at a point P for a time t_P, where electrons in the metastable triplet state can tunnel to the leads, and the ground state of the double dot (0,2)S is filled. Then $V_{\rm diag}$ is rapidly changed to the point P' for a time $t_{P'}$, near the avoided crossing. This reduces experimental ringing in the pulse sequence. The voltage is then changed to the point I for a time t_I, near the degeneracy between the singlet and the lowest energy state of the Zeeman-split triplet. Finally, the voltage is changed to M for a time $t_M \gg t_P, t_{P'}, t_I$, where the different charge states (1,1) and (0,2) may be measured by the QPC.

a large ($\sim 400\mu$eV) energy spacing from the (0,2)S state at the magnetic fields used ($\lesssim 100$ mT), and is neglected in the following discussion. When $V_{\rm diag}$ was below the transition, the low energy (1,1) singlet and (1,1) triplet are nearly degenerate. At intermediate $V_{\rm diag}$ values, the two singlet states hybridize at the anti-crossing, as shown in Fig. 7.1c. The external magnetic field produces a Zeeman splitting of the $T_\pm$ triplet states of $E_z = \mp g^* \mu_B B_{\rm ext}$. For $g^* = -0.44$, we define T_- to be the lowest energy state of the triplet.

High frequency coaxial lines were connected to two gates (L and R, Fig. 7.1a) allowing for fast manipulation of the local electric field by applying pulses using a Tektronix AWG 520. A pulse sequence is shown in Fig. 7.1d: the system starts with large $V_{\rm diag}$ (point P), and the (0,2) singlet ground state is filled by co-tunneling to the leads in a time $t_P = 400$ ns. Shorter t_P times (< 200 ns) led to a noticeable dependence of the signal on t_P due to imperfect preparation of (0,2)S. A pulse brings the system near the transition (point P'), where it waits for a time $t_{P'} = 100$ ns, allowing for ringing of the pulse to damp before proceeding. Then, a pulse brings the system near the degeneracy between the singlet state (hybridized $|(1,1)S\rangle$ with the $|(0,2)S\rangle$ state) and the lowest energy Zeeman-split state of the triplet, $|(1,1)T_+\rangle$. After waiting for a time t_I, during which the electron spin states may mix by spin flip mechanisms such as hyperfine coupling to lattice nuclei, a final pulse brings the system to point M where the (1,1) triplet is metastable, while the lowest energy singlet is the $|(0,2)S\rangle$ state. At this point, the spin state of the electron has been mapped to the charge state, and waiting for a time t_M at this point allows for the QPC to distinguish between the two states. The pulse sequence is repeated. By integrating the QPC conductance measurement over many pulse cycles, the average probability of returning to the singlet state, $|(0,2)S\rangle$, can be determined. Using bias-T junctions, we can change the DC value of $V_{\rm diag}$ while keeping the high speed changes to $V_{\rm diag}$ fixed. As the P, P', and M points are insensitive to small changes in $V_{\rm diag}$, the observed features discussed below

mainly correspond to physics occurring at the point I.

7.2 Electron spin-nuclear spin interactions

We now consider the interaction at point I of the pulse sequence. The system is initially prepared (at P) in the singlet state, with spin $|S\rangle = (|\uparrow\downarrow\rangle - |\downarrow\uparrow\rangle)/\sqrt{2}$. At the interaction point (I), the singlet becomes near-resonant with the Zeeman-split triplet, $|T_-\rangle = |\downarrow\downarrow\rangle$. Taking into account the hybridization of the (1,1) and (0,2) singlet states, the Hamiltonian in the basis $|S\rangle, |T_-\rangle$ can be written [39] (see also Chapter 6)

$$H = -\begin{pmatrix} J & B^+\cos\theta/\sqrt{2} \\ B^-\cos\theta/\sqrt{2} & B_{\rm ext} + B^z \end{pmatrix} \tag{7.1}$$

where θ is the mixing angle between the (1,1) and (0,2) singlets and

$$J(V_{\rm diag}) = \frac{1}{2}[\kappa(V_{\rm diag} - V_0) - \sqrt{\kappa^2(V_{\rm diag} - V_0)^2 + 4t^2}] \ , \tag{7.2}$$

is the exchange energy. The propotionality constant κ, offset V_0, and tunnel coupling t are determined by fitting below. In the absence of transverse nuclear fields, a degeneracy occurs when the detuning, $\delta = B_{\rm ext} + B^z - J$, is zero, as observed in Fig. 7.3a. The effective nuclear field due to the hyperfine contact interaction is $B^z = B^z_{{\rm nuc},l} + B^z_{{\rm nuc},r}$ and $B^\pm = B^\pm_{{\rm nuc},l} - B^\pm_{{\rm nuc},r}$, where $\vec{B}_{{\rm nuc},l,r} = \sum_{k\in l,r} \lambda_k \vec{I}_k$. [1] Previous experiments with the same device indicate that $B_{\rm nuc} \approx 3$ mT and the number of nuclear spins in one dot is $N \approx 2\times 10^6$.

Near the detuning $\delta = 0$, the transverse field from nuclear spins mediates mixing between $|S\rangle$ and $|T_-\rangle$. Using the quasi-static approximation, the probability of an intial singlet returning to the singlet state as a function of time t_I spent at point I is

$$P_S(t_I) = 1 - \int dB^3 \rho(\vec{B}) \left[\frac{\cos^2\theta\{B_+, B_-\}_+}{2\omega^2}\sin^2(\omega t_I/2)\right] \tag{7.3}$$

[1] While $B^{z,\pm}$ are operators, in the large N and high temperature limit, we will treat them as classical random variables with an rms $B_{\rm nuc} \approx 4.0/\sqrt{N}$ Tesla in a quasi-static approximation [164, 134] (and also Appendix A), where N is the number of nuclear spins in one of the dots.

where $\omega = \frac{1}{2}\sqrt{\delta^2 + \cos^2\theta\{B_+, B_-\}_+}$ and $\rho(\vec{B})$ is the distribution of possible values of $\vec{B}$. We expect dynamics to occur on a time scale given by the average Overhauser-induced Larmor precession frequency, $\Omega_{\rm nuc} = g^*\mu_B \cos\theta\sqrt{\langle\{B_+, B_-\}_+\rangle}/2 \approx 0.1$ ns^{-1}.

Using our experimental setup, we measured $P_T = 1 - P_S(t_I)$ (c.f. Eq. 7.3). Setting $t_M = 16$ μs to have minimal polarization (as discussed in the next section), we scanned the point I for different interaction times t_I. Several field values (16, 24, 32 mT) were used, but the data for 16 mT gives the widest voltage window over which the feature could be observed and, correspondingly, the least sensitivity to electrical noise on the gates. A schematic of this is shown in Fig. 7.2a; different $V_{\rm diag}$ correspond to different detunings, δ. In principle, this technique allows us to determine $P_S(t_I, \delta)$. $P_T(= 1 - P_S)$ is plotted versus these parameters in Fig. 7.2b. Several characteristic features are notable: for $t_I \lesssim 10$ ns, the probabilty of returning to the singlet was high. For somewhat longer times, when $\delta = 0$, P_T was maximal (white). For even longer times, P_T *decreased* somewhat. In addition, for larger detunings $\delta > \Omega_{\rm nuc}$, two peaks can be observed in P_T. This additional peak is characteristic of the expected "ringing" from the coherent nature of the electron spin-nuclear spin interaction [164, 39].

We investigated the ringing in more detail. A simple theoretical model in which the nuclear magnetic fields are taken as classical, random variables with two fitting parameters (contrast and $B_{\rm nuc}$) was fit to several slices at fixed δ (fixed $V_{\rm diag}$) and varying t_I. We use a fixed nuclear polarization $\Delta B = 3$ mT based upon the measurements described in the following section. The fits and data are shown in Fig. 7.2c. Only times ≤ 40 ns were used in the fitting. We found $B_{\rm nuc} = 3 \pm 0.5$ mT from the fitting; agreement is good only if the "ringing" oscillations (expected from the classical random variable model) are included. To investigate the long time behavior, over which corrections to the classical model may become important, we measured P_T for times up to 1 μs (Fig. 7.2d). For long times P_T

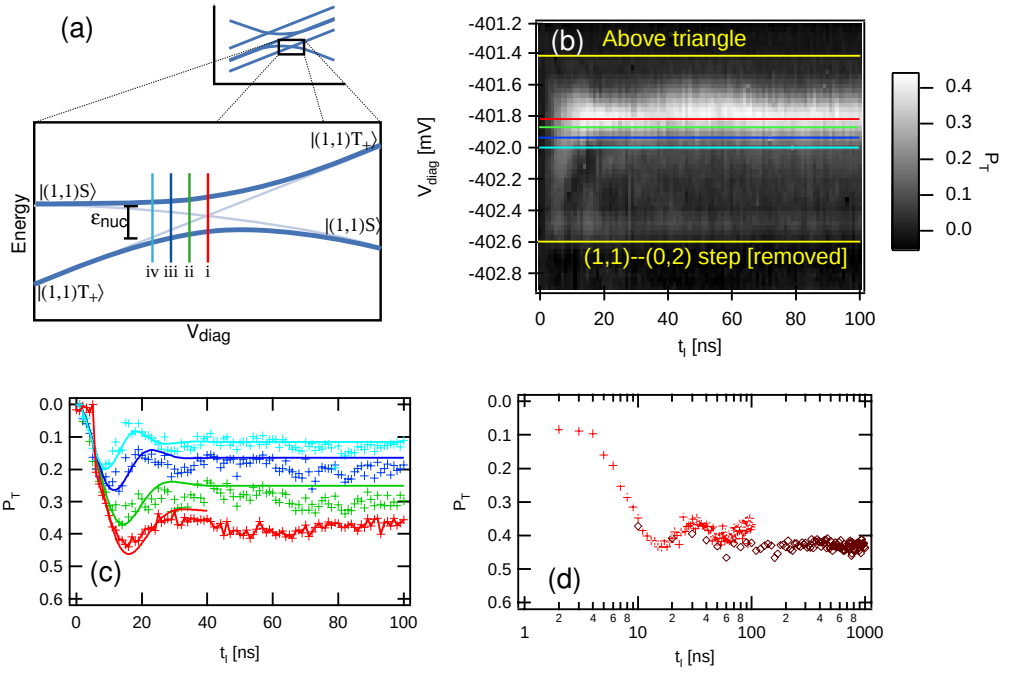

Figure 7.2: Time and energy dependence of the singlet–T_+ resonance. (a) The low energy states of the double dot are shown with a zoom in of the singlet–T_+ resonance. Four points of interest (i–iv) are given colors, used in (b) and (c). (b) With $B_{\text{ext}} = 16$ mT, measured $B_{\text{N}} = 3$ mT, and $t_P, t_{P'}, t_M$ fixed, t_I is varied. The probability of ending in a triplet state is shown in grayscale. For $t_I < T_2^*$, no appreciable population of triplet is observed, while for long times the probability goes to 0.4. Ringing can be seen for V_{diag} slightly off the resonance. (c) Four detunings (i–iv, shown in colors red, green, dark blue, light blue) are plotted versus t_I. The experimental data is shown with (+), while theoretical fits are shown as solid lines. The fit involves three parameters: T_2^*, the contrast C, and the Overhauser field B_{N}. The fitted values are consistent with previous experiments in the same device and with the measured value of B_{N} for the given pulse parameters. (d) Long time data showing increasing P_T for interacting times approaching 1 μs. The system shows possible additional decay from the expected saturation value of $P_T = 1/3$ at long times.

continues to increase, approaching 45%. A small offset between the shorter time and longer time data is observed, which we attribute to somewhat different calibrations. Correcting for the offset would indicate a reduction of P_T of 0.05 at long times. It has been argued that $P_T < 50\%$ at long times is expected in these models [1].

In addition to showing the expected behavior with respect to the hyperfine interaction, the time dependence of the $S - T_-$ resonance leads to a bound on the anisotropy parameter α expected from the Dzyaloshinskii-Moriya interaction [32]. In the configuration chosen, with external magnetic field applied in the perpendicular direction, the interaction leads to additional mixing between S and T_- at a rate $\alpha J/\hbar^2$. For the experiments, $J/g^*\mu_B = 19$ mT, while the nuclear field mixing occurs due to a field of order 2.5 mT. With error bars $< 10\%$, this suggests that $\alpha < 10\%$ in the current device.

7.3 Nuclear spin polarization

When the interaction time t_I is much longer than the precession period of the electron spins in the transverse nuclear field ($\Omega_{\rm nuc}^{-1} = 2/g^*\mu_B \cos\theta \sqrt{\langle\{B_+, B_-\}_+\rangle}$), the probability of remaining in the singlet state is [39]

$$P_S(t_I \to \infty) = 1 - \frac{2\Omega_{\rm nuc}^2}{\delta^2 + 4\Omega_{\rm nuc}^2} \ . \tag{7.4}$$

By observing the probability of ending in the singlet as a function of exchange energy (and thus detuning) we would expect to find a Lorentzian dip at $\delta = 0$. Accordingly, the centroid of the peak in $P_S(t_I \to \infty)$ provides a measure of $\langle B_z \rangle$ if the voltage dependence of J is known (Fig. 7.3a,c).

The measured $\langle B_z \rangle$ has two components: a thermal polarization ($B_T = (0.02K)B_{\rm ext}/T$ for a spin temperature > 1 mK) and a possible, anamolous polarization ΔB due to pumping

[2]The D-M interaction leads to mixing from a term $\alpha J \hat{r} \cdot (S^1 \times S^2) = J\alpha/\sqrt{2}|T_-\rangle\langle S| + H.c.$.

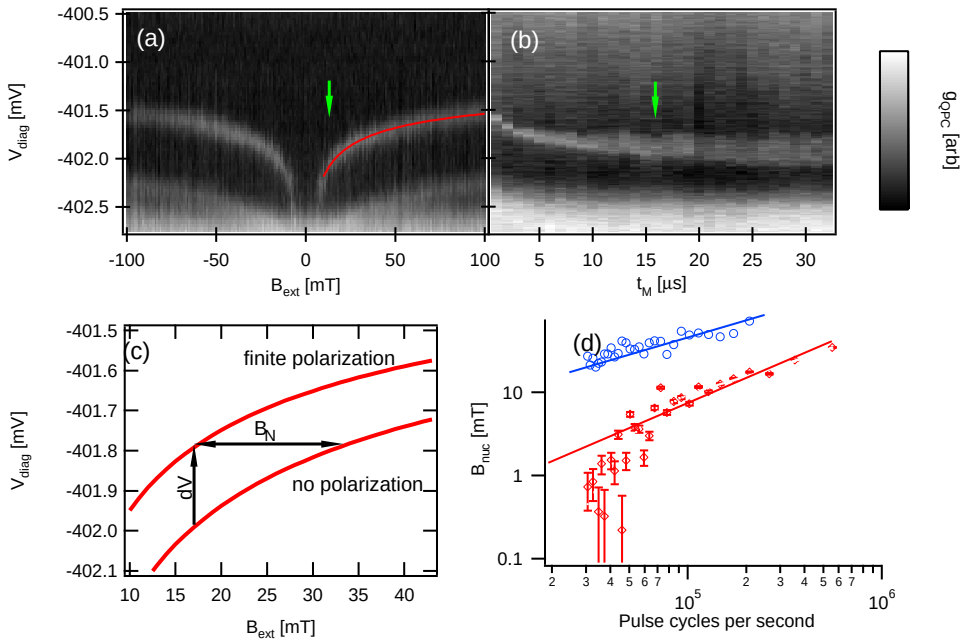

Figure 7.3: The singlet–T_+ crossing. The operating point for Figure 3 is shown with the green arrow. (a) The QPC conductance is shown as V_{diag} for the point I with times $\{t_P, t_{P'}, t_I, t_M\} = \{0.4, 0.1, 0.1, 16\}\mu s$ and the external magnetic field B_{ext} are varied. For $V_{\text{diag}} < -402.6$ the entire pulse sequence is within the (1,1) charge stability island, with a signal given in white, while for $V_{\text{diag}} > -401.2$ the sequence is within the (0,2) charge stability island, with a signal given in black. The narrow white feature (with the fit (red)) occurs at the degeneracy between the singlet and the T_+ state, when the Zeeman energy matches the bending of the singlet state's energy near the avoided crossing. The additional feature near $V_{\text{diag}} = -402.5$ occurs due to the P' point being near the resonance, and is an expected signal. (b) A plot of the expected shift of the resonance line's position as the nuclear spin polarization in the double dot system increases. A finite polarization leads to an effective increase in the Zeeman energy, and is observable as a shift of the resonance to higher V_{diag}. (c) Holding $B_{\text{ext}} = 16$ mT and $t_P, t_{P'}, t_I$ fixed, t_M and V_{diag} are varied. As the over pulse sequence becomes longer, the resonance occurs for lower V_{diag}, corresponding to less nuclear spin polarization. (d) Using the fit from (a), the value of the Overhauser field B_N is plotted versus the number of pulse sequences per second, going both "with" (blue circles) and "against" (red circles) the direction of polarization. A linear fit for "against" and a square-root fit for "with" (red and blue lines) are consistent with the data for nuclear fields larger than 3 mT $\sim B_{\text{nuc}}$.

of nuclear spins by electron spins. We remark that the small corrections due to thermal polarization in the fitting above are only necessary for $T_{\rm spin} \lesssim 50$ mK; the non-equilibrium polarization is largely independent of the thermal component.

When the nuclear spin polarization is negligble (for example, if a long measurement time is used between cycles to let nuclear polarization decay), measuring $P_S(t \gg 1/\Omega_{\rm nuc})$ as a function of the position of the I point and magnetic field allows us to find a mapping between gate voltage and exchange energy, J (Fig. 7.3a). Assuming $g^* = -0.44$, a fit to Eq. 7.2 (Fig. 7.3a), indicates that tunnel coupling $t/|g^*|\mu_B = 51 \pm 1$ mT. To determine the extent of residual nuclear polarization, we set the external field to $B_{\rm ext} = 24$ mT, held all the pulse parameters fixed and varied t_M from 1 to 32 μs. For times $t_M \gg 32$ μs, the dip is significantly reduced [3]. The location of the dip in P_S was observed to move as a function of t_M, which corresponds with decreasing number of cycles per second and is consistent with decreasing non-equilibrium polarization for lower spin flips per second (Fig. 7.3b). The fit for $J(V_{\rm diag})$ was obtained with $t_M = 16$ μs indicates 3 mT of nuclear spin polarization, as used above. With this fit form, we can use the measured location of a P_S dip to determine the shift in the effective magnetic field ΔB due to nuclear spin polarization.

We investigated the polarization of nuclear spins, ΔB, as a function of number of pulse cycles per second, f. The frequency f is controlled by changing t_M while keeping the other times constant: $t_I = 0.2, t_P = 0.4, t_{P'} = 0.1$ μs. For each frequency, the I point was scanned, starting at $V_{\rm diag} = -400.5$ and ending at $V_{\rm diag} = -402.8$ mV (this direction of scan is denoted "against"). The fit for $J(V_{\rm diag})$ allowed us to converting peak position to a value for ΔB. As cycles tends to zero, we expect that $\Delta B \to 0$; the long t_M time data points were used to set the zero for ΔB. The polarization, ΔB is plotted versus cycle frequency in Fig. 7.3d. For cycle frequencies above 80 kHz, the polarization is a linear function of

[3] By measuring this reduction at longer times, we can deduced the half-life of the metastable states $|(1,1)T_{0,\pm}\rangle$ at the M point to be ~ 60 μs.

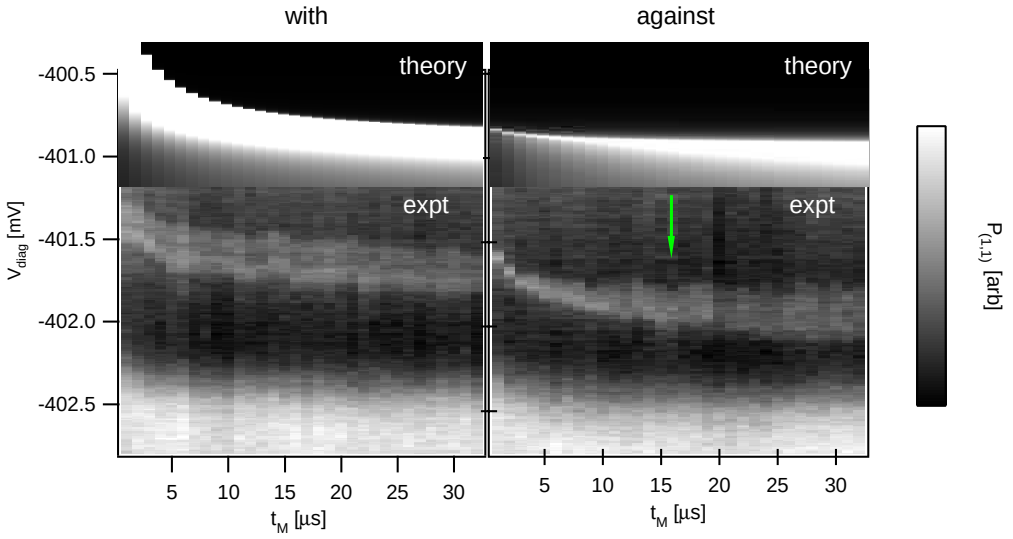

Figure 7.4: Simulation (top) and experimental results (bottom) of the polarization process for different measurement times and "with" and "against" sweep directions. A spin diffusion constant of $D = 10^{-13}$ cm^2/s is taken.

the cycle frequency, which is consistent with a fixed probability of spin flip per cycle and a fixed out-diffusion rate. However, for cycle frequencies from 30 to 80 kHz, the polarization grows much more rapidly (apparently $\propto f^4$) as a function of cycle frequency.

Curiously, a different polarization was observed when the I point was scanned in the other ("with") direction (starting at -402.8 mV and ending at -400.5 mV), as shown in Fig. 7.4(left). The measured polarization is also shown in Fig. 7.3d. Even at low cycle frequencies, the polarization is appreciable, and it appears to go as $\sqrt{f}$. We expect the difference in the two sweep directions to correspond to whether the sweep direction leads to $J(V_{\rm diag})$ following the changing Zeeman energy due to polarization ("with") or going against the changing Zeeman energy ("against"). We now develop a heurestic theory for both directions.

7.4 Theory of polarization in the weak polarization limit

We now consider a simple theoretical model for the polarization of the double-dot system. During each cycle of the polarization process a spin-flip occurs when the singlet is *not* detected, which occurs with probability $p = 1 - P_S(t_I)$. there is a (polarization-dependent) probability of spin flip, $p(\rho_{nuc})$. Solving the dynamics of the system exactly remains a difficult problem: each spin-flip event leads to correlations between different nuclear spins, and would in principle require exactly solution of an extremely large Hilbert space. It is these correlations that form the basis of the dark-state cooling model described in Chapter 3. However, in this chapter, the long waiting time between cycles leads to dephasing of the dark states through the Knight shift.

With this in mind, we develop a simple, heuristic model based upon several observations. First, uncorrelated nuclear spins described by density matrices $\rho^k \propto \exp(-\beta^k I_z^k)$ lead to a calculable probability of spin flip, $p(\{\rho^k\})$. We will parameterize the density matrix by the polarization P^k of the nuclear spins, to make the discussion more straightforward. Second, in between each spin flip, a long measurement time ($t_M > 1\mu$s) allows for phases to randomize. If we make the further assumption that population correlations randomize as well ($\rho^{qq'} \rightarrow \rho^q \otimes \rho^{q'}$), we may describe the polarization process by a set of iterative equations

$$P^k(mT + T) = P^k(mT) + f_k[p(\{P^k(mT)\}), P^k(mT)] \tag{7.5}$$

In what follows, we will develop a form for f_k, expand the analysis to include nuclear spin diffusion due to dipole-dipole interations, and then simulate the two sweep directions, "with" and "against", using the same parameters (sweep time, etc.) as the experiment.

We start by determing the form of f_k. Spin conservation requires that $\sum_k f_k = p(\{P^k\})$. Using second-order perturbation theory for the Heisenberg operators I_z^k, the

probability of flip for a given spin I_z^k should be proportional to $\lambda_k^2\langle (I^k)^2 - I_z^k(I_z^k+1)\rangle$. [4] For polarizations considered below, we may approximate this by λ_k^2. Neglecting diffusion effects for now, during one pulse cycle we find the mapping

$$P^k \to P^k + p(\{P^k\})\lambda_k^2 \tag{7.6}$$

where we use the normalization $\sum_k \lambda_k^2 = 1$. The probability of any given nuclear spin flipping in one cycle is small ($\sim 1/N$) so we can consider a differential equation over times $t \gg T$:

$$\frac{dP^k}{dt} = p(\{P^k\})\lambda_k^2/\tau \ . \tag{7.7}$$

To include the effect of spin diffusion, we use the continuum limit (see Appendix E), with $P^k \to P(r)d^3r/v_0$. Then

$$\frac{dP(r)}{dt} = -D\nabla^2 P(r) + \frac{p(\bar{P})\lambda^2(r)}{\tau} \tag{7.8}$$

where

$$\bar{P} = \frac{\int \lambda(r)P(r)d^3r}{\int \lambda(r)d^3r} \tag{7.9}$$

is the polarization observed by the Overhauser shift of the Zeeman energy. The effective magnetic field due to nuclei contributes as

$$\langle B_z\rangle = B_{\rm nuc} I_0 \sqrt{\frac{N}{I_0(I_0+1)}}\bar{P} \tag{7.10}$$

Finally, a related parameter is the experimentally-measured $dn(t)/dt$, i.e., the number of electron spin flips per unit time. This is

$$\frac{dn}{dt} = p(\bar{P})/\tau \tag{7.11}$$

[4] The same calculation indicates that spin-spin correlations will develop during the polarization cycle. This can lead to trapping in dark states [94, 181], as coherences prevent further cooling due to destructive interference. However, in our pulse cycle, there is a long (≥ 1 μs) period of time t_M spent far-off resonance in the state $|T_-\rangle$; this leads to effective dephasing of the different nuclear spins through the $B_z(S_z^1 + S_z^2)$ part of the hyperfine interaction, and allows for the unentangled state approximation, above, to be used. The necessary condition is $\gamma_e B_{\rm nuc}\lambda_k t_M \gtrsim 1$, which is achieved for $t_M \geq 1$ μs.

We now seek a solution to the diffusion equation under these conditions. In general, the position dependence of the spin-flip process leads to mixing of different diffusion modes, q, making it a non-local process and not immediately soluable in momentum space. As a simplifying assumption, instead of solving the complete problem, we may consider an approximation where the polarization is described by the aggregate polarizations of the left and right dots, P_l and P_r. The total polarization is $\bar{P} = P_l + P_r$, and the effective master equation is

$$\frac{dP_{l,r}}{dt} = -\Gamma_{l,r} P_{l,r} + \frac{p(\bar{P})}{N\tau} \frac{q_{l,r}^2}{q_l^2 + q_r^2} \tag{7.12}$$

where $N \propto \sigma_z(\sigma_l^2 + \sigma_r^2)$ is the number of nuclei in the two quantum dots. The left, right dependence arises from the potentially different dot sizes, with vertical extent σ_z and horiztonal extent $\sigma_{l,r}$. Accordingly, $\Gamma_{l,r} \approx D/(\sigma_{l,r}^2 \sigma_z)^{2/3}$ and $q_{l,r} \propto 1/\sigma_{l,r}$.

Simulation with these parameters is directly possible using the measured diffusion coefficient for GaAs of $D \approx 10^{-13}$ cm^2/s and the estimated dot sizes, $\sigma_{l,r} \approx 30$ nm. We present simulations and experiment in Fig. 7.4 for both sweep directions. The agreement in both cases is good, but some discrepancy is observed for fast cycle rates. Changing the diffusion constant over the range $0.3 - 3 \times 10^{-13}$ cm^{-s}/s made little qualitative difference in the high rate result. A more exact theory may be necessary to explain this discrepancy.

7.5 Conclusions

We have demonstrated a controlled approach to polarization of nuclear spins in double quantum dots using the exchange interaction and charge-based measurement. Details of the interaction, including time-domain correlation functions of the electronic spin wavefunction, are in good agreement with a simple quasi-static theory, with coherence between nuclear spins preserved over time scales up to 100 ns. In addition, observed po-

larizations of 3% are consistent with a simple theory with Knight-shift induced dephasing breaking dark state coherences. The polarization is currently limited by dipole-dipole diffusion. Substantially higher polarizations could be achieved by slower sweep rates, adaptive techniques for staying on resonance, or faster cycle rates. Fast cycle rates could also allow one to reach a regime where dark state coherences play a more direct role in the polarization process.

Chapter 8

Robust non-local entanglement generation in quantum dots

J. M. Taylor[1], W. Dür[2,3], P. Zoller[2,3], A. Yacoby[1,4], C. M. Marcus[1], and M. D. Lukin[1]

[1] Department of Physics, Harvard University, Cambridge, Massachusetts 02138, USA
[2] Institut für Theoretische Physik, Universität Innsbruck, Technikerstraße 25, A-6020 Innsbruck, Austria
[3] Institut für Quantenoptik und Quanteninformation der Österreichischen Akademie der Wissenschaften, Innsbruck, Austria
[4] Department of Condensed Matter Physics, Weizmann Institute of Science, Rehovot 76100, Israel

We describe a procedure for generating robust non-local electron spin entanglement in quantum dots coupled by electronic channels. It is based upon the preparation and measurement of singlet and triplet states in single or double quantum dots. We show that homogeneous unitary rotations and either a measurement procedure, indicated in this paper, or an exchange-based two-qubit gate are sufficient to enable an electron-spin based quantum repeater. In addition, using just the measurement procedure without homogeneous rotations or exchange-based gates, we develop a robust technique for non-local entanglement preparation that circumvents the most common sources of errors by introducing *dynamical* decoherence free subspaces. Purification and connection, leading to a complete repeater protocol, are also possible with these resources. This approach may find application in quantum computation, communication, and metrology.

Entangled states are a basic resource for quantum information processing, including quantum communication, teleportation, measurement-based quantum computation [83], and quantum-based metrology. EPR pairs exemplify entangled states, contributing both to theoretical insight into the nature of entanglement, and to experimental proofs of Bell's inequalities [5]. In addition, entangled pairs are a fundamental component in scaling up quantum computers, by connecting small-scale processors in a quantum network. EPR pair generation and purification is traditionally discussed in the context of long distance quantum communication via photons in a quantum repeater setup. In the presence of errors in noisy communication channels, robust generation of high-fidelity EPR pairs can be achieved via purification [10, 49, 18], where a single high-quality pair is distilled in a probabilistic manner from many low-fidelity singlets. In a solid state environment, these ideas remain relevant, for example for spin-based qubits in quantum dots, from the perspective of connecting "distant" parts of mesoscopic circuits, as well as from the more fundamental perspective of protection of entanglement in a complex environment. This letter develops a protocol for generation and purification of electron spin-based EPR pairs in mesoscopic circuits, which builds directly on emerging experimental techniques, and is tailored to the specific decoherence mechanisms in a semiconductor environment.

We consider a setup consisting of an array of electrically gated quantum dots (see Fig. 8.1), where electrons, with spin representing the qubit, can be transported by applying appropriate gate voltages ([144, 106], Fig. 8.1b). In its simplest form, a nonlocal EPR pair of electrons can be produced by local preparation of a ground singlet state of two electrons in one of the quantum dots, splitting the pair into two adjacent dots and shuttling the electrons to the end nodes. A *purification protocol* corrects for qubit errors from transport and storage. In addition, consistent with quantum computation based only upon exchange [51], local exchange-based gates are sufficient for implementing entanglement purification and

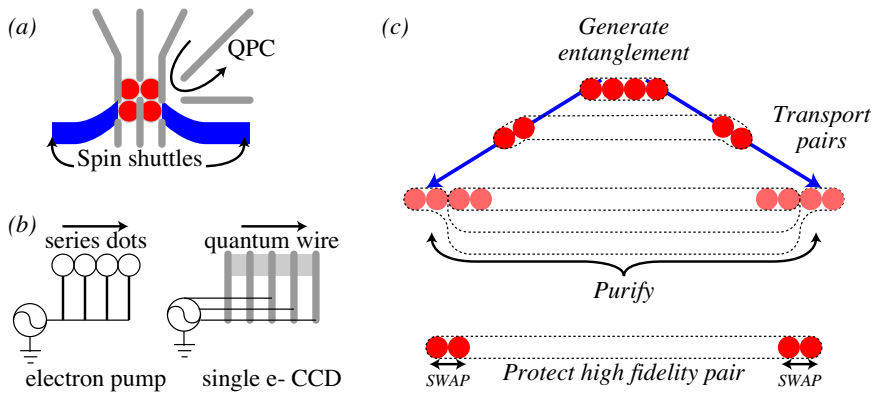

Figure 8.1: (a) Schematic outline of a node, as it might be implemented in an gate-defined quantum dots (red). A nearby quantum point contact (QPC) measures charge, gates (gray) are pulsed for state generation and control, and spin transport channels (blue) allow the entangled state to be sent to distant locations. (b) Schematic outline of two spin transport channels: electron pump and single electron CCD. (c) Overview of robust entanglement generation.

connection protocols on such pairs. In this way, pairs of entangled electrons, each separated by a distance $L/2$, may be used to prepare a higher fidelity entangled pair at a distance L, realizing a complete quantum repeater. This allows for high fidelity non-local entanglement generation with required resources, e.g., qubits and time, scaling polylogarithmic in the distance of the final pair.

Our strategy is to then develop such a purification protocol on a more advanced level, where the qubits are encoded in *logical states* of a decoherence free subspace (DFS) of two electrons, which from the beginning immunizes our logical qubits against the dominant source of decoherence, represented by hyperfine interactions. Thus the goal is to produce local pairs of *logical entangled states*, represented by four entangled electrons, transport logical pairs to the end nodes, and run an Oxford-type [49] purification protocol on these logical qubits that corrects all errors. We will show below that exchange interactions and (partial) Bell measurements for the physical qubits are sufficient to implement this protocol. We remark that the required physical resources are already available at present in the lab.

8.1 A single electron quantum repeater

We start by discussing the realization of the building blocks of a quantum repeater [18] in quantum dot systems: (i) the generation of (noisy) singlets over short distances; (ii) the purification of noisy singlets; (iii) the creation of large-distance singlets by connection of short distance singlets. In this section, we will introduce novel methods especially suited for implementation in quantum dot systems using single electron spins as logical qubits, which take current experimental limitations into account. In particular, we will restrict ourselves to two-qubit gates based on the exchange interaction and homogeneous local unitaries, i.e., the same unitary operation acting on each qubit (which can be achieved by global ESR or global, pulsed magnetic fields). In choosing these constraints, we recognize the difficulty of performing local ESR, though we note that even global ESR has yet to be demonstrated in electrically controlled quantum dots.

8.1.1 Generation of singlet states

Exchange interactions in single and double quantum dots have been shown to be extremely powerful for quantum information processing [122, 21, 44, 200]; given the critical role it plays in our analysis, we briefly outline the details of the exchange interaction as used here.

When in a molecular configuration where the tunnel coupling strength $t \ll \upsilon$ (the single dot orbital level spacing), a two electron, double-dot system (Fig. 8.2a) must be total spin $S = 0$ or $S = 1$. The overall antisymmetry of the two-electron wavefunction leads to splitting of the two subspaces, expressed in the Hamiltonian

$$H_{ex} = J\hat{\vec{S}}^A \cdot \hat{\vec{S}}^B, \tag{8.1}$$

where A, B refer to the two electrons. As J is determined by dot geometry and magnetic

field, for reasonable parameters the singlet state can be set as the ground state, where the exchange energy J splits the singlet ground state ($S = 0$) from the triplet excited states ($S = 1$). In small double quantum dots J can be large, $J \gtrsim 0.1$ meV [156, 206]. Similarly, the two-electron ground state of single quantum dot is a singlet, and the next excited state is a triplet, with a splitting J between them.

As the ground state, the singlet state can be prepared by tunneling from the leads when the double-dot is in the (1,1) stability island (the double-dot's charge state is labeled by (n_A, n_B) for the number of electrons in dots A and B) with large exchange, or in the (2,0) stability island when the double-dot exchange is small (Fig. 8.2c). By reducing the tunnel coupling between the two dots or by shifting to the (1,1) charge configuration, respectively, the exchange energy is suppressed and the small capacitances of the two dots naturally lead to an adiabatic separation of electrons in the singlet state, leading to two, detached, one-electron dots. The spin configuration of the detached (atomic) state is then a well separated EPR pair, $|S\rangle = 1/\sqrt{2}(|\uparrow_A\downarrow_B\rangle - |\downarrow_A\uparrow_B\rangle)$.

Reversing the process (starting in the atomic configuration) maps the singlet-triplet subspace of the separated system, where the singlet and triplet $m_s = 0$ ($|T_0\rangle = 1/\sqrt{2}[|\uparrow_A\downarrow_B\rangle + |\downarrow_A\uparrow_B\rangle]$) states are degenerate, to the exchange split molecular state or the (2,0) charge state, where there is a large energy gap between the two. When this process is faster than spin dephasing processes but slow with respect to higher orbital states, such that the single occupancy Heitler-London wavefunction is a good approximation to the overall system, the population follows exactly. The energy difference between the singlet and triplet states allows state selective ionization in the molecular configuration, where the triplet to single-electron state transition is above the Fermi sea in the leads while the singlet transition is below the leads, while the splitting between the (2,0) triplet and singlets allows state selective adiabatic transfer from the (1,1) state to the (2,0) state. This in turn enables

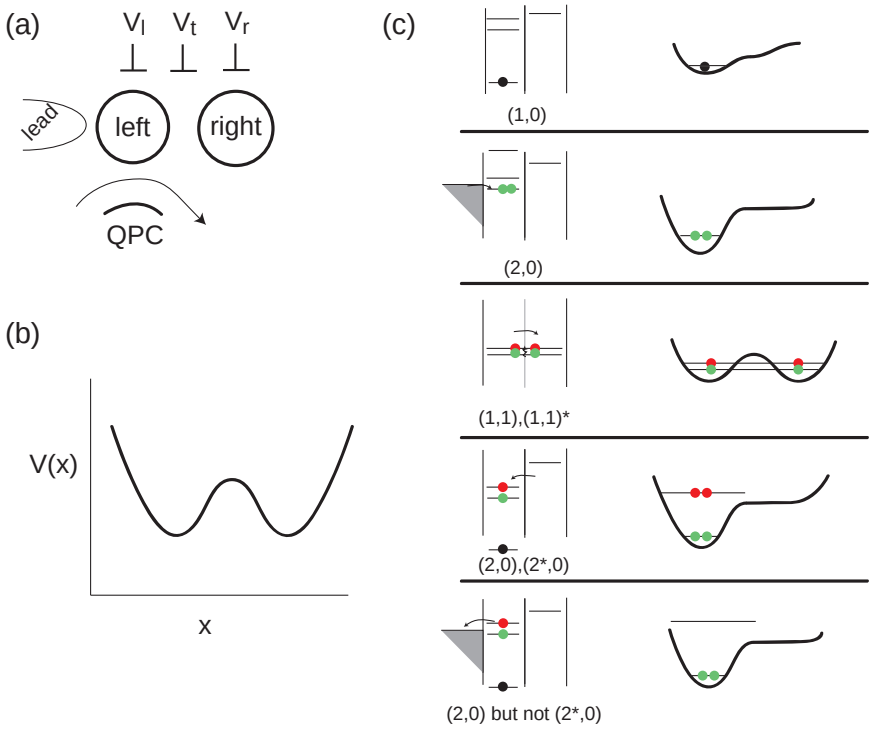

Figure 8.2: Scheme (shown in (a)) for using a double dot, with an effective double-well potential (b), to (c) generate entanglement and measure spin decoherence. Steps shown in (c) are: 1) start in (1,0) charge state, 2) load from leads (2,0) ground state, 3) split the singlet by adiabatic transfer, generating a separated singlet state. This state may dephase or rotate; step 4) the singlet and triplet states are transferred back to the (2,0) charge configuration; and 5) the triplet tunnels to the leads, giving a measurable charge difference between singlet and triplet.

a charge sensitive measurement to distinguish between the two different states, in direct analogy to Ref. [87] (see Fig. 8.2c).

After creating an EPR pair, the two electrons, initially in a singlet state $|S\rangle_{AB}$, are transported separately to their final locations. Transport is achieved by "clocking" the electrons through a series of quantum dots, in direct analogy to the operation of a CCD [144]. The resulting state ρ will be mixed due to imperfections in the transport process, discussed in Section 3. Noise limits the distance over which electrons can be transported, as the resulting state eventually becomes disentangled. However, if the distance

is small enough, the final states will be mixed states with residual, partial entanglement. We will show in the following that given several copies of such mixed states ρ, the ability to perform exchange-based unitaries and homogeneous single qubit unitaries, together with single qubit measurements are sufficient to implement *entanglement purification* and *entanglement connection* and hence allow one to create high fidelity singlets over larger distances. This also requires that electron spin be a reliable quantum memory, though extending the electron spin by coupling to nuclear degrees of freedom has some potential to provide such memory [183, 181].

8.1.2 Entanglement purification

In the following we describe a novel entanglement purification protocol using only homogeneous single qubit unitary operations and two-qubit unitary operations based on exchange interaction, i.e., operations of the form

$$U(\phi) = \exp(-i\phi H_{ex}/J), \tag{8.2}$$

where $U(\pi/4)$ corresponds (up to an irrelevant global phase factor of $e^{-i\pi/4}$ to the SWAP operation [1], while $U(\pi/8) = \mathrm{SWAP}^{1/2} e^{-i\pi/8}$ ("square root of SWAP") and $U(-\pi/8) = \mathrm{SWAP}^{-1/2} e^{i\pi/8}$. We restrict ourselves to homogeneous local unitary operations and unitary gates based on exchange interactions because these operations are significantly simpler to implement in a quantum dot system than arbitrary single- and two-qubit unitary operations. We remark that previously known entanglement purification protocols [10, 49] are based on CNOT gates, which cannot be implemented by sequences of gates we consider here. This can easily be seen by exploiting the fact that any sequence of homogeneous local unitary operations and two-qubit gates of the form $U(\phi)$ are invariant under permutations, while CNOT gates

[1] The CNOT [SWAP] operation is defined by the following mapping of states: $|i\rangle_A|j\rangle_B \rightarrow |i\rangle_A|i \oplus j\rangle_B$ $[|i\rangle_A|j\rangle_B \rightarrow |j\rangle_A|i\rangle_B]$, where $\oplus$ denotes addition modulo 2, and $|\downarrow\rangle = |0\rangle, |\uparrow\rangle = |1\rangle$.

are not.

Consider a system of two qubits in some mixed state ρ_{AB} with fidelity $F \equiv \langle S|\rho|S\rangle$, where $|S\rangle = 1/\sqrt{2}(|\uparrow\downarrow\rangle - |\downarrow\uparrow\rangle)$ is the singlet state and $|T_0\rangle = 1/\sqrt{2}(|\uparrow\downarrow\rangle + |\downarrow\uparrow\rangle)$, $|T_1\rangle = 1/\sqrt{2}(|\uparrow\uparrow\rangle + |\downarrow\downarrow\rangle)$, $|T_2\rangle = 1/\sqrt{2}(|\uparrow\uparrow\rangle - |\downarrow\downarrow\rangle)$ are triplet states. By applying a random homogeneous unitary rotation of the form $U_A \otimes U_B$, i.e., the same unitary operation on system A and B, one can depolarize ρ to a standard form, the so called Werner state $\rho_W(F)$, without changing the fidelity F. This can be accomplished, e.g., by small changes of magnetic field near $|B| = 0$ or by randomly detuned global ESR pulses. The depolarization map $\mathcal{D}$ is defined as

$$\mathcal{D}(\rho) = \int d\mu_U (U \otimes U)\rho(U \otimes U)^\dagger \tag{8.3}$$

where the integral is extended to all unitary operators acting on $\mathbb{C}^2$ and $\int d\mu_U = 1$. We have that

$$\mathcal{D}\rho = \rho_W(F) \equiv x|S\rangle\langle S| + \frac{1-x}{4}\mathbb{1}_{AB}, \tag{8.4}$$

with $x \equiv \frac{4F-1}{3}$.

Given two identical copies of a Werner state $\rho_W(F)$, $\sigma = \rho_W(F)^{(A_1B_1)} \otimes \rho_W(F)^{(A_2B_2)}$ one can use the following probabilistic purification protocol to increase the fidelity F of the resulting state:

- Apply $U(\pi/8)^{(A_1A_2)} \otimes U(-\pi/8)^{(B_1B_2)}$
- Measure observable σ_z on particles A_2 and B_2 (i.e., projective measurement in z-basis), keep state of particles A_1B_1 if and only if the results are different (i.e., $0_{A_2}1_{B_2}$ or $1_{A_2}0_{B_2}$). Otherwise the protocol has failed.
- Apply $\mathcal{D}^{(A_1B_1)}$ to remaining system.

The resulting state of this procedure is again a Werner state, $\rho_W(F')$, with new fidelity F'. One can calculate F' as a function of F and finds

$$F' = \frac{F^2 + 1/2\{F(1-F)/3 + [(1-F)/3]^2\}}{F^2 + 3F(1-F)/3 + 4[(1-F)/3]^2} \tag{8.5}$$

In order to perform this analysis, one has to determine the action of the protocol on states of the form $|\chi_1\rangle_{A_1B_1}|\chi_2\rangle_{A_2B_2}$, where $|\chi_i\rangle \in \{|S\rangle, |T_0\rangle, |T_1\rangle, T_2\rangle\}$. For instance, one finds that $U(\pi/8)^{(A_1A_2)} \otimes U(-\pi/8)^{(B_1B_2)}|S\rangle_{A_1B_1} \otimes |S\rangle_{A_2B_2} = |S\rangle_{A_1B_1} \otimes |S\rangle_{A_2B_2}$, leading to a state $1/\sqrt{2}|S\rangle_{A_1B_1}$ after the measurement process for both, outcome '01' and '10'. This gives rise to a contribution of 1/2 in the singlet subspace $|S\rangle_{A_1B_1}\langle S|$ after depolarization. Similarly, $U(\pi/8)^{(A_1A_2)} \otimes U(-\pi/8)^{(B_1B_2)}|S\rangle_{A_1B_1} \otimes |T_0\rangle_{A_2B_2} = 1/2(|S\rangle|T_0\rangle + |T_0\rangle|S\rangle + i|T_1\rangle|T_2\rangle - i|T_2\rangle|T_1\rangle)$, where the measurement leads to an unnormalized state $1/(2\sqrt{2})(|S\rangle \pm |T_0\rangle)$ and the $'+'['-']$ sign corresponds to the outcome $'01'$ $['10']$ respectively. The final depolarization leads to a contribution of 1/8 in singlet subspace, $1/8|S\rangle\langle S|$. The action of the protocol on the initial two copies of the Werner state can then be determined by using that $\rho_W^{\otimes 2}$ can be written as an incoherent mixture of states of the form $|\chi_1\rangle_{A_1B_1}|\chi_2\rangle_{A_2B_2}$, and by properly normalizing the resulting state. Entanglement purification takes place by an iterative application of the protocol, thereby increasing the fidelity F in each step.

The entanglement purification protocol described above (protocol 1') can be considered as the analog of the recurrence protocol introduced in Ref. [10] (protocol 1), where here we restrict ourselves to exchange interactions. In a similar way, one can obtain the analogue of the quantum privacy amplification protocol of Ref. [49] (protocol 2)—which is known to have higher efficiency and to be more robust against the influence of imperfections in local control operations as compared to the protocol of Ref. [10]—which we shall call protocol 2'. To complete this analogy, one replaces the depolarization procedure (step 3) by a partial depolarization which produced states diagonal in the singlet-triplets basis (while

keeping the diagonal elements unchanged). That is, the depolarization map Eq. 8.3 is replaced by probabilistic applications of homogeneous local unitary operations of the form $\mathbb{1}\otimes\mathbb{1}, \sigma_x\otimes\sigma_x, \sigma_z\otimes\sigma_z, \sigma_y\otimes\sigma_y$, i.e.,

$$\mathcal{D}'(\rho) = \frac{1}{4}\sum_{k\in\{0,x,y,z\}} \sigma_k\otimes\sigma_k\rho\sigma_k\otimes\sigma_k, \tag{8.6}$$

where $\sigma_0 = \mathbb{1}$. In addition, one applies at the beginning of the protocol (as a step 0) a homogeneous local unitary operation $U_{\rm Had}^{\otimes 4}$ to the particles $A_1B_1A_2B_2$, where

$$U_{\rm Had} = \frac{1}{\sqrt{2}}\begin{pmatrix} 1 & 1 \\ 1 & -1 \end{pmatrix} \tag{8.7}$$

is the Hadamard operation [2].

Let us compare the entanglement purification protocol(s) we have introduced here with the protocols of Refs. [10, 49]. It is easy to see that protocol 1', whose action is described by the map Eq. 8.5, has fixed points $F = 1/2$ and $F = 1$ and is capable of producing perfect singlet states from all Werner states fulfilling $F > 1/2$ by successive application. The purification curve F' as a function of F, however, turns out to be flatter than the one of protocol 1 (see Fig. 8.3). This implies that our protocol is less efficient, requiring more purification operations to achieve a desired final fidelity, although it has the same purification regime (i.e., can purify all states which could be purified using protocol 1). We remark that the purification regime is given by the interval where $F' > F > 1/2$, that is, the interval where $(F' - F) > 0$. The flatter purification curve also implies that the protocol is more sensitive to errors in local control operations. The effect of imperfections of order $1-p$ in local control operations can essentially be described by 'shifting down' the purification curve by a certain amount [56]. A simple model which captures the features of imperfections is replacing each unitary superoperation acting on qubits i, j with $\hat{U}_{ij}\hat{\rho} \rightarrow$

[2] Hadamard can be accomplished by global sequence $\exp(i\pi\sigma_z/4)\exp(i\pi\sigma_x/4)\exp(i\pi\sigma_z/4)$.

$\hat{U}_{ij}\hat{N}_i\hat{N}_j\hat{\rho}$, where $\hat{N}_j = p\hat{\rho} + (1-p)(\frac{1}{2}\mathbb{1}_j) \otimes \mathrm{Tr}_j\hat{\rho}$. For a fixed error rate, the fixed points $F' = F$ determine the purification regime, where the lower fixed points gives the minimal required fidelity such that entanglement purification can be successfully applied, while the upper fixed point gives the maximum reachable fidelity. The threshold value for local control operations is reached if lower and upper fixed points coincide, as in this case no purification is possible. The flatter purification curve of our protocol 1' has the consequence that the lower fixed point is higher than the one of protocol 1, while the upper fixed point is lower. Thus the purification regime as well as the reachable fidelity are smaller for our protocol, and the threshold value for errors in local control operations is smaller. However errors up to two percent still yield potential purification gains, but of particular importance is the lower fixed point. As this determines the minimum input pair fidelity, it will determine the maximum length a pair can be separated before purification becomes useless. This also suggests a natural distance limit for generating such purified pairs without implementing the rest of the protocol (i.e., connection). Similarly, one finds that protocol 2' is more efficient and less sensitive to errors than protocol 1', but is slightly worse than protocol 2.

We remark that also weakly entangling two-qubit operations (other than $U(\pi/8)$ or CNOT, which are strongly entangling) enable one to purify Werner states. In fact, when replacing the operation $U(\pi/8)^{(A_1A_2)} \otimes U(-\pi/8)^{(B_1B_2)}$ in protocol 1' by an operation of the form $U(\phi)^{(A_1A_2)} \otimes U(-\phi)^{(B_1B_2)}$ with arbitrary $0 > \phi > \pi/4$, one still obtains a purification protocol with the same purification regime $1/2 < F \leq 1$ and upper fixed point $F = 1$ as protocol 1'. The only difference is that the resulting purification curve is even flatter and hence the resulting protocols are less efficient and more sensitive to imperfections in local control operations. This observation might be of relevance in cases where only weak interactions between systems are available. Figure 8.3 summarizes these observations for protocols 1 and 1'.

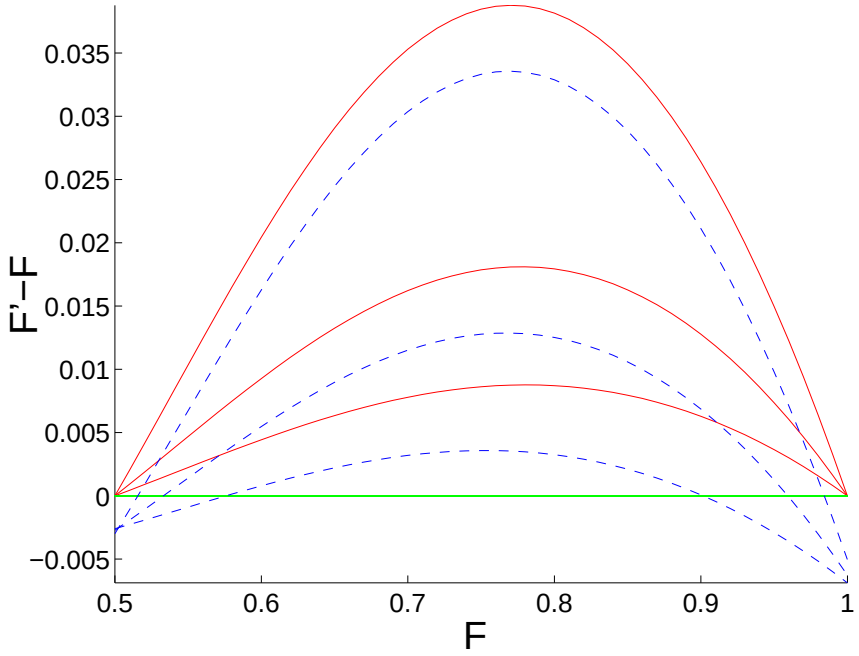

Figure 8.3: Purification curve $F' - F$ plotted against initial fidelity F, where F' is the fidelity of the resulting state after a successful purification step. Solid curves (red) from top to bottom correspond to protocol 1 (Ref. [10]), and protocol 1' with $\phi = \pi/8, \pi/16$ respectively. The dotted curves (blue) show the corresponding purification curves when local control operations (CNOT, $U(\phi)$) are imperfect. Imperfections are modeled by noisy operations with local white noise of 0.5 percent, i.e., an imperfect operation as describe in the text with $p = 0.995$.

Note that in all protocols discussed above, in each step two identical copies of the state (resulting from previous purification steps) are used. This implies that a physical implementation would require a whole two dimensional array of dots ($2 \times N$, with N the number of initial copies to obtain at least one entangled pair with a certain final higher fidelity). Moreover, additional SWAP gates will be required in order to operate always on adjacent dots at later stages of the protocol, though shuttling electrons may be used in lieu of true exchange-based SWAP gates. There exists, however, an alternative method, namely *(nested) entanglement pumping* [55], which circumvents these problems. In entanglement pumping, the output state of a successful previous purification step together with a standard pair of constant fidelity (which may be the pair resulting from the singlet state after the transport process) are used as input states for the next purification step. Iterative application of one of the entanglement purification protocols discussed above still allows one to increase the fidelity of the pairs by a certain amount, however the fixed point of the protocol(s) are no longer $F = 1$, i.e., no perfect singlet states can be generated. As compared to the standard recurrence protocols, however, only *two* (rather than N) quantum dots at each site are required throughout the process. The spatial resources necessary for the original recurrence scheme are translated in this scheme to temporal resources, as standard pairs have to be sequentially generated. In our case, this can be done by transporting "buckets" of entangled electrons in close series, i.e., by "clocking" a whole train of entangled electrons, each pair initially in the singlet state, through a series of quantum dots. As the time scales for purification and transport are similar, this may work with high efficiency.

One may also use nested entanglement pumping, i.e., one takes pairs whose fidelity is close to the fixed point at a given nesting level as standard pairs at the next nesting level. Using such a nested scheme, one can indeed produce perfect singlet states (in the case of noiseless local control operation) or the same maximal fidelity as is reachable

using a standard recurrence protocol (in the case of imperfect local control operations) [55]. Only a few nesting levels—which corresponds to the number of quantum dots required at each location—are needed. For instance, when using protocol 2 [49], 3-4 nesting levels are sufficient (however, this protocol has the difficulty that CNOT operations have to be implemented). Due to the fact that protocols 1' and 2' are less efficient, one needs more nesting levels (about 15-20) and hence a larger number of quantum dots is required in this case. Nevertheless, for a first demonstration experiment (just one purification step) the protocols 1' and 2' introduced here seem to be ideally suited.

Unfortunately, nested entanglement pumping requires a long-lived quantum memory, relying as it does upon temporal resources in lieu of additional electron spins. While nuclear spin degrees of freedom may provide such memory [183], when unaccounted for they produce fast dephasing of the electron spins and will provide a hard limit to the protocols presented so far. We address this issue in more depth in Sections 3 and 4.

8.1.3 Connection process

Up to this point we have discussed how to generate entangled pairs of electrons with high fidelity over distances limited by the local generation and transport process fidelities. To generate entangled pairs over arbitrary large distances, an additional process is required which *connects* two (or more) short distance pairs in such a way that a long distance pair (typically with lower fidelity) is generated. These long-distance pairs can then be purified again, thereby generating long-distance pairs with high fidelity. Arbitrary distances can be reached by concatenating this procedure of connections and re-purification at different nesting levels, thereby realizing a quantum repeater [18].

In the connection process, one starts with two entangled pairs shared between sites (A, B_1) and (B_2, C) respectively, where B_1, B_2 are in our case two adjacent dots, while A

and C are dots further away in opposite directions. One then performs a *Bell measurement*, i.e., a measurement in the singlet/triplet basis on electrons in sites B_1B_2. This corresponds to the teleportation of the (entangled) electron at site B_1 to site C. If both pairs AB_1 and B_2C were initially in the singlet state $|S\rangle$, the resulting pair of electrons at sites A, C will be in the singlet or one of the triplet states, depending on the measurement outcome, and single qubit unitary operations at site C would be required to restore the state to the singlet state in all cases. If the two initial pairs where non-maximally entangled, e.g., in a Werner state with fidelity F, the resulting pair AC will also be in a Werner state but with smaller fidelity $F' < F$ [18], where

$$F' = F^2 + \frac{(1-F)^2}{3} \tag{8.8}$$

In our case, the connection process cannot be performed exactly as described above: of the four Bell states, we only have (so far) a means of measuring the singlet state, and we only have homogeneous unitary operations.

We show now how to achieve connection of two pairs in a probabilistic manner using the singlet measurement described in Section 2A. We remark that in the context of a quantum repeater, such a probabilistic implementation of the connection process does not represent a fundamental problem, as the purification process is also probabilistic. In particular, the polylogarithmic Al scaling of the required resources with the distance remains valid [18, 56]. Let us consider the connection process of two singlet states, $|S\rangle_{AB_1}, |S\rangle_{B_2C}$. Connection can be performed probabilistically by measuring the B_1, B_2 pair to be in the singlet subspace. Explicitly, we write

$$\begin{aligned} |S\rangle\langle S|_{B_1,B_2}|S\rangle_{AB_1}|S\rangle_{B_2C} &= |S\rangle\langle S|_{B_1,B_2}(|\uparrow\downarrow\uparrow\downarrow\rangle - |\downarrow\uparrow\uparrow\downarrow\rangle - |\uparrow\downarrow\downarrow\uparrow\rangle - |\downarrow\uparrow\downarrow\uparrow\rangle)_{AB_1B_2C}/2 \\ &= 1/2\sqrt{2}(|\downarrow\uparrow\rangle - |\uparrow\downarrow\rangle)_{AC}|S_0\rangle_{B_1B_2} \end{aligned} \tag{8.9}$$

Thus, measuring the singlet of B_1, B_2 yields exactly a singlet of A, C, where the mea-

surement result occurs with probability 1/4, leading to an increase in the time needed to perform the repeater protocol, but still giving polynomial scaling. For a pair of Werner states (AB_1, B_2C) with fidelity F, the fidelity of the new AC pair is $F' = F^2 + (1-F)^2/3$, the same as for the full Bell state measurement case.

8.2 Limits to the single-electron scheme

The singlet generation process, the singlet-triplet measurement process, and resonant exchange gates are limited by several errors. Charge-related errors may play a role, but as most charge manipulation is done adiabatically, this may be negligible when compared to electron spin dephasing and relaxation. Of particular importance is the quality of electron spin as a quantum memory. We find that pure dephasing due to hyperfine interactions provides a strong limit to effective implementation, as discussed below. However, anisotropic terms, also considered, do not limit the single-electron repeater proposal.

Before proceeding, we remark that it may be possible to work in a nuclear-spin free environment, such as ^{2}8Si quantum dots [155, 117] or isotopically pure CdSe dots in a CdSe ZnSe heterostructure, ^{1}2C nanotubes, or other materials, though we will assume for the remainder of this paper that the quantum dots involved have lattice nuclei with non-zero spin and hyperfine coupling to the electron spin.

8.2.1 Hyperfine effects

Pure dephasing due to nuclear spins in the quantum dot will produce a potentially sizeable error. The hyperfine interaction for an electron spin in a quantum dot interacting with lattice nuclear spins is

$$V_{hf} = A \sum \alpha_k \hat{\vec{I}}^k \cdot \hat{\vec{S}}, \tag{8.10}$$

where A is the hyperfine interaction constant (~ 0.1 meV for GaAs) and α_k is proportional to the electron wavefunction's probability of being at the lattice site k. In an intermediate or strong magnetic field ($|B| > 100$ mT) along the z-axis, Eq. 8.10 can be written in the rotating wave approximation as $A\sum_k \alpha_k \hat{I}_z^k \hat{S}_z$, which acts as an additional, dot dependent magnetic field component parallel to the applied field, $\hat{B}_z = A\sum_k \alpha_k \hat{I}_z^k / g^* \mu_B$. The mean-field contribution is the well known Overhauser field, though this contribution is almost zero even at dilution refrigerator temperatures. On the other hand, slow root-mean-square variations can occur; spin diffusion through nuclear dipole-dipole interactions between nuclei in the dot and nuclei in the rest of the heterostructure lead to a decay of the field correlator,

$$\langle \hat{B}_z(t+\tau)\hat{B}_z(t)\rangle \simeq \left(\frac{A}{g^*\mu_B\sqrt{N}}\right)^2 f(\tau), \tag{8.11}$$

where N is the number of nuclei in the dot and $f(x)$ depends upon the particulars of the decay process. This indicates a quasi-static field, static on the time scales of electron spin manipulation, with rms strength $\sim$ 3-30 mT that fluctuates at least on a time scale given by dipolar diffusion, $\gamma_{dd} \simeq 6$ ms^{-1} is produced by nuclear spins, and leads to a large fluctuating gradient between different dots. In terms of a quantum repeater, the hyperfine field leads to short electron spin memory times, destroying any stored entanglement on a time scale of $A/\hbar\sqrt{N} \sim 100\mu$s^{-1}.

Due to hyperfine coupling shows, using only EPR pairs (i.e., entanglement between only two electrons) may be insufficient for the storage of a high fidelity entangled pair. In particular, the hyperfine coupling considered above produces a large, fluctuating gradient both between dots. In principle, the gradient can be compensated by quantum bang-bang [201] with fast, homogeneous rotations (by, e.g., ESR), with the requirement that the ESR Rabi frequency $\Omega_{ESR} \gg A/\hbar\sqrt{N}$ [134]. Such fast ESR may not be realistic with current technologies; we explore in Section 4 methods of correction that do not involve ESR.

To evaluate the effect of the hyperfine field on the transported electron spin, the case of a series of connected quantum dots used for "shuttling" is taken. The time scale τ for adiabatic transfer from one dot to the next is set by the orbital level spacing, $\upsilon \gg \tau^{-1}$, which in turn sets the confinement length of the dot, $a_B = \sqrt{\hbar^2/m_*\upsilon}$. Thus, to travel a distance L, it requires l steps of distance order $a_B \propto \sqrt{\tau}$, each of which takes a time τ. The overall time to "clock" the electron is then $\tau(L/a_B) \propto L\sqrt{\tau} \propto L/\sqrt{\upsilon}$. Increasing the level spacing therefore increases the number of "buckets" required at a rate slower than the decrease in transfer time required to send the electron. For a bucket with $N \propto a_B^\beta \propto \tau^{\beta/2}$ nuclear spins, the phase error due to the random hyperfine field goes as

$$\langle \delta\phi^2 \rangle^{1/2} \simeq \tau A/\hbar\sqrt{N} \propto \tau^{1-\beta/4}, \tag{8.12}$$

where A is the hyperfine contact interaction constant, and $\beta = 1$ for a 2D dot and 3/2 for a 3D dot [3]. For L/a_B buckets, each with a different random field, the total error then is proportional to $\epsilon \sim L\tau^{1/2(3-\beta)}$. Thus, with respect to both the adiabaticity condition and hyperfine contact-related dephasing, decreasing the dot size improves the distance that can be traveled for the same phase error, for both 2D and 3D dot geometries. As an example, we consider a series of 2D dots in a 10 nm GaAs well, each of size $a_B \sim 100nm$, and spaced one dot every 200 nm. We set $\tau = \hbar 0.01/(\upsilon) \simeq 0.5$ ns, $N \simeq 10^6$, and $A = 0.12$ meV. This gives an error of 10^{-3} per 200 nm, or approximately a fidelity of 0.9 at 20 μm. The long correlation time of the hyperfine field means that phase errors encountered by one electron traveling in a given channel will be highly correlated with errors encountered by the next electron traveling the same channel. We note that in principle, a singlet-triplet measurement would allow metrology, i.e., measurement of the fluctuating field that characterizes the transport channel, and does not require any type of ESR.

[3] This analysis presumes that while intermediate to high polarization of nuclear spins into dark states can be realized in quantum dots, the same may be extremely difficult for the bulk or for transport channels.

8.2.2 Anisotropic exchange

In general, spin-orbit terms (both Rashba and Dresselhaus) lead to corrections to Eq. 8.1. The expected full form is [58, 139]

$$\tilde{H}'_{ex} = J(\hat{S}_z^A \hat{S}_z^B + \frac{1 + i\sin(\gamma)}{2} \hat{S}_+^A \hat{S}_-^B + h.c.) \tag{8.13}$$

where the z axis is the axis of the spin-orbit vector and γ a measure of the anisotropy. In a (100) GaAs quantum well, z is parallel to the inter-dot axis, and [101]

$$\gamma = (2\alpha\hbar/\sqrt{2m_* E_g})\langle k_x^2 \rangle d \ , \tag{8.14}$$

where x is the growth direction and d is the distance between the two quantum dots. For quantum dots in a 10 nm quantum well separated by 100 nm, $\gamma \lesssim 0.5$ is possible. By a unitary transformation, $U = \exp[-i\hat{S}_z^B \arctan(\sin(\gamma))]$, we rewrite the anisotropic Hamiltonian as

$$H'_{ex} = J_\parallel \hat{S}_z^A \hat{S}_z^B + J_\perp/2(\hat{S}_+^A \hat{S}_-^B + \hat{S}_-^A \hat{S}_+^B) \tag{8.15}$$

with $J_\perp = J_\parallel \sqrt{1 + \sin^2(\gamma)} \simeq J_\parallel(1 + \gamma^2/2)$.

For H'_{ex}, the $m_s = 0$ singlet and triplet states have energies $(-J_\parallel \mp 2J_\perp)/4$, respectively, while the $|m_s| = 1$ triplet states have energy $J_\parallel/4$. The purification protocol, relying upon measurements that restrict the final result to a total $m_s = 0$ subspace, is insensitive to this variation. However, any external magnetic field that is not aligned with the inter-dot axis and/or variations of the inter-dot axis lead to potential spin-flip errors. If Zeeman energy is much less than the anisotropic contribution, $J_\perp - J_\parallel$, this error may be neglected.

We show in Appendix F how the inherent anisotropy may in fact be a resource, as has been noted previously [200].

8.3 Two electron encoding

8.3.1 Choice of encoded states

We begin by describing a specific encoding that allows suppression of the dominant error mechanism. We focus on hyperfine effects as theory and experiment have demonstrated their detrimental effect on electron spin coherences (dephasing), with $T_2^* \sim 10$ ns [14, 96], while spin-orbit-phonon and other spin-flip processes (relaxation) are observed to enter only for times on the order of 1 ms in the presence of a large magnetic field [61, 82]. Given the long correlation time of the electron spin-nuclear spin interaction [131, 134], storing entanglement in the logical states of a DFS with total S_z quantum number $m_s = 0$, $|0_L\rangle = (|\uparrow\downarrow\rangle - |\downarrow\uparrow\rangle)/\sqrt{2}$ and $|1_L\rangle = (|\uparrow\downarrow\rangle + |\downarrow\uparrow\rangle)/\sqrt{2}$, allows for suppression of such dephasing by repeatedly exchanging the two electrons [200]. The four-particle entangled state

$$|\phi^+\rangle = |0_L\rangle|0_L\rangle + |1_L\rangle|1_L\rangle = |\uparrow\downarrow\uparrow\downarrow\rangle + |\downarrow\uparrow\downarrow\uparrow\rangle \tag{8.16}$$

takes full advantage of these properties, suppressing phase noise. This combination of subspace choice and exchanging electrons corresponds to a dynamical DFS (DDFS) and is a de facto implementation of Carr-Purcell spin echo in the DFS. We show below that using a DDFS, memory and transport errors will be dominated by spin-flip terms, an improvement of order 10^5 over hyperfine-related noise. Errors in the DDFS procedure, and spin-flip errors, are so far uncorrected. Starting with several copies of the entangled state $|\phi^+\rangle$, our purification protocol corrects for spin-flip errors entirely, by detection of the total m_s quantum number of the states, while it corrects for phase errors by analogy to the protocol of Ref. [49].

We now consider the ingredients and recipe for EPR pair generation and purification in the DDFS: (I) charge manipulation and measurement techniques for performing exchange gates ($U_{AB}(\phi)$), singlet generation, and partial Bell state measurements M_{AB}; (II)

the dynamical DFS's properties with regards to different noise sources, its behavior during storage (memory) and transport, to show suppression of better than 10^5 for low frequency phase noise; (III) a purification protocol that works in the encoded space and corrects for arbitrary errors, using only the partial Bell state measurement and exchange gate described in (I).

8.3.2 Charge manipulation and measurement

We suggest an implementation of the necessary resources for each node: exchange gate, singlet generation, and partial 2 electron Bell state measurement. In principle, other techniques could be used to generate the same set of operations.

The Loss-Divincenzo exchange gate [122] between two electrons in separate dots, A and B, is defined as $U_{AB}(\phi) = \exp(-i\phi\vec{S}^A \cdot \vec{S}^B)$; for example, $U(\pi/8)$ is $\sqrt{\text{SWAP}}$. By control of the tunnel coupling T_c between A and B, or by changing their relative bias, arbitrary ϕ may be achieved. It requires only pulsed-gate manipulation, i.e., it relies on charge control.

Singlet states of double dots may be created using the large exchange splitting of single dots. For a double-dot system, starting in the (1,0) stability island (Fig. 8.4a) resets the state of the double-dot (position A); changing configuration to the (2,0) stability island (position B) and coupling to the leads results in a singlet state of (2,0) ($|S_{(2,0)}\rangle$) if the single dot exchange is large, $J_{(2,0)} \gg k_b T$, which prevents filling of the triplet states. We remark that this is the only strict temperature requirement in this paper. Adiabatically changing the bias of the double dot system to the (1,1) stability island (position C, Fig. 8.4b) results in adiabatic passage of the (2,0) singlet to the (1,1) singlet ($|S_{(1,1)}\rangle = (|\uparrow\downarrow\rangle - |\downarrow\uparrow\rangle)_{(1,1)}/\sqrt{2}$). If this is accomplished much faster than dephasing mechanisms, the (1,1) singlet can be prepared with high fidelity. Assuming a linear ramp of detuning with a time

τ, the probability of error goes as $\pi(\tau/T_2^*)^2(10^{-2} + (\hbar/\epsilon_z T_2^*)^2)$; for $\tau = 1$ ns and $T_2^* = 10$ ns, the fidelity is > 0.99.

In addition, we can exploit the double-dot system to make a partial Bell measurement that leaves the logical subspace of our system untouched (up to a correctable phase). To achieve this, two spins are placed separated but adjacent quantum dots and the detuning is adiabatically changed from position C to position B. Only the singlet ($|S\rangle$) transfers; waiting a time t_1 in this configuration allows a charge measurement to distinguish between (2,0) ($|S\rangle$ result) and (1,1) (one of three triplet states). Adiabatically returning to C and waiting a time T_2^* switches the singlet and $m_s = 0$ triplet ($|T_0\rangle$) states with probability 1/2. Going again to B, if the triplet state was switched to $|S\rangle$, it transfers to (2,0), producing a noticeable charge signal. Repeating this process k times can generate, with probability $1 - 1/2\sqrt{k}$, a charge signal for the $m_s = 0$ subspace; the total time for charge measurement is $t_M/2 \simeq k(T_2^* + t_m) + t_1$, where t_m is the time to make a single charge measurement. In our present implementation, long t_m may be the main limitation for the purification protocol discussed below [4]. The three results of measurement are (a) singlet, (b) $m_s = 0$ triplet, or (c) $|m_s| = 1$. During this time, the $|m_s| = 1$ states remain untouched except for a phase; we now show how this measurement procedure, denoted M_{AB}, can generate our desired entangled state, $|\phi^+\rangle$, and adjust the phase for such a state.

Starting with four dots (1–4) (Fig. 8.1c), we prepare singlets in 12 and 34; this initial state is $|S\rangle_{12}|S\rangle_{34}$. Applying M_{23} and keeping only the $|m_s| = 1$ result (occurring with probability 1/2) yields the state $|\phi^+\rangle$. This is shown in figure 8.5. To correct the accumulated phase error on it, we use a sequence: [wait($t_M/4$), SWAP_{12}, SWAP_{34}, M_{23}, SWAP_{12}, SWAP_{34}, wait($t_M/4$)], which we now study.

[4] Alternatively, an external magnetic field gradient or slow adiabatic passage allows for deterministic rotation of $|T_0\rangle$ to $|S\rangle$, and greatly improves the measurement efficiency and time.

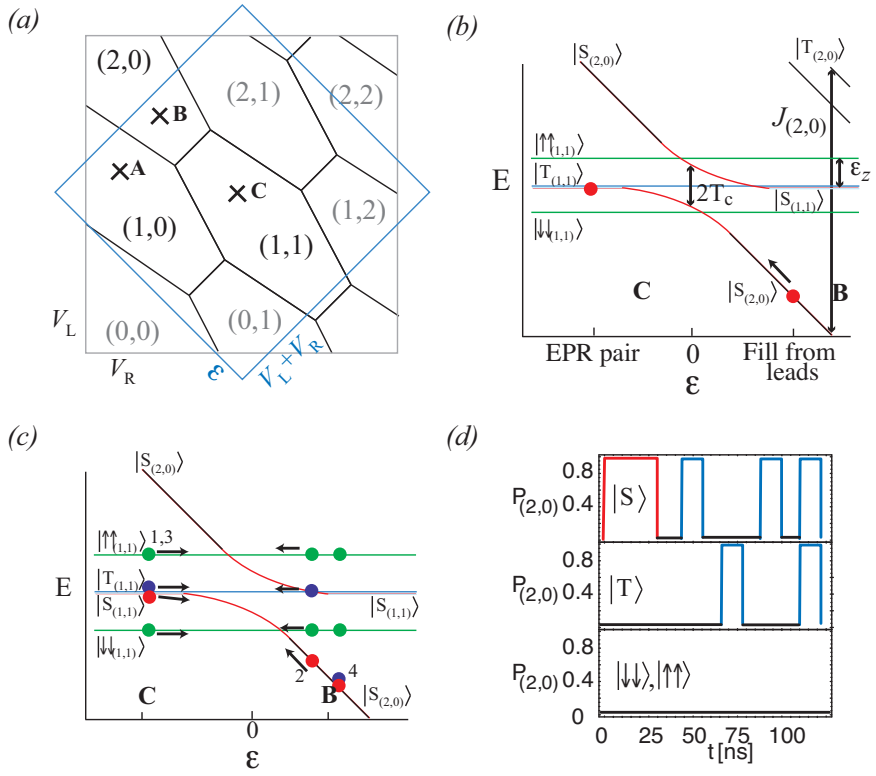

Figure 8.4: (a) Stability diagram of a double dot system, with gate voltages for left and right dots, V_L, V_R and alternative axes of detuning and total voltage, $\epsilon, V_L + V_R$. The three positions A, B, and C are marked (b) Energy level diagram for detuning between B and C. An external magnetic field Zeeman (E_z) splits the triplet levels of the (1,1) configuration; tunnel coupling leads to an avoided crossing at $\epsilon = 0$; by starting in $|S_{2,0}\rangle$ at B and adiabatically changing ϵ to C a separated singlet is generated. (c) The four stage measurement procedure, as described in the text. (d) Example signals of the measurement for four possible initial states, as labeled; section in red occurs only for $|S\rangle$; blue only for $|S\rangle, |T_0\rangle$.

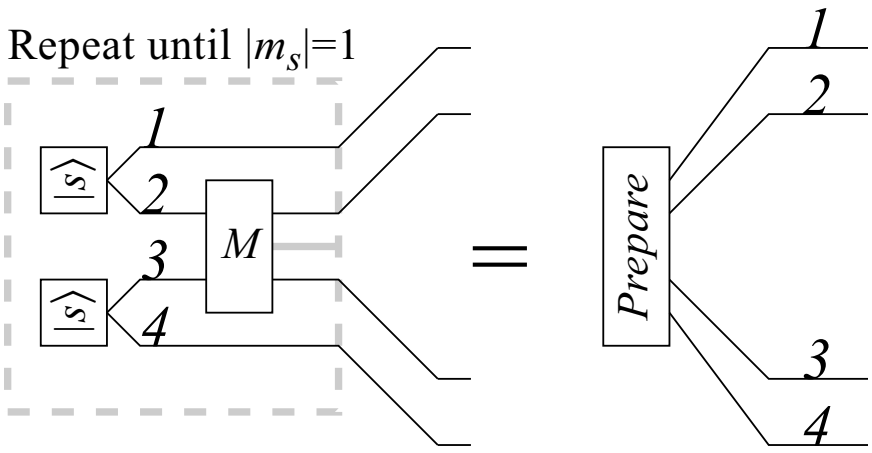

Figure 8.5: Scheme for entanglement generation that is independent of quasi-static fields. Generate two singlets ($|S\rangle_{12}$ and $|S\rangle_{34}$), followed by M^{23}. Keep, and transport, if the measurement result is $|m_s| = 1$; otherwise, restart the process.

8.3.3 Dynamical DFS

We examine the dynamical DFS in detail, with a general noise formulation. While we focus on hyperfine terms, other low frequency noise will be similarly corrected. To be specific, we assume a phase noise term $\eta(t)$ acts on electron spins, characterized by a power spectrum, $S(\omega)$ of integrated power $(T_2^*)^2$ with a (possibly polynomial) high frequency cutoff at $\gamma \ll 1/T_2^*$. For example, the hyperfine interaction in quantum dots, with long-time scale non-Markovian dynamics, is well described by this process [134].

In a frame rotating with external magnetic field (which also defines up and down spin), the phase term acts on a spin state as $|\uparrow\rangle \pm |\downarrow\rangle \rightarrow |\uparrow\rangle \pm e^{-i\int_0^t \eta(t')dt'}|\downarrow\rangle$. Using two electron spins in separate, adjacent dots to create the encoded space, $|0_L\rangle, |1_L\rangle$, this action may be represented by a stochastic evolution operator, $U(t,0) = e^{-i\int_0^t \eta(t')dt'\sigma_x^L}$, where σ_x^L is a Pauli matrix for the encoded space, i.e., flips the logical bit. As the dots are adjacent, they may easily be SWAPed. The pulse sequence [wait($\tau/4$), SWAP, wait($\tau/2$), SWAP,

wait$(\tau/4)$] gives a reduced power spectrum,

$$S_{DDFS}(\omega) = S(\omega)\frac{256}{\tau^2\omega^2}\cos^2(\frac{\tau\omega}{8})\sin^6(\frac{\tau\omega}{8}) \ . \tag{8.17}$$

For frequencies below $1/\tau$, $S_{DDFS}(\omega) \simeq S(\omega)\frac{\tau^4\omega^4}{1024}$; if the dominant noise mechanism has only low frequency components (such as hyperfine terms) the suppression can be dramatic. For SWAP operations performed by use of exchange gates, the gate must be performed in a time $\tau_{ex} \ll T_2^*$; with physical exchange of electrons, e.g., by use of an auxiliary dot, this requirement is relaxed.

The DFS also reduces phase errors incurred during transport of the electron spins. For example, two electrons forming a logical state are moved sequentially through the same channel (i.e., same series of quantum dots) with a separation time τ_T ($\approx 4\sigma/v$, where σ is the lateral radius of each dot, and v the average velocity of transport). Replacing $\eta(t)$ with $\eta(x,t)$, we set $\langle\eta(x,t)\eta(x',t')\rangle = C(|x-x'|)\int_{-\infty}^{\infty} S(\omega)e^{i\omega(t-t')}d\omega$ for transport through a series of quantum dots, where $C(x) = e^{-x^2/2\sigma^2}$. The resulting spectral function is

$$S_T(\omega) = \int_{-\infty}^{\infty} S(\nu)\sin^2[\frac{\nu\tau_T}{2}]\frac{e^{-(\frac{\tau_T}{4})^2(\nu-\omega)^2/2}}{\sqrt{2\pi(4/\tau_T)^2}}\ d\nu \ . \tag{8.18}$$

This shows a suppression of noise with frequencies $\ll 1/\tau_T$ by $\tau_T^2\omega^2/8$.

Considering practical parameters, we set $\gamma = \gamma_{dd} = 1$ ms^{-1}, $T_2^* = 10$ ns, and use $S(\omega) = e^{-\frac{\omega^2}{2\gamma^2}}/(T_2^*\sqrt{2\pi\gamma^2})$. For states stored in the DDFS with a cycle time τ, after one cycle the probability of error is $p_{\rm err} = \frac{3}{2^{12}}\frac{\gamma^4\tau^6}{(T_2^*)^2}$. Transporting through $n = L/v$ quantum dots, we find the probability of a phase error occurring for the encoded states is $p_{{\rm err},T}(n) \approx \sqrt{\frac{\pi}{128}}\left(\frac{\gamma}{T_2^*}\right)^2\tau_T^4 n$. Even for cycle and transport times (τ,τ_T) approaching T_2^*, phase errors due to low frequency terms occur with rates much slower than milliseconds, indicating a suppression of more than 10^5. Thus the dynamical DFS technique provides a powerful quantum memory and low-error transport channel, limited by errors in SWAP operations and spin-flip processes.

8.3.4 Purification

We now introduce a purification protocol for encoded entangled states that can remove all remaining errors, based on partial Bell measurement and exchange gates. Errors during the generation, transport, and storage processes can lead to (i) errors within the $\{|0_L\rangle, |1_L\rangle\}$ logical subspace, and (ii) population of states $|2_L\rangle = 1/\sqrt{2}(|\uparrow\uparrow\rangle + |\downarrow\downarrow\rangle)$, $|3_L\rangle = 1/\sqrt{2}(|\uparrow\uparrow\rangle - |\downarrow\downarrow\rangle)$ outside the logical subspace. Both kind of errors reduce the fidelity of the encoded entangled state $|\phi^+\rangle_{A_1A_2B_1B_2}$ and need to be corrected. We introduce a purification protocol that completely corrects arbitrary strength errors of type (ii), and corrects for errors of type (i) that occur with probability less than 1/2.

We start by reviewing the measurement scheme (Fig. 8.4c,d), which has three possible outcomes: (a) P_S: measure $|S\rangle$, state after measurement is $|S\rangle$; (b) P_{T_0}: measure $|T_0\rangle = 1/\sqrt{2}(|\uparrow\downarrow\rangle + |\downarrow\uparrow\rangle)$, state is $|S\rangle$; (c) $P_{|m_s|=1}$: state is coherently projected into the two–dimensional subspace spanned by $\{|\uparrow\uparrow\rangle, |\downarrow\downarrow\rangle\}$. Consider the following sequence of measurements of this type with indicated results: $O_A^{(0)} = P_S^{(A_1'A_2')} P_{|m_s|=1}^{(A_1A_1')} P_{|m_s|=1}^{(A_2A_2')}, O_A^{(1)} = P_{T_0}^{(A_1'A_2')} P_{|m_s|=1}^{(A_1A_1')} P_{|m_s|=1}^{(A_2A_2')}$. The action of $O_A^{(k)}$ on logical basis states is given by

$$O_A^{(k)} |i_L\rangle_{A_1A_2} |j_L\rangle_{A_1'A_2'} = P_{\{0,1\}} |i_L \oplus j_L \oplus k\rangle_{A_1A_2} |0_L\rangle_{A_1'A_2'},$$

where the projector $P_{\{0,1\}}$ indicates that, in both A, A', all components outside the $\{|0_L\rangle, |1_L\rangle\}$ subspace are projected out. The measurement sequence can thus be used to detect all errors of type (ii), while the operations $O_A^{(k)}$ act within the logical subspace similarly to a CNOT operation ($\oplus$ denotes bit-wise addition modulo 2).

Consider a mixed state $\rho_{A_1A_2B_1B_2}$ resulting from imperfect distribution of $|\phi^+\rangle$. We decompose ρ into three terms, $\rho = \rho(\vec{x}) + \rho_{\rm od} + \rho_R$. We have $\rho(\vec{x}) = x_0 |\phi^+\rangle\langle\phi^+| + x_1 |\phi^-\rangle\langle\phi^-| + x_2 |\psi^+\rangle\langle\psi^+| + x_3 |\psi^-\rangle\langle\psi^-|$, where $|\phi^\pm\rangle = (|0_L0_L\rangle \pm |1_L1_L\rangle)/\sqrt{2}$ and $|\psi^\pm\rangle = (|0_L1_L\rangle \pm |1_L0_L\rangle)/\sqrt{2}$ are the logical Bell states. All off-diagonal elements in the Bell basis

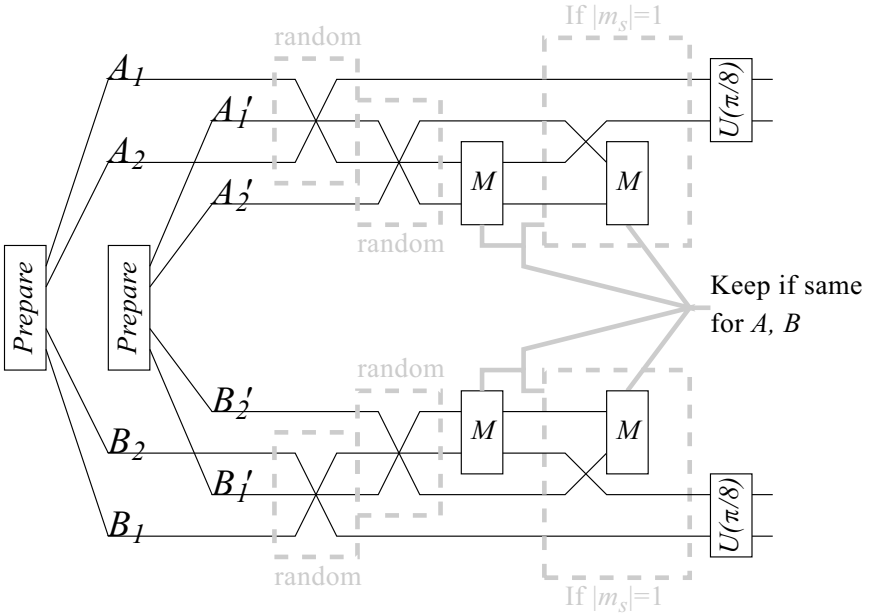

Figure 8.6: A quantum gate network outlining the purification process. Two logical entangled pairs (AB and $A'B'$) are generated. Random swap operations remove off-diagonal components of the density matrix. The M operation is performed on one physical pair of each side; if necessary, additional measurement and swap is performed. If all measurement results are the same for AA' and for BB', keep the final pair, and perform resonant exchange to give the protocol 2 purification map.

($\rho_{\rm od}$) and terms containing $\{|2_L\rangle, |3_L\rangle\}$ (ρ_R) are made irrelevant by the protocol.

Given two mixed states $\rho_{A_1A_2B_1B_2} \otimes \rho'_{A_1'A_2'B_1'B_2'}$, described by $\vec{x}$ and $\vec{x}'$ (and the irrelevant $\rho_{\rm od} + \rho_R$) respectively, the following sequence of *local* operations obtains with certain probability a state with higher fidelity and hence purifies the state: (i) partial depolarization of ρ using, with probability $p = 1/2$, $\mathrm{SWAP}_{A_1A_2} \otimes \mathrm{SWAP}_{B_1B_2}$ or identity, and similarly for ρ'; (ii) exchange gates $U(\pi/8)_{A_1A_2} \otimes U(-\pi/8)_{B_1B_2}$ at $\rho_{A_1A_2B_1B_2}$ (and same for ρ'); (iii) Sequence of measurements $O_A^{(k)}$, $O_B^{(l)}$; keep state $\rho_{A_1A_2B_1B_2}$ only if $k = l$, i.e. the results in final measurement coincide in A and B. The entire procedure is shown in Fig. 8.6

The effect of (i) is to erase off–diagonal terms of the form $|\phi^{\pm}\rangle\langle\psi^{\pm}|$ which may

contribute to the protocol. The operation in (ii) exchanges logical states $|\psi^+\rangle \leftrightarrow |\psi^-\rangle$ while keeping $|\phi^\pm\rangle$ invariant. Finally (iii) realizes—in addition to the projection into the $\{|0_L\rangle, |1_L\rangle\}$ logical subspace in A and B which erases all terms ρ_R, ρ'_R—a purification map. In particular, we find that the remaining off diagonal elements do not contribute and the action of the protocol can be described by the non-linear mapping of corresponding vectors $\vec{x}$, $\vec{x}'$. The resulting state is of the form $\rho(\vec{y}) + \tilde{\rho}_{\rm od}$ (note that $\rho_R = 0$), where

$$\begin{aligned} y_0 &= (x_0x'_0 + x_2x'_2)/N \quad , \quad y_1 = (x_1x'_1 + x_3x'_3)/N \ , \\ y_2 &= (x_1x'_3 + x_3x'_1)/N \quad , \quad y_3 = (x_0x'_2 + x_2x'_0)/N \ , \end{aligned} \tag{8.19}$$

and $N = x_0x'_0 + x_2x'_2 + x_1x'_1 + x_3x'_3 + x_1x'_3 + x_3x'_1 + x_0x'_2 + x_2x'_0$ is the probability of success of the protocol. This map is equivalent (up to a reduced success probability by a factor of 1/8) to the purification map obtained in Ref. [49] for non–encoded Bell states. It follows that iteration of the map—which corresponds to iteratively applying the purification procedure (i-iii) to two identical copies of states resulting from successful previous purification rounds—leads to a (encoded) maximally entangled state $|\phi^+\rangle$. That is, the map has $\vec{y} = (1, 0, 0, 0)$ as attracting fixed point whenever $x_0 > x_1 + x_2 + x_3$. We emphasize that *all* errors leading outside the logical subspace (in particular all spin flip errors), independent of their probability of occurrence, can be corrected. This implies that even states with a very small fidelity F can be purified, provided that errors within the logical subspace do not exceed probability 1/2.

Additionally, since the resulting maps are identical to those of [49], the purification protocol shows a similar robustness against noise in local control operations. That is, errors of the order of several percent in local control operations can be tolerated while still leading to purification. We also remark that methods such as (nested) entanglement pumping can be applied [55].

While we have focused on gate controlled quantum dots, these ideas may find implementation in electro-optically manipulated small arrays of self-assembled quantum dots [113]. In general, the prescription for entanglement generation in solid-state environments we describe here could also be followed in other solid-state systems such as superconductor-based qubit designs [195]. We anticipate that such long-range entangled state generation will have wide application, in scalable quantum computer architectures and in tomography based on entangled states.

8.4 Conclusions

We have suggested a means of implementing entangled pair generation in quantum dot systems. Combining this generation with a simple scheme for singlet-triplet measurement, means of measuring the local magnetic field are indicated. More powerfully, the means to transport the entangled spin and using only local operations purify the entangled pairs leads to the possibility of robust, long-distance entanglement generation and purification using local preparation and measurement with current quantum dot technology.

By analyzing the dominant sources of dephasing, dynamical decoherence free subspaces that take full advantage of the long correlation time of nuclear spins in quantum dots extends these non-local generation techniques to the regime of relaxation-limited decoherence. Such averaging demonstrates that some four-particle maximally entangled (GHZ) states may be more robust that even two-particle states when the dominant forms of dephasing are quasi-static bath sources. These states may be generated with a straightforward measurement, relying upon the nuclear-spin-induced magnetic field gradient or a small external field gradient. The same measurement procedure further allows for a complete purification protocol, robust to both additional phase errors and spin flip errors.

With a resource such as non-local, high purity entangled pair generation on demand, quantum cryptography, quantum repeater, and even larger scale quantum computation schemes become feasible. The ideas promulgated in this paper provide a means for producing non-local entanglement, which can be used with local operations to produce non-local two-particle entangling gates between qubits. We suggest that experiments with the current generation of quantum dot devices can robustly implement these ideas.

We gratefully acknowledge helpful conversations with J. Petta and A. Johnson. The work at Harvard was supported by ARO, NSF, Alfred P. Sloan Foundation, and David and Lucile Packard Foundation. The work at Innsbruck was supported by the ÖAW through project APART (W.D.), the European Union, Austrian Science Foundation, and the DFG.

Chapter 9

Cavity quantum electrodynamics with semiconductor double-dot molecules on a chip

J. M. Taylor and M. D. Lukin

Department of Physics, Harvard University, 17 Oxford Street, Cambridge, MA 02138 USA

We describe a coherent control technique for coupling electron spin states associated with semiconductor double-dot molecule to a microwave stripline resonator on a chip. We identify a novel regime of operation in which strong interaction between a molecule and a resonator can be achieved with minimal decoherence, reaching the so-called strong coupling regime of cavity QED. We describe potential applications of such a system, including low-noise coherent electrical control, fast QND measurements of spin states, and long-range spin coupling.

Controlling quantum behavior of realistic solid-state systems is an intriguing challenge in modern science and engineering. While over the past several decades much progress has been made in manipulation of isolated atomic and optical systems, only recently have solid-state systems demonstrated controlled, coherent behavior at a single quantum

level [140, 138, 194, 128, 195, 151]. The complex environment of solid state systems make them significantly more challenging to isolate and operate coherently. Furthermore, robust quantum control techniques analogous to those used in AMO physics still need to be developed.

Recently, a novel approach to quantum manipulation of spin-based quantum systems in semiconductor quantum dots has been proposed and experimentally realized [119, 151, 184]. This approach combines spin and charge manipulation to take advantage of the long memory times associated with spin states and, at the same time, to enable efficient readout and coherent manipulation of coupled spin states using intrinsic interactions. While this allows one to consider architectures based on pulsed quasi-static electrical control and static magnetic field [179], for many purposes it is desirable to develop fast and robust quantum control techniques based on microwave manipulation.

In this Letter we describe a technique for electrical coupling of electron spin states associated with semiconductor double-dot molecule to microwave stripline resonator on a chip [29, 12, 195]. The essential idea is to use an effective electric dipole moment associated with exchange coupled spin states of a double-dot molecule to couple to the oscillating voltage associated with a stripline resonator. Taking into account the main decoherence mechanisms for both spin and charge degrees of freedom, we identify an optimal point of operation in which strong interaction between molecule and resonator can be achieved with minimal decoherence, thereby enabling the strong coupling regime of cavity QED. Finally, we describe potential applications including low-noise coherent electrical control, fast QND measurements of spin states, and long-range coupling of pairs of spins.

Before proceeding we note the early proposals for achieving the strong coupling regime of cavity QED with Cooper pair qubits and single electrons in double-dot molecules [29, 12]. Strong coupling of superconducting qubits to stripline cavities have been recently im-

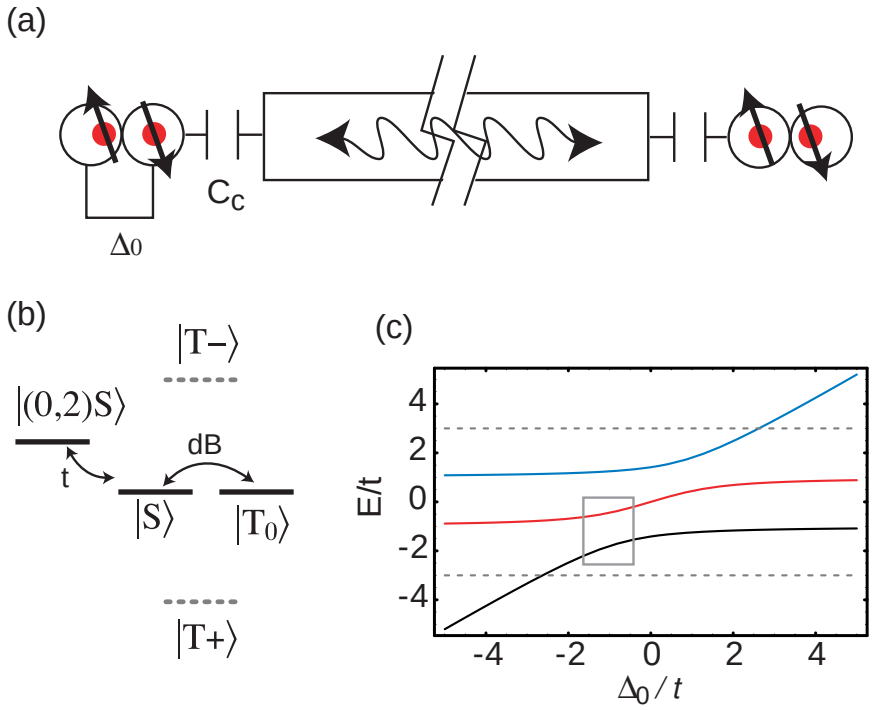

Figure 9.1: (a) Schematic of two double dots, biased with external potential Δ_0, capacitively coupled to a transmission line resonator. (b) Energy level diagram showing the (0,2) singlet and the four (1,1) two-spin states. (c) Low energy spectrum in units of t with small gradient $dB = t/10$: for large, negative Δ_0, the ground state is $|(0,2)S\rangle$. The T_0 triplet (red) and $T_\pm$ triplets (dashed grey) are far from resonance with the $(0,2)$ triplet. Note the optimal point (gray box) occurs at the left-most avoided crossing.

plemented in pioneering experiments by Schoelkopf and co-workers [195]. This system has enabled a range of beautiful demonstrations ranging from control and measurement of the qubit through the resonator to SWAP of the qubit with the state of the resonator. Finally, ideas similar to the present work have been proposed recently, using vertical quantum dot systems [20].

9.1 Effective Hamiltonian

We consider the specific system outlined in the Figure 9.1. Here two electron spins are localized in adjacent quantum dots, coupled via tunneling. One of the dots is capacitively

coupled to a transmission line resonator. A modest (100 mT) external magnetic field along an axis z Zeeman-splits the spin-aligned states, $|T_+\rangle = |\uparrow\uparrow\rangle$ and $|T_-\rangle = |\downarrow\downarrow\rangle$, while the spin-anti-aligned states are used as a qubit degree of freedom: $|(1,1)T_0\rangle = (|\uparrow\downarrow\rangle + |\downarrow\uparrow\rangle)/\sqrt{2}$ and $|(1,1)S\rangle = (|\downarrow\uparrow\rangle - |\downarrow\uparrow\rangle)/\sqrt{2}$. The notation (n_L, n_R) labels the number of electrons in the left and right quantum dots. In addition to the qubit states, an auxiliary singlet state with two electrons in one quantum dot, $|(0,2)S\rangle$, is coupled via tunneling t to the separated singlet, $|(1,1)S\rangle$ (Fig. 9.1b). The energy of the auxiliary state is determine largely by the bias Δ due to the electric field; control of Δ allows to control the qubit's evolution. The Hamiltonian for this three state system is:

$$\begin{aligned} H_{DD} &= \Delta|(0,2)S\rangle\langle(0,2)S| + t|(1,1)S\rangle\langle(0,2)S| + \\ &\quad dB|(1,1)S\rangle\langle(1,1)T_0| + \text{H.c.}. \end{aligned} \tag{9.1}$$

We have introduced a static magnetic field gradient between the two dots $dB = g^*\mu_B(B_z^L - B_z^R)$, which mixes the singlet and triplet states. This system has been studied in detail in Refs. [16, 29, 39, 184]. Parameter ranges for experiments are $t \simeq 0 - 10\mu$eV and $dB \sim 0.1 - 1\mu$eV. State preparation, measurement, 1-qubit gates, and local 2-qubit gates can be achieved by changing the bias Δ between $|(0,2)S\rangle$ and $|(1,1)S\rangle$ [119, 179, 151].

Interaction with the resonator is included naturally by writing the bias as a contribution from static fields, Δ_0, set by voltages on the gates defining the double dot, and a contribution from the resonator itself:

$$\Delta = \Delta_0 + e\hat{V}\frac{C_c}{C_{\text{tot}}}\ , \tag{9.2}$$

where C_c is the capacitive coupling of the resonator to the dot, while C_{tot} is the total capacitance of the double dot. The voltage due to the resonator of length l, capacitance

per unit length C_0, and impedance Z_0 is quantized as [29]

$$\hat{V} = \sum_k \sqrt{\frac{\hbar\omega_k}{lC_0}}(\hat{a}_k + \hat{a}_k^\dagger) \ . \tag{9.3}$$

We now deduce an effective Hamiltonian for the system when the splitting between eigenstates of Eq. 9.1, ω, is comparable to the fundamental mode frequency of the resonator, $\omega_0 = \pi/lZ_0C_0$ (i.e., the cavity detuning $\delta = \omega - \omega_0$ is small). Neglecting the higher energy modes, we write the Hamiltonian for the resonator itself as $H_{TLR} = \hbar\omega_0\hat{a}^\dagger\hat{a}$, where $\hat{a}$ is the lowest energy mode destruction operator, and the interaction with the dot is

$$U = g(\hat{a} + \hat{a}^\dagger)|(0,2)S\rangle\langle(0,2)S| \tag{9.4}$$

where $g = e\frac{C_c}{C_{\rm tot}lC_0}\sqrt{\hbar\pi/Z_0} = \eta\omega_0$ is the vacuum Rabi coupling between the double dot and the resonator. In practice, for $\omega_0 = 2\pi \times 10$ GHz, $g = 2\pi \times 100$ MHz (i.e., $\eta = 10^{-2}$) is achievable [29, 195, 12]). A reduction of ω_0 by lowering lC_0 results in a comparable reduction of g. Finally, as $Q > 10^6$ resonators are possible in the microwave domain [29, 195], the quantization of the resonator voltage is appropriate. In practice, the need to work with a finite local external magnetic field (100 mT) may limit $Q \approx 10^4$ [73].

9.2 Operating point

We seek a set of parameters $\{\Delta_0, T_0, dB\}$ such that the system can be coupled to and controlled by the resonator. This "operating point" should maximize the coupling to the resonator and minimize the noise in the combined system. To motivate the optimal choice, let us first proceed with small tunnel coupling t and cavity coupling g. In this case the eigenstates are $|{\downarrow\uparrow}\rangle, |(0,2)S\rangle, |{\uparrow\downarrow}\rangle$, with eigenenergies $-dB, \Delta_0, dB$. Setting the energy difference $\tilde{\Delta} = dB - \Delta_0 \approx 0$, degenerate perturbation theory in the tunnel coupling t reveals an avoided crossing at this balanced point between $|{\downarrow\uparrow}\rangle$ and $|(0,2)S\rangle$ with an energy gap

$\omega = \sqrt{\tilde{\Delta}^2 + 4t^2}$ around $\tilde{\Delta} = 0$ (Fig. 9.1b) and mixing angle $\theta = \frac{1}{2}\tan^{-1}(2t/\tilde{\Delta})$. Working in the rotating frame with the rotating wave approximation, we find an effective Hamiltonian for the combined system to be

$$H = \hbar(\omega - \omega_0)|1\rangle\langle 1| + g_{\text{eff}}\hat{a}|1\rangle\langle 0| + \text{H.c.} \tag{9.5}$$

where, at $\theta = \pi/4$, $|0(1)\rangle = (|{\downarrow\uparrow}\rangle - (+)|(0,2)S\rangle)/\sqrt{2}$ and

$$g_{\text{eff}} = -\frac{1}{2}\eta\omega_0 \sin 2\theta \approx -\eta t \ . \tag{9.6}$$

We choose $\theta = \pi/4$ for two reasons. First, at this point the gap ω is insensitive to first-order changes in Δ_0 and dB. Such zero-derivative points are optimal for controlling quantum bits with imperfect electronics and in the presence of low frequency noise [124, 194, 167, 69, 203]. In our case this suppresses fluctuations in control electronics (Δ_0) and in the magnetic field gradient (due to hyperfine interactions), which are the dominant dephasing terms. Second, the coupling coefficient g_{eff} is directly proportional to the energy splitting in the system, as would be expected of a "bare" coupling of comparable strength.

The cost of working at this point is increased sensitivity to fluctuations in t (it effects both g_{eff} and ω at first order) and a higher probability of relaxation due to the enhanced charge admixture of the qubit states (see the analysis of inelastic effects below). The former could be mitigated: as no time-dependent control of t is required, the gates that set t can be heavily filtered to greatly reduce potential noise.

For long term storage of the quantum information, we can adiabatically map the states $|0\rangle, |1\rangle$ to the spin states $|{\downarrow\uparrow}\rangle, |{\uparrow\downarrow}\rangle$ via change of Δ_0, going to a well separated regime. As long as the change of Δ_0 is slow with respect to the splitting dB, the process is entirely adiabatic; furthermore, we are only sensitive to charge fluctuations on a frequency scale faster than $\sim dB$. The spin states, protected by occassional refocusing, are mostly insensitive to charge relaxation and dephasing [122, 21]. Thus, when long quantum memory

times or insensitivity to charge-based relaxation is necessary, the system can be adiabatically mapped to such a separated regime; when operation with the resonator is necessary, they can be mapped back to the balanced regime of $\Delta_0 \approx -dB$.

9.3 Generalized approach

We now proceed to generalize the above analysis to an arbitrary set of parameters $p = \{dB, t, \Delta_0\}$, treating the interaction with the cavity as a perturbation. We write the eigenenergies of H_{DD} as $E_m(p)$ ($m = 0, 1, 2$, and $E_0 \leq E_1 \leq E_2$) and the eigenvectors as

$$\begin{pmatrix} |0\rangle \\ |1\rangle \\ |2\rangle \end{pmatrix} = \chi^\dagger(p) \begin{pmatrix} |(1,1)T_0\rangle \\ |(1,1)S\rangle \\ |(0,2)S\rangle \end{pmatrix} \tag{9.7}$$

where χ is a 3x3 unitary matrix. In the rotating wave approximation, we may neglect all cavity interaction terms diagonal in the eigenstates. Furthermore, when the energy differences are non-degenerate ($E_1 - E_0 \neq E_2 - E_1$), we may also only keep coupling to the transition with energy $E_1 - E_0 \approx \hbar\omega_0$. Then,

$$U = g\hat{a}^\dagger \chi_{02}\chi_{21}^* |0\rangle\langle 1| + \text{H.c.} \tag{9.8}$$

Thus, $g_{\text{eff}}(p) = g\chi_{02}(p)\chi_{21}^*(p)$. Keeping t fixed, we plot g_{eff} and the expected error in operations due to relaxation (calculated below). Of immediate interest is the regime of $dB \sim t$, where $g_{\text{eff}}/g > 0.3$ and $\xi \neq 0$. This suggests that maximal coupling to the cavity occurs when $t, -\Delta_0$, and dB are all comparable.

9.4 Noise and decoherence

We now demonstrate the favorable noise properties of the balanced system. Three kinds of error are considered: relaxation of the charge system in a time T_1, additional

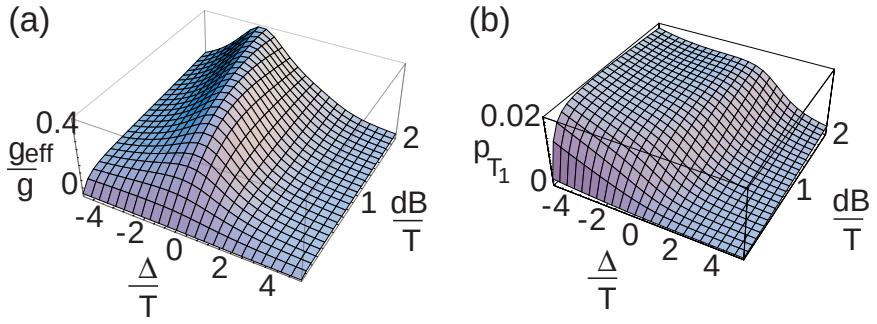

Figure 9.2: (a) Coupling strength, $g_{\rm eff}$, in units of bare coupling g, as a function of field gradient dB and bias Δ_0. (b) Calculated probability of error in swapping a double-dot state with the resonator state due to charge-based relaxation using $t = 4$ μeV and an inverse temperature of 10 μeV.

dephasing of the charge system in a time $T_{2,a} = T_2 - 2T_1$, and decay of the cavity photon at a rate κ. We assume the additional dephasing arises from low frequency fluctuations [194, 127, 167, 203, 179, 184], due to changes of the electrostatic gates and magnetic field gradient, e.g., as noise on Δ_0 and dB.

For charge-based relaxation, coupling to a phonon bath with spectral density $\rho(\omega) = \sum_k |g_k|^2 \delta(\omega - \omega_k)$ will lead to decay [24]. Using the spin-boson model in the perturbative regime yields an overall error rate from relaxation and incoherent excitation:

$$1/T_1 = 2\pi\rho(\omega_{10})|\chi_{20}\chi_{12}|^2 \coth(\omega_{10}\beta/2) \ . \tag{9.9}$$

We estimate $\rho(\omega)$ at $\omega = 76\mu\text{eV}/\hbar$ using measured charge relaxation times [88, 150]. For a double quantum dot system in GaAs and small ω, $\rho(\omega) \propto \omega^3$ [16]. This indicates $2\pi\rho(\omega) \approx \hbar^2\omega^3/(1\text{meV})^2$ for the low energy limit. Reducing the resonant frequency lowers relaxation rates. Near the optimal point, with $\omega_{10} \sim 2\pi\times$ 2 GHz, $T_1 \sim 1\mu$s.

Additional dephasing ($T_{2,a}$ term) arises from variations of the energy gap, $\Delta_0(t) = \Delta_0 + \epsilon(t)$ with $\langle\epsilon(t)\epsilon(t')\rangle = \int d\omega \ S(\omega)e^{i\omega(t-t')}$. We assume a high frequency cutoff of the noise at $\gamma \ll E_1 - E_0, \omega_0$. The contribution to error at first order arises from $\omega_{10}(t) = \omega_{10} + \epsilon(t)(\partial\omega_{10}/\partial\Delta_0)$. When the pre-factor $\eta_\Delta = |\partial\omega_{10}/\partial\Delta_0|^2$ is non zero, there is first-

order dephasing. In the rotating frame, the off-diagonal density matrix element evolves as

$$\rho_{01}(t) \sim \exp\left[-\eta_{\Delta_0}\int d\omega\ S(\omega)\frac{\sin^2(\omega\tau/2)}{(\omega/2)^2}\right]\ . \tag{9.10}$$

For example, when $\gamma \ll 1/\tau$, the decay is Gaussian with a time constant $T_2 \sim T_{2,\mathrm{bare}}/\sqrt{\eta_{\Delta_0}}$, where the characteristic time $T_{2,\mathrm{bare}} = 1/\sqrt{\int d\omega\ S(\omega)}$. Bare dephasing times of ~ 1 ns were observed for qubit frequencies of $\sim 2\pi \times 20$ GHz [88, 150]. However, longer $T_{2,\mathrm{bare}}$ times might be achieved for qubits at $\sim 2\pi \times 1$ GHz through better high- and low-frequency filtering of electronics noise. We will take $T_{2,\mathrm{bare}} = 10$ ns for the remainder of the paper; this limit arises from the combined effect of charge-based terms and nuclear spin-related dephasing [14, 112, 151].

At the zero derivative point ($\partial\omega/\partial\Delta_0 = 0$) second-order terms must be considered [194, 69, 133]. To the leading order [69], we find dephasing occurs over a timescale $T_2 \sim \omega_{10}(T_{2,\mathrm{bare}})^2$. More detailed calculations indicate that the underlying physics of the bath becomes important near zero-derivative points [69, 133]. Thus the optimal point combines the maximal coupling g_{eff} to the resonator with an extended T_2 time (Fig. 9.3). In this regime, with $\omega_0 = 2\pi \times 1.5$ GHz, $g_{\mathrm{eff}}T_2 \approx 100$. We note that away from the optimal point, even assuming maximal coupling, $g_{\mathrm{eff}}T_2 \lesssim 1$. For example, in the strongly biased regime ($\Delta/t \gg 1$), $g_{\mathrm{eff}}T_2 \approx gT_{2,\mathrm{bare}} \lesssim 1$. We conclude that only near the optimal point may the strong coupling regime be achieved.

9.5 Quantum control

We now discuss potential applications. Coherent control of the system with little sensitivity to low frequency noise is achieved by driving the resonator on resonance with a microwave pulse. We can describe this scenario by making the cavity state a coherent state,

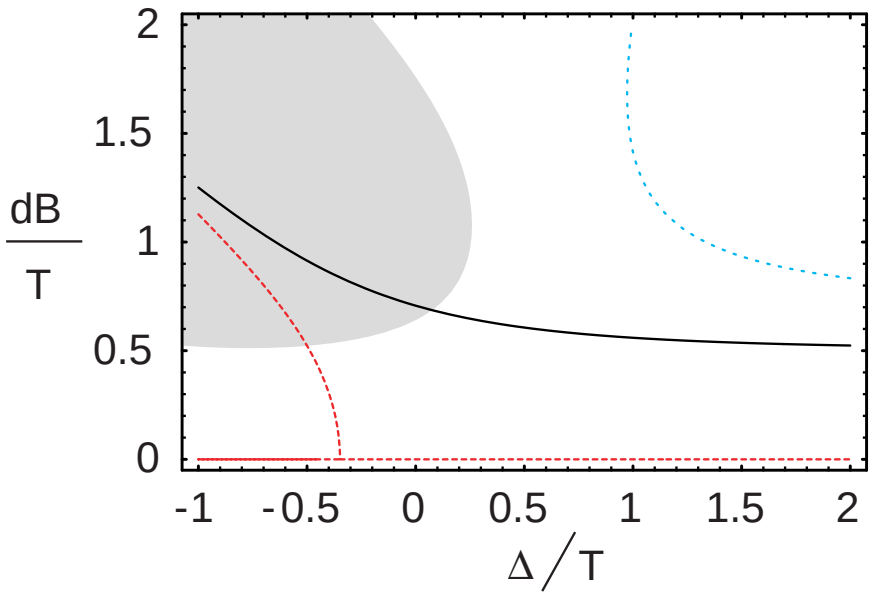

Figure 9.3: Solutions of $\partial\omega_{10}/\partial\Delta_0 = 0$ (black), $\partial\omega_{10}/\partial t = 0$ (blue), and $\partial\omega_{10}/\partial dB = 0$ (red). The region of $g_{\text{eff}}/g > 0.3$ is marked in grey.

$|\alpha\rangle$, letting us replace $\hat{a}$ with α. We would expect Rabi oscillations between $|0\rangle$ and $|1\rangle$ with Rabi frequency $\Omega = g_{\text{eff}}\alpha$. Low frequency components of the driving field (DC offsets) are greatly reduced because of the gap induced by t and the insensitivity of the gap energy ω on variations of Δ.

Another technique is a quantum non-demolition measurement. When the microwave transition is detuned from the cavity by $\tilde{\Delta}$, the evolution yeilds a qubit-dependent phase of $\phi_{QND} = \pm g^2\tau/\tilde{\Delta}$ (for $|0\rangle, |1\rangle$ states respectively) for an injected microwave field over a time τ (limited by qubit decay). Assuming that the noise level of the detector exceeds the background by about a factor of ten, the fidelity of such a QND measurement of the encoded spin qubits is given by $F = 1 - 10\kappa/g^2 T_1$ [12]. This single qubit QND measurement can be completed in a time $1/\kappa \sim 1$ μs.

In addition, a wide variety of cavity QED quantum control techniques may be accessible. As an example, we focus on the SWAP operation, where the qubit state is

"swapped" with a photonic state of the resonator. When there are no photons in the cavity and $\delta = 0$, the state $|0\rangle|0\rangle_{\rm cav}$ is stationary, while $|1\rangle|0\rangle_{\rm cav}$ oscillates with Rabi frequency $g_{\rm eff}/\hbar$ to the state $|0\rangle|1\rangle_{\rm cav}$) (we use $|n\rangle_{\rm cav}$ to indicate n photons in the cavity mode). When the time spent oscillating is $\pi\hbar/g_{\rm eff}$, a quantum state of the singlet–triplet system is mapped to the existence or absence of a cavity photon:

$$(\alpha|0\rangle + \beta|1\rangle)|0\rangle_{\rm cav} \rightarrow |0\rangle(\alpha|0\rangle + i\beta|1\rangle)_{\rm cav} \ . \tag{9.11}$$

This process can be controlled by rapidly changing δ to and from zero. In essence, we can convert one quantum bit (the double-dot system) to another quantum bit (the cavity photon), which can then be used for a variety of quantum information tasks, such as long-distance quantum gates, quantum communication, and quantum repeaters [35, 30, 163]. Furthermore, it may allow for coupling to other qubit systems, such as atoms, molecules [169], or superconducting qubits [12].

As an example, we now detail the expected errors for the SWAP operation. Both T_1 and κ contribute to the decay of the system, which lead to population of the state $|0\rangle|0\rangle$, while dephasing, T_2, leads to phase errors in the transformation. Including only relaxation terms, yields a probability of error in "SWAP" of $p_{T_1} = \pi\frac{\kappa+1/T_1}{g_{\rm eff}}$. In addition, pure dephasing (T_2) leads to an error with probability $p_{T_2} = \pi^2/(T_2 g_{\rm eff})^2$. The optimal point has $g_{\rm eff} \approx 0.4\eta E_{10}$, $1/T_1 \approx 0.2\Gamma(E_{10})$, and $T_{2,a} \approx \omega_{10} T_{2,\rm bare}^2$ from noise in Δ_0 and dB. Optimizing against both noise sources suggests that for a bare dephasing time of $T_{2,\rm bare} = 10$ ns, a cavity frequency of ~ 1.5 GHz is optimal for SWAP operations, with a probability of error $\approx 2\%$.

9.6 Conclusions

In summary, we have shown how spin states of double quantum dots can be coupled directly to microwave resonators. An optimal operating point with maximum coupling to the resonator and minimum coupling to some sources of charge and spin noise is found. This suggests a variety of powerful quantum control techniques may become possible for such a system.

We thank A. Imamoglu, G. Burkard, and L. Childress for helpful discussions. This work was supported by ARO, NSF, the Sloan Foundation, and the David and Lucille Packard Foundation.

Chapter 10

Fault-tolerant architecture for quantum computation using electrically controlled semiconductor spins

J. M. Taylor[1], H.-A. Engel[1], W. Dür[2,3], A. Yacoby[4], C. M. Marcus[1], P. Zoller[2,3], M. D. Lukin[1]

[1] Department of Physics, Harvard University, Cambridge, Massachusetts 02138, USA
[2] Institut für Theoretische Physik, Universität Innsbruck, Technikerstraße 25, A-6020 Innsbruck, Austria
[3] Institut für Quantenoptik und Quanteninformation der Österreichischen Akademie der Wissenschaften, Innsbruck, Austria
[4] Department of Condensed Matter Physics, Weizmann Institute of Science, Rehovot 76100, Israel

Information processing using quantum systems provides new paradigms for computation and communication and may yield new insights into our understanding of the limits of quantum mechanics. However, realistic systems are never perfectly isolated from their environment, hence all quantum operations are subject to errors. Realisation of a physical system for processing of quantum information that is tolerant of errors is an outstanding problem in quantum

science and engineering. We develop an architecture for quantum computation using electrically controlled semiconductor spins by extending the Loss–DiVincenzo scenario and by combining an actively protected quantum memory and long-distance coupling mechanisms. Our approach is based on a recently demonstrated encoding of qubits in long-lived two-electron states, which immunizes qubits against the dominant error from hyperfine interactions. We develop a universal set of quantum gates compatible with active error suppression for these encoded qubits and an effective long range interaction between the qubits by controlled electron transport. This approach yields a scalable architecture with favourable error thresholds for fault tolerant operation, consistent with present experimental parameters.

Over the past decade, significant effort has been directed toward the physical realisation of quantum computation. The promise of solid-state systems such as quantum dots[122] and superconducting islands [125, 140] was identified early. Recently, coherent manipulation of solid-state quantum bits, analogous to well developed realisations in atomic physics[28, 36], was experimentally demonstrated[31, 89, 195, 151]. However, achieving fault tolerant quantum computation entails a significant mitigation of environmental couplings, which is particularly challenging in the solid-state. Here, we develop a scalable architecture for solid-state quantum computation based on actively protected two electron spin states in quantum dots[54, 204, 120, 193, 200, 119, 135, 178]. We find a universal set of gates for these encoded states that can be implemented using only local electrical control, and that suppress the effect of hyperfine interactions, the dominant source of error[14, 96, 151, 112, 134, 103, 45]. Our architecture allows for a modular, hierarchical design, and includes autonomous control and non-local coupling via controlled electron transport. Fault tolerant operation[173] appears to be achievable with present experimental methods.

As recently demonstrated experimentally[151], exchange interactions can be used to prepare qubits in well-defined states, protect them from low-frequency noise[200, 178], perform certain single qubit rotations[119, 135], and allow measurement via charge readout with a nearby electrometer[50, 202, 62]. Control of the exchange energy J between adjacent

quantum dots is achieved by electrical means. We expand these operations to include single-qubit rotations based on waiting in small static magnetic field gradients, and two-qubit gates based on the capacitive interaction of four electrons in proximal double dots, completing the universal set of quantum gates compatible with dynamical protection and electrical control. Effective long-range coupling between qubits is provided by moving electrons by use of a single-electron pump or charge-coupled device[144], which allow for many electrons to be transported in parallel before and after two-qubit operations such that they are immune to most dephasing processes during transport[178]. Together, these elements allow us to develop a fully electrical architecture for controlling and coupling qubits (Fig. 10.1) that is highly modular and designed for efficient quantum error correction. By analogy with scalable ion trap schemes[106, 172, 200], we find a better fault tolerant error threshold than nearest-neighbour architectures[177].

10.1 Protected qubits and quantum gates

The present approach takes singlet and triplet states of two electron spins in adjacent quantum dots[150] to encode one qubit (Fig. 10.1a, Fig. 10.2a). The logical basis of our qubits is defined by $|0_L\rangle = (|\uparrow\downarrow\rangle - |\downarrow\uparrow\rangle)/\sqrt{2}$ and $|1_L\rangle = (|\uparrow\downarrow\rangle + |\downarrow\uparrow\rangle)/\sqrt{2}$. This decoherence free subspace immediately protects the system from collective phase noise due, e.g., to uniform magnetic field fluctuations[54, 204, 120]. In addition, *dynamical* protection from differential phase noise, e.g., due to hyperfine interaction with nuclear spins[178], is possible within this subspace[193] via periodic exchange (SWAP) of the two electrons[200, 151]. An external magnetic field produces an energy gap between the unused states $|\uparrow\uparrow\rangle, |\downarrow\downarrow\rangle$ and the logical subspace, thereby suppressing spin-flip errors[87, 96, 104]. With these protections, a quantum memory with decoherence times approaching milliseconds may be achieved[178].

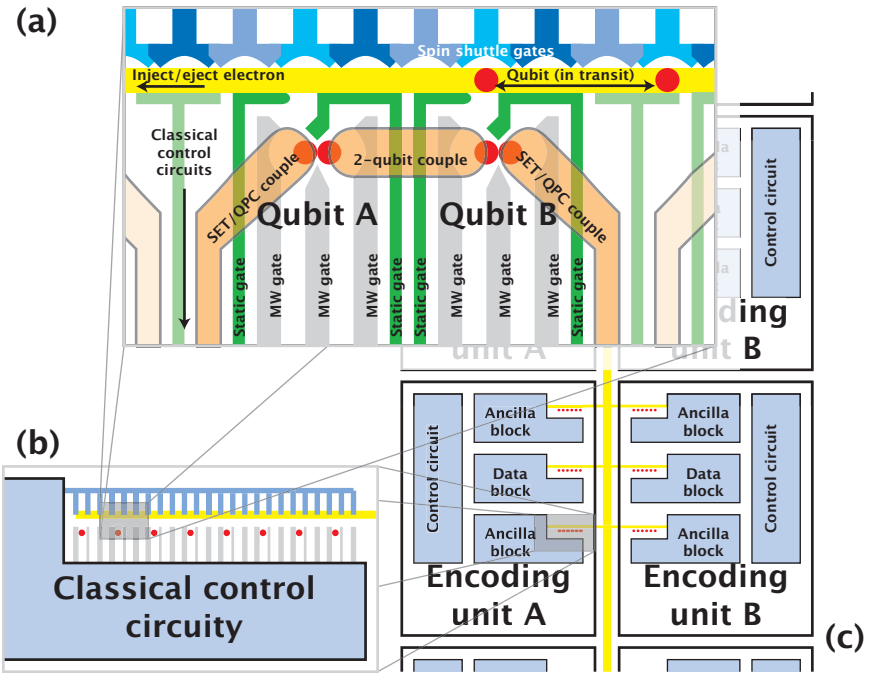

Figure 10.1: (a) Two adjacent depletion-gate-defined double quantum dots (one qubit comprising two spins) built on a semiconductor heterostructure, with tuning gates (green), high frequency microwave (MW) gates (gray, blue), and capacitive coupling gates (orange) forms a node. Coupling to a nearby quantum point contact (QPC) or single-electron transistor (SET) provides for charge measurement. Alternating gates along the top form the spin shuttle, and a Fermi sea can be selectively coupled to the spin shuttle for electron injection / ejection (preparation and erasure). The transport-channel double-dot (qubit B) is only occupied during two-qubit gates. (b) Qubits (red) connected by a spin shuttle (yellow), along with semi-autonomous classical control circuitry (blue-gray), forming a single block. A single "data" block, used for the logical computation, is adjacent to R ancilla blocks, making up an "encoding unit" (c). Ancilla blocks may operate in parallel; as soon as a verified ancilla is available, it may be used for error correction within the unit. Encoding units, in turn, operate autonomously, allowing for the massive parallelism necessary for large-scale error correction. Replacing the 2-qubit "node" of (a) with two encoding units in (c) allows for recursive implementation of QEC codes; such code *concatenation* improves the error correcting abilities of the system, eventually allowing for arbitrary computations so long as physical error rates are less than some threshold values.

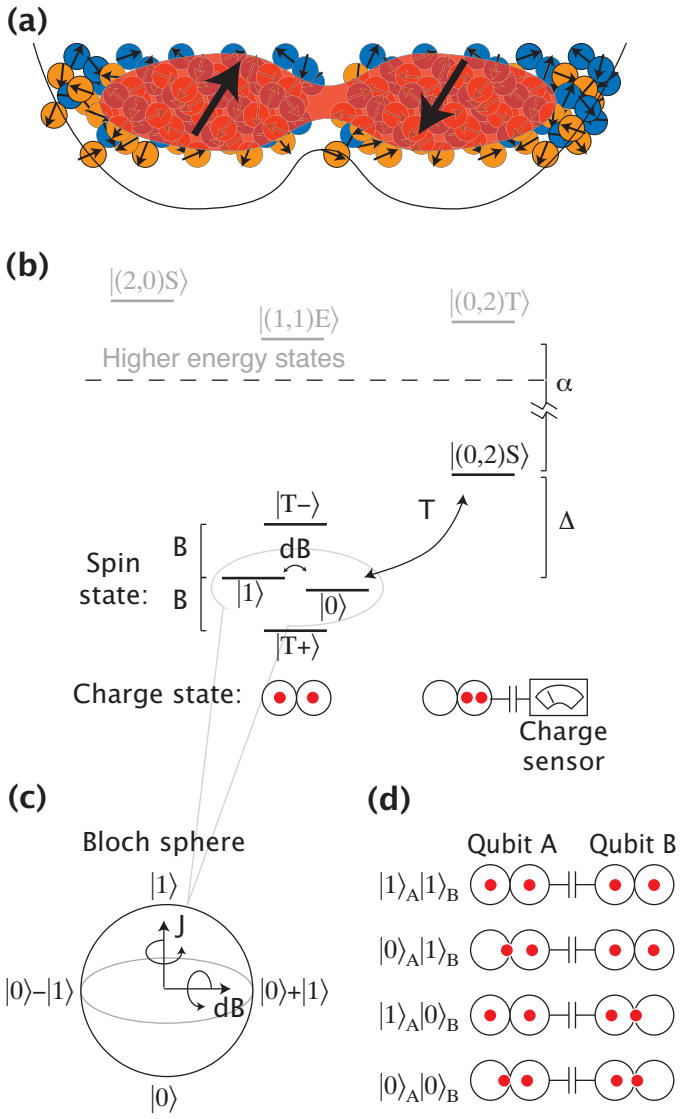

Figure 10.2: (a) Schematic of a double quantum dot, with two-electron spins (red) confined in double-well potential (black line) and interacting with lattice nuclei (orange and blue). (b) Level diagram, indicating logical states coupled by magnetic field gradient, additional coupling of the (0,2) charge state $|(0,2)S\rangle$ to the singlet ($|0_L\rangle$), and the "leakage" states, $|T_\pm\rangle$. The triplets of the biased system are neglected due to a large exchange energy $J_\mathrm{d} \approx \upsilon$, and the spin-aligned triplets with one electron in each well ($|T_\pm\rangle$) are detuned by Zeeman energy. Higher energy states, separated by an orbital level spacing $\upsilon \approx 0.5 - 1$ meV, may be included as additional renomalization corrections. (c) The Bloch sphere of the logical space, with rotation axes due to exchange interactions, J, and gradient field terms, dB. (d) Truth table for interaction between two adjacent double dots (schematically shown as coupled quantum double dots), used for the 2-qubit CPHASE gate as described in the text.

We model each double dot (Fig. 10.2a) as a three level system (Fig. 10.2b): the two logical states $|0_L\rangle, |1_L\rangle$, and the state $|(0,2)S\rangle$, used for preparation, for measurement, and for quantum gate operations. The logical states have one electron in each well, a charge configuration labeled (1,1), while the state $|(0,2)S\rangle$ is a spin singlet of the biased system with two electrons in a single dot and no electrons in the other, a charge configuration labeled (0,2). Its energy detuning Δ from the logical subspace and its tunneling couple T to the singlet $|0_L\rangle$ is controlled by local electric gates. When detuning is large and negative ($\Delta \ll -T$), $|(0,2)S\rangle$ is the ground state of the system. For $\Delta \gg T$, the state $|(0,2)S\rangle$ is only virtually populated, which leads to an effective exchange energy $J \sim T^2/\Delta$ (see Methods); in terms of practical parameters, J may be 0–100 μeV. Rapid control of the exchange energy may be accomplished through control of any combination of T and Δ. To complete the set of single qubit operations, we require a static magnetic field gradient dB between two dots. It mixes states within the logical subspace, acting as a qubit-flip term. This gradient could be produced by steady-state nuclear polarisations, g-factor differences, or permanent magnets. Polarizations of $\sim 0.5\%$ or a dot-to-dot difference in g factor of 1% at 3 tesla of external field gives a 30 mT gradient between dots; similarly, nearby permanent magnets can product gradients upwards of 100 mT/μm[137].

For a universal set of gates we choose rotations around the Z ($|0_L\rangle, |1_L\rangle$) and X ($|\uparrow\downarrow\rangle, |\downarrow\uparrow\rangle$) axes of the effective Bloch sphere shown in Fig. 10.2c, and a controlled-phase two-qubit gate. Preparation, measurement, and Z rotations within the logical space have already been demonstrated experimentally[151]. In brief, the state $|0_L\rangle$ can be prepared by loading two electrons from a nearby Fermi sea into the ground state of a single quantum dot, $|(0,2)S\rangle$ when $\Delta < 0$. The two electrons are then split by changing the detuning Δ from large and negative to large and positive, fast with respect to the gradient energy $\epsilon_{dB} = 2g^*\mu_B dB$ but adiabatic with respect to T, yielding adiabatic passage of $|(0,2)S\rangle$ to

$|0_L\rangle$. The reversed process adiabatically transfers the singlet state ($|0_L\rangle$) to $|(0,2)S\rangle$; this state differs in charge from $|1_L\rangle$ which still has one electron in each dot, thereby allowing for measurement of the logical states via charge measurement. As illustrated in Fig. 10.2c, exchange interaction[122, 119], with $J \neq 0$ for a time $t = \hbar\phi/J$, yields a Z axis rotation of angle ϕ: $R_Z^\phi = e^{-i\phi\sigma_z/2}$, where $\sigma_{x,y,z}$ are the Pauli matrices within the logical subspace. Similarly, the gradient, dB, produces logical X rotations; by waiting with $J = 0$ for a time $t = \hbar\phi/\epsilon_{dB}$, an X rotation $R_X^\phi = e^{-i\phi\sigma_x/2}$ is obtained. In the regime of large J and relatively small gradients dB, an arbitrary rotation is created by choosing the timing of Z rotations such that the desired X rotation is accomplished during free evolution (when $J = 0$). Undesired X rotations, such as those accumulated during waiting intervals, are removed by the SWAP operation used to refocus the system for protection against nuclear spins. Alternative approaches for the regime of large dB and small J are possible by working in the rotating frame of the gradient and oscillating J at a frequency commeasurate with the energy difference, ϵ_{dB}[119].

Coulomb interaction between two double dots (qubits A and B in Fig. 10.2d) is used for two-qubit gates. It is described by the Hamiltonian $V_{AB} = E_{cc}|(0,2)S\rangle\langle(0,2)S|_A \otimes |(0,2)S\rangle\langle(0,2)S|_B$ where E_{cc} is the differential cross capacitance energy between the two double-dot systems, corresponding to the difference in Coulomb energy from the (0,2)–(0,2) configuration and the (1,1)–(1,1) configuration. Simultaneously reducing the detuning of two nearby qubits (A and B) makes the states $|0_L\rangle_{A,B}$ adiabatically transfer to a state that has an admixture of $|(0,2)S\rangle_{A,B}$: $|\tilde{0}_L\rangle_{A,B} = \cos\theta|0_L\rangle_{A,B} + \sin\theta|(0,2)S\rangle_{A,B}$, while the triplets remain in the states $|\tilde{1}_L\rangle_{A,B} = |1_L\rangle_{A,B}$; see Methods for details. As illustrated in Fig. 10.2d, this produces a spin-selective charge dipole, which enables an effective dipole-dipole interaction. For small θ, the probability of populating $|(0,2)S\rangle$ is small ($\sim \sin^2\theta$); however, in the adiabatic basis, $V_{AB} = E_{cc}\sin^4\theta|\tilde{0}_L\rangle\langle\tilde{0}_L|_A \otimes |\tilde{0}_L\rangle\langle\tilde{0}_L|_B$, which allows for a

controlled phase gate of angle π when the biasing is on for a time $\pi\hbar/E_{cc}\sin^4\theta$. As the cross capacitance energy may be large (0.1 to 1 meV)[189], this time can be within sub-ns time scales. In principle, exchange-based approaches are also applicable[119, 200]. However, they would temporarily take the qubit out of the logical space, leading to unprotected error accumulation.

Reliable qubit transport is an essential feature of any scalable implementation of quantum computation[166, 171]. Low-error transport is difficult to achieve through pairwise SWAP gates. In our approach, we transport spin states by moving the electron charge, as described in Fig. 10.3. Early experiments demonstrated coherent spin transport in bulk GaAs[107]; here, we use a deterministic transport mechanism, greatly reducing charge-related errors. Essentially, a travelling wave potential for quantum dots is produced by modulation of fixed depletion gates. Many electrons may be carried in separate, adjacent minima, allowing parallel movement of all of the physical bits encoding a logical bit and leading to efficient blockwise two-qubit operations. With high barriers between adjacent minima, such a shuttle forms a series of unconnected quantum dots each moving with a constant velocity $\mathbf{v}$. Adiabatic transport is achieved if $|v|^2 m^*/2 \ll \upsilon$, where υ is the orbital level spacing of the moving dot, implying $|v| \ll 10^4$ m/s for an orbital level spacing of 0.5 meV. For example, with a feature size of 50 nm, one cycle of the shuttle yields a distance of 300 nm and is adiabatic for cycle periods $\tau \sim 1$ ns.

10.2 Errors in quantum operations

We now consider sources of error. The temperature must be sufficiently low for efficient preparation of singlet states in a single quantum dot, requiring $k_{\mathrm{B}}T \ll J_{\mathrm{d}} \sim 0.5$ meV (= 5 K). In this regime, the dominant errors are low-frequency (spin) phase noise

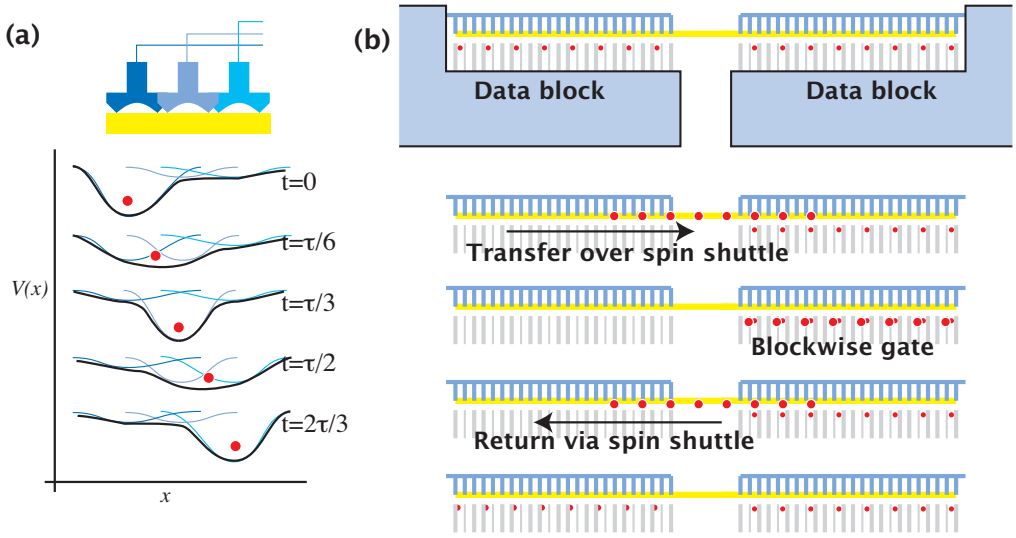

Figure 10.3: (a) A single electron CCD or electron pump[144] operates by applying AC varying voltages to three sets of gates $\pm 2\pi/3$ out of phase. The sign determines the direction of travel. Electrons are injected/ejected in the transport channel by means of adiabatic pulses applied before starting or stopping motion. A gate design for the spin "shuttle" (top) and potential energies along the transport direction at five points in time are shown at the bottom. The black curve is the total potential the electron encounters, given as the sum of the three blue curves. (b) Many electrons may be carried in separate, adjacent minima, allowing parallel movement of all of the physical bits encoding a logical bit and leading to efficient blockwise two-qubit operations.

due to hyperfine coupling[96, 151] and charge-based dephasing and relaxation. The spin noise is modeled as a position-dependent spin phase noise term, $V = \hbar\eta(t,x)\hat{S}_z$, where $\eta(t,x)$ is independent for each dot with a power spectrum $S(\omega)$, and $\hat{S}_z$ is the electron spin projection on the external field. The spin phase noise power spectrum due to nuclei is characterized by a time ensemble averaged dephasing time $T_2^* \approx 10$ ns and a high frequency cutoff $1/\tau_c \ll 1/T_2^*$[134, 103, 45, 178, 151]. Within this error model, nuclear spin-related dephasing can be refocused with periodic Z rotations to produce a long-lived quantum memory with potential lifetimes expected to exceed milliseconds[178].

Errors incurred during Z rotations arise from charge-based dephasing due both gate voltage fluctuations and intrinsic coupling to environmental degrees of freedom such as phonons[16, 8, 90]. We choose a noise model for charge dephasing where the rate for inelastic transitions from (0,2) to (1,1) is given by T_1^{-1} and where the energy difference Δ fluctuates, inducing characteristic charge dephasing with a rate T_2^{-1}. After elimination of the (0,2) state (see Methods) the effective error rate during an exchange gate is given by $\sin^2(\theta)T_1^{-1}[1+\sin^2(\theta)(T_1/T_2)]$, while the exchange energy is $J = T\tan(\theta)/2$. In principle, the error vanishes for $\theta \to 0$; however, in practice, we require that $J \gg 1/T_2^*$ due to the spin phase noise. As an example, taking $T_1 = 3$ ns, $T_2 = 1$ ns, and tunnel coupling $T = 120\mu$eV, $\theta \approx 0.06\pi$ is optimal with an error per SWAP of $\sim 3\times10^{-3}$.

Charge noise can be further reduced by working at points where the response of the exchange energy to gate voltages is zero, i.e., $dJ/dV_i = 0$ for all gate voltages $\{V_i\}$, in analogy to such zero-derivative points in superconductor-based qubit designs[194]. While this is true for $J = 0$, this could be achieved for finite J as well if sufficient perpendicular field is applied to change the sign of J while in the separated configuration and while maintaining the singlet as the ground state of the biased configuration[21] (also M. Stopa, private communication). This naturally leads to an extremum for $J(\{V_i\})$ associated with

a maximally negative J value. Only intrinsic errors and higher order processes are not be suppressed by these techniques. Finally, a Landau-Zener excitation to $|(0,2)S\rangle$ is suppressed by an energy gap on the order of the orbital level spacing. We may neglect it in a low temperature approximation, which is justified in our regime as no phonons of 1 meV are available in the environment to drive the inelastic transition, and if gate control is adiabatic with respect to the orbital level spacing.

For X rotations, composite pulses allow high fidelity operations even in the presence of substantial low frequency (spin) phase noise. For example, the slowly varying nuclear field leads to correlated under/over rotation errors. The BB1 composite pulse sequence from NMR is effective in eliminating these errors[191]: for an under/over rotation angle $\delta\phi = \phi\hbar/T_2^*\epsilon_{dB}$, X rotation has an error $p_1 \propto \delta\phi^{-6}$. Errors due to the drift of the nuclear field over the time scale of the BB1 composite pulse can be calculated as a shift occurring over a time τ_c and enters as $p_1' = (\tau_c\epsilon_{dB})^{-1}\delta\phi^{-4}$. As a concrete example, we now consider a $\frac{\pi}{2}$ X-rotation. Setting $U = R_X^{\pi/4}$, the required sequence is $R_{x,\mathrm{BB1}}^{\pi/2} = UR_Z^{-\phi}U^4R_Z^{-2\phi}U^8R_Z^{2\phi}U^4R_Z^{\phi}U$ with $\phi = \cos^{-1}(-1/8)$. For a field difference between two GaAs dots of 30 mT, a spin phase noise with $T_2^* = 10$ ns, and high frequency cutoff $\gamma \lesssim 1\ \mu\mathrm{s}^{-1}$, the error due to under/over rotation is $p_1 \lesssim 10^{-4}$, the error due to drift is $p_1' \ll 10^{-4}$, and the total gate time is 3 ns. Imperfect exchange gates increase this error linearly (for small exchange errors), while a larger gradient reduces gate time and error. In practise, our suggested techniques for higher fidelity exchange gates may be necessary to make composite pulses worthwhile.

While the energy gap between singlet and triplet subspaces suppresses the spin noise during exchange gates and the 2-qubit gate, charge noise becomes important due to the finite admixture of different charge states. Taking the same charge noise model used for Z rotations, we estimate that a dephasing error during the 2-qubit gate occurs with probability $p_2 = (\pi\hbar/E_{cc})(1/T_2 + 1/T_1\sin^2\theta)$. With $E_{cc} = 1$ meV and taking $\theta = 0.1\pi$,

the error is $p_2 \lesssim 6 \times 10^{-3}$. Improved charge dephasing terms would lead to substantially improved operation.

During the transport process, motional averaging reduces the error due to low frequency phase noise. The error is reduced further for our encoded qubits; by transporting individual spins of a qubit in close proximity, the encoded qubit is immune to most dephasing, as we recently analysed in detail[178]. Qualitatively, as the two spins of the qubit travel through the same channel, all static phase terms (including spin-orbit interaction) are cancelled exactly. Focusing on a specific case, for hyperfine terms in GaAs, with $T_2^* \sim 10$ ns, $\gamma \lesssim 1\ \mu\text{s}^{-1}$, and average dot-to-dot time of 1 ns, we find $T_{2,\text{eff}}^* \gg 1$ ms. The spin shuttle error per dot-to-dot transfer, $p_t \simeq 10^{-6}$, is likely to be limited by the Zeeman-suppressed spin flip terms. We note that transport over 100 sites will have higher fidelity than a single 2-qubit gate.

10.3 Fault tolerance and error thresholds

The physical qubits discussed above are used to encode and protect logical computations of a quantum computer by using quantum error correction (QEC)[166, 171]. We adopt an approach in which most QEC operations are performed on ancillary qubits, allowing for verification of successful preparation, before interacting with qubits used for the logical computation for error correction[172]. This prevents errors occurring in the bulk of the QEC operations from effecting the logical operation. To facilitate parallel preparation and verification of ancillae, qubits are grouped into independent blocks, comprising N_b qubits, as shown in Fig. 10.1b. N_b is the number of qubits required to implement logical ancilla creation and verification for a given quantum error correcting code; for example, the Steane [[7,1,3]] code typically has $N_b \geq 10$, where the choice depends on choice of verifica-

tion circuitry, which could be optimized for a given error model. Blocks of R ancillae and a data block are grouped into units for a hierarchical architecture illustrated in Fig. 10.1.

Some errors, such as spin-flips, make qubits leave the logical subspace. These leakage errors must be corrected. In addition to standard QEC[172], which only corrects within the logical subspace, at the lowest level of encoding we introduce a "T" gate network to detect leakage errors, i.e., spin-flips, and replace them with errors within the logical subspace. Because our two-qubit gate is insensitive to which triplet state the system is in, checking the parity of the qubit under a logical bit flip, $X = R_X^\pi$ detects leakage to $|\uparrow\uparrow\rangle, |\downarrow\downarrow\rangle$. More specifically, preparing an ancilla (A) in $|0_L\rangle$, the T network on a data bit (D) and ancilla is the sequence $\mathrm{H}_A X_D \, {}^C\mathrm{Z}_{AD} X_D \, {}^C\mathrm{Z}_{AD} \mathrm{H}_A$. Here H_A is a hadamard on the ancilla qubit, and ${}^C\mathrm{Z}_{AD}$ is a controlled phase between A and D. Then, the ancilla is measured in the Z basis; the result 1 indicates no leakage error, and computation proceeds. The result 0 indicates leakage, we replace the data qubit with the state $|0_L\rangle$. This maps errors outside of the logical space to errors within the logical space, and allow the normal circuitry of error correction to proceed within the logical subspace. As each qubit of the encoded qubit is operated on with independent ancilla qubits, the procedure is fault tolerant.

Finally, for scalable architectures, teleportation-based gates may be used[83, 205]. Specifically high fidelity prior entanglement and measurement provides an alternative to the CPHASE two-qubit gate that may be appropriate for higher level encoding and/or fault tolerant gate operations where large transport distances or long times between gates are common. Such entangled states may be prepared using the charge measurement on spins belonging to different qubits, and their fidelity may be improved by entanglement purification[178].

We now consider teleportation-based gates in more detail. By preparing entanglement in ancillary qubits in advance, Bell measurements are used to teleport the data

through the gate yielding the desired logical operation[83]. In addition, teleportation-based gates allow for the correction of arbitrary leakage errors such as electron loss and spin flips, because the data qubit is replaced with the new ancillary qubit.

Teleportation-based single-qubit gates and two-qubit gates start with a prepared, ancilla state with the desired unitary operation already applied to one qubit of a Bell pair, and are completed by Bell measurements on the the other qubit of the pair and the data qubit (Fig. 10.4). This teleports the desired operation onto the remaining qubit, with an additional known Pauli operator applied to the result. This Pauli operator may be undone, as shown in Fig. 10.4a with σ_ν and Fig. 10.4b with $\sigma_\nu\sigma_\mu$. Thus, the operation of a given gate can be reduced to the preparation of a known, entangled state of ancillas (occuring inside the dashed lines), followed by Bell measurements.

The power of this teleportation technique derives from the ability to make the difficulty of gates a state-preparation problem (where states may be prepared in a probabilistic manner, e.g., using measurements and without using two–qubit gates, and in addition purification techniques[178] can be used to improve fidelity), and in the ability to remove arbitrary leakage errors, such as spin-flips taking the system out of the logical space or even loss of an electron, by teleporting the data to the freshly prepared ancilla qubit. It also allows a $\pi/8$ Z-rotation in a fault tolerant manner[205], completing the set of universal, fault-tolerant gate operations. In our architecture, the preparation of states could occur in the transport channel qubit (qubit B, in Fig. 1c). However, the time scale and overhead in ancilla number for such gates may make teleportation-based leakage correction less efficient than the T network.

Recently, detailed analysis showed that thresholds for fault tolerance depend sensitively upon both fidelity of quantum memory, quantum gate operations and errors associated with long-range qubit coupling[172, 173]. With the quantum memory provided from

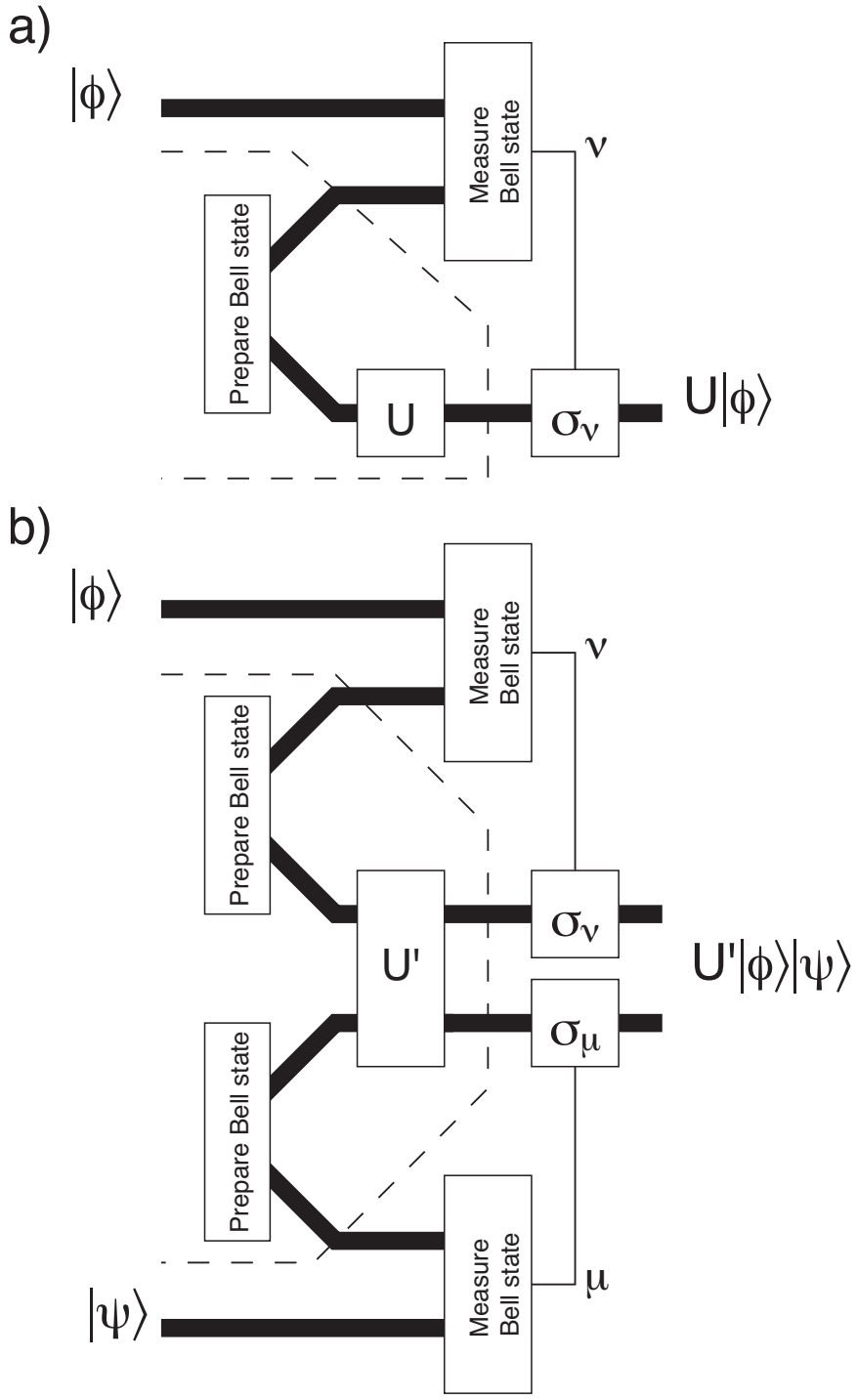

Figure 10.4: Teleportation-based single-qubit gates (a) and two-qubit gates (b). The desired operation (U or U') is teleported onto the remaining qubit(s), with an additional known Pauli operator(s) applied to the result. These Pauli operators are, as shown, (a) σ_ν and (b) $\sigma_\nu\sigma_\mu$.

refocusing of the logical qubit states, and the transport mechanism described above, we now analyse the error requirements for reaching the fault tolerant threshold by direct analogy to ion trap-based schemes[173]. In both cases, transporting quantum information has low error rates, measuring quantum states take many time steps, and 2-qubit gates are slower than 1-qubit gates. If 2-qubit gates have an error probability p_2, we can rate the overall system as follows. For 1-qubit gates, the error is $p_1 < p_2$; for transport $p_t \ll p_2$. Memory error rates at critical times (such as during measurement) are $p_m \sim p_1$ due to the use of 1-qubit gates to implement dynamical protection; and transport within a block produces errors in memory and transport similar to those of a single 2-qubit gate. This is analogous the situation of Ref.[173] where a threshold was numerically estimated for the [[7,1,3]] Steane code. In particular, memory error during measurement is less than 2-qubit gate errors, and transport of distances up to RN_b occurs with negligible overhead, giving the ultimate threshold for a 2-qubit gates of $p_2 \simeq 2 \times 10^{-4}$. Note that this estimate assumes that classical, local information processing requires only a few time steps of the quantum computer. Given our expected error rates, achieving fault tolerance will require error-reducing approaches, such as composite pulses and zero-derivative points. In addition, higher thresholds may be possible through better code choice and other optimizations[111].

10.4 Methods

The capacitive two-qubit gate is based on the differential charge coupling E_{cc} between two double quantum dots, A and B, of states with one electron in each quantum dot (1,1) and two electrons on one side, (0,2). These correspond to the logical states and the doubly occupied singlets, $|(0,2)S\rangle_A$ and $|(0,2)S\rangle_B$, for each double dot. We choose a labelling of dots such that the second dot of A and the second dot of B are adjacent,

maximizing their Coulomb interaction. The Coulomb interaction gives a charge-based interaction that has a factorizable component, $V_A + V_B = \Delta_A(P_A^L - |(0,2)S\rangle\langle(0,2)S|_A) + \Delta_B(P_B^L - |(0,2)S\rangle\langle(0,2)S|_B)$, and an entangling component, $V_{AB} = E_{cc}|(0,2)S\rangle\langle(0,2)S|_A \otimes |(0,2)S\rangle\langle(0,2)S|_B$, where $P_{A(B)}^L = |0_L\rangle\langle 0_L|_{A(B)} + |1_L\rangle\langle 1_L|_{A(B)}$ projects into the logical subspace of $A(B)$. The residual term leads to capacitive coupling in the charge stability diagram of the combined system and is set by the device geometry. It has been observed in parallel quantum dots to be of the order $E_{cc} = 0.1 - 1$ meV[189].

A simple form of the capacitive two qubit gate can be realized by starting in the unbiased configuration, in which the logical states are both (1,1) charge states. Then, rapid adiabatic passage to the (0,2) configuration for qubits A and B will lead to state-selective transfer: only the singlet states will go to the doubly-occupied states $|(0,2)S\rangle$. The Coulomb interaction $V_A + V_B$ leads to an exchange gate for l and r, while V_{AB} leads to additional phase evolution for the state $|(0,2)S\rangle_A|(0,2)S\rangle_B$. By waiting at time $\hbar\pi/E_{cc}$ an additional π phase is accumulated for this state, realizing a controlled-phase operation and two Z rotations. The Z rotations can be undone with additional, independent exchange gates performed in series on qubits A and B.

In a realistic situation, charge dephasing limits the fidelity of this gate[8, 16], and the strength of the interaction makes control delicately sensitive to pulse parameters at picosecond timescales. To mitigate these factors, a partial transfer to the $(0,2)S$ states is achieved when the system is biased only slightly. This reduces the coupling to charge-related dephasing and increases the time scale for gate operation leading to lower sensitivity to pulse parameters. For a double quantum dot with the level structure given in Fig. 2, we may eliminate the doubly occupied states when the gap Δ is much larger than manipulation frequencies. To do so, we start by writing the three level Hamiltonian for $|1_L\rangle$, $|0_L\rangle$, and

$|(0,2)S\rangle$:

$$H = \begin{pmatrix} 0 & \epsilon_{dB}/2 & 0 \\ \epsilon_{dB}/2 & 0 & T \\ 0 & T & \Delta \end{pmatrix} .$$

Adiabatic elimination[37] yields an effective Hamiltonian to order T/Δ for the states $|1_L\rangle, |\tilde{0}_L\rangle$:

$$H_{\text{eff}} = \begin{pmatrix} 0 & \epsilon_{dB}/2 \\ \epsilon_{dB}/2 & T^2/\Delta \end{pmatrix} ,$$

where the effective exchange energy is $J = T^2/\Delta$, as in the main text. Higher order corrections may be kept within the logical subspace so long as manipulation times are much slower than $\hbar/\Delta$. By changing the bias parameter in each dot to be near the (1,1) to (0,2) singlet transition, the singlet state is mapped to the adiabatic ground state, $|\tilde{0}_L\rangle = \cos(\theta)|(1,1)S\rangle + \sin(\theta)|(0,2)S\rangle$, where $\theta = \arctan[(\Delta - \sqrt{\Delta^2 + 4T^2})/2T]$ is the adiabatic angle and $J = T\tan(\theta)/2$. The renomalized interaction V_{cc} becomes $E_{cc}\sin^4(\theta)|\tilde{0}_L\rangle\langle\tilde{0}_L|_A \otimes |\tilde{0}_L\rangle\langle\tilde{0}_L|_B$. Critically, the effective exchange energy between $|1_L\rangle$ and $|\tilde{0}_L\rangle$ becomes only quadratically sensitive to fluctuations of the energy differences Δ_A and Δ_B, reducing the sensitivity to charge dephasing.

10.5 Outlook

We described and analysed a modular solid-state architecture, based on spin qubits in double quantum dots, which can be used for scalable quantum computation. The qubits were chosen for potential long quantum memory times, and we developed a long-range, low-error transport mechanism for them. From a technical perspective, static field gradients $\gtrsim 100$ mT/μm and electronic gate control at 1–10 GHz are shown to be sufficient to achieve the fault tolerant regime. In practical terms, taking a clock speed of 1 GHz, measurement within 10 clock cycles with, e.g., an rf-SET[50, 202], exchange gates with less than 1 error per

10^4 clock cycles, and our low-error single-spin transport mechanism yields fault tolerance. This result is robust to low frequency spin-phase noise corresponding to $T_2^* = 10$ clock cycles and to realistically fast charge dephasing. These parameters are consistent with the current measurements for GaAs quantum dots[87, 96, 151].

We gratefully acknowledge conversations with J. Folk, A. Houck, A. C. Johnson, D. Loss, and especially J. Petta. The work at Harvard was supported by ARO/ARDA, DARPA-QuIST, NSF Career award, NSF grant DMR-02-33773, Alfred P. Sloan Foundation, and David and Lucile Packard Foundation. The work at Innsbruck was supported by the ÖAW through project APART (W.D.), the European Union and the Austrian Science Foundation.

Appendix A

Details for Chapters 1: breakdown of the quasi-static approximation

In this appendix we develop in more detail the quasi-static approximation when $B_{\rm ext} \gg B_{\rm nuc}$. We start with the Hamiltonian for an electron spin in a quantum dot interactng with N nuclear spins via the hyperfine contact interaction (units such that $\hbar\gamma_e = 1$) from Eqn. 1.1. We rewrite it as $H = H_0 + V$ with

$$H_0 = B_{\rm ext}\hat{S}_z + B_{\rm ext}\sum_{\beta,k}\gamma_\beta \hat{I}_z^k + \hat{B}_z\hat{S}_z \ , \tag{A.1}$$

and

$$V = \frac{1}{2}(\hat{B}_+\hat{S}_- + \hat{B}_-\hat{S}_+) \ . \tag{A.2}$$

The H_0 term includes the Zeeman interactions with an external magnetic field $B_{\rm ext}$ for the electron and nuclear spins; the nuclei have gyromagnetic ratios γ_β for each species β, respectively. H_0 also includes the commuting terms of the hyperfine interaction that lead to

the Knight and Overhauser shifts. The field-aligned component of the hyperfine interaction gives $\hat{B}_z = \sum_{\beta,j} b_{\beta,j}\alpha_{\beta,j}\hat{I}_z^{\beta,j}$. The term V corresponds to interactions that flip nuclear and electronic spin; $\hat{B}_+, \hat{B}_-$ are defined analogously to $\hat{B}_z$.

We will concentrate on the regime of large magnetic field, where $\xi = (B_{\rm ext} + \langle\hat{B}_z\rangle)/B_{\rm nuc} \gg 1$ provides a parameter for expansion in $1/\xi$. For convienence, we define $E_z = B_{\rm ext} + \langle\hat{B}_z\rangle$ as the effective Zeeman splitting of the electron spin states, and similarly, $\delta_q = B_{\rm ext}\gamma_\beta$ for the nuclear spin q of species β. We index nuclear spins of species β and lattice site k by $q = \{\beta, k\}$, and note that $\hat{\vec{B}} = \sum_q \lambda_q \hat{\vec{I}}^q$ with $\lambda_q = b_q\alpha_q$. Removing the mean field component of $\hat{B}_z$, we also define $\delta\hat{B}_z = \hat{B}_z - \langle\hat{B}_z\rangle$. Accordingly,

$$H_0 = E_z\hat{S}_z + \sum_q \delta_q\hat{I}_z^q + \delta\hat{B}_z\hat{S}_z \ . \tag{A.3}$$

When $\xi \gg 1$, the large Zeeman energy of the electron spin suppresses spin flip processes (due to V). We can approximate the dynamics in this regime by adiabatic elimination of the terms varying quickly, i.e., at E_z. First, spin flips are suppressed. At times longer than E_z, there is a time-independent probability of order $1/\xi^2$ for measurement to give a spin-flipped state [103]. This allows us to take $\hat{S}_z = S$ as a constant of motion in the system. Writing the Heisenberg equations of motion, we have

$$\frac{d}{dt}\hat{S}_+ = i(E_z + \delta\hat{B}_z)\hat{S}_+ - i\hat{S}_z\hat{B}_- \ . \tag{A.4}$$

Setting $d\hat{S}_+/dt = 0$, we find to lowest order in $1/\xi$

$$\hat{S}_+ = \xi^{-1}S\frac{\hat{B}_+}{B_{\rm nuc}} + O(\xi^{-2}) \ . \tag{A.5}$$

It will be convenient to work with scale independent parameters, $\hat{\vec{A}} = \hat{\vec{B}}/B_{\rm nuc}$. Substituting

into the other Heisenberg equations of motion

$$\begin{aligned}\frac{d}{dt}\hat{I}_z^q &= \frac{\lambda_q}{2i}(\hat{I}_+^q\hat{S}_- - \hat{I}_-^q\hat{S}_+) \\ &= \frac{\lambda_q S}{2i\xi}(\hat{I}_+^q\hat{A}_- - \hat{I}_-^q\hat{A}_+) \qquad \text{(A.6)} \\ \frac{d}{dt}\hat{I}_+^q &= i(\delta_q + \lambda_q S)\hat{I}_+^q - i\lambda_q\hat{I}_z^q\hat{S}_+ \\ &= i(\delta_q + \lambda_q S)\hat{I}_+^q - i\frac{\lambda_q S}{\xi}\hat{I}_z^q\hat{A}_+ \qquad \text{(A.7)}\end{aligned}$$

We can write the effective Hamiltonian corresponding to these eliminations:

$$\begin{aligned}H_{\text{eff}} &= E_z\hat{S}_z + \sum_q(\delta_q + \lambda_q\hat{S}_z)(\hat{I}_z^q - \langle\hat{I}_z^q\rangle) + \\ &\quad \frac{1}{\xi}\sum_{qq'}\lambda_q\lambda_{q'}[(\hat{S}_z + 1/2)\hat{I}_-^q\hat{I}_+^{q'} - \\ &\quad (1/2 - \hat{S}_z)\hat{I}_+^q\hat{I}_-^{q'}] \qquad \text{(A.8)}\end{aligned}$$

It becomes apparent that, by working in the interaction picture of nuclear spins, the effective Hamiltonian may be rewritten

$$H_{\text{eff},I} = \hbar[\gamma_e B_{\text{ext}} + \sum_q \lambda_q\hat{I}_z^q(t)]\hat{S}_z \qquad \text{(A.9)}$$

as suggested in Section 1. Accordingly, $\delta\hat{B}_z(t) = \sum_q \lambda_q(\hat{I}_z^q(t) - \langle\hat{I}_z^q\rangle)$ is the slowly varying component of the Overhauser shift which leads to dephasing in echo experiments.

Within the Heisenberg equations of motion a useful mean-field approximation is readily apparent. Working with mean values and factorizing:

$$\begin{aligned}\frac{d}{dt}\langle\hat{I}_z^q\rangle &= \frac{\lambda_q S}{2i\xi}(\langle\hat{I}_+^q\rangle\langle\hat{A}_-\rangle - \langle\hat{I}_-^q\rangle\langle\hat{A}_+\rangle \\ &\quad + \frac{2\lambda_q}{B_{\text{nuc}}}\langle\hat{I}_z^q\rangle) \qquad \text{(A.10)} \\ &= \frac{\lambda_q S}{2i\xi}(\langle\hat{I}_+^q\rangle\langle\hat{A}_-\rangle - \langle\hat{I}_-^q\rangle\langle\hat{A}_+\rangle) \qquad \text{(A.11)} \\ \frac{d}{dt}\langle\hat{I}_+^q\rangle &= i(\delta_q + \lambda_q S)\langle\hat{I}_+^q\rangle - i\frac{\lambda_q S}{\xi}(\langle\hat{I}_z^q\rangle\langle\hat{A}_+\rangle \\ &\quad + \frac{\lambda_q}{B_{\text{nuc}}}\langle\hat{I}_z^q\hat{I}_+^q\rangle) \qquad \text{(A.12)}\end{aligned}$$

As each spin q has different coefficients, the motion of the collective variable $\langle \hat{A}_+ \rangle$ will be fluctuating mildly from its equilibrium value, and drift from this value slowly compared to individual spin precision. The final approximation consists of replacing the operator $\hat{A}_-$ in the equations of motion with a complex number, A, which will be considered a classical fluctuating variable. Averaging over the classical fluctuations gives $\overline{A} = 0$ and $\overline{A^* A} = 1/2 \langle \{\hat{A}_+, \hat{A}_-\}_+ \rangle$; more generally, for large N, A becomes a gaussian-distributed complex number with rms given by $\sqrt{\overline{A^* A}}$.

With the substitution of A for $\hat{A}_-$, we can solve explicitly for the motion of $\hat{\vec{I}}^q$. This approach assumes that the starting configuration of nuclear spins corresponds to a factorizable initial state, such that, e.g., $\langle \hat{I}_z^q \hat{I}_z^{q'} \rangle = \langle \hat{I}_z^q \rangle \langle \hat{I}_z^{q'} \rangle$ for $q \neq q'$. Fixing A, each spin q has a solution (see, e.g., Ref. [134]) given by

$$\begin{aligned} \hat{\vec{I}}^q(t, A) &= (\vec{n}_q \cdot \hat{\vec{I}}^q)\vec{n}_q + [\hat{\vec{I}}^q - (\vec{n}_q \cdot \hat{\vec{I}}^q)\vec{n}_q] \cos(\omega_q t) + \\ &\quad (\hat{\vec{I}}^q \times \vec{n}_q) \sin(\omega_q t) \end{aligned} \tag{A.13}$$

where

$$\omega_q^2 = (\delta_q + \lambda_q S)^2 + (\lambda_q S/\xi)^2 (2A^* A) \tag{A.14}$$

$$\vec{n}_q = \frac{1}{\omega_q} \begin{pmatrix} \lambda_q S \mathrm{Re}[A]/\xi \\ \lambda_q S \mathrm{Im}[A]/\xi \\ \delta_q + \lambda_q S \end{pmatrix} \tag{A.15}$$

Thus, the spin q's z component becomes

$$\begin{aligned} \hat{I}_z^q(t) &= \frac{\delta_q + \lambda_q S}{\omega_q^2} [\frac{\lambda_q S}{\xi \omega_q} (\mathrm{Re}[A] \hat{I}_x^q + \mathrm{Im}[A] \hat{I}_y^q) + \\ &\quad (\delta_q + \lambda_q S) \hat{I}_z^q][1 - \cos(\omega_q t)] \\ &\quad + \hat{I}_z^q \cos(\omega_q t) \\ &\quad + \frac{\lambda_q S}{\xi \omega_q} (\mathrm{Im}[A] \hat{I}_x^q - \mathrm{Re}[A] \hat{I}_y^q) \sin(\omega_q t) \end{aligned} \tag{A.16}$$

Accordingly for initial conditions with $\langle \hat{I}_z^q \rangle \neq 0$ and $\langle \hat{I}_x \rangle = \langle \hat{I}_y \rangle = 0$,

$$\langle \hat{I}_z^q(t) \rangle = \langle \hat{I}_z^q \rangle \overline{f_q}(t) \tag{A.17}$$

where

$$f_q(t) = 1 - (1 - \cos(\omega_q t)) \frac{(\lambda_q S)^2 (2|A|^2)}{\xi^2 \omega_q^2} \ . \tag{A.18}$$

We can now evaluate the correlator $C_{qq'}(t) = \langle (\hat{I}_z^q(t) - \langle \hat{I}_z^q \rangle)(\hat{I}_z^{q'}(0) - \langle \hat{I}_z^{q'} \rangle) \rangle = \langle \hat{I}_z^q(t) \hat{I}_z^{q'}(0) \rangle - \langle \hat{I}_z^q(t) \rangle \langle \hat{I}_z^{q'}(0) \rangle$. The calculation proceeds:

$$\begin{aligned} C_{qq'}(t) \ = \ & \langle \{ \frac{\delta_q + \lambda_q S}{\omega_q^2} [\frac{\lambda_q S}{\xi \omega_q} (\mathrm{Re}[A] \hat{I}_x^q + \mathrm{Im}[a] \hat{I}_y^q) + \\ & (\delta_q + \lambda_q S) \hat{I}_z^q] [1 - \cos(\omega_q t)] \\ & + \hat{I}_z^q \cos(\omega_q t) \\ & + \frac{\lambda_q S}{\xi \omega_q} (\mathrm{Im}[A] \hat{I}_x^q - \mathrm{Re}[A] \hat{I}_y^q) \sin(\omega_q t) \} \hat{I}_z^{q'} \rangle \\ & - \langle \hat{I}_z^q \rangle \langle \hat{I}_z^{q'} \rangle f_q(t) \end{aligned} \tag{A.19}$$

We get

$$C_{qq'}(t) \approx \delta_{qq'} \langle (\hat{I}_z^q)^2 - \langle \hat{I}_z^q \rangle^2 \rangle \overline{f_q}(t) \tag{A.20}$$

This indicates that the short time behavior of the correlator, $\langle \delta \hat{B}_z(t) \delta \hat{B}_z(0) \rangle$ goes as

$$\langle \delta \hat{B}_z(0)^2 \rangle - \sum_q \lambda_q^2 \langle (\hat{I}_z^q)^2 - \langle \hat{I}_z^q \rangle^2 \rangle (\frac{(\lambda_q S)^2 2 \overline{A^* A}}{\xi^2}) t^2 \tag{A.21}$$

Roughly,

$$\frac{\langle \delta \hat{B}_z(t) \delta \hat{B}_z(0) \rangle - \langle \delta \hat{B}_z(0)^2 \rangle}{\langle \delta \hat{B}_z(0)^2 \rangle} \simeq - \frac{3 B_{\mathrm{nuc}}^4}{B_{\mathrm{ext}}^2 N} \frac{t^2}{2} \ . \tag{A.22}$$

This suggests that the spectral function $S(\omega)$ for $\delta \hat{B}_z(t)$ has a high frequency cutoff $\gamma \sim B_{\mathrm{nuc}}^2 / B_{\mathrm{ext}} \sqrt{N}$. For example, in experiments with $N \sim 10^6$, $B_{\mathrm{nuc}} = 3$ mT, and $B_{\mathrm{ext}} = 100$ mT, $\gamma \sim 10 \mathrm{ms}^{-1}$. The expected spin-echo time (Section 6.4) is $T_{2,SE} = 8^{1/4} \sqrt{T_2^* / \gamma} \sim 2 \mu$s.

We note that this value is consistent with other work (Ref. [203]) after accounting for the substantially different dot size considered in this paper.

The short time behavior, and thus high frequency behavior, is independent of the nuclear Zeeman and Knight shift terms in the Hamiltonian. However, longer time behavior depends upon these parameters. For example, when the distribution of $\delta_q + S\lambda_q$ is highly inhomogeneous, we may expect that electron-spin-mediated nuclear spin exchange is suppressed due to the very different energies associated with individual nuclei.

Appendix B

Details for Chapter 2: spin bath-related integrals and models

B.1 Integrals involved in driven evolution

We now solve the integrals necessary to evaluate $\langle \hat{f} \rangle$ and $\langle \hat{\zeta}(t) \rangle$ for a given bath density matrix, ρ_{bath}. Taking the continuum limit for this density matrix, we can evaluate a function $h(\lambda \hat{A}_z)$ as

$$\begin{aligned} \mathrm{Tr}[h(\lambda \hat{A}_z)\hat{\rho}_{bath}] &= \sum_{\Lambda} h(\Lambda)\rho_{\Lambda} && \text{(B.1)} \\ &\rightarrow \int_{-\infty}^{\infty} d\Lambda h(\Lambda)\rho(\Lambda) && \text{(B.2)} \end{aligned}$$

Accordingly, the long time population difference, given by $\langle \hat{f} \rangle$ has the form

$$\langle \hat{f} \rangle = 1 - \sum_{\Lambda} \rho_{\Lambda} \langle \Lambda | \frac{1}{1 + (\frac{\delta + \lambda \hat{A}_z}{\Omega})^2} | \Lambda \rangle \tag{B.3}$$

where Λ is the eigenvalue of $\lambda \hat{A}_z$. Going to the continuum limit, and assuming the power is weak (appropriate for lineshape measurements),

$$\langle \hat{f} \rangle = 1 - \int_{-\infty}^{\infty} d\Lambda \ \rho(\Lambda) \frac{\Omega^2}{(\Lambda + \delta)^2 + \Omega^2} \tag{B.4}$$

Furthermore, the integral depends only upon $\tilde{\omega} = \sqrt{(\Lambda+\delta)^2+\Omega^2}$, so we define the symmetric density,

$$\rho_{sym}(\omega) = \rho(-\delta - \sqrt{\omega^2-\Omega^2}) + \rho(-\delta + \sqrt{\omega^2-\Omega^2}). \tag{B.5}$$

Then,

$$\langle \hat{f} \rangle = 1 - \int_{\Omega}^{\infty} d\omega \frac{\omega}{\sqrt{\omega^2-\Omega^2}} \rho_{sym}(\omega) \frac{\Omega^2}{\omega^2} \tag{B.6}$$

$$= 1 - \Omega^{1/2} \int_0^{\infty} d\tilde{\omega} \frac{\rho_{sym}(\tilde{\omega}+\Omega)}{(\tilde{\omega}/\Omega+1)\sqrt{(\tilde{\omega}/\Omega+2)(\tilde{\omega})}}, \tag{B.7}$$

While this integral can be solved for certain density of states, we note that for small frequencies ($\lesssim \Omega$) a relatively flat density of states can be approximated in a Taylor series, while for large frequencies, the $1/\tilde{\omega}^2$ behavior kills the higher frequencies components of the bath. Expanding all of these, except for the pole at $\tilde{\omega}=0$ the non-singular, non-oscillatory terms in Eqn. B.14 near $\tilde{\omega}=0$ are

$$\frac{\rho_{sym}(\tilde{\omega}+\Omega)}{(\tilde{\omega}/\Omega+1)\sqrt{\tilde{\omega}/\Omega+2}} = \sqrt{2}\rho(-\delta)\Big[1 - u\tilde{\omega} + ...\Big] \tag{B.8}$$

$$\approx \sqrt{2}\rho(-\delta)\exp\left[-u\tilde{\omega}\right] \tag{B.9}$$

where the time scale is

$$u = \frac{5}{4\Omega} - \frac{\Omega\rho''(-\delta)}{\rho(-\delta)}. \tag{B.10}$$

Solving the integral yields

$$\langle \hat{f} \rangle \simeq 1 - \rho(-\delta)\sqrt{2\pi\Omega/u} \tag{B.11}$$

The oscillations at large t can be evaluated in a manner similar to the lineshape.

$$\langle \hat{\zeta}(t) \rangle = \int_{-\infty}^{\infty} d\Lambda \rho(\Lambda) \frac{\Omega^2 \exp(-i\sqrt{(\Lambda+\delta)^2+\Omega^2}t)}{(\Lambda+\delta)^2+\Omega^2} \tag{B.12}$$

$$= \int_{\Omega}^{\infty} d\omega \frac{\omega}{\sqrt{\omega^2-\Omega^2}} \rho_{sym}(\omega) \frac{\Omega^2 \exp(-i\omega t)}{\omega^2} \tag{B.13}$$

$$= \Omega^{1/2} e^{-i\Omega t} \int_0^{\infty} d\tilde{\omega} \frac{\rho_{sym}(\tilde{\omega}+\Omega)\exp(-i\tilde{\omega}t)}{(\tilde{\omega}/\Omega+1)\sqrt{(\tilde{\omega}/\Omega+2)(\tilde{\omega})}}, \tag{B.14}$$

where we have transformed once more to an offset variable, $\tilde{\omega} = \omega - \Omega$. For this final integral we use the stationary phase approximation at long times, requiring that $\rho_{sym}(\omega \geq \Omega)$ not be singular.

This linear term (Eqn. B.9) determines the corrections to the stationary phase integral. We now define a time dependent angle and an effective time,

$$\theta(t) = 1/2 \tan^{-1}[t/u] \tag{B.15}$$

$$\tau(t) = \sqrt{t^2 + u^2}. \tag{B.16}$$

Using these substitutions, we can solve for the stationary phase result exactly:

$$\langle \zeta(t) \rangle \approx \sqrt{2\Omega}\rho(-\delta)e^{-i\Omega t}\int_0^\infty d\tilde{\omega}\frac{e^{-i\tilde{\omega}t-\tilde{\omega}u}}{\sqrt{\tilde{\omega}}} \tag{B.17}$$

$$= \rho(-\delta)e^{-i\Omega t}\frac{\sqrt{2\pi\Omega}e^{-i\theta(t)}}{\sqrt{\tau(t)}}. \tag{B.18}$$

B.2 Comparison with superconducting qubits: model

We develop a theory describing superconducting qubit systems that includes both the spin-bath model of this paper and incoherent heating from microwave pulses used to implement driving. To characterize the experiment, a simple model involving several static parameters was used. One is the preparation efficiency, I, which is the probability of preparing "down" (the desired initial state) minus the probability of preparing "up" (through bad preparation, probably due to high temperature). I is set entirely by the microwave temperature. Assuming that the only signficant source of heating is the incident microwave field, Stefan's law gives $T \propto \sqrt{\Omega}$. Accordingly, $I = \tanh(\sqrt{\Gamma/\Omega})$, where Γ^2 is a measure of the cooling power.

In addition, there is a finite probability of measuring the wrong state, given by the conditional probabilities, $M_{\uparrow,\uparrow}$ and $M_{\downarrow,\downarrow}$. The first is the probability of measuring up if

the system is in the up state at the time of measurement, and the second is the same, but for down. Assuming that $M_{\uparrow,\uparrow} + M_{\uparrow,\downarrow} = 1$ and similarly for the $\downarrow$ case, the measured signal is then

$$2s_z = M_{\uparrow\uparrow} - M_{\downarrow\downarrow} + I_p S_z(\downarrow)(2M_{\uparrow\uparrow} + 2M_{\downarrow\downarrow} - 2) \tag{B.19}$$

where $S_z(\downarrow)$ is the result given by the model of this paper for an initial $\downarrow$ state (see Eqns. B.11 and B.18, and recall that $2S_z = \mathrm{Re}[\langle \hat{f} + \hat{\zeta}(t) \rangle]$).

To include bath effects, a Gaussian density of states (appropriate if the size of the bath is $\gtrsim 20$ effective spins) is assumed. Then $\rho(\delta) = \exp[-\delta^2/(2\lambda^2)]/\sqrt{2\pi\lambda^2}$, where λ is the bath strength parameter. While non-Gaussian effects, leading to mesoscopic fluctuations, are important, their inclusion leads to too many highly correlated fitting parameters.

Appendix C

Details for Chapter 6: inelastic decay and charge-based dephasing

C.1 Adiabatic elimination for nuclear-spin-mediated inelastic decay

We will transform the superoperator (Eqn. 6.15) into the interaction picture, but first introduce matrix elements between the eigenstates of the quasi-static fields and the state $|S\rangle$ occurring in the superoperator. For a single spin in a magnetic field $\vec{B} = B_{\text{nuc}}(x, y, z)$ and $|B| = B_{\text{nuc}}n$ (the roman variables x, y, z, n are chosen such that the nuclear field contribution will be of order unity), the eigenstates may be written by rotation from spin states aligned with the z-axis ($\{|\uparrow\rangle, |\downarrow\rangle\}$):

$$\begin{pmatrix} |1/2\rangle \\ |-1/2\rangle \end{pmatrix} = \lim_{x' \to x^+} \frac{1}{\sqrt{2n(n+z)}} \begin{pmatrix} n+z & x'-iy \\ x'+iy & -n-z \end{pmatrix} \begin{pmatrix} |\uparrow\rangle \\ |\downarrow\rangle \end{pmatrix} \tag{C.1}$$

The limit is taken only to remove the degenerate case of field anti-aligned with the z-axis, i.e., $\vec{B} = (0, 0, -B)$, which would be degenerate for this matrix, and is implicit in what

follows. The corresponding eigenvalues of the Hamiltonian are $\pm\hbar\Omega n/2$ in this notation.

Setting $|S\rangle = (|\uparrow\downarrow\rangle - |\downarrow\uparrow\rangle)/\sqrt{2}$ and using the single spin transformations for l and r separately (with $\vec{B}^l = B^l_{\rm nuc}(x_l, y_l, z_l), |B^l| = n_l$ and similarly for r), we write

$$\begin{aligned} c_{1/2,1/2} = \langle \tfrac{1}{2}, \tfrac{1}{2}|S\rangle &= \frac{1}{\mathcal{N}}\left[(x_l + iy_l)(n_r + z_r) - (n_l + z_l)(x_l + iy_l)\right] \\ c_{1/2,-1/2} = \langle \tfrac{1}{2}, -\tfrac{1}{2}|S\rangle &= \frac{1}{\mathcal{N}}\left[-(n_l + z_l)(n_r + z_r) - (x_l + iy_l)(x_r - iy_r)\right] \\ c_{-1/2,1/2} = \langle -\tfrac{1}{2}, \tfrac{1}{2}|S\rangle &= -c^*_{1/2,-1/2} \\ c_{-1/2,-1/2} = \langle -\tfrac{1}{2}, -\tfrac{1}{2}|S\rangle &= c^*_{1/2,1/2} \\ \text{and } \mathcal{N} &= \sqrt{8 n_l n_r (n_l + z_l)(n_r + z_r)} \end{aligned}$$

It is convenient to define $c_{++} = c_{1/2,1/2}$ and $c_{+-} = c_{1/2,-1/2}$ as the spin-aligned and spin-anti-aligned coefficients, respectively. This allows us to express $|S\rangle$ occurring in Eqn. 6.15 in terms of the eigenstates of the Hamiltonian as

$$|S\rangle = \sum_{s,s'} c_{s,s'}|s,s'\rangle = c_{++}|\tfrac{1}{2},\tfrac{1}{2}\rangle + c_{+-}|\tfrac{1}{2},-\tfrac{1}{2}\rangle - c^*_{+-}|-\tfrac{1}{2},\tfrac{1}{2}\rangle + c^*_{++}|-\tfrac{1}{2},-\tfrac{1}{2}\rangle \tag{C.2}$$

In the interaction picture, each eigenstate $|s,s'\rangle$ evolves according to

$$|s,s'(t)\rangle = e^{-iE_{s,s'}t/\hbar}|s,s'\rangle = e^{-i(s n_l \gamma_e B_{{\rm nuc},l} + s' n_r \gamma_e B_{{\rm nuc},r})t} \ , \tag{C.3}$$

and $|S(t)\rangle = \sum_{s,s'} c_{s,s'}|s,s'(t)\rangle$.

With these results, the Louivillian may be put into the interaction picture:

$$\dot{\tilde{\rho}} = \Gamma(\mathcal{E})/2 \sum_{s,s',r,r'} c_{s,s'} c^*_{r,r'} e^{i[(r-s)n_l\gamma_e B_{{\rm nuc},l} + (r'-s')n_r\gamma_e B_{{\rm nuc},r}]t} L_{s,s',r,r'}[\tilde{\rho}] \tag{C.4}$$

where

$$L_{s,s',r,r'}[\tilde{\rho}] = [|s,s'\rangle\langle r,r'|\tilde{\rho} + \tilde{\rho}|s,s'\rangle\langle r,r'| - 2|G\rangle\langle r,r'|\tilde{\rho}|s,s'\rangle\langle G|] \tag{C.5}$$

So far, this result is exact within the QSA.

When $\Gamma(\mathcal{E}) \ll \gamma_e B_{{\rm nuc},l}, \gamma_e B_{{\rm nuc},r}$, the exponential phase terms of Eqn. C.4 oscillate substantially faster than $\tilde{\rho}$ evolves. Adiabatic elimination becomes an appropriate

approximation when we may neglect quickly rotating terms, i.e., if we may neglect certain degenerate cases, such as situations with $|n_l\gamma_e B_{\mathrm{nuc},l} - n_r\gamma_e B_{\mathrm{nuc},r}| \lesssim \Gamma(\mathcal{E})$. In addition, we are implicitly assuming that $\Gamma(\mathcal{E}) \simeq \Gamma(\mathcal{E} + E_{s,s'} - E_{r,r'})$, which is appropriate for large $\mathcal{E}$ and smooth phonon density of states.

More explicitly, we can average each term of over several spin rotations and make a Born approximation:

$$\begin{gathered} e^{i[(r-s)n_l\gamma_e B_{\mathrm{nuc},l} + (r'-s')n_r\gamma_e B_{\mathrm{nuc},r}]t} L_{s,s',r,r'}[\tilde{\rho}(t)] \rightarrow \\ \left[\tfrac{1}{\tau}\int_{t-\tau}^{t} e^{i[(r-s)n_l\gamma_e B_{\mathrm{nuc},l} + (r'-s')n_r\gamma_e B_{\mathrm{nuc},r}]t'} dt'\right] L_{s,s',r,r'}[\tilde{\rho}(t)] \end{gathered} \tag{C.6}$$

The time averaging for a given s, s', r, r' is straightforward so long as $n_l B_{\mathrm{nuc},l} \neq n_r {B_{\mathrm{nuc},r}}$[1], giving

$$\lim_{\tau\to\infty} \frac{1}{\tau}\int_{t-\tau}^{t} e^{i[(r-s)n_l\gamma_e B_{\mathrm{nuc},l} + (r'-s')n_r\gamma_e B_{\mathrm{nuc},r}]t'} dt' = \delta_{s,r}\delta_{s',r'} \tag{C.7}$$

Thus terms with quickly varying phase go to zero.

C.2 Dephasing power spectra

We now evaluate dephasing in exchange gates due to charge fluctuations for a variety of spectal functions. The error should go as $[1 - \exp(-\eta^2 P)]/2$, where the value η depends only on the bias parameter. The impact of the particular spectral function is encompassed in $P = \int d\omega\ S(\omega)\frac{\sin^2(t\omega/2)}{(\omega/2)^2}$. We have assumed that $S(\omega)$ has a high frequency cutoff $\gamma \ll 1/t$.

C.2.1 White noise

We set $S(\omega) = \frac{\nu}{2\pi}e^{-\omega/\gamma}$. Then we can evaluate

$$P = \frac{\nu}{2\pi}\int d\omega\ \frac{\sin^2(\omega t/2)}{(\omega/2)^2} e^{-\omega/\gamma} \approx \nu t\ . \tag{C.8}$$

[1] When integrating over nuclear spin degrees of freedom, this corresponds to a surface of measure 0.

This indicates the expected exponential decay of coherence due to white noise dephasing.

C.2.2 $1/f$ noise

With $S(\omega) = \nu^2/\omega$ and frequency cutoffs $B < \omega < \gamma \ll 1/t$,

$$P = 2\log[\gamma/B](\nu t)^2 \ . \tag{C.9}$$

For a bath of $1/f$ distributed fluctuators, the initial dephasing is quadratic in the time of interaction, and increases as the measurement timescale $(1/B)$ increases. At long times, the decay is gaussian, with super-exponential suppression of coherence.

C.2.3 Ohmic noise

Taking $S(\omega) = g\omega e^{-\omega/\gamma}$, evaluation of P is possible, giving

$$P = 2g\log[1 + (\gamma t)^2] \ . \tag{C.10}$$

When considered in the decay function $\exp(-\eta^2 P)$, this gives a non-exponential decay law, $\exp(-\eta^2 P) = [1 + (\gamma t)^2]^{-2g\eta^2}$. In the short time limit, this is quadratic decay, going as $1 - 2(g\eta^2)(\gamma t)^2 + O((\gamma t)^4)$, while the long time behavior is a power law with power $-4g\eta^2$.

C.2.4 Super-ohmic noise

For the final spectral function considered here, we set $S(\omega) = \nu^{1-\alpha}\omega^\alpha e^{-\omega/\gamma}$ where $\alpha > 1$ indicates super-ohmic noise. Evaluation of P proceeds in a straightforward manner, giving

$$\begin{aligned} P &= \frac{1}{4}\Gamma(\alpha-1)\left(\frac{\nu}{\gamma}\right)^{1-\alpha}\Big\{1 - \\ &\qquad \left[1 + (\gamma t)^{\frac{1}{2}-\frac{\alpha}{2}}\right]\cos[(\alpha-1)\tan^{-1}(\gamma t)]\Big\} \ . \end{aligned} \tag{C.11}$$

where $\Gamma(x)$ is the gamma function. This type of decay has a limiting value of

$$\lim_{t\to\infty} P = 4\Gamma(\alpha-1)\left(\frac{\nu}{\gamma}\right)^{1-\alpha} \tag{C.12}$$

and short time behavior according to

$$P(t) = 2\alpha(\alpha-1)\Gamma(\alpha-1)\left(\frac{\nu}{\gamma}\right)^{1-\alpha}(\gamma t)^2 + O((\gamma t)^4)\ . \tag{C.13}$$

For visual comparison, we calculate the expected, observable Rabi oscillations using SAP as a function of time in the biased regime (t_E) and detuning ϵ in Fig. 6.16. In essence, increasing the exponent of the noise spectra (from $1/\omega$ to constant to ω^α) leads to more oscillations as detuning is made more negative, i.e., as the admixture of charge decreases.

Appendix D

Reprint of Ref. [96], "Triplet-singlet spin relaxation via nuclei in a double quantum dot"

doi:10.1038/nature03815 nature

LETTERS

Triplet–singlet spin relaxation via nuclei in a double quantum dot

A. C. Johnson[1], J. R. Petta[1], J. M. Taylor[1], A. Yacoby[1,2], M. D. Lukin[1], C. M. Marcus[1], M. P. Hanson[3] & A. C. Gossard[3]

The spin of a confined electron, when oriented originally in some direction, will lose memory of that orientation after some time. Physical mechanisms leading to this relaxation of spin memory typically involve either coupling of the electron spin to its orbital motion or to nuclear spins[1–7]. Relaxation of confined electron spin has been previously measured only for Zeeman or exchange split spin states, where spin-orbit effects dominate relaxation[8–10]; spin flips due to nuclei have been observed in optical spectroscopy studies[11]. Using an isolated GaAs double quantum dot defined by electrostatic gates and direct time domain measurements, we investigate in detail spin relaxation for arbitrary splitting of spin states. Here we show that electron spin flips are dominated by nuclear interactions and are slowed by several orders of magnitude when a magnetic field of a few millitesla is applied. These results have significant implications for spin-based information processing[12].

The coupling of nuclear spins to electrons in low-dimensional semiconductors is known from optical and transport studies in quantum Hall systems to yield rich physical effects and provide new probes of the relatively isolated quantum system of nuclear spins in solids[13–16]. Confined electrons interacting with relatively few nuclei are particularly sensitive to hyperfine coupling. This can lead to dramatic effects such as tunnelling currents that slowly oscillate in time and electrical control and readout of nuclear polarization[17,18]. Here we show that the interaction between single electrons confined in quantum dots with ensembles of lattice nuclei can dominate electron spin relaxation.

We use high-frequency pulsed gates to measure spin relaxation in a GaAs double quantum dot (Fig. 1a). Measurements are performed near the (1,1) to (0,2) charge transition, where (n,m) denotes the absolute number of electrons on the left and right dots. In the (0,2) configuration, the two electrons form a spin singlet to avoid the large Pauli exclusion energy cost ($0.4\ \mathrm{meV} \gg kT \approx 10\ \mu\mathrm{eV}$) of occupying an excited orbital state[19,20]. In the separated (1,1) configuration, the two electrons may occupy any spin state. That is, apart from any Zeeman energy ($\sim$2.5 μeV at 100 mT), the singlet, (1,1)S, and three triplets, (1,1)T_-, (1,1)T_0, and (1,1)T_+ ($m_s = -1,0,1$ respectively), are effectively degenerate, given the weak interdot coupling to which the system is tuned.

Spin relaxation is measured by preparing an unpolarized mixture of (1,1) states and monitoring the probability of transition to (0,2)S

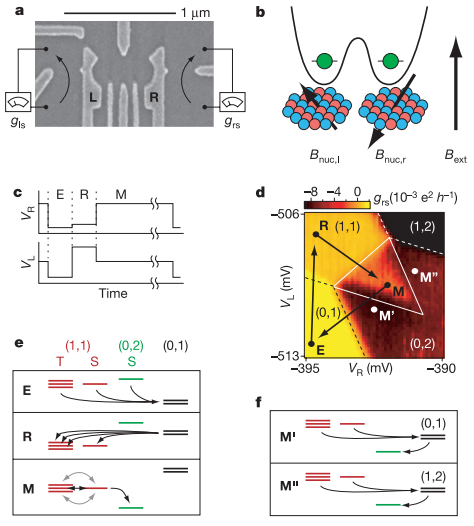

Figure 1 | Spin-selective tunnelling in a double quantum dot. a, Micrograph of a device similar to the one measured. Metal gates deplete a two-dimensional electron gas 100 nm below the surface, with density $2 \times 10^{11}\ \mathrm{cm}^{-2}$. A double dot is defined between gates L and R. Electrons tunnel between the dots and to conducting leads. Conductances g_{ls} and g_{rs} of the left and right QPCs reflect average occupation of each dot. **b**, In (1,1), spatially separated electrons feel different effective fields from hyperfine interaction with the local Ga and As nuclei, plus a uniform external field. **c**, Voltage pulses on gates L and R cycle through three configurations: empty (E), reset (R) and measure (M). **d**, Right sensor conductance g_{rs} as a function of direct-current voltages on the same two gates around the (1,1) to (0,2) transition, with pulse displacements shown by points E, R, and M. Dashed lines outline the (0,1), (1,1), (0,2), and (1,2) charge state plateaus during step M. Inside the solid-outlined 'pulse triangle', the ground state is (0,2), but higher sensor conductance indicates partially blocked tunnelling. A plane is subtracted from the raw data to remove direct gate–QPC coupling. **e**, Energetics of the pulse sequence. In (0,2), only the singlet is accessible, whereas in (1,1), singlet and triplet are degenerate. (0,1) and (1,2) are spin-1/2 doublets. Step E empties the second electron, then R loads a new electron into the left dot, occupying all four (1,1) states equally. At M, (0,2)S is the ground state, but only (1,1)S and the $m_s = 0$ triplet (1,1)T_0 can tunnel. Mixing of (1,1)T_+ and (1,1)T_- with the singlet is weak away from zero field, so their tunnelling is blocked. **f**, At M′, (0,1) has lower energy than (1,1) and provides an alternate, spin-independent path to (0,2). At M″, (1,2) provides this alternate path.

[1]Department of Physics, Harvard University, Cambridge, Massachusetts 02138, USA. [2]Department of Condensed Matter Physics, Weizmann Institute of Science, Rehovot 76100, Israel. [3]Materials Department, University of California, Santa Barbara, California 93106, USA.

© 2005 Nature Publishing Group

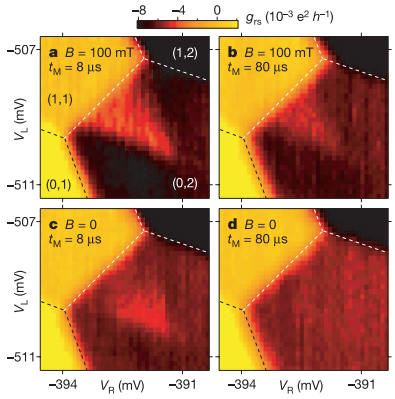

Figure 2 | Dependence of the occupancy of the (1,1) state on measurement time, t_M, and external field, B. a, Charge sensor conductance, g_{rs}, as a function of V_L and V_R with short pulses ($t_M = 8\,\mu s$) at $B = 100$ mT. Large average occupation of (1,1) is seen throughout the pulse triangle. Near the triangle edges, thermally activated tunnelling to the leads allows fast relaxation to (0,2), (see Fig. 1f). **b**, For longer pulses ($t_M = 80\,\mu s$), thermally relaxed triangle edges expand towards the centre of the triangle. **c**, At $B = 0$, the (1,1) occupation is extinguished at low detuning (near the (1,1)-(0,2) charge transition) as tunnelling to (0,2) becomes possible from the (1,1)T_+ and (1,1)T_- states. **d**, Combine these two effects at zero field with long pulses, and no residual (1,1) occupation is seen, indicating complete relaxation to (0,2).

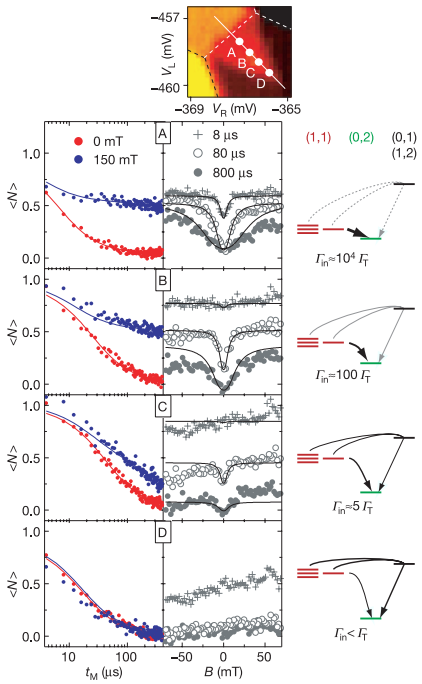

Figure 3 | Detailed measurements of blockaded (1,1) occupation. Average occupation $\langle N \rangle$ of the (1,1) charge state, based on calibrated charge sensor conductances, at four detuning points (labelled A, B, C, D in the uppermost panel). Left panels show $\langle N \rangle$ as a function of t_M at $B = 0$ and $B = 150$ mT. Middle panels show $\langle N \rangle$ as a function of B for different t_M times. Diagrams at right show schematically the relative position of energy levels and the extracted ratios of inelastic (Γ_{in}) to thermal (Γ_T) decay rates.

after the latter is made lower in energy by changing the electrostatic gate configuration. The different local environments acting on the two spins cause the two-electron spin state to evolve in time, and only if this spin state passes near (1,1)S is a transition to (0,2)S allowed. The average occupancy of the left dot, which reflects the probability of this transition, is monitored using local quantum point contact (QPC) charge sensors[19]. Conductances g_{ls} and g_{rs} of the left and right sensors change by several per cent when an electron enters the dot nearest the sensor[21–24].

The energy levels of each dot were controlled by voltage pulses on gates L and R, as shown in Fig. 1c (ref. 19, and see also Supplementary Information). The double dot was cycled through three configurations, depicted in Fig. 1e, while measuring the average QPC conductances. In the 'empty' (E) step, the second electron is removed, leaving a (0,1) state. In the 'reset' (R) step, a new second electron is added, initializing the (1,1) state to an unbiased mixture of the singlet, (1,1)S, and the three triplets (1,1)T_-, (1,1)T_0, and (1,1)T_+. In the 'measurement' (M) step, (0,2) is lowered relative to (1,1) until (0,2)S becomes the ground state, while the (0,2) triplets remain inaccessible, above the (1,1) states. Because tunnelling preserves spin, only (1,1)S can relax to (0,2)S, while the (1,1) triplets are spin-blockaded from making this transition[25,26].

The measurement step accounted for 80% of the pulse period (E and R were each 10%) so the time-averaged charge-sensor signal mainly reflects the charge state during the measurement time, t_M. Figure 1d shows g_{rs} as a function of the constant offsets to gate voltages V_L and V_R with pulses applied. The dashed lines indicate locations of ground-state transitions during the M step, as seen in unperturbed double dots[22]. Gate pulses alter this signal only within the 'pulse triangle' (outlined by solid white lines). Here g_{rs} is intermediate between the (0,2) and (1,1) plateaus, indicating that although (0,2) is the ground state, the system is often stuck in the excited (1,1) state. In the regions labelled M′ and M″, alternate, spin-independent relaxation pathways, shown in Fig. 1f, circumvent the spin blockade.

The magnetic field, B, and t_M dependence of the charge sensor signal is shown in Fig. 2. With $t_M = 8\,\mu s$, a large signal is seen in the pulse triangle, indicating that some of the (1,1) to (0,2) transitions are spin blocked. As t_M is increased this signal decreases (Fig. 2b), indicating that t_M is approaching the (1,1) singlet–triplet relaxation time. This is accompanied by a reduction in the pulse triangle size due to thermally activated processes as in Fig. 1f. Similar data, but at $B = 0$, are plotted in Figs 2c and d. The signal in the pulse triangle is noticeably weaker for the same t_M, particularly near the (1,1)-to-(0,2) charge transition, indicating enhanced spin relaxation.

Detailed measurements of residual (1,1) occupation as a function of detuning (the energy difference between the (1,1) and (0,2) states) are shown in Fig. 3. Conductances g_{ls} and g_{rs} were measured along the diagonal white line in the upper panel of Fig. 3, for various values of B and t_M, and converted to occupation $\langle N \rangle$ by scaling to the average (1,1) and (0,2) levels outside the pulse triangle. Data are shown in detail for the points labelled A through D. As in Fig. 2, strong field dependence was found at low detuning (point A), where

© 2005 Nature Publishing Group

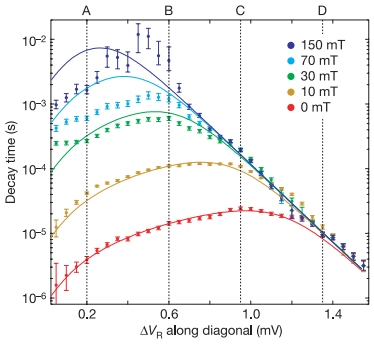

Figure 4 | Decay of (1,1) occupancy as a function of detuning at various magnetic fields. Dotted lines mark the locations of points A through D from Fig. 3. Fit of zero field theory (red curve) to data (red circles) sets all fit parameters except B_{nuc}, which is determined by fitting to the 10-mT data (gold). Theory curves at other fields are then fully determined. Error bars at zero field result from the least-squares fitting. Error bars at non-zero field reflect changes in the resulting decay rate as the zero-field fitting parameters are varied within their uncertainties.

inelastic interdot tunnelling dominates. This field dependence vanishes at higher detuning where thermally activated tunnelling to the leads dominates.

As in previous work[4,11], we model spin evolution in (1,1) by treating the ensemble of nuclear spins within each dot as a static effective field $\mathbf{B}_{nuc}$ with slow internal dynamics, that adds to any applied Zeeman field (see Fig. 1b). $\mathbf{B}_{nuc}$ is randomly oriented with root mean square strength $B_{nuc} = b_0\sqrt{I_0(I_0+1)/N_{nuc}}$, where $b_0 = 3.5$ T is the hyperfine constant in GaAs, $I_0 = 3/2$ is the nuclear spin and N_{nuc} is the effective number of nuclei with which the electron interacts[2,3,27,28]. In our dots, N_{nuc} is estimated at 10^6–10^7, giving $B_{nuc} \approx 2$–6 mT. The spins precess in a characteristic time $t_{nuc} = \hbar/g^*\mu_B B_{nuc} \approx 3$–10 ns, which can be regarded as an inhomogeneous dephasing time T_2^*. At $B = 0$, all four (1,1) spin states mix in this time, and tunnelling will appear insensitive to spin. With $B > B_{nuc}$, however, only (1,1)T_0 and (1,1)S are degenerate. These will continue to mix with the same rate, but (1,1)T_+ and T_- will be frozen out.

To model this mixing, we assume static nuclear fields during each pulse, a spin-preserving inelastic interdot tunnelling rate Γ_{in} from (1,1)S to (0,2)S, and a spin-independent rate Γ_T due to thermally activated tunnelling via the (0,1) and (1,2) charge states (see Supplementary Information for details). Zeeman eigenstates for two spins in fields $B\hat{\mathbf{z}} + \mathbf{B}_{nuc,l}$ and $B\hat{\mathbf{z}} + \mathbf{B}_{nuc,r}$, denoted $|(1,1)s,s'\rangle$ ($s,s' = \pm 1/2$), decay to (0,2)S on the basis of their overlap with (1,1)S, with rates $\Gamma_{s,s'} = \Gamma_{in}|\langle(1,1)S|(1,1)s,s'\rangle|^2$ as long as $\Gamma_{in} \ll g^*\mu_B B_{nuc}$. Averaging over nuclear field configuration and short-time dynamics gives decay rates for the $T_\pm$-like states:

$$\Gamma_{\pm 1/2,\pm 1/2} = \frac{\Gamma_{in}}{4(1+(B/B_{nuc})^2)} \qquad (1)$$

and $\Gamma_{\pm 1/2,\mp 1/2} = \Gamma_{in}/2 - \Gamma_{\pm 1/2,\pm 1/2}$ for the S-like and T_0-like states. At $B = 0$, total transition rates for all (1,1) states into (0,2)S are the same, $\tau_0^{-1} = \Gamma_{in}/4 + \Gamma_T$. For $B > B_{nuc}$, transition rates $\tau_B^{-1} = \Gamma_{\pm 1/2,\pm 1/2} + \Gamma_T$ from (1,1)$T_\pm$ to (0,2)S are suppressed by field, while transitions from (1,1)S and (1,1)T_0 to (0,2)S are accelerated by up to a factor of two because they no longer mix with (1,1)$T_\pm$. During the gate-pulse transition from R to M, the relatively fast transition from (1,1)S to (0,2)S allows a fraction q of the (1,1)S state to transfer adiabatically to (0,2)S, reducing the initial occupation of (1,1)S. The resulting average occupancy N of (1,1) after a time t_M is:

$$N(t_M) = \frac{1}{t_M}\int_0^{t_M} dt\left(\frac{1}{2}e^{-t/\tau_B} + \frac{2-q}{4}e^{-t(2\tau_0^{-1}-\tau_B^{-1})}\right). \qquad (2)$$

Experimentally measured values for N as functions of t_M and B for various detunings are shown in Fig. 3, along with fits to the above theory. An additional field-independent parameter, N_∞, accounts for non-zero $N(t_M)$ at long times owing to thermal occupation of (1,1). N_∞ is zero at large detuning but increases, as expected, near zero detuning. Non-zero q values are found only at very low and very high detuning (where the R point is near zero detuning), where the slew rate of the pulse is low as it crosses to (0,2). With these parameters and τ_0 set for a given detuning by fitting the zero-field data (red), the high-field data (blue) are fitted with just the longer decay times τ_B for the (1,1)$T_\pm$ states. The field-dependence curves (black) are then fully determined by B_{nuc}, which is most accurately determined from data in Fig. 4, as discussed below. Drift in sensor conductance over long field sweeps is compensated by allowing a vertical shift in the field-dependence curves. The depth and width of the dips in these curves are not adjustable.

Figure 4 shows the extracted decay times τ_0 and τ_B versus detuning for various fields. As the magnetic field increases, more points at high detuning fall along a line in this semi-log plot, denoting exponential energy dependence as expected for a thermally activated process. This persists over three orders of magnitude at the highest field, and with calibration from transport measurements yields a temperature of 160 ± 20 mK. At zero field, thermal decay dominates only at the highest detunings, and the low-detuning times are well fitted by a power-law function of detuning with exponent 1.2 ± 0.2 and offset 700 ns, typical of inelastic tunnelling in double quantum dots[29]. Adding these two processes gives the red curve in Fig. 4, in good agreement with the zero-field data. The 10-mT curve is fitted using these zero-field parameters, but with times for the inelastic component increased by the factor $(1 + (B/B_{nuc})^2)$ from equation (1). The fit gives $B_{nuc} = 2.8 \pm 0.2$ mT, or $N_{nuc} \approx 6 \times 10^6$, within expectations. This value uniquely determines the remaining theory curves. For τ_B longer than about 1 ms the decay is faster than theory predicts (though still 10^3 times slower than at $B = 0$), indicating that another mechanism such as spin-orbit coupling may operate on millisecond timescales[8–10]. Spin-orbit coupling is expected to dominate spin relaxation at external fields of several tesla[9]. This regime is better suited to parallel fields, which couple almost exclusively to spin, than to the perpendicular orientation used here, which affects orbital wavefunctions at high fields.

Given B_{nuc} above, the model predicts an inhomogeneous dephasing time $T_2^* \approx 9$ ns for this device, which is independent of external field despite the enhanced relaxation times measured at higher fields. Up to 1 ms, the excellent agreement between experiment and theory indicates that hyperfine interaction is the only relevant source of spin relaxation in this system. Several strategies are available to circumvent this short dephasing time. Materials with zero nuclear spin, such as carbon nanotubes, avoid hyperfine effects entirely. Controlling $\mathbf{B}_{nuc}$ via nuclear polarization[11,17] is tempting, but high polarization is required for T_2^* to increase substantially[30]. An alternative is to use spin echo techniques such as pulsed electron spin resonance to extend coherence to the nuclear spin correlation time, expected to be of the order of 100 μs in these devices[4].

Received 25 February; accepted 19 May 2005.
Published online 8 June 2005.

1. Khaetskii, A. V. & Nazarov, Y. V. Spin relaxation in semiconductor quantum dots. *Phys. Rev. B* **61**, 12639–12642 (2000).
2. Erlingsson, S. I., Nazarov, Y. V. & Fal'ko, V. I. Nucleus-mediated spin-flip transitions in GaAs quantum dots. *Phys. Rev. B* **64**, 195306 (2001).
3. Khaetskii, A. V., Loss, D. & Glazman, L. Electron spin decoherence in quantum dots due to interaction with nuclei. *Phys. Rev. Lett.* **88**, 186802 (2002).

© 2005 Nature Publishing Group

4. Merkulov, I. A., Efros, Al. L. & Rosen, M. Electron spin relaxation by nuclei in semiconductor quantum dots. *Phys. Rev. B* **65,** 205309 (2002).
5. de Sousa, R. & Das Sarma, S. Theory of nuclear-induced spectral diffusion: Spin decoherence of phosphorus donors in Si and GaAs quantum dots. *Phys. Rev. B* **68,** 115322 (2003).
6. Coish, W. A. & Loss, D. Hyperfine interaction in a quantum dot: Non-Markovian electron spin dynamics. *Phys. Rev. B* **70,** 195340 (2004).
7. Golovach, V. N., Khaetskii, A. & Loss, D. Phonon-induced decay of the electron spin in quantum dots. *Phys. Rev. Lett.* **93,** 016601 (2004).
8. Fujisawa, T., Austing, D. G., Tokura, Y., Hirayama, Y. & Tarucha, S. Allowed and forbidden transitions in artificial hydrogen and helium atoms. *Nature* **419,** 278–281 (2002).
9. Elzerman, J. M. *et al.* Single-shot readout of an individual electron spin in a quantum dot. *Nature* **430,** 431–435 (2004).
10. Kroutvar, M. *et al.* Optically programmable electron spin memory using semiconductor quantum dots. *Nature* **432,** 81–84 (2004).
11. Bracker, A. S. *et al.* Optical pumping of the electronic and nuclear spin of single charge-tunable quantum dots. *Phys. Rev. Lett.* **94,** 047402 (2005).
12. Loss, D. & DiVincenzo, D. P. Quantum computation with quantum dots. *Phys. Rev. A.* **57,** 120–126 (1998).
13. Wald, K. R., Kouwenhoven, L. P., McEuen, P. L., Van der Vaart, N. C. & Foxon, C. T. Local dynamic nuclear polarization using quantum point contacts. *Phys. Rev. Lett.* **73,** 1011–1014 (1994).
14. Salis, G. Optical manipulation of nuclear spin by a two-dimensional electron gas. *Phys. Rev. Lett.* **86,** 2677–2680 (2001).
15. Kumada, N., Muraki, K., Hashimoto, K. & Hirayama, Y. Spin degree of freedom in the $\nu = 1$ bilayer electron system investigated via nuclear spin relaxation. *Phys. Rev. Lett.* **94,** 096802 (2005).
16. Smet, J. H. *et al.* Gate-voltage control of spin interactions between electrons and nuclei in a semiconductor. *Nature* **415,** 281–286 (2002).
17. Ono, K. & Tarucha, S. Nuclear-spin-induced oscillatory current in spin-blockaded quantum dots. *Phys. Rev. Lett.* **92,** 256803 (2004).
18. Bracker, A. S. *et al.* Optical pumping of the electronic and nuclear spin of single charge-tunable quantum dots. *Phys. Rev. Lett.* **94,** 047402 (2005).
19. Petta, J. R. *et al.* Pulsed gate measurements of the singlet-triplet relaxation time in a two-electron double quantum dot. Preprint at ⟨http://arxiv.org/abs/cond-mat/0412048⟩ 2004.
20. Ashoori, R. C. *et al.* N-electron ground-state energies of a quantum-dot in a magnetic field. *Phys. Rev. Lett.* **71,** 613–616 (1993).
21. Field, M. *et al.* Measurements of Coulomb blockade with a non-invasive voltage probe. *Phys. Rev. Lett.* **70,** 1311–1314 (1993).
22. DiCarlo, L. *et al.* Differential charge sensing and charge delocalization in a tunable double quantum dot. *Phys. Rev. Lett.* **92,** 226801 (2004).
23. Elzerman, J. M. *et al.* Few-electron quantum dot circuit with integrated charge readout. *Phys. Rev. B* **67,** 161308 (2003).
24. Petta, J. R., Johnson, A. C., Marcus, C. M., Hanson, M. P. & Gossard, A. C. Manipulation of a single charge in a double quantum dot. *Phys. Rev. Lett.* **93,** 186802 (2004).
25. Ono, K., Austing, D. G., Tokura, Y. & Tarucha, S. Current rectification by Pauli exclusion in a weakly coupled double quantum dot system. *Science* **297,** 1313–1317 (2002).
26. Johnson, A. C., Petta, J. R., Marcus, C. M., Hanson, M. P. & Gossard, A. C. Singlet-triplet spin blockade and charge sensing in a few-electron double quantum dot. Preprint at ⟨http://arxiv.org/abs/cond-mat/0410679⟩ 2004.
27. Paget, D., Lampel, G., Sapoval, B. & Safarov, V. I. Low field electron-nuclear spin coupling in gallium-arsenide under optical-pumping conditions. *Phys. Rev. B* **15,** 5780–5796 (1977).
28. Dobers, M., von Klitzing, K., Schneider, J., Weimann, G. & Ploog, K. Electrical detection of nuclear magnetic-resonance in GaAs-AlxGa1-xAs heterostructures. *Phys. Rev. Lett.* **61,** 1650–1653 (1988).
29. Fujisawa, T. *et al.* Spontaneous emission spectrum in double quantum dot devices. *Science* **282,** 932–935 (1998).
30. Das Sarma, S., de Sousa, R., Hu, X. & Koiller, B. Spin quantum computation in silicon nanostructures. *Solid State Commun.* **133,** 737–746 (2005).

Supplementary Information is linked to the online version of the paper at www.nature.com/nature.

Acknowledgements We thank H. A. Engel and P. Zoller for discussions. This work was supported by the ARO, the DARPA-QuIST programme, and the NSF, including the Harvard NSEC.

Author Information Reprints and permissions information is available at npg.nature.com/reprintsandpermissions. The authors declare no competing financial interests. Correspondence and requests for materials should be addressed to C.M. (marcus@harvard.edu).

© 2005 Nature Publishing Group

Appendix E

Details for Chapter 7: spin diffusion via nuclear dipole-dipole interactions

On distance scales much larger than the lattice spacing constant a, and time scales much longer than the nearest-neighbor dipole-dipole interaction t_{dd}, the dipole-dipole interaction of lattice nuclear spins is well described by the diffusion equation, under the approximation $\hat{\vec{I}}^j \rightarrow \hat{\vec{I}}(r_j)$, with diffusion constants specific to the material parameters. That is,

$$\partial_t \hat{\vec{I}}(\vec{r}) = -D\nabla^2 \hat{\vec{I}}(\vec{R}) \tag{E.1}$$

Diffusion constants may be determined analytically and experimentally by a variety of means, as discussed elsewhere [168, 48]. For example, GaAs has a diffusion constant $D = 10^{-11}$ cm^2/s [147].

At finite magnetic field, when nuclear spin-electron spin exchange is suppressed by energy conservation considerations, we may evaluate the correlator $\langle \hat{A}_z(t')\hat{A}_z(t)\rangle$ by

transforming the problem by a fourier transform. For example, setting

$$\hat{J}_z^k = \frac{1}{\sqrt{N}} \sum_j e^{i\vec{k}\cdot\vec{r}_j} \hat{I}_z^j \tag{E.2}$$

and neglecting Knight shift terms,

$$\partial_t \hat{J}_z^k = -Dk^2 \hat{J}_z^k + \sqrt{2Dk^2}\eta^k(t) \tag{E.3}$$

where $\eta(t)$ is a (quantum) stochastic noise force necessary for any quantum Langevin equation [79]. This can be solved starting at t_0 with initial conditions $\hat{J}_z^k(t_0)$:

$$\hat{J}_z^k(t) = e^{-\Gamma_k(t-t_0)}\hat{J}_z^k(t_0) + \sqrt{2\Gamma_k}\int_{t_0}^{t} e^{-\Gamma_k(t-t')}\eta(t')\ dt' \ . \tag{E.4}$$

where $\Gamma_k = Dk^2$.

To find the statistics for $\eta^k(t)$, we set $\langle \hat{I}_z^j \hat{I}_z^{j'} \rangle = \delta_{j,j'} I$ (for example, for spin-1/2, $I = 1/4$) and evaluate

$$\begin{aligned}
\langle \hat{J}_z^{-k} \hat{J}_z^{k'} \rangle &= \frac{1}{N} \sum_{j,j'} e^{-i(\vec{k}\cdot\vec{r}_j - \vec{k'}\cdot\vec{r}_{j'})} \langle \hat{I}_z^j \hat{I}_z^{j'} \rangle & \text{(E.5)} \\
&= \frac{1}{N} \sum_{j,j'} e^{-i(\vec{k}\cdot\vec{r}_j - \vec{k'}\cdot\vec{r}_{j'})} \delta_{j,j'} I & \text{(E.6)} \\
&= \frac{I}{N} \sum_{j} e^{-i(\vec{k}-\vec{k'})\cdot\vec{r}_j} & \text{(E.7)} \\
&= \delta_{k,k'} I & \text{(E.8)}
\end{aligned}$$

As this must be satisfied at all times for a system in thermodynamic equilibrium, we set $t_0 \to -\infty$, and

$$\begin{aligned}
\langle \hat{J}_z^{-k}(t) \hat{J}_z^{k'}(t) \rangle &= \sqrt{4\Gamma_k \Gamma_k'} e^{-\Gamma_k t - \Gamma_{k'} t} \int_{-\infty}^{t}\int_{-\infty}^{t} e^{\Gamma_k \tau + \Gamma_{k'}\tau'} \langle \eta^{-k}(\tau)\eta^{k'}(\tau')\rangle d\tau'\ d\tau \\
\frac{I}{2\Gamma_k}\delta_{k,k'} e^{2\Gamma_k t} &= \int_{-\infty}^{t}\int_{-\infty}^{t} e^{\Gamma_k \tau + \Gamma_{k'}\tau'} \langle \eta^{-k}(\tau)\eta^{k'}(\tau')\rangle d\tau'\ d\tau
\end{aligned}$$

This equation requires $\langle \eta^{-k}(\tau)\eta^{k'}(\tau')\rangle = I\delta_{k,k'}\delta(\tau - \tau')$. In principle, the spin diffusion

problem is now solved, and arbitrary correlators may be evaluated. For example,

$$\langle \hat{J}_z^{-k}(t)\hat{J}_z^{k'}(t')\rangle = \delta_{k,k'}2\Gamma_k I\int_{-\infty}^{t}\int_{-\infty}^{t'} e^{\Gamma_k(\tau-t+\tau'-t')}\delta(\tau-\tau')d\tau'\,d\tau \tag{E.9}$$

$$= \delta_{k,k'}2\Gamma_k I\int_{-\infty}^{\min(t',t)} e^{\Gamma_k(2\tau-t-t')}d\tau \tag{E.10}$$

$$= \delta_{k,k'}Ie^{-\Gamma_k|t-t'|} \tag{E.11}$$

We seek to rewrite $\hat{A}_z$ in terms of $\hat{J}_z^k$. In practice, each nuclear species diffuses independently of the others (secular approximation at finite magnetic field) with diffusion constant D_β. So we set $\hat{A}_z = \sum_\beta \hat{A}_z^\beta$, and for each species, β,

$$\hat{A}_z^\beta = \sum_j \lambda_{j,\beta}\hat{I}_z^{j,\beta} = \sum_k \Lambda_{k,\beta}\hat{J}_z^{k,\beta} \tag{E.12}$$

where $\Lambda_{k,\beta} = N^{-1/2}\sum_j e^{i\vec{k}\cdot\vec{r}_{j,\beta}}\lambda_{j,\beta}$, and $\Lambda^*_{-k,\beta} = \Lambda_{k,\beta}$. Finally,

$$\langle \hat{A}_z^\beta(t)\hat{A}_z^{\beta'}(t')\rangle = \delta_{\beta,\beta'}\sum_{k,k'}\Lambda^*_{k,\beta}\Lambda_{k',\beta}\langle \hat{J}_z^{-k}(t)\hat{J}_z^{k'}(t')\rangle \tag{E.13}$$

$$= I\delta_{\beta,\beta'}\sum_k |\Lambda_{k,\beta}|^2 e^{-\Gamma_{k,\beta}|t-t'|} \tag{E.14}$$

$$\approx \frac{Ix_\beta}{I\int|\psi(k)|^4 d^3k}\delta_{\beta,\beta'}\int |\psi(k)|^4 e^{-D_\beta|t-t'|k^2}\,d^3k\ . \tag{E.15}$$

The final result depends upon the choice of wavefunction. For a oblate spheroid, such as a lateral quantum dot, with z-axis width σ_z and x, y axis width σ_{xy} (and $\tau \geq 0$):

$$\langle \hat{A}_z^\beta(t+\tau)\hat{A}_z^\beta(t)\rangle = \frac{x_\beta}{[1+\tau D_\beta/\sigma_z^2]^{1/2}[1+\tau D_\beta/\sigma_{xy}^2]} \tag{E.16}$$

This indicates that, for $\langle \hat{A}_z(t)\hat{A}_z(t')\rangle = \int d\omega\ S(\omega)e^{i\omega(t-t')}$,

$$S(\omega) = \frac{1}{2\pi}\sum_\beta x_\beta\int d\tau\ e^{-i\omega\tau}[1+\tau D_\beta/\sigma_z^2]^{-1/2}\times[1+\tau D_\beta/\sigma_{xy}^2]^{-1}\ . \tag{E.17}$$

Roughly speaking, the correlation time of $\hat{A}_z(t)$ due to diffusion is given by $t_c = \min_{\beta,\mu}(D_\beta/\sigma_\mu^2)$. For GaAs dots with a 10 nm wide transverse wavefunction, and of lateral extent $\gg 10$ nm, $t_c \simeq 1$ s.

Appendix F

Details for Chapter 8: electron spin-based quantum repeaters and $m_s = 0$ measurement methods

In this appendix we consider an alternative means of preparation and measurement that focuses on keeping the $m_s = 0$ subspace ($|S\rangle, |T_0\rangle$) undisturbed. These may be more difficult to implement experimentally.

F.1 Measurement-based preparation

The four particle state $|\Psi\rangle$ can be prepared by a different projective measurement on two-particle singlet states, as we demonstrate below. A measurement of the two electron spin projection ($\hat{S}_z = \hat{S}_z^A + \hat{S}_z^B$ for electrons A and B) that preserves the $m_s = 0$ subspace is sufficient.

The protocol starts with the generation of a singlet-pair in the center dot, labeled electrons one and two. The pair is separated, and electron one is shuttled to the left dot,

while electron two goes to the right dot. Another singlet is prepared in the center dot, and electrons three and four follow one and two, respectively. At the destination, one and three are joined in a single-dot for am m_s sensitive measurement, as are two and four. At this point,

$$(\cos(\theta)|S\rangle_{12} + i\sin(\theta)|T_0\rangle_{12})(\cos(\theta)|S\rangle_{34} + i\sin(\theta)|T_0\rangle_{34}) \tag{F.1}$$

where θ is determined by the difference in the quasi-static fields encountered in the left and right channels. Using the m_s sensitive measurement, a positive result projects both left and right subsystems into the $m_s = 0$ subspace with a joint probability of success of 50%. The projected state is

$$1/\sqrt{2}(|\uparrow\downarrow\downarrow\uparrow\rangle_{1234} + |\downarrow\uparrow\uparrow\downarrow\rangle_{1234}) = 1/\sqrt{2}(|S\rangle_{13}|S\rangle_{24} + |T_0\rangle_{13}|T_0\rangle_{24}). \tag{F.2}$$

This is equal to the state $|\Psi\rangle$ under exchanging electrons 3 and 4. Correspondingly, using the cycling procedure on the left and right subsystems preserves this superposition state.

Now we show how a projective m_s measurement can be implemented using either anisotropic exchange (Eq. 8.15) or using magnetic field gradients. In the case of anisotropic exchange, the rotation angle γ depends upon the geometry of the double-dot configuration. In the (1,1) configuration, γ can be large, while in the (0,2) configuration, $\gamma \to 0$ in the case of cylindrical symmetry. With finite tunnel coupling near the (1,1)-(0,2)-(0,1) triple-point, the $|m_s| = 1$ states can be on resonance for tunneling from (1,1) to (0,2), as shown in Fig. F.1a. Opening the left lead only means the (0,1)-(1,1) transition is not allowed. However, population in a (0,2) excited state (i.e., the $|m_s| = 1$ triplets) will tunneling out to the Fermi sea quickly. Thus measuring the (0,2) or (0,1) charge configuration indicates the system was in a $|m_s| = 1$ triplet, while the (1,1) configuration corresponds to the $m_s = 0$ subspace; in addition, it leaves that subspace untouched. The tunneling events should occur on a time scale much faster than state relaxation and dephasing. The smallest

energy difference in the model, $J_\perp/2 - J_\parallel/2 \simeq J_\parallel\gamma^2/4$, determines the limiting time scale, and for GaAs lateral dots separated by 100 nm, may be as large as 50 μeV (a time scale of 30 ps).

In a material with small spin-orbit coupling, anisotropy will be small, and instead a magnetic field gradient may be used to distinguish $|m_s| = 1$ and $m_s = 0$ states, as shown in Fig. F.1b. Permanent magnets may produce field gradients as large as 1 mT/nm; then the limiting time scale in the problem is $\hbar/(g^*\mu_B 0.1\text{T}) \simeq 70$ps, much faster than pure dephasing and relaxation terms.

F.2 Purification with $m_s = 0$ measurement for single electron proposal

In this subsection, we show that the measurement which enables one to project (non-destructively) into the $m_s = 0$ subspace, allows one to implement an entanglement purification protocol. We consider again the case where each electron serves as a qubit, i.e., the non-encoded case considered in Sec. 8.1. We show that the resulting entanglement purification protocol has exactly the same purification curve as protocol 1 (Ref. [10]), however the success probability is decreased by a factor of 1/8.

The essential part of protocol 1 (and also protocols 1',2,2') is the local projection into a (correlated) two-dimensional subspace, where the second particle is factored out. In the case of protocol 1, this is achieved by performing a CNOT operation and measuring the second particle in the z-basis. We will show that there exists an alternative procedure based on m_s sensitive measurements which has exactly the same effect on arbitrary input states. We start by considering the action CNOT followed by z-measurement on basis states $\{|i\rangle_{A_1}|j\rangle_{A_2}\}$, $i, j \in \{0, 1\}$ where we identify $|0\rangle \equiv |\uparrow\rangle, |1\rangle \equiv|\downarrow\rangle$. For measurement outcome

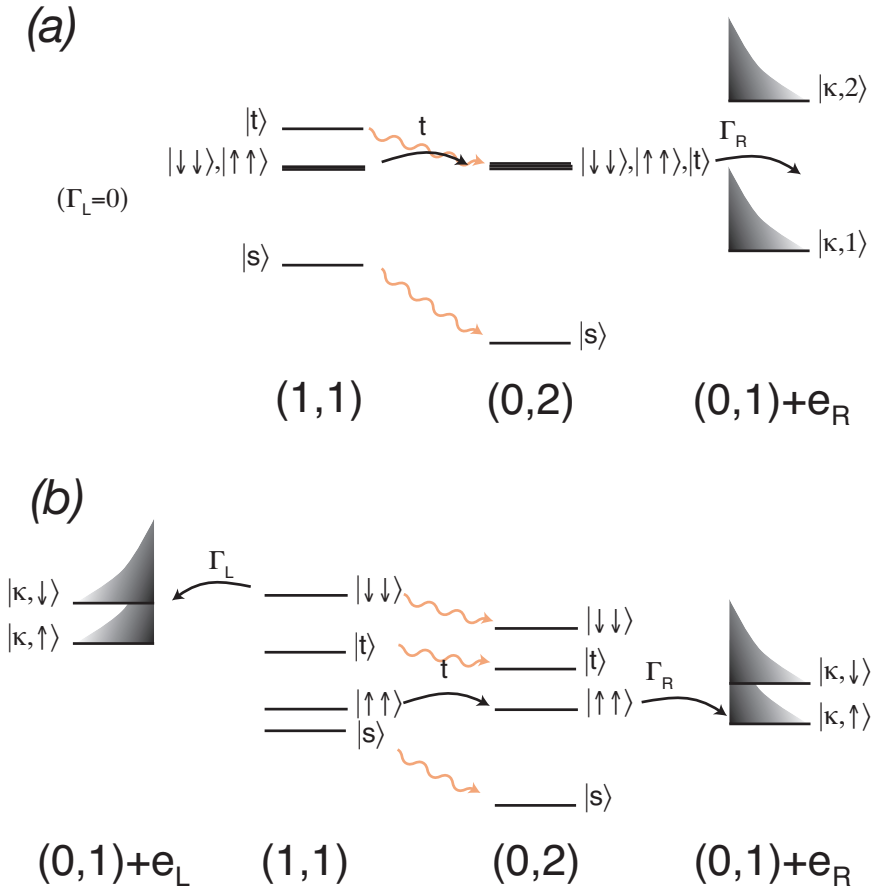

Figure F.1: m_s projective measurement. Initial population is in the (1,1) configuration; allowed transitions are in black, forbidden transitions in orange. (a) Differing anisotropy and exchange coupling leads to state selective tunneling from (1,1) to (2,0) charge configurations. Coupling to the leads of the right dot lead to electron tunneling; turning tunneling t back to zero freezes further evolution, and a charge measurement distinguishes between (1,1) ($m_s = 0$, subspace preserved) and (0,1) ($|m_s| = 1$, but destructive). (b) A magnetic field gradient leads to greater Zeeman splitting of the triplet levels in the extended configuration, (1,1) than the (0,2) configuration. Potential bias from left to right allows state selective tunneling from the (1,1) to (0,1) configuration only for the highest energy triplet, while (0,2) to (0,1) is allowed for all three triplets. State selective tunneling from (1,1) to (0,2) prevents the $m_s = 0, m_s = 1$ states from tunneling across. Closing the leads and tunnel coupling freezes the system, allowing for measurement of the charge configuration. As for (a), a (1,1) charge configuration measures $m_s = 0$ but does not destroy the $m_s = 0$ subspace.

'1', we have that

$$P_1^{A_2} U_{\mathrm{CNOT}}^{A_1 A_2} |i\rangle_{A_1} |j\rangle_{A_2} = \delta_{i,j\oplus 1} |i\rangle_{A_1} |1\rangle_{A_2}, \tag{F.3}$$

where $\oplus$ denotes addition modulo 2, i.e., $\delta_{i,j\oplus 1} = 1$ iff $ij = 01$ or 10. We remark that the projection into the $m_s = 0$ subspace, $P_{m_s=0} = |01\rangle\langle 01| + |10\rangle\langle 10|$, also leads to a $\delta_{i,j\oplus 1}$, however the second particle is not factored out. This factorization can be achieved by measuring the second particle in the eigenbasis of σ_x and considering only the measurement outcome '+', i.e., the projector $P_+^{A_2}$ where $P_\pm = |\pm\rangle_{A_2}\langle\pm|$ and $|\pm\rangle = 1/\sqrt{2}(|0\rangle \pm |1\rangle)$. That is

$$P_+^{A_2} P_{m_s=0}^{A_1 A_2} |i\rangle_{A_1} |j\rangle_{A_2} = \delta_{i,j\oplus 1} |i\rangle_{A_1} |+\rangle_{A_2}, \tag{F.4}$$

i.e., the action of the $m_s = 0$ measurement followed by the x-measurement of particle A_2 is—up to a basis change for the particle A_2—exactly the same as the CNOT operation followed by z-measurement on particle A_2. Note that the basis change of particle A_2 is irrelevant in our context, as in the purification protocol particles A_2, B_2 are discarded and hence traced out. The reduced density operator of particles $A_1 B_1$ does not depend on local unitary operations in A_2. Note that the action of these two procedures is the same only for *specific* measurement outcomes.

Given that the basic building block of the entanglement purification protocol 1 [10] can also be obtained by the sequence of measurements described in Eq. F.4, it is now straightforward to see that an entanglement purification protocol can be realized in this way. We consider the entanglement purification protocol of Ref. [10]. In the case where after the bilateral CNOT operation in both z-measurements on particles A_2, B_2 the result '1' is found can also be obtained by measurements of $P_+^{A_2} P_{m_s=0}^{A_1 A_2}$ and $P_+^{B_2} P_{m_s=0}^{B_1 B_2}$. The output state is in this case exactly the same for both procedures. The success probability to obtain this result is, however, reduced by a factor of 1/4 for the second procedure, as one is limited

to outcome '+' in the x-measurement. In addition, the case where both outcomes are '0' in the original purification protocol (which also corresponds to a successful purification step) cannot be obtained by the second procedure, which leads to another loss factor of 1/2 in the success probability.

We have neglected until now an initial basis change in protocol 1 which maps $|s\rangle \rightarrow |t_1\rangle$, as the procedure described above (bilateral CNOT operations and z-measurements) purifies triplet states $|t_1\rangle$ rather than singlet states $|s\rangle$. One can avoid this basis change (which would require inhomogeneous single qubit unitary operations) by considering the outcome of the projectors $\tilde{O}_{\mathbf{A}} = P_{-}^{A_2} P_{m_s=0}^{A_1 A_2}$ and $O_{\mathbf{B}} = P_{+}^{B_2} P_{m_s=0}^{B_1 B_2}$ (i.e., taking the '-' outcome of the x-measurement on particle A_2). This sequence of measurements purifies singlet states directly. That is, when applying $\tilde{O}_{\mathbf{A}} O_{\mathbf{B}}$ to two copies of a Werner state with fidelity F, followed by depolarization, the resulting state $\rho' = \mathcal{D}\tilde{O}_{\mathbf{A}} O_{\mathbf{B}} \rho_W(F) \tilde{O}_{\mathbf{A}}^{\dagger} O_{\mathbf{B}}^{\dagger}$ is (after proper normalization) again a Werner state with fidelity F', where

$$F' = \frac{F^2 + [(1-F)/3]^2}{F^2 + 2F(1-F)/3 + 5[(1-F)/3]^2}. \tag{F.5}$$

Note that this is exactly the same output fidelity that is achieved by the original protocol 1 (Ref. [10]). The only difference is that the success probability of our protocol, as compared to protocol 1, is reduced by a factor of 1/8 due to the restrictions to specific measurement outcomes in the sequence of four measurements. It follows that the purification curve is that same for both protocols (while the one of protocol 1', based on exchange interaction, is flatter), and hence the influence of imperfections in local control operations will be the same. Note that also an analogue of protocol 2 [49] can be obtained using similar sequences of measurements $P_{m_s=0}$ and $P_{\pm}$, together with homogeneous Hadamard operations $U_{\mathrm{Had}}^{\otimes 4}$, leading to the same output states but again the success probability (and hence the yield) is reduced by a factor of 1/8.

Such a non-destructive measurement can be accomplished as follows. Consider the case where the (1,1) system has a small exchange splitting, j, while the (0,2) system has a large exchange splitting, J and a large anisotropy parameter, i.e., due to an elongate dot design, γ. Starting with the tunnel coupling closed entirely, we can align the system such that the triplet $|m_s| = 1$ states are slightly above the (1,1) configuration triplet states. Then turning on the tunneling coupling and lowering the right potential leads to adiabatic transfer of the $|m_s| = 1$ subspace, without differentiating those two states, and without differentiating the $|m_s| = 0$ subspace states as well. It does lead to a phase shift between the two $|m_s| = 0$ states due to the finite exchange coupling during the adiabatic transfer procedure.

F.3 Adiabatic preparation

It may be that probabilistic entanglement generation is less desirable than "on-demand" generation. We seek to do so by adiabatic means, as described below. We work with four dots and two auxiliary dots, as shown in Fig. F.3.

When exchange energy is much less than the orbital level spacing we can write the Hamiltonian of the four-electron, four-dot system as

$$H = \sum_{<ij>} J_{ij} \hat{\vec{S}}^i \cdot \hat{\vec{S}}^j \tag{F.6}$$

where J_{ij} is in general a function of perpendicular magnetic field and inter-dot spacing; only adjacent site are coupled as shown in the Figure. For the following analysis we use the Fock-Darwin ground state of each dot as an estimate of the isolated dot ground state, following the work of Ref. [21]. At finite perpendicular magnetic field, there is a crossing from positive to negative J for a given pair as a function of dot size, bias, and inter-dot distance d (e.g., Eq. 7 of [21]). We wish to work in a regime near the crossing, as shown in

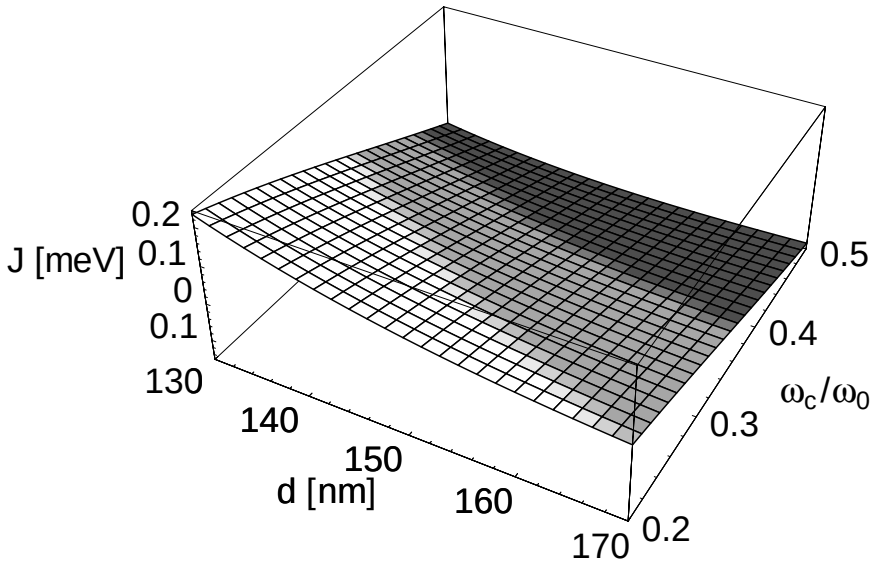

Figure F.2: For 50 nm dots spaced an average of 130 nm from each other, J as a function of perpendicular magnetic field (given in terms of cyclotron frequency to quantum dot level spacing) and inter-dot distance, d. Working near $B = 1$ T, a variation of d from 120 to 140 nm is sufficient to tune the two-dot J value from -0.05 meV to 0.05 meV. (white: $J > 0.05$; lt. gray: $0.05 > J >$ -0.05; dk. gray: $J <$ -0.05)

Fig. F.2.

As the Hamiltonian commutes with $\hat{S}_z = \sum_i \hat{S}_z^i$, starting the system in the $m_s = 0$ subspace will restrict evolution adiabatic or otherwise to that subspace; only spin-flip events, i.e., spin relaxation will move the system out of the $m_s = 0$ subspace. In what follows we define to points in parameter space: $J_{12} = J_{23} = J_{34} = J_{41} = J$ (positive regime) and $J_{12} = J_{23} = -J_{34} = -J_{41} = |J|$ (negative regime).

The first excited state of the $m_s = 0$ subspace in the positive regime is exactly the desired four particle entangled state, $|\Psi\rangle$. To prepare this state reliably, several methods may be used. For example, when J_{34} and J_{41} are adiabatically tuned to negative values while holding J_{12}, J_{23} constant, moving parameters adiabatically to the negative regime, the excited state $|\Psi\rangle$ adiabatically follows to the $m_s = 0$ ground state through a crossing at $J_{34} + J_{14} = 0$.

Preparation of the ground state of the $m_s = 0$ subspace in this negative regime populates, via adiabatic following, the state $|\Psi\rangle$. As all J values are adiabatically tuned to zero from the positive regime, $|\Psi\rangle$ follows to itself. Furthermore, the other states of the $m_s = 0$ subspace are gapped with a energy gap of order J. In this manner, preparation of $|\Psi\rangle$ is protected from small errors in any given J_{ij}, i.e., the effect of fluctuations is suppressed by the gap. The tuning of J values from the negative regime to positive regime and corresponding adiabatic motion is shown in Fig F.3.

Rather than tuning all J to zero directly, raising the potentials of dots 2 and 4 while having finite tunnel coupling to dots A and B will adiabatically reduce the effect J values to zero as the electrons on 2 and 4 tunnel to A and B. Thus, the state $|\Psi\rangle$ can be prepared by adiabatic means.

Several complications and errors may occur in this preparation process. First, in the absence of magnetic field gradients, the ground state in the negative regime is triply degenerate, with $m_s = \pm 1, 0$ states. To select only the $m_s = 0$ state, we note that any anisotropy in the exchange interaction splits the $m_s = 0$ states from their degenerate $|m_s| = 1$ states. Numerically, it is found that for $J_{34} = J_{14} \lesssim -2J_{12} (= J_{23})$ the ground state is the $m_s = 0$ state that adiabatically follows to $|\Psi\rangle$, while the previously degenerate $|m_s| = 1$ states are split, with the relevant energy scale given by $|J_\perp - J_\parallel|$, which can be large (50 μeV, as noted above). In addition, $|\Psi\rangle$ is insensitive to anisotropic terms in the exchange Hamiltonian.

Deviations of the final state from $|\Psi\rangle$ may occur due to errors in two points, when the state that adiabatically follows to $|\Psi\rangle$ crosses with other states. If the error there is primarily due to magnetic field gradients, e.g., hyperfine fields, time dependent perturbation theory gives an error of

$$\epsilon \simeq \frac{A^2}{\hbar N \frac{\partial J}{\partial t}}. \tag{F.7}$$

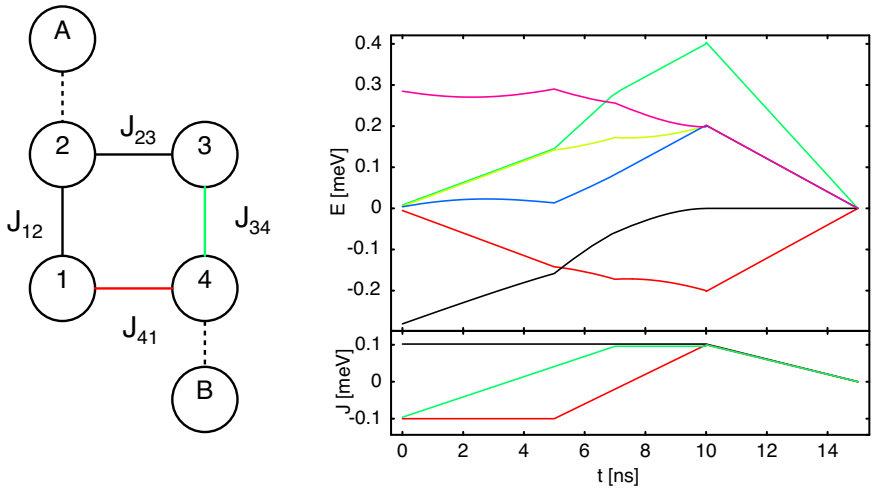

Figure F.3: Four dots (shown left) used for adiabatic preparation $|\Psi\rangle$. Graph shows energy spectrum for the $m_s = 0$ subspace, with exchange constants in lower plot ($J_{12} = J_{23}$ (black), J_{34} (green) and J_{41} (red)). Initial ground state (black) follows via shown adiabatic pathway to $|\Psi\rangle$. The process is insensitive to the exact values of the different exchange couplings.

This error may be made small, e.g., with $(\partial J/\partial t)\hbar^{-1} \simeq 75\text{ns}^{-2}$ corresponding to a complete change of J_{34}, J_{41} from -50 μeV to 50 μeV, $\epsilon \lesssim 10^{-3}$.

Bibliography

[1] K. A. Al-Hassanieh, V. V. Dobrovitski, E. Dagotto, and B. N. Harmon. *e-print: cond-mat/0511681*, (2005).

[2] Robert Alicki, Michal Horodecki, Pawel Horodecki, and Ryszard Horodecki. *Phys. Rev. A*, **65**, 062101, (2002).

[3] Panos Aliferis, Daniel Gottesman, and John Preskill. *Quantum Inf. and Comp.*, **165**, 97, (2006).

[4] F. T. Arecchi, E. Courtens, R. Gilmore, and H. Thomas. *Phys. Rev. A*, **6**, 2211, (1972).

[5] A. Aspect, P. Grangier, and G. Roger. *Phys. Rev. Lett.*, **49**, 1804, (1982).

[6] A. Auerbach. *Interacting Electrons and Quantum Magnetism*. Spinger, (1994).

[7] D. D. Awschalom, N. Samarth, and D. Loss, editors. *Semiconductor Spintronics and Quantum Computation*. Springer-Verlag, Berlin, (2002).

[8] S. D. Barrett and C. H. W. Barnes. *Phys. Rev. B*, **66**, 125318, (2002).

[9] C. H. Bennett, G. Brassard, S. Popescu, B. Schumacher, J. A. Smolin, and W. K. Wootters. *Phys. Rev. Lett.*, **76**, 722, (1996).

[10] C. H. Bennett, G. Brassard, S. Popescu, B. Schumacher, J. A. Smolin, and W. K. Wootters. *Phys. Rev. Lett.*, **76**, 722, (1996).

[11] M. T. Björk, B. J. Ohlsson, T. Sass, A. I. Persson, C. Thelander, M. H. Magnusson, K. Deppert, L. R. Wallenberg, and L. Samuelson. *App. Phys. Lett.*, **80**, 1058, (2002).

[12] Alexandre Blais, Ren-Shou Huang, Andreas Wallraff, S. M. Girvin, and R. J. Schoelkopf. *Phys. Rev. A*, **69**, 062320, (2004).

[13] J. Bollinger and *et al. Phys. Rev. A*, **54**, 4649, (1996).

[14] A. S. Bracker, E. A. Stinaff, D. Gammon, M. E. Ware, J. G. Tischler, A. shabaev, Al. L. Efros, D. Park, D. Gershoni, V. L. Korenev, and I. A. Merkulov. *Phys. Rev. Lett.*, **94**, 047402, (2005).

[15] T. Brandes and B. Kramer. *Phys. Rev. Lett.*, **83**, 3021, (1999).

[16] T. Brandes and T. Vorrath. *Phys. Rev. B*, **66**, 075341, (2002).

[17] S. L. Braunstein, C. M. Caves, R. Jozsa, N. Linden, S. Popescu, and R. Schack. *Phys. Rev. Lett.*, **83**, 1054, (1999).

[18] H.-J. Briegel, W. Dür, J. I. Cirac, and P. Zoller. *Phys. Rev. Lett.*, **81**, 5932, (1998).

[19] G. Burkard, H.-A. Engel, and D. Loss. *Fortschr. Phys*, **48**, 965–986, (2000).

[20] G. Burkard and A. Imamoglu. *e-print: cond-mat/0603119*, (2006).

[21] G. Burkard, D. Loss, and D. P. DiVincenzo. *Phys. Rev. B*, **59**, 2070, (1999).

[22] Guido Burkard, Roger H. Koch, and David P. DiVincenzo. *Phys. Rev. B*, **69**, 064503, (2004).

[23] C. Cabrillo, J. I. Cirac, P. Garcia-Fernandez, and P. Zoller. *Phys. Rev. A*, **59**, 1025, (1999).

[24] A. O. Caldeira and A. J. Leggett. *Ann. of Phys.*, **149**, 347, (1983).

[25] H.Y. Carr and E.M. Purcell. *Phys. Rev.*, **80**, 580, (1954).

[26] Veronica Cerletti, Oliver Gywat, and Daniel Loss. *Phys. Rev. B*, **72**, 115316, (2005).

[27] Ana K. Chattah, Gonzalo A. lvarez, Patricia R. Levstein, Fernando M. Cucchietti, Horacio M. Pastawski, Jesus Raya, and Jerome Hirschinger. *Journal of Chemical Physics*, **119**, 7943, (2003).

[28] J. Chiaverini, J. Britton, D. Leibfried, E. Knill, M. D. Barrett, R. B. Blakestad, W.M. Itano, J.D. Jost, C. Langer, R. Ozeri, T. Schaetz, and D.J. Wineland. *Science*, **308**, 997, (2005).

[29] L. I. Childress, A. S. Sorensen, and M. D. Lukin. *Phys. Rev. A*, **69**, 042302, (2004).

[30] Andrew M. Childs and Isaac L. Chuang. *Phys. Rev. A*, **63**, 012306, (2000).

[31] I. Chiorescu, Y. Nakamura, C.J.P.M. Harmans, and J.E. Mooij. *Science*, **299**, 1869, (2003).

[32] Sucismita Chutia, Mark Friesen, and Robert Joynt. *e-print: cond-mat/0601098*, (2006).

[33] M. Ciorga, A. S. Sachrajda, P. Hawrylak, C. Gould, P. Zawadzki, S. Jullian, Y. Feng, and Z. Wasilewski. *Phys. Rev. B*, **61**, R16315–R16318, (2000).

[34] J. I. Cirac, W. Dür, B. Kraus, and M. Lewenstein. *Phys. Rev. Lett.*, **86**, 544, (2001).

[35] J. I. Cirac and P. Zoller. *Phys. Rev. Lett.*, **74**, 4091, (1995).

[36] J.I. Cirac and P. Zoller. *Physics Today*, (2004).

[37] C. Cohen-Tannoudji, J. Dupont-Roc, and G. Grynberg. *Atom-Photon Interactions: Basic Processes and Applications*. Wiley, New York, (1992).

[38] W. A. Coish and D. Loss. *Phys. Rev. B*, **70**, 195340, (2004).

[39] W. A. Coish and D. Loss. *Phys. Rev. B*, **72**, 125337, (2005).

[40] D. G. Cory, A. F. Fahmy, and T. F. Havel. *Proc. Nat. Acad. Sci. USA*, **94**, 1634, (1997).

[41] A. Cottet, A. Steinbach, P. Joyez, D. Vion, H. Pothier, D. Esteve, and M.E. Huber. In D. Averin, B. Ruggiero, and Silvestrini P., editors, *Macroscopic Quantum Coherence and Quantum Computing*, p. 111, New York, (2001). Kluwer/Plenum.

[42] E. P. Danieli, H. M. Pastawski, and G. A. Álvarez. *Chem. Phys. Lett.*, **402**, 88, (2005).

[43] R. de Sousa and S. Das Sarma. *Phys. Rev. B*, **67**, 033301, (2003).

[44] R. de Sousa, X. Hu, and S. Das Sarma. *Phys. Rev. A*, **64**, 042307, (2001).

[45] Rogerio de Sousa and S. Das Sarma. *Phys. Rev. B*, **68**, 115322, (2003).

[46] Rogerio de Sousa, Neil Shenvi, and K. Birgitta Whaley. *Phys. Rev. B*, **72**, 045330, (2005).

[47] C. Deng and X. Hu. *e-print: cond-mat/0501379*, (2005).

[48] C. Deng and X. Hu. *Phys. Rev. B*, **72**, 165333, (2005).

[49] D. Deutsch, A. Ekert, R. Jozsa, C. Macchiavello, S. Popescu, and A. Sanpera. *Phys. Rev. Lett.*, **77**, 2818, (1996).

[50] M.H. Devoret and R.J. Schoelkopf. *Nature*, **406**, 1039, (2000).

[51] D. P. Divincenzo, D. Bacon, J. Kempe, G. Burkard, and K. B. Whaley. *Nature*, **408**, 339, (2000).

[52] D.C. Dixon, K.R. Wald, P.L. McEuen, and M.R. Melloch. *Phys. Rev. B*, **56**, 4743, (1997).

[53] L.-M. Duan, M. D. Lukin, J. I. Cirac, and P. Zoller. *Nature*, **414**, 413, (2001).

[54] Lu-Ming Duan and Guang-Can Guo. *Phys. Rev. Lett.*, **79**, 1953–1956, (1997).

[55] W. Dür and H.-J. Briegel. *Phys. Rev. Lett.*, **90**, 067901, (2003).

[56] W. Dür, H.-J. Briegel, J. I. Cirac, and P. Zoller. *Phys. Rev. A*, **59**, 169, (1999).

[57] M. V. Gurudev Dutt, Jun Cheng, Bo Li, Xiaodong Xu, Xiaoqin Li, P. R. Berman, D. G. Steel, A. S. Bracker, D. Gammon, Sophia E. Economou, Ren-Bao Liu, and L. J. Sham. *Phys. Rev. Lett.*, **94**, 227403, (2005).

[58] I. Dzyaloshinsky. *J. Phys. Chem. Solid*, **4**, 241, (1958).

[59] Benoit Eble, Olivier Krebs, Aristide Lemaitre, Katarzyna Kowalik, Arkadiusz Kudelski, Paul Voisin, Bernhard Urbaszek, Xavier Marie, and Thierry Amand. *e-print: cond-mat/0508281*, (2005).

[60] Artur Ekert and Richard Jozsa. *Rev. Mod. Phys.*, **68**, 733–753, (1996).

[61] J. M. Elzerman, R. Hanson, L. H. Willems van Beveren, B. Witkamp, L. M. K. Vandersypen, and L. P. Kouwenhoven. *Nature*, **430**, 431, (2004).

[62] Hans-Andreas Engel, Vitaly N. Golovach, Daniel Loss, L. M. K. Vandersypen, J. M. Elzerman, R. Hanson, and L. P. Kouwenhoven. *Phys. Rev. Lett.*, **93**, 106804, (2004).

[63] S. I. Erlingsson and Y. V. Nazarov. *Phys. Rev. B*, **66**, 155327, (2002).

[64] S. I. Erlingsson, Y. V. Nazarov, and V. I. Fal'ko. *Phys. Rev. B*, **64**, 195306, (2001).

[65] Sigurdur I. Erlingsson, Oleg N. Jouravlev, and Yuli V. Nazarov. *e-print: cond-mat/0309069*, (2003).

[66] Sigurdur I. Erlingsson and Yuli V. Nazarov. *Phys. Rev. B*, **70**, 205327, (2004).

[67] M. Eto. *e-print: cond-mat/0210231*, (2002).

[68] P. Facchi, S. Tasaki, S. Pascazio, H. Nakazato, A. Tokuse, and D.A. Lidar. *Phys. Rev. A*, **71**, 022302, (2005).

[69] G. Falci, A. D'Arrigo, A. Mastellone, and E. Paladino. *Phys. Rev. Lett.*, **94**, 167002, (2005).

[70] R. P. Feynman. *Int. J. Theor. Phys.*, **21**, 467, (1982).

[71] R. P. Feynman and F. L. Vernon. *Annals of Physics*, **24**, 118, (1963).

[72] M. Field, C. G. Smith, M. Pepper, D. A. Ritchie, J. E. F. Frost, G. A. C. Jones, and D. G. Hasko. *Phys. Rev. Lett.*, **70**, 1311–1314, (1993).

[73] Luigi Frunzio, Andreas Wallraff, David Schuster, Johannes Majer, and Robert Schoelkopf. *IEEE Trans. Appl. Supercond.*, **15**, 860, (2005).

[74] Toshimasa Fujisawa, Tjerk H. Oosterkamp, Wilfred G. van der Wiel, Benno W. Broer, Ramôn Aguado, Seigo Tarucha, and Leo P. Kouwenhoven. *Science*, **282**, 932–935, (1998).

[75] Toshimasa Fujisawa, Yasuhiro Tokura, and Yoshiro Hirayama. *Phys. Rev. B*, **63**, 081304R, (2001).

[76] Yu. M. Galperin and V. L. Gurevich. *Phys. Rev. B*, **43**, 12900, (1991).

[77] D. Gammon, Al. L. Efros, T. A. Kennedy, M. Rosen, D. S. Katzer, D. Park, S. W. Brown, V. L. Korenev, and I. A. Merkulov. *Phys. Rev. Lett.*, **86**, 5176, (2001).

[78] C. W. Gardiner. *Handbook of stochastic methods*. Berlin: Spinger, 2nd edition edition, (1985).

[79] C. W. Gardiner and P. Zoller. *Quantum Noise: A Handbook of Markovian and Non-Markovian Quantum Stochastic Methods with Applications to Quantum Optics*. Springer-Verlag, 3rd edition, (2004).

[80] G. Giedke, J. M. Taylor, D. D'Alessandro, M. D. Lukin, and A. Imamoglu. *e-print: quant-ph/0508144*, (2005).

[81] V. Giovanetti, S. Lloyd, and L. Maccone. *Phys. Rev. Lett.*, **96**, 010401, (2006).

[82] V. N. Golovach, A. Khaetskii, and D. Loss. *Phys. Rev. Lett.*, **93**, 016601, (2004).

[83] D. Gottesman and I. L. Chuang. *Nature*, **402**, 390, (1999).

[84] Robert B. Griffiths and Chi-Sheng Niu. *Phys. Rev. Lett.*, **76**, 3228, (1996).

[85] Oliver Gywat, Hans-Andreas Engel, Daniel Loss, R. J. Epstein, F. Mendoza, and D. D. Awschalom. *Phys. Rev. B*, **69**, 205303, (2003).

[86] B. I. Halperin, A. Stern, O. Yuval, J. N. H. J. Cremers, J. A. Folk, and C. M. Marcus. *Phys. Rev. Lett.*, **86**, 2106, (2001).

[87] R. Hanson, B. Witkamp, L. M. K. Vandersypen, L. H. Willems van Beveren, J. M. Elzerman, and L. P. Kouwenhoven. *Phys. Rev. Lett.*, **91**, 196802, (2003).

[88] T. Hayashi, T. Fujisawa, H. D. Cheong, Y. H. Jeong, and Y. Hirayama. *Phys. Rev. Lett.*, **91**, 226804, (2003).

[89] C.P. Heij, D.C. Dixon, C.H. van der Wal, P. Hadley, and J.E. Mooij. *Phys. Rev. B*, **67**, 144512, (2003).

[90] X. Hu and S. Das Sarma. *e-print: cond-mat/0507725*, (2005).

[91] S. F. Huelga, C. Macchiavello, T. Pellizzari, A. K. Ekert, M. B. Plenio, and J. I. Cirac. *Phys. Rev. Lett.*, **79**, 3865, (1997).

[92] A. Imamoglu. *Fortschr. Phys.*, **48**, 987, (2000).

[93] A. Imamoglu, D. D. Awschalom, G. Burkard, D. P. DiVincenzo, D. Loss, M. Sherwin, and A. Small. *Phys. Rev. Lett.*, **83**, 4204, (1999).

[94] A. Imamolgu, E. Knill, L. Tian, and P. Zoller. *Phys. Rev. Lett.*, **91**, 017402, (2003).

[95] G. Ithier, E. Collin, P. Joyez, P. J. Meeson, D. Vion, D. Esteve, F. Chiarello, A. Shnirman, Y. Makhlin, J. Schriefl, and G. Schön. *e-print: cond-mat/0508588*, (2005).

[96] A. C. Johnson, J. R. Petta, J. M. Taylor, M. D. Lukin, C. M. Marcus, M. P. Hanson, and A. C. Gossard. *Nature*, **435**, 925, (2005).

[97] Oleg N. Jouravlev and Yuli A. Nazarov. *Phys. Rev. Lett.*, **96**, 176804, (2006).

[98] R. E. Kalman. *Transact. ASME - J. Basic Eng.*, **82**, 35, (1960).

[99] B.E. Kane. *Nature*, **393**, 133, (1998).

[100] R.L. Kautz and J.M. Martinis. *Phys. Rev. B*, **42**, 9903, (1990).

[101] K. V. Kavokin. *Phys. Rev. B*, **69**, 075302, (2004).

[102] A. Khaetskii, D. Loss, and L. Glazman. *Phys. Rev. B*, **67**, 195329, (2003).

[103] A. V. Khaetskii, D. Loss, and L. Glazman. *Phys. Rev. Lett.*, **88**, 186802, (2002).

[104] A. V. Khaetskii and Yu. V. Nazarov. *Phys. Rev. B*, **64**, 125316R, (2001).

[105] Alexander V. Khaetskii and Yuli V. Nazarov. *Phys. Rev. B*, **61**, 12639, (2000).

[106] D. Kielpinski, C.R. Monroe, and D.J. Wineland. *Nature*, **417**, 709, (2002).

[107] J. M. Kikkawa and D. D. Awschalom. *Nature*, **397**, 139, (1999).

[108] B. E. King, C. S. Wood, C. J. Myatt, Q. A. Turchette, D. Leibfried, W. M. Itano, C. Monroe, and D. J. Wineland. *Phys. Rev. Lett.*, **81**, 1525, (1998).

[109] A. Kitaev. *e-print: quant-ph/9511026*, (1995).

[110] D. Klauser, W. A. Coish, and D. Loss. *Phys. Rev. B*, **73**, 205302, (2006).

[111] E. Knill. *Nature*, **434**, 39, (2005).

[112] Franck H. L. Koppens, Joshua A. Folk, Jeroen M. Elzerman, Ronald Hanson, Laurens H. Willems van Beveren, Ivo T. Vink, Hans-Peter Tranitz, Werner Wegscheider, Leo P. Kouwenhoven, and Lieven M. K. Vandersypen. *Science*, p. 1113719, (2005).

[113] H. J. Krenner, M. Sabathil, E. C. Clark, A. F. Kress, D. Schuh, M. Bichler, G. Abstreitr, and J. J. Finley. *Phys. Rev. Lett.*, **94**, 057402, (2005).

[114] M. Kroutvar, Y. Ducommun, D. Heiss, M. Bichler, D. Schuh, G. Abstreiter, and J. J. Finley. *Nature*, **432**, 81, (2004).

[115] C. W. Lai, P. Maletinsky, A. Badolato, and A. Imamoglu. *Phys. Rev. Lett.*, **96**, 167403, (2006).

[116] C.K. Law and J.H. Eberly. *Phys. Rev. Lett.*, **76**, 1055, (1996).

[117] S. D. Lee, S. J. Kim, J. S. Kang, Y. B. Cho, J. B. Choi, Sooa Park, S.-R. Eric Yang, S. J. Lee, and T. H. Zyung. *e-print:cond-mat/0410044*, (2004).

[118] Seungwon Lee, Paul von Allmen, Fabiano Oyafuso, Gerhard Klimeck, and K. Birgitta Whaley. *J. Appl. Phys.*, **97**, 043706, (2005).

[119] J. Levy. *Phys. Rev. Lett.*, **89**, 147902, (2002).

[120] D. A. Lidar, I. L. Chuang, and K. B. Whaley. *Phys. Rev. Lett.*, **81**, 2594–2597, (1998).

[121] E. M. Lifshitz and L. D. Landau. *Quantum Mechanics: Non-Relativistic Theory.* Butterworth-Heinemann, 3rd edition, (1981).

[122] D. Loss and D. P. DiVincenzo. *Phys. Rev. A*, **57**, 120, (1998).

[123] W. Magnus. *Communications of Pure and Applied Mathematics*, **7**, 649, (1954).

[124] Y. Makhlin, G. Schön, and A. Shnirman. *Nature*, **398**, 305, (1999).

[125] Y. Makhlin, G. Schön, and A. Shnirman. *Rev. Mod. Phys.*, **73**, 357–400, (2001).

[126] Y. Makhlin and A. Shnirman. *Phys. Rev. Lett.*, **92**, 178301, (2004).

[127] J.M. Martinis, S. Nam, J. Aumentado, K.M. Lang, and C. Urbina. *Phys. Rev. B*, **67**, 94510, (2003).

[128] J.M. Martinis, S. Nam, J. Aumentado, and C. Urbina. *Phys. Rev. Lett.*, **89**, 117901, (2002).

[129] Lluis Masanes, Guifre Vidal, and J. Ignacio Cirac. *unpublished*, (2002).

[130] K. A. Matveev, L. I. Glazman, and A. I. Larkin. *Phys. Rev. Lett.*, **85**, 2789, (2000).

[131] M. Mehring. *High Resolution NMR Spectroscopy in Solids.* Berlin: Springer-Verlag, (1976).

[132] F. Meier and B. P. Zakharchenya. *Optical Orientation.* Elsevier, (1984).

[133] Florian Meier and Daniel Loss. *Phys. Rev. B*, **71**, 094519, (2005).

[134] I. A. Merkulov, Al. L. Efros, and M. Rosen. *Phys. Rev. B*, **65**, 205309, (2002).

[135] M. Mohseni and D. A. Lidar. *Phys. Rev. Lett.*, **94**, 040507, (2005).

[136] C. Monroe. *Nature*, **416**, 238, (2002).

[137] F. G. Monzon, M. Johnson, and M. L. Roukes. *App. Phys. Lett.*, **71**, 3087, (1997).

[138] J. E. Mooij, T. P. Orlando, L. Levitov, Lin Tian, Caspar H. van der Wal, and Seth Lloyd. *Science*, **285**, 1036–1039, (1999).

[139] Tôru Moriya. *Phys. Rev.*, **120**, 91–98, (1960).

[140] Y. Nakamura, Yu.A. Pashkin, and J.S. Tsai. *Nature*, **398**, 786, (1999).

[141] M.A. Nielsen and I.L. Chuang. *Quantum Computation and Quantum Information.* Cambridge University Press, Cambridge, (2000).

[142] Michael A. Nielsen and Isaac. L. Chuang. *Quantum Computation and Quantum Information*. Cup, (2000).

[143] K. Ono and S. Tarucha. *Phys. Rev. Lett.*, **92**, 256803, (2004).

[144] Yukinori Ono, Akira Fujiwara, Katsuhiko Nishiguchi, Hiroshi Inokawa, and Yasuo Takahashi. *Journal of Applied Physics*, **97**, 031101, (2005).

[145] M. Oskin, F. T. Chong, and I. L. Chuang. *IEEE Computing*, **18**, 79, (2002).

[146] D. Paget. *Phys. Rev. B*, **25**, 4444, (1982).

[147] D. Paget, G. Lampel, B. Sapoval, and V.I. Safarov. *Phys. Rev. B*, **15**, 5780, (1977).

[148] S. Parker and M. B. Plenio. *Phys. Rev. Lett.*, **85**, 3049, (2000).

[149] Yu. A. Pashkin, T. Yamamoto, O. Astafiev, Y. Nakamura, D.V. Averin, and J.S. Tsai. *Nature*, **421**, 823, (2003).

[150] J. R. Petta, A. C. Johnson, C. M. Marcus, M. P. Hanson, and A. C. Gossard. *Phys. Rev. Lett.*, **93**, 186802, (2004).

[151] J. R. Petta, A. C. Johnson, J. M. Taylor, E. Laird, A. Yacoby, M. D. Lukin, and C. M. Marcus. *Science*, **309**, 2180, (2005).

[152] J. R. Petta, A. C. Johnson, A. Yacoby, C. M. Marcus, M. P. Hanson, and A. C. Gossard. *Phys. Rev. B.*, **72**, 161301, (2005).

[153] N V Prokof'ev and P C E Stamp. *Reports on Progress in Physics*, **63**, 669–726, (2000).

[154] J.M. Raimond, M. Brune, and S. Haroche. *Rev. Mod. Phys.*, **73**, 562, (2001).

[155] L. P. Rokhinson, L. J. Guo, S. Y. Chou, and D. C. Tsui. *Phys. Rev. Lett.*, **87**, 166802, (2001).

[156] M. Rontani, S. Amaha, K. Muraki, F. Manghi, E. Molinari, S. Tarucha, and D. G. Austing. *Phys. Rev. B*, p. 85327, (2004).

[157] G. Rose and A. Yu. Smirnov. *J. Phys.: Cond. Mat.*, **13**, 11027, (2001).

[158] G. Salis, D. D. Awschalom, Y. Ohno, and H. Ohno. *Phys. Rev. B*, **64**, R195304, (2001).

[159] G. Salis, Y. Kato, K. Ensslin, D. C. Driscoll, A. C. Gossard, and D. D. Awschalom. *Nature*, **414**, 619, (2001).

[160] R. Schack and C. M. Caves. *Phys. Rev. A*, **60**, 4354, (1999).

[161] J. Schliemann, D. Loss, and A. H. MacDonald. *Phys. Rev. B*, **63**, 085311, (2001).

[162] John Schliemann, Alexander Khaetskii, and Daniel Loss. *Journal of Physics: Cond. Matter*, **15**, R1809, (2003).

[163] F. Schmidt-Kaler, H. Häffner, M. Riebe, S. Gulde, G. P. T. Lancaster, T. Deuschle, C. Becher, C. F. Roos, J. Eschner, and R. Blatt. *Nature*, **422**, 408, (2003).

[164] K. Schulten and P. G. Wolynes. *J. Chem. Phys.*, **68**, 3292, (1978).

[165] Neil Shenvi, Rogerio de Sousa, and K. Birgitta Whaley. *Phys. Rev. B*, **71**, 224411, (2005).

[166] P. W. Shor. *Phys. Rev. A*, **52**, R2493, (1995).

[167] R.W. Simmonds, K. M. Lang, D. A. Hite, S. Nam, D. P. Pappas, and John M. Martinis. *Phys. Rev. Lett.*, **93**, 077003, (2004).

[168] C. P. Slichter. *Principles of Magnetic Resonance*. Springer-Verlag, 3rd edition, (1996).

[169] A. Sorensen, L. I. Childress, C. Wan Der Wal, and M. D. Lukin. *Phys. Rev. Lett.*, **92**, 063601, (2004).

[170] P.C.E. Stamp. *The Physics of Communication*, chapter 3, pp. 39–82. New Jersey: World Scientific, (2003).

[171] A. M. Steane. *Phys. Rev. Lett.*, **77**, 793, (1996).

[172] A. M. Steane. *Quantum Inf. and Comp.*, **2**, 297, (2002).

[173] A. M. Steane. *Phys. Rev. A*, **68**, 042322, (2003).

[174] A. M. Steane. *e-print: quant-ph/0412165*, (2004).

[175] A.M. Steane. *Nature*, **399**, 124, (1999).

[176] Dimitrije Stepanenko, Guido Burkard, Geza Giedke, and Atac Imamoglu. *Phys. Rev. Lett.*, **96**, 136401, (2006).

[177] K. M. Svore, B. M. Terhal, and D. P. DiVincenzo. *Phys. Rev. A*, **72**, 022317, (2005).

[178] J. M. Taylor, W. Dür, P. Zoller, A. Yacoby, C. M. Marcus, and M. D. Lukin. *Phys. Rev. Lett.*, **94**, 236803, (2005).

[179] J. M. Taylor, H.-A. Engel, W. Dür, A. Yacoby, C. M. Marcus, P. Zoller, and M. D. Lukin. *Nature Physics*, **1**, 177, (2005).

[180] J. M. Taylor, G. Giedke, H. Christ, B. Paredes, J. I. Cirac, P. Zoller, M. D. Lukin, and A. Imamoglu. *e-print: cond-mat/0407640*, (2004).

[181] J. M. Taylor, A. Imamoglu, and M. D. Lukin. *Phys. Rev. Lett.*, **91**, 246802, (2003).

[182] J. M. Taylor and M. D. Lukin. *e-print: quant-ph/0512059*, (2005).

[183] J. M. Taylor, C. M. Marcus, and M. D. Lukin. *Phys. Rev. Lett.*, **90**, 206803, (2003).

[184] J. M. Taylor, J. R. Petta, A. C. Johnson, A. Yacoby, C. M. Marcus, and M. D. Lukin. *e-print: cond-mat/0602470*, (2006).

[185] G. Teklemariam, E. M. Fortunato, C. C. Lopez, J. Emerson, J. P. Paz, T. F. Havel, and D. G. Cory. *e-print: quant-ph/0303115*, (2003).

[186] Barbara M. Terhal and Guido Burkard. *Phys. Rev. A*, **71**, 012336, (2005).

[187] Akihisa Tomita and Kazuo Nakamura. *Int. J. Quant. Inf.*, **2**, 119, (2004).

[188] Lev Vaidman and Zion Mitrani. *Phys. Rev. Lett.*, **92**, 217902, (2004).

[189] W. G. van der Wiel, S. De Franceschi, J. M. Elzerman, T. Fujisawa, Tarucha S., and L. P. Kouwenhoven. *Rev. Mod. Phys.*, **75**, 1, (2003).

[190] L. M. K. Vandersypen, R. Hanson, L. H. Willems van Beveren, J. M. Elzerman, J. S. Greidanus, S. De Franceschi, and L. P. Kouwenhoven. In *Quantum Computing and Quantum Bits in Mesoscopic Systems*. Kluwer Academic Plenum Publishers, (2002).

[191] Lieven M.K. Vandersypen and I. L. Chuang. *Rev. Mod. Phys.*, **76**, 1037, (2004).

[192] L. Viola and S. Lloyd. *Phys. Rev. A*, **58**, 2733, (1998).

[193] Lorenza Viola, Emanuel Knill, and Seth Lloyd. *Phys. Rev. Lett.*, **85**, 3520–3523, (2000).

[194] D. Vion, A. Aassime, A. Cottet, P. Joyez, H. Pothier, C. Urbina, D. Esteve, and M.H. Devorett. *Science*, **296**, 886, (2002).

[195] A. Wallraff, D. I. Schuster, A. Blais, L. Frunzio, R.-S. Huang, J. Majer, S. Kumar, S. M. Girvin, and R. J. Schoelkopf. *Nature*, **431**, 162, (2004).

[196] J.S. Waugh, L.M. Huber, and U. Haeberlen. *Phys. Rev. Lett.*, **20**, 180, (1968).

[197] M. B. Weissman. *Rev. Mod. Phys.*, **60**, 537, (1988).

[198] D. J. Wineland, J. C. Bergquist, J. J. Bollinger, W. M. Itano, F. L. Moore, J. M. Gilligan, M. G. Raizen, D. J. Heinzen, C. S. Weimer, and C. H. Manney. In E. Arimondo, W. D. Phillips, and F. Strumia, editors, *Laser Manipulation of Atoms and Ions, Proc. Enrico Fermi Summer School, Course CXVIII, Varenna, Italy, July, 1991*, p. 539. North-Holland, Amsterdam, (1992).

[199] W. M. Witzel, Rogerio de Sousa, and S. Das Sarma. *e-print: cond-mat/0501503*, (2005).

[200] L.-A. Wu and D. A. Lidar. *Phys. Rev. A*, **66**, 062314, (2002).

[201] L.-A. Wu and D. A. Lidar. *Phys. Rev. Lett.*, **88**, 207902, (2002).

[202] L.-A. Wu and D. A. Lidar. *Phys. Rev. Lett.*, **91**, 097904, (2003).

[203] W. Yao, Ren-Bao Liu, and L. J. Sham. *e-print: cond-mat/0508441*, (2005).

[204] P. Zanardi and M. Rasetti. *Phys. Rev. Lett.*, **79**, 3306, (1997).

[205] Xinlan Zhou, Debbie W. Leung, and Isaac L. Chuang. *Phys. Rev. A*, **62**, 052316, (2000).

[206] D. M. Zumbühl, C. M. Marcus, M. P. Hanson, and A. C. Gossard. *Phys. Rev. Lett.*, **93**, 256801, (2004).

[207] W. H. Zurek. *Phys. Rev. D*, **24**, 1516, (1981).